FINITE ELEMENT ANALYSIS OF SAMPLING DISTURBANCE IN CLAY SOILS

by

MOHAMED BENDAHGANE

Ingenieur Civil (Ecole Polytechnique d'Alger)

A Thesis submitted for the degree of

Master of Science

Department of Civil Engineering,

University of Glasgow.

March, 1989.

CONTENTS

ACKNOWLEDGEMENTS

The author would like to express his appreciation to the head of department, Dr. D.R. Green for the provision of facilities in the Department of Civil Engineering at Glasgow University where the work described in this thesis was carried out.

The author is greatly indebted to Dr. T.G. Davies for valuable supervision, encouragement and advice during the course of this study and to Professor D. Muir Wood for his interest in this work.

My grateful thanks are also due to:

* Dr I.McConnochie for the administrative matters.

* My friends S.E. Djellab, R. Manaa and M. Benredouane for their useful discussions and comments.

* My friends Z. Merouani, J. Moussa, A. Bouazza, M. Souici, L. Bensmail, A. Bensalem, T. Bouden and Y.K To for their encouragement.

* The Algerian Government for the financial support during the period of the research.

* Finally, my special thanks are reserved for my family for their boundless patience and continual encouragement throughout the years.

SUMMARY

The work presented in this thesis describes a numerical (Finite Element Method) analysis of sampling disturbance in clay soils during the sampling operation.

Of all sampling methods, block sampling appears to disturb soils least but this method is extremely tedious and is restricted to shallow depths. For this reason thin walled sampling is the usual choice for most practical purposes although soils may be grossly distorted both during the sampling process itself and the subsequent laboratory testing. The major objective of this study is to improve existing finite element analyses of sampling disturbance of clays during sampling. An investigation into the parameters having the greatest effects on sampling disturbance has been carried out. These parameters include the effect of sampler geometry, roughness of the sampling tube and soil stress history. Atotal stress analysis using the Von Mises criterion was carried out as well as an effective stress analysis using a critical state elastoplastic model.

From the analysis of the results it is shown that the rough thick walled tubes cause the greatest downdrag on samples during penetration and in general yielding of the soil initiates close to the sampler tip and propagates along both sides of the sampling tube and into the soil below the sampler. Eventually, the yield zone reaches the central part of the sample ahead of the sampling tube. Maximum pore water pressures devlop close to the sampler tip which suggests that during subsequent delays before testing water would migrate from the sides to the central portion of the sample. The results of this investigation also show that highly overconsolidated clays are more susceptible to disturbance than lightly overconsolidated clays. Further work in this area is needed and it is suggested, among other recommendations, that instrumented test on carefully controlled sampling operations should be carried out in the future.

NOTATION

Major symbols used in the text are listed below. others are defined as they first appear.

B Strain matrix

Cu Undrained shear strength of the soil

Cu_{se} Undrained shear strength of the slip elements

D Sampler diameter

D^e Elastic constitutive matrix

D^{ep} Elato-plastic constitutive matrix

E Young's modulus

e Void ratio

f Yield function

H Hardening parameter

(I_1, I_2, I_3) and (J_1, J_2, J_3) Stress invariants

J Jacobian matrix

K Global stiffness matrix

K_0 Coefficient of earth pressure at rest

K_{nc} Coefficient of earth pressure at rest for normally consolidated soil

K Bulk modulus

K^e Element stiffness matrix

L Length of the sampling tube

M Frictional constant

N_i Shape function

P Point load

p Mean effective stress

p_0 Past maximum mean effective stress

Q Plastic potential

q Deviator stress

r Radius of the sampling tube

t Thickness of the sampling tube

u_0 Initial pore water pressure

u_i Displacement vector

z Depth

α Adhesion factor for the slip elements

σ Effective stress

σ^t Total stress

σ_{ij} Stress tensor

$\sigma_1, \sigma_2, \sigma_3$ Principal stresses

$\underline{\epsilon}$, $\underline{\epsilon^e}$, $\underline{\epsilon^p}$ Total, Elastic and Plastic strain vectors

ϵ_v , ϵ_d Volume and deviatoric strains

ϵ_{ij} Strain tensor

ν Poisson's ratio

φ Angle of friction

τ_f Shear stress on the failure plane

λ Plasticity multiplier

λ Slope of the normal consolidation line

κ Slope of the swelling line

CHAPTER 1

INTRODUCTION

1.1 BACKGROUND

HVORSLEV [27] wrote in 1949 in his monumental thesis a set of specifications for fixed–piston samplers with thin–walled tubes to take "undisturbed" samples in soft clays. This early work is the most comprehensive treatment of the subject of sampling disturbance and it has ever since formed the basis for the design of samplers all over the world. His systematic analysis of the sampling process included a critical examination of factors influencing the quality of clay samples, such as transport, storage conditions, extrusion, trimming and mounting in laboratory apparatus.

Of all sampling methods, block sampling appears to disturb soils least but this method is extremely tedious and is restricted to shallow depths. For this reason thin–walled sampling is the usual choice for most practical purposes although soils may be grossly distorted both during the sampling process itself and the subsequent laboratory sample preparation. In essence, thin walled sampling involves pushing a thin tube into the soil and then freeing the sample from the parent soil, Fig. 1.1 .

The mechanical disturbance of clays resulting from the sampling process is the most obvious source of destruction of their original structure. This affects the soil properties , particularly shear strength and compressibility. These soil disturbances lead to an underestimation of soil strength and stiffness which is economically

undesirable.

Research carried out since Hvorslev's day has quantified some of the effects of sampling disturbance. These studies have included both laboratory investigations as well as numerical studies of the load–deflection and strength characteristics of soils and these are discussed in detail in the following section.

In general, causes of soil disturbances are, stress changes prior and during sampling, pore water pressure equalisation and dissipation , protracted periods of storage, and extrusion of soil from the sampling tube. Examination of all these factors is outside the scope of this thesis. The more limited objectives of this study is to carry out a numerical (Finite Element Method) analysis of sampling disturbance during the sampling process itself. In particular, to investigate the stress and pore water pressure changes which occur in the sample. In this way, the distortions suffered by samples and the degree of yielding undergone during field sampling can be assessed.

1.2 LITERATURE REVIEW

In this section, the review of research studies pertaining to sampling disturbances is confined to thin–walled tube sampling of cohesive soils. Experimental as well as theoretical studies are presented.

1.2.1 Experimental Work

The literature review is most conveniently subdivided into studies relating to disturbances which occur (i) before sampling, (ii) during sampling ,and (iii) after sampling.

(i) Disturbance before sampling

SKEMPTON and SOWA (1964)

The effect of stress release caused by sampling on the strength of soil was the subject of an experimental investigation by Skempton and Sowa [52]. Experiments were carried out to determine the undrained strength of a saturated clay under conditions representing (i) the clay in the ground and (ii) samples unaffected by any mechanical disturbances. Skempton and Sowa [52] consolidated Weald clay from the slurry state under K_0 conditions in a conventional triaxial chamber. To simulate the undisturbed state of the sample (termed an ideal sample by Skempton and Sowa [52]) one specimen was tested under undrained conditions immediately after consolidation. Stress relief was simulated by reducing the vertical total stress of another specimen under undrained conditions until the vertical total stress became equal to the cell pressure (lateral total stress). This second sample was termed a perfect sample. The difference between the undrained shear strengths of these two specimens was 2%. The clay used in the experiment is only moderately sensitive to micro–structural effects. However a clay more sensitive to such effects might show a rather large drop in strength and further research is required on this point.

LADD and LAMBE (1963)

Ladd and Lambe [36] conducted experiments similar to those of Skempton and Sowa [52] on Kawasaki clay and Boston Blue clay but also studied tube samples. Their results showed that the undrained shear strengths of ideal samples were about 12% higher than perfect samples.

Other investigators also carried out similar tests but using different soils to those reported by Skempton and Sowa[52] (Seed and Noorany[51], Noorany and

Smith[46], Okamura[47], Atkinson and Kubba[5]). These reported that the differences between the undrained shear strengths of ideal samples and perfect samples ranged from 0 to 6%.

For practical purposes , the observed differences in undrained shear strengths due to in−situ stress release do not appear to be significant. But Kirkpatrick and Rennie [35], Alonso et al[1] and Atkinson and Kubba [5] showed that the undrained elastic moduli of perfect samples could be as much as 50% lower than ideal samples.

In summary, it appears that normally consolidated clays do not suffer any significant decrease of undrained shear strength due to stress release but the undrained elastic modulus decreases by a substantial amount. For overconsolidated soils, stress release does not appear to have any effect on the undrained shear strength.

(ii) Disturbance during sampling

Soil remolding, migration of pore water, sampler geometry, friction between soil and sampling tube, soil type, rate of penetration of sampler and the method of advancing the sampler have all ben cited as pertinent factors in the mechanics of sampling disturbance.

HVORSLEV (1949)

Hvorslev [27] stated that the principal causes of sampling disturbance during sampling are:

1− Displacement of the soil by the sampler

2− Inside friction between the sample and the sampler or its liner

3− Pressure on top of the sampler

While a sampler is being forced into the soil, the pressure on top of the sample

and the inside wall friction tend to compress and distort the soil layers and to increase the pressure on the area directly below the sampler. As the sampler advances, a part of the soil underneath is displaced by the walls of the sampler and pushed aside. During the first part of the drive , while the inside wall friction and the top pressure still are small, some of the displaced soil (called excess soil by Hvorslev[27]) may be forced into the sampler. It increases the thickness (and causes convex distortions) of the soil layers in the upper part of the sample. When the entrance of excess soil is relatively small, the distortions have a fairly uniform curvature , Fig. 1.2.a, but when the entrance of excess soil is so large that the thickness of the soil layers is increased by more than 30%, the distortions assume a characteristic shape resembling that of flattened bulb, Fig. 1.2.b . Entrance of excess soil increases with increasing amounts of displaced soil or increasing wall thickness of the sampler, and also with increasing pressure on top of the sampler. Inside wall friction also tends to increase the convex curvature of the soil layers. The distortion is generally small in the central part but increases sharply (and may be confined entirely to a zone of 'drag') close to the sampler wall, Fig. 1.3.a . However, very large convex distortions, nearly parabolic in shape, are in some cases produced by inside wall friction, Figure. 1.3.b . Inside wall friction also governs the pressure on and the disturbance of the soil below the sampler, and it is the most important single source of disturbance of the soil during the sampling operations.

Hvorslev[27] recognized that the geometry of the sampler is an important factor in soil sampling. Indeed, during the sampling operation, the amount of soil displaced which causes soil distortions depends greatly on the thickness of the tube wall. Consequently, a thin– walled tube is generally used to minimize soil disturbance. The shape of the cutting edge is also an important factor in soil sampling. It should be sharp and never rounded or blunt, and the angle of taper should be as small as practicable.

KALLSTENIUS (1958)

Kallstenius [29] investigated the effect of friction between the soil and the walls of sample tubes in soft clays and in dense sand. Large variations of wall frictional resistance were observed for soft clays and if sample penetraton was interrupted for a few seconds, these frictional forces increased. Wall friction developed in dense sand was about 40% of the coefficient of friction of the sand. The conclusions drawn by Kallstenius in his research on mechanical disturbances in clay samples taken with piston samplers are that sample quality is mainly influenced by the sampler in the following ways:

a— Disturbance of soil ahead of the sampler caused by pushing the sampler down to the sampling depth.

b— Disturbance of soil outside the sampler during pushing to accomodate the displaced volume of the sampler wall.

c— Disturbance of soil inside and outside the sampler caused by friction between soil and sampler wall.

LANG (1971)

Lang [41] carried out a series of tests on a stiff clay using a thin—walled, Open Drive Samper. The forces applied to the sampler, and displacements of the sampler and the soil sample were measured . Undrained triaxial compression tests were carried out on specimens cut from the tube samples. The two methods used for estimating what proportions of the total applied force was transmitted from the inside of the sample tube to the sample were based on measurements made on the widthdrawal force and the intrusion force. The total force required to push the sampler into the soil was measured directly while the part of this total force which was transmitted from the inside of the tube to the sample was estimated by two methods. The first method probably over—estimates the inside

force while the second probably under-estimates it. Using these two methods , the ratio of inside force to total force gave mean values of 0.48 to 0.28 respectively, for the peak values of these forces .

For both advance and withdrawal of the sampler , the average peak surface shear stress on the area of the sampler in contact with the soil was calculated. Both gave very similar results; the average wall friction in stiff clays was 64% of the undrained shear strength of the soil. It was also noted that when two test specimens were cut from the same tube sample, the strength of the lower specimen was about 40% higher than that of the upper specimen.

SCHJETNE (1971)

Schjetne [50] carried out an experimental investigation on the pore pressure changes in a soft clay during sampling. He inserted a small piezometer connected to a vibrating-wire pore water pressure transducer into the piston of a Norwegian Geotechnical Institute fixed piston sampler. The sampler used was 95 mm in diameter and 100 mm long. The area ratio and inside clearance as defined in Fig. 1.4 were approximately 14% and 1.4% respectively. Two tests were carried out during sampling; one on a plastic clay and one on a quick clay. Schjetne measured pore pressures during each stage of the test. His results revealed that the excess pore water pressures developed by pushing the sampler into the clay were between 150 and 200 percent of the initial pore water pressure . When the sampler was removed, negative pore water pressures were developed which were about 20% of the initial effective overburden pressure. After a few hours, the negative pore water pressures dropped to zero.

From these results , it is apparent that the centre of the sample swelled and that the pore water migrated from the distorted outer zone to the relatively undisturbed central zone.

EDEN (1971)

Eden [19] compared the undrained shear strengths and preconsolidation pressures of tube samples recovered by four different types of fixed piston samplers from a highly sensitive Canadian clay (Lada clay) with those from block samples. He found that the undrained shear strengths of tube samples were about one half those of block samples.

LA ROCHELLE (1981)

La Rochelle et al [43] studied the behaviour of a sensitive clay during the sampling operation. Their laboratory study on block samples showed that the lateral strain produced by the change of volume resulting from the intrusion of a thin–wall tube sampler was six times as large as the strain required to destructure the clay. It was thus evident that these displacements should be minimized and that reducing the area ratio by using thinner tubes was one way to accomplish this aim. However there is a practical lower limit to the thickness of tubes which may be used, but other possibilities exist. The area ratio, as illustrated in Fig. 1.4, is increased by the existence of the inside clearance of the tube. This has the disadvantage of allowing and even forcing a lateral expansion of the sample within the tube, since that space is under suction due to the tightness of the piston inside the tube. As a result, a large part of the change of the volume will take place towards the inner side of the tube, so that the sample will be squeezed in around the cutting edge as illustraed in Fig. 1.4 . As this effect was thought to be one of the main causes of the disturbance during sampling, it was decided to eliminate the inside clearance. No significant friction was expected to develop between the tube and the sensitive clay which may be considered to be self lubricating. It was also reasoned that if the angle of attack of the cutting edge was small as suggested by Kallstenius [29,30], the change of

volume would occur towards the outside of the tube and the influence of the thickness of the tube would be minimized. However, the elimination of inside clearance brings one difficulty; the fact that commercially available tubes are not perfectly cylindrical.

La Rochelle [29] carried out a series of tests with a 54 mm piston tube sampler with internal clearance and exactly similar samplers using tubes of 54, 75 and 100 mm diameter without internal clearances. These included mainly unconfined compression and unconsolidated undrained compression tests. From the data obtained in this study, the following conclusions were drawn. The specimens located in the middle part of the tubes were of better quality than those at the ends. The upper parts of the tubes were systematically disturbed either by the action of the piston being pushed into the ground or by the suction applied during the extrusion of the tube. Also, the lower parts were occasionally disturbed, probably by the suction produced during the extraction of the tube. Fig. 1.5 gives the results of unconfined compression tests made on eight specimens from 75 mm tubes; the specimens are numbered 1 to 8 from top to bottom. In order to take into account the increase of shear strength with depth along the length of the tube, the ratio of the undrained shear strength C_{uf} obtained by unconfined compression tests to the field vane strength C_{uv} was used. It is seen that the upper three specimens (number one to three) and possibly the lower specimen (number eight), Fig. 1.5, are of lesser quality than the specimens numbered four to seven. The lesser quality of the samples at the ends of the tube may be associated with the effects of suction during and after sampling. It can be avoided only by eliminating this suction, in other words eliminating the internal clearance and by avoiding the 'piston effect' during sampler withdrawal. The 54 mm tubes without internal clearance ratio seem to give better results than the 54 mm tube with inside clearances; the improvement in strength being 20% or more and the moduli are higher by 50 to 100%. In most cases the 75 mm and 100 mm tubes gave better results than the 54 mm tubes and sometimes there

was a marked improvement: of over 100% in the strengths and 150% in the tangent moduli.

From this study, La Rochelle et al [29] concluded that the tubes should be shaped according to the principles illustrated in Fig. 1.4 and that larger sizes are preferable, 75 mm diameter beeing the acceptable minimum for routine investigations. La Rochelle et al [29] added that in order to ensure that the middle third of the sample is of good quality when the diameter is increased , the length of the sampling tube should also be increased, otherwise the upper and the lower disturbed zones might cover the whole length of the sample.

Finally, it is worth nothing that La Rochelle studied only sensitive clays where the friction between sampler and soil might be neglected. However, it is well established (Hvorslev [29]) that the inside wall friction is the most important single source of disturbance during the sampling process in less sensitive soils.

(iii) Disturbance after sampling

Disturbance after sampling relates to sample sealing, transportation, storage and extrusion.

KALLSTENIUS (1971)

Kallstenius [31] pointed out that damage from deformation of samples, shocks, heavy vibration and changes in water content after sampling are major sources of disturbance. These effects may be time dependent. Kallstenius carried out tests on a normal–sensitive clay and a quick clay. Samples were tested by the fall–cone test at the site immediately after sampling and in the laboratory 24 hours later. The transport was very carefully organised to prevent strong vibratons

or shocks. Laboratory testing yielded much lower strength values and, therefore, the time effect was suspected to be the main reason for the strength reduction. Such a time delay can be explained by water migration from the more disturbed parts of the samples to the less disturbed parts. The influence was smaller where the clay had dried slightly near the soil surface. The effects of shock loads were investigated by dropping samples contained in plastic tubes from a height of 1 m onto an asphalt floor. The peak acceleration of the samples was estimated to be 500 g . The reduction of the undrained shear strength which was measured by the fall–cone test was found to increase with liquidity index, LI, of the soil. The maximum reduction for the normal sensitive clays was 30%. Some samples of quick clays showed no such decrease but it was assumed that they had already been damaged during transport.

Samples of soft clay were also vibrated for about 10 minutes to simulate the disturbance due to transport by train for about 500 Km. The frequency of vibration was 50 Hz and the amplitude 0.025 mm – 0.050 mm. Both an increase (max 26%) and a reduction (max 22%) of the shear strength were observed.

SONE et al (1971)

Soil samples are subject to considerable disturbance when they are extruded from sampling tubes. Sone et al [54] studied this aspect of sample disturbance on alluvial samples extruded from thin–walled brass tubes. Wire strain gauges were used to measure the axial and circumferential strain. Sone et al [54] drew the following conclusions:

1– The extrusion pressures on these soil samples were several times larger than their unconfined compressive strengths, which resulted in average compressive

strains of about 1%.

2– The largest strains took place in the lower parts of the sample tubes where the extruding pressures were applied; the unconfined compressive strengths of the lower samples were consequently, 10 to 20% smaller than those of the upper samples.

3– The maximum strains measured during extrusion were approximately equal to the failure strain in unconfined compression.

1.2.2 Numerical Studies

ALONSO et al (1981)

Alonso et al [1] described a numerical analysis of sampling disturbance by means of an axisymmetric finite element algorithm. They used Zienckiewicz's [62] viscoplastic 'flow' approach to solve a variety of extrusion, rolling and other forming processes. In Alonso's work, the soil was modelled as a Drucker– Prager solid; that is, a uni– phase material. Sample tube advancement was simulated by displacing three surface nodes progressively downwards into the soil which was modelled by means of fifty (50) nine– noded finite elements , Fig 1.6 . The simulation of tube advancement (which, realistically must incorporate slip at the soil interface) and the discretization employed are too crude to permit quantitative interpretation of the results of this study. Although Alonso et al [1] suggest that the contours of mean pressure , Fig. 1.7 , derived from their analysis may be interpreted as contours of equal excess pore water pressure , this contention is difficult to justify in real soils subjected to gross distortions. Moreover, the dissipation of pore water pressure during sampling and during the delay before laboratory testing is carried out cannot be predicted by this algorithm which does not differentiate between the solid and fluid phases. It should be

noted, however, that the authors of this study view their algorithm as a first step to a more rigorous analysis of the problem.

KARIM (1984)

Karim [32] analysed the sampling operation by means of the finite element method using the finite element mesh shown in Fig. 1.8 . He idealised the soil as a Von Mises solid, and, also as a two–phase critical state material. Three series of numerical tests were carried out using both large and small deformation algorithms. In the first and second series, the sampler was assumed to be perfectly smooth. In the third series, friction was specified on the inner surface of the sampler equal to 0.42 Cu (Cu: undrained shear strength of the soil) and 0.94 Cu in order to simulate different tube roughnesses. Numerical tests were carried out using samplers of various thicknesses.

The main results for smooth samplers, are that the samples are dragged down to a certain extent with the sampler, Fig. 1.9, while the sample top surface remains very nearly horizontal. Close to the tip, the displacements are slightly larger along the wall than in the centre. In the case of rough samplers, Fig. 1.10, large downward movements start to take place from the early stages of penetration. Zones of failure within the sample occur initially close to the edge of the sampler and propagate downwards. The most extensive soil failure occurs for the thickest roughest tubes, Fig. 1.11 and 1.12. Maximum pore water pressures develop close to the sampler tip and then water tends to migrate from to the sides to the central portion of the sampler, Fig. 1.13 and 1.14 . Karim confirmed Terzaghi's judgement that an area of ratio of less than 13% is necessary if disturbance is to be kept within tolerable values. He recommended that slip elements should be used for modelling frictional boundary conditions accurately at the soil/sampler interface. He also advocated further parametric studies into the effects of soil properties and tube geometry.

BALIGH (1984)

Baligh's strain path method[6] provides an integrated and systematic framework for elucidating and predicting pile foundation behaviour, interpreting in situ stresses , assessing sampling disturbance effects and, in general, approaching 'deep geotechnical problems'.

Observations of soil deformation caused by the undrained penetration of rigid objects in saturated clays led Baligh to hypothesize that, due to the severe kinematic constraints that exist in 'deep' penetration problems, soil deformation and strains are, by and large, independent of the shearing resistance of the soil. This means that these problems are essentially strain–controlled and implies that even if relatively simple soil properties (e.g isotropy) are utilized to estimate deformation and strains caused by penetration, the errors introduced are likely to be reasonably small.

The strain path method is a theoretical analysis of the flow of incompressible soil based on the construction of streamlines from a combination of appropriate sources and uniform flow. The procedure for the analysis of undrained clays is as follows.

A steady state flow pattern which is compatible with the boundary conditions is first chosen. For undrained (incompressible) flow this may be conveniently expressed in terms of a stream function, from which the velocities are determined by differentiation. The 'simple pile' shape shown in Fig. 1.15 has been used by Baligh for pile analysis and is derived from a single source located in a uniform flow . The stream function is :

$$\Psi = \frac{V}{4\pi(r^2 + z^2)^{1/2}} - \frac{v_0 r^2}{2} \qquad (1.1)$$

v_0 : uniform vertical velocity.

r : radial coordinate in cylindrical system.

z : vertical coordinate in cylindrical system.

V : rate of volume emitted by point source.

where the radial and the vertical velocities are defined as :

$$U = \frac{1}{r} \frac{\partial \Psi}{\partial z} \qquad (1.2)$$

$$V = -\frac{1}{r} \frac{\partial \Psi}{\partial r} \qquad (1.3)$$

The strain rates can be determined from the velocities at every point and thus the strain history of any material point can be determined. Fig. 1.16 shows the strain histories of three material elements as the simple pile is driven past them. The diagram shows the vertical strain plotted against the hoop strain and, for comparison, the hatched area shows the range of strains encountred in triaxial compression and extension tests and the pressumeter test. Clearly the soil adjacent to a pile (or penetrometer) is subjected to very large strains.

Given stress boundary conditions in the upstream direction it is possible to integrate a stress–strain law along each streamline to give the stresses throughout the soil. Finally, it is worth noting that the strain path method considers only smoothly curved boundaries. Consequently, the effects of a cutting shoe on sampling disturbance for example cannot be studied properly. An analysis of sampling disturbance by means of the strain path method has been given by Baligh [6,7]. Fig 1.17 shows the vertical strain of an element located at the centerline of the tube at various positions. It can be seen that (a) the soil is subjected to considerable distortions and (b) the peak strain varies between 1%

for the thin samplers and 4% for the thick samplers. These strains would result in failure. Thus Baligh pointed out that the gross soil distortions due to sampler penetration indicate the necessity of reevaluating standard sampling and laboratory testing procedures utilized at present to estimate the in situ behaviour of soils. Improvements in current tube sampling and laboratory testing practices can be achieved by systematic investigations of the following factors; sampler geometry, inside wall friction, water content and volume changes during and after sampling.

1.3 CONCLUSION

On the Experimental Work

Clearly, the process of sampling results in significant irreversible changes in soil properties. Of all the various ways in which a soil sample is disturbed before testing, two links in the chain of disturbance – tubing and extrusion– appear to be the most significant. Indeed, Hvorslev [27] stated that the inside wall friction is the most important single source of disturbance of soil during sampling operation. Nevertheless, tubing and extrusion have received scant attention compared with investigations on the changes in soil strength due to stress release despite the fact that losses in undrained strength due to stress release amount to only about 10% or less. Part of the reason for this disparity of effort seems to be due to the difficulties of monitoring and controlling the requisite tests.

On Numerical Studies

a) Finite Element Method

So far very few numerical studies on the subject have been reported in the literature. Alonso et al [1] described a numerical analysis of sampling disturbance by means of a finite element algorithm. In Alonso's work, the soil was modelled very simply as Drucker– Prager solid; that is , a uniphase material. This algorithm is not adequate for soils since it does not differentiate between the solid and fluid phases. However Alonso et al [1] view their algorithm as as a first step to a more rigorous analysis of the problem.

Karim [32] analysed the same problem using a more sophisticated model in which the soil was idealised as a critical state elastoplastic material. He believed that further advances were necessary , i.e including slip elements at the soil/sampler interface and that parametric studies on the effects of soil properties would be useful.

b) Strain Path Method

A recently developed method which is attracting much attention is the Strain Path Method pioneered by Baligh (1984). The Strain Path Method is particularly applicable to problems of deeply buried structures where the pattern of deformations can be described by steady state flow. It is a theoretical analysis of the flow of incompressible soil based on the construction of streamlines from a combination of appropriate sources and uniform flow. Baligh [6,7] used this method to assess sampling disturbance effects. One of his important conclusions is that during the sampling process, soils fail before entering the sampler. Consequently, Baligh concluded that it is necessary to reevaluate standard sampling and laboratory testing procedures used at present. He added that further investigation is needed into several aspects of the problem.

1.4 OBJECTIVES

The major objective of this thesis is to improve existing finite element analyses of sampling disturbance in order to study the mechanical disturbance of clays during sampling. Proper constitutive laws for soil are needed for this purpose and, consequently, appropriate constitutive models for clays are examined and their behaviour under various loading conditions investigated. The problem of sampler wall friction is overcome by using the so called slip elements as discussed in chapter 3. The results of a parametric study which includes the following factors, diameter to thickness ratio of the sampler, geometry of the sampler tip, wall–soil adhesion as well as soil properties and history are given in chapter 4. This study aims to investigate the stress and pore water pressure changes which occur during sampling as well as the progressive mechanism of failure and displacement fields occuring in the soil mass. In this way, some quantitative measures of the effects of sampling disturbance can be obtained which may be relevant to field practice.

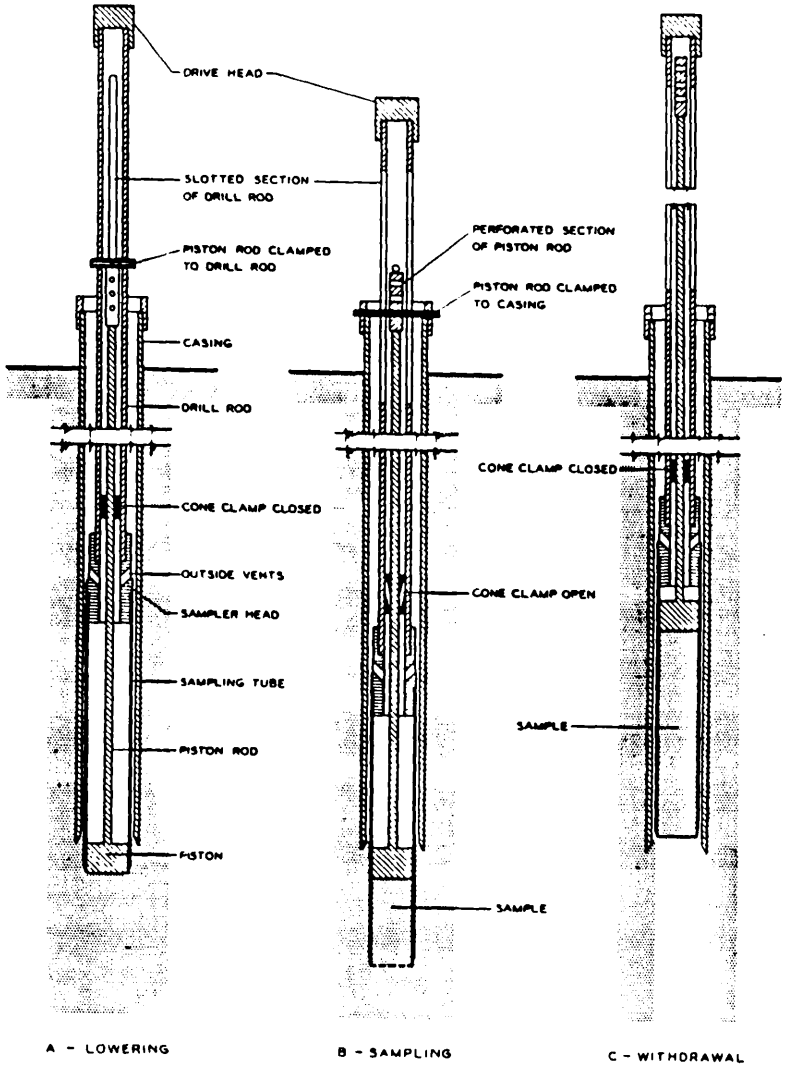

Figure 1.1 Piston sampler with stationary piston (27)

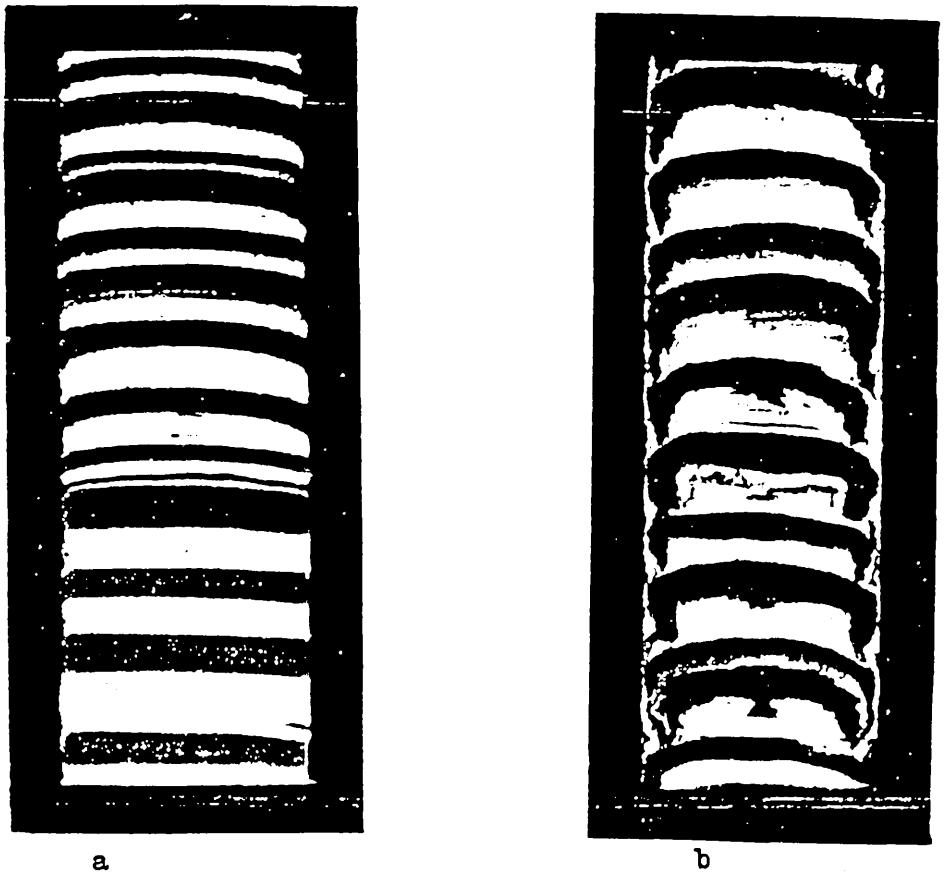

Figure 1.2 Distortions by entrance of excess soil. (27)

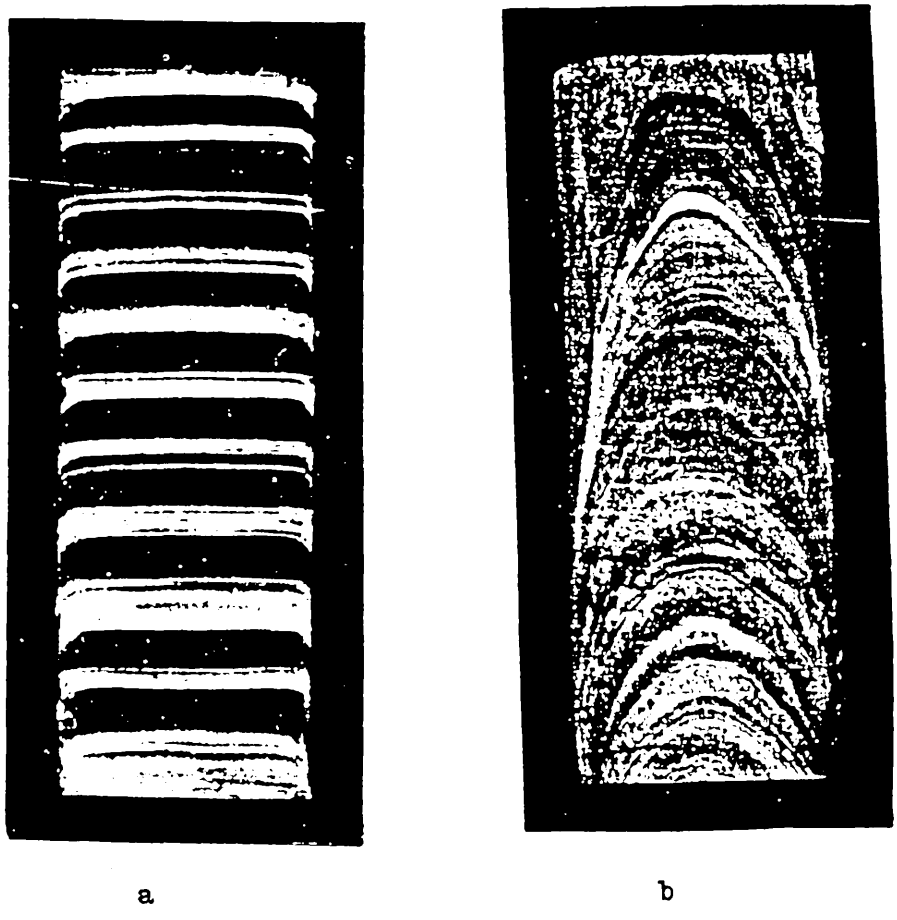

a b

Figure 1.3 Drag and distortion by inside friction (27)

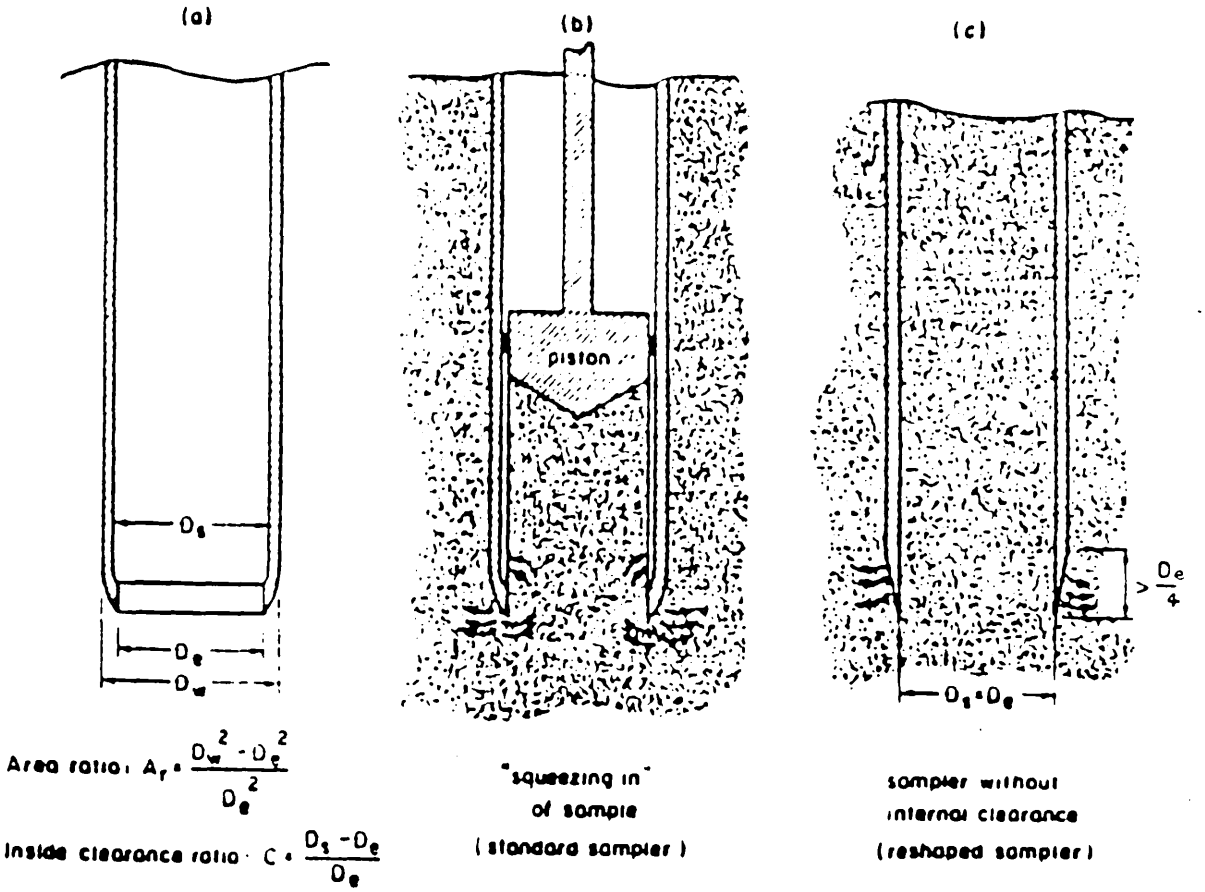

Figure 1.4 Sampling tubes with and without internal clearance (43)

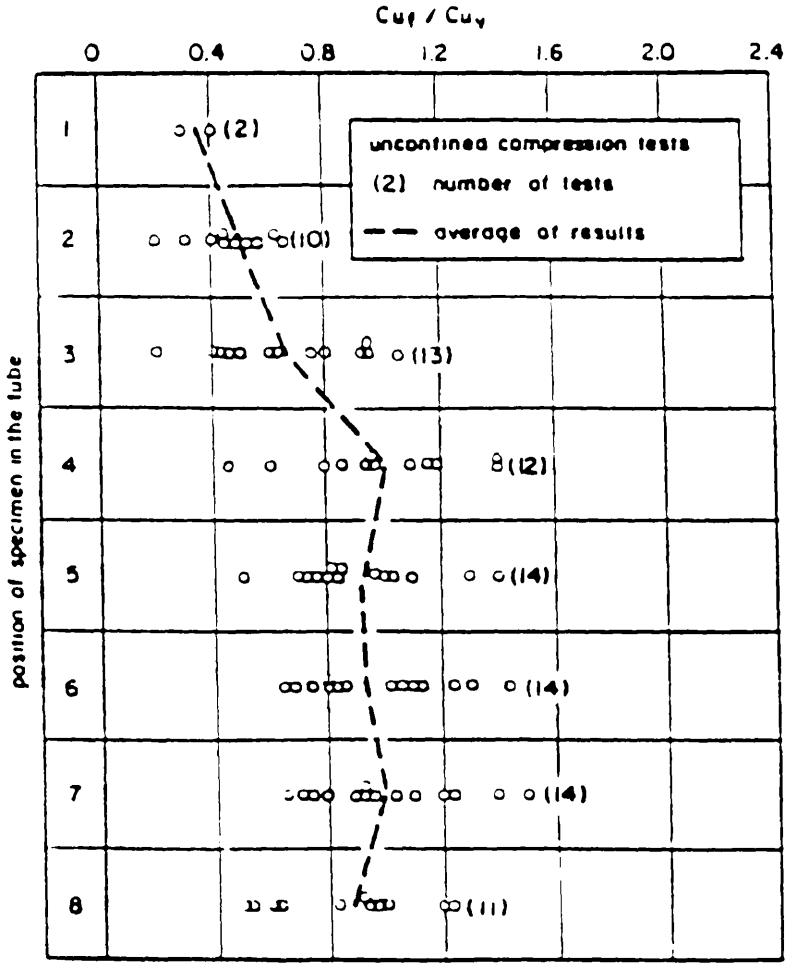

Figure 1.5 Variation of the quality of the specimens within the 75 mm diameter tubes (43)

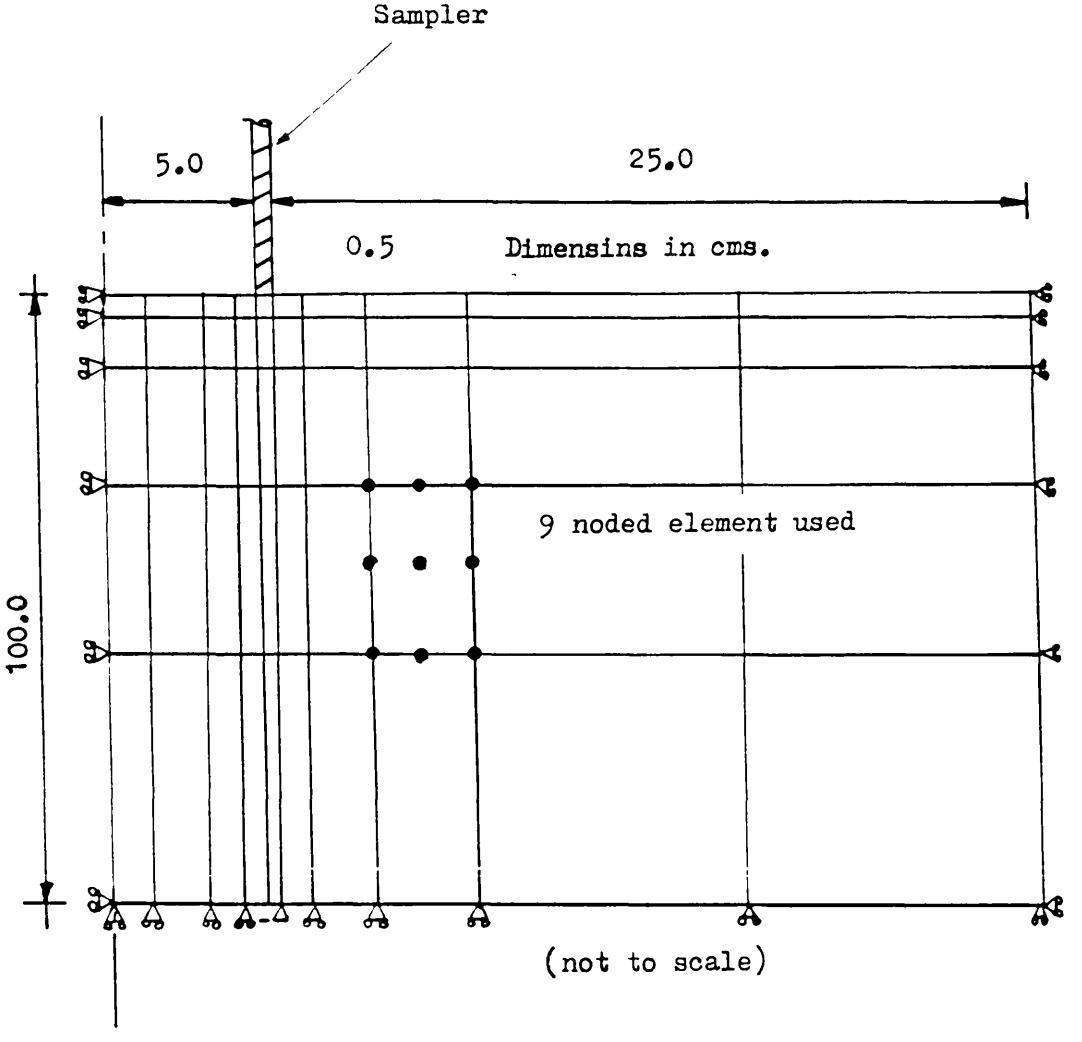

Figure 1.6 Finite element mesh for the sampling problem (1)

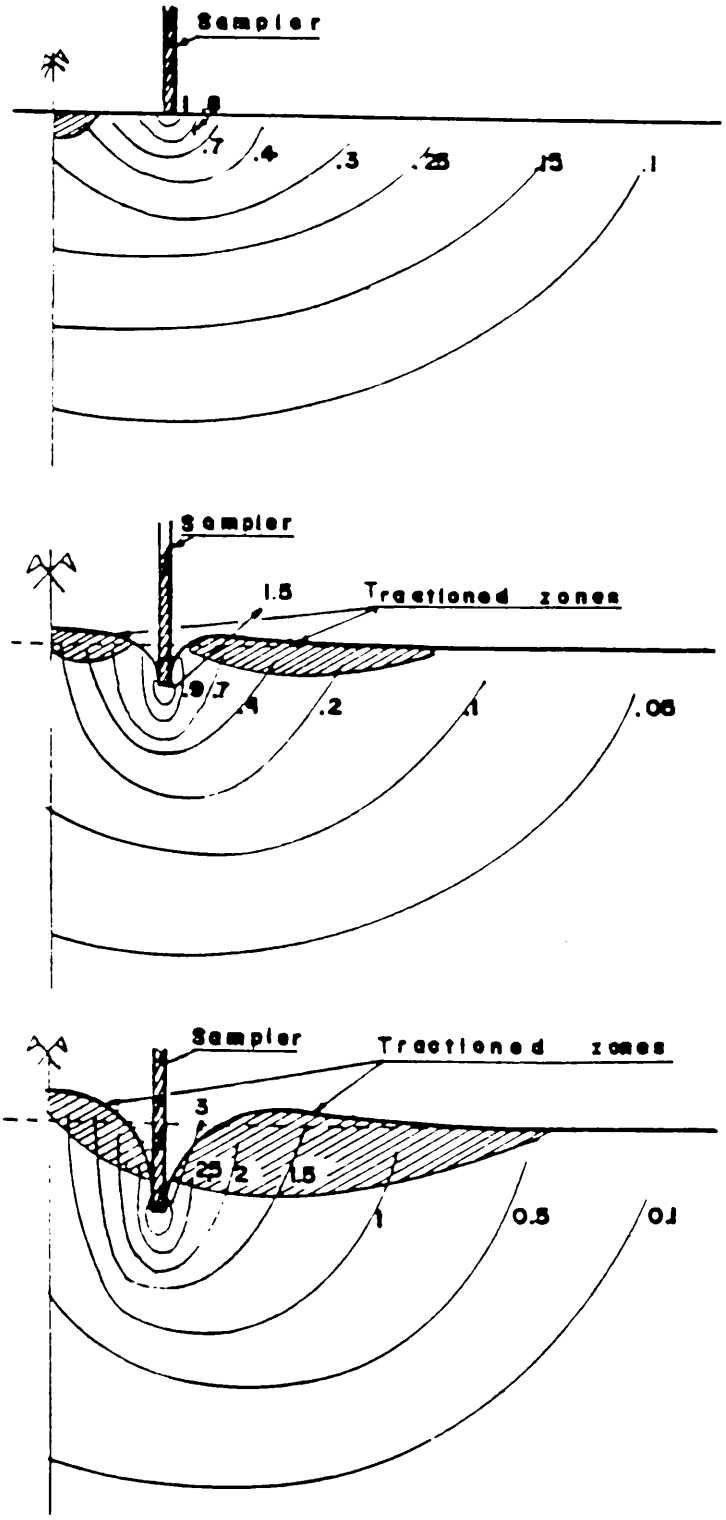

Figure 1.7 Contours of mean stress (kg/cm^2) for sampler travels of 0.0, 2.0 and 4.0 cm (1)

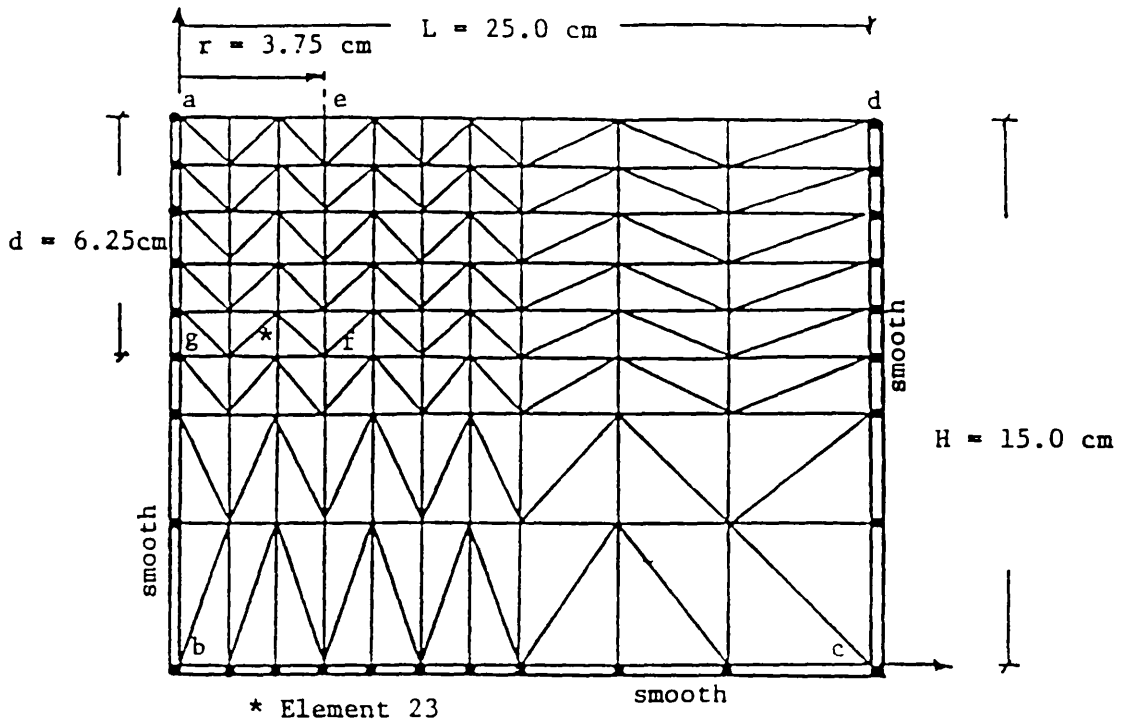

Figure 1.8 Finite element mesh for the sampling problem. (32)

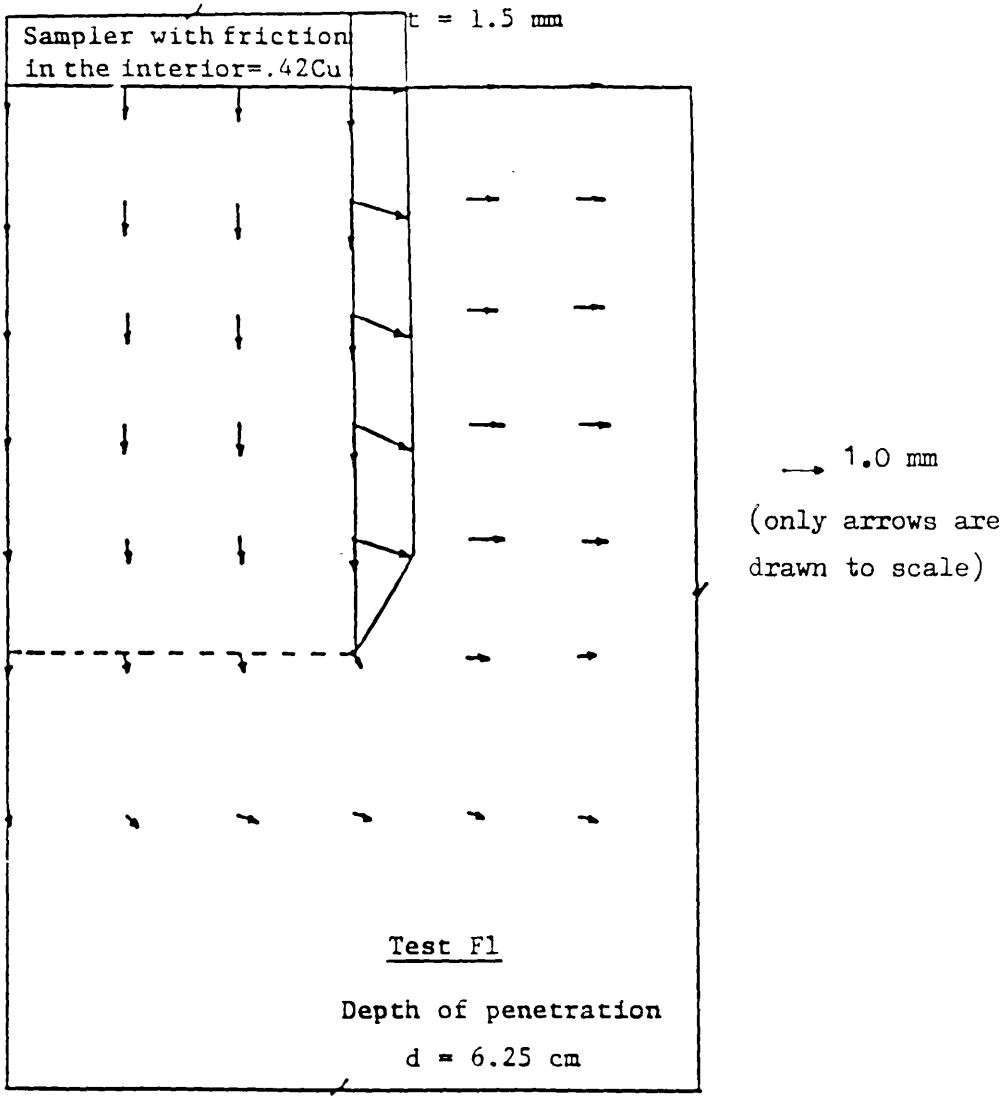

Figure 1.10 Displacement field in the vicinity of the sampler at full penetration. (32)

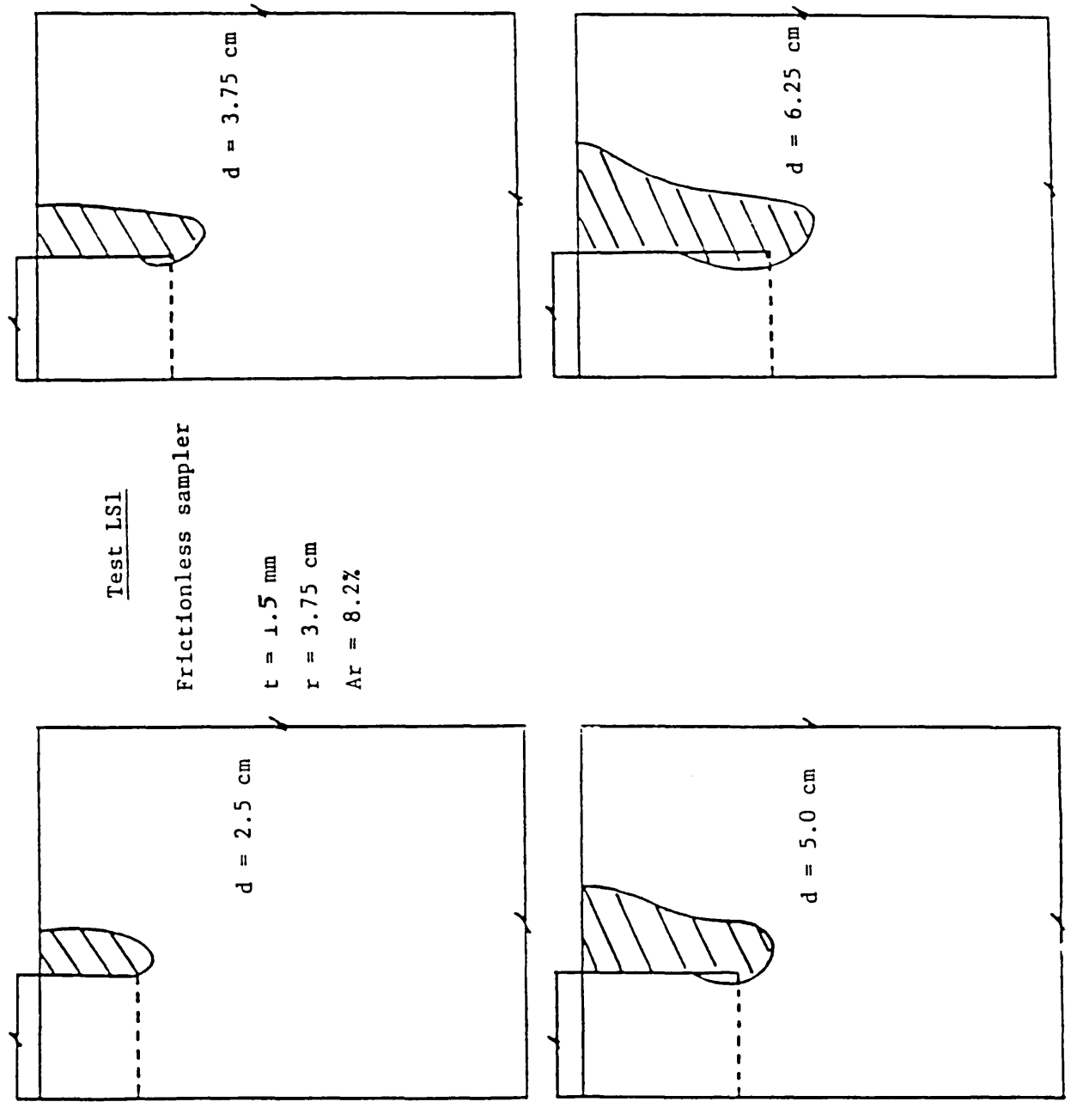

Figure 1.11 Growth of failure zones at various stages of penetration. (32)

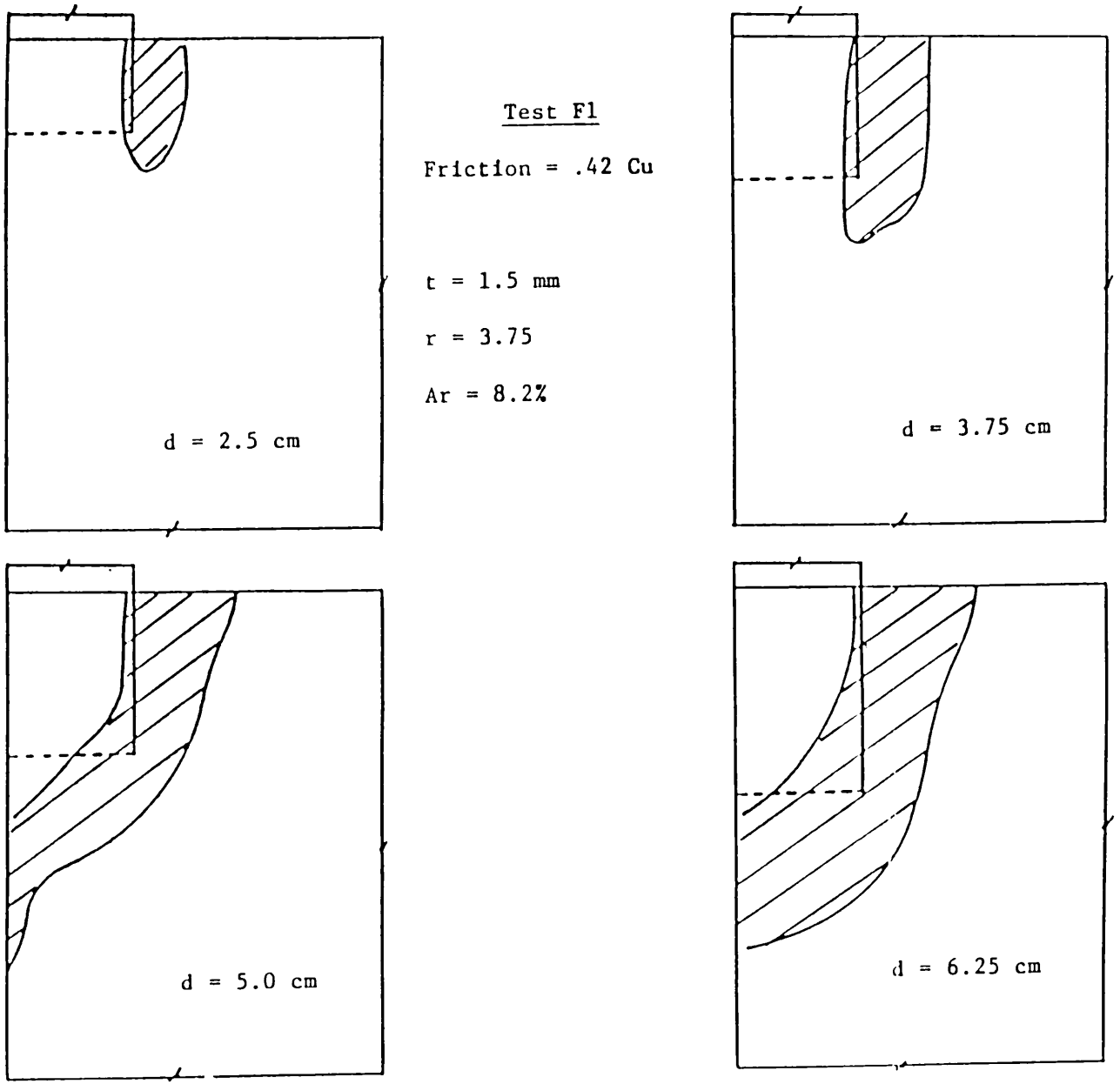

Figure 1.12 Growth of failure zones at various stages of penetration. (32)

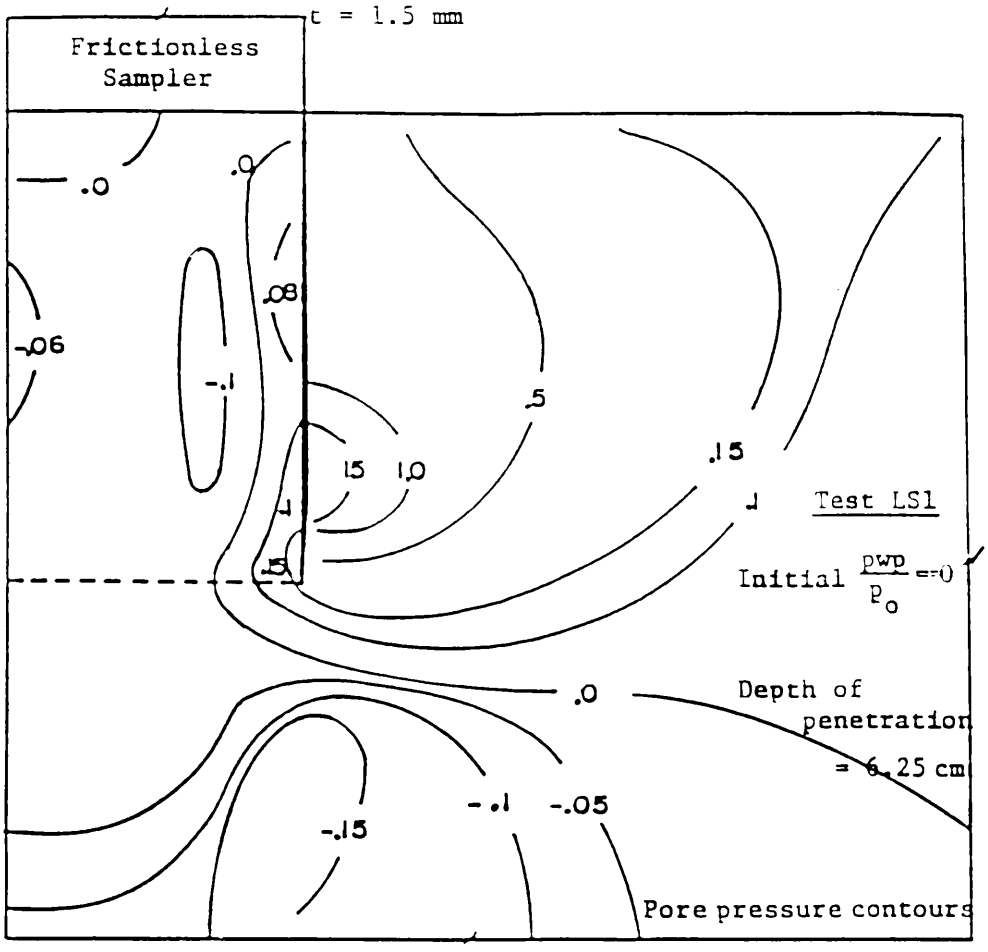

Figure 1.13 $\frac{pwp}{p_o}$ contours at the end of penetration (32)

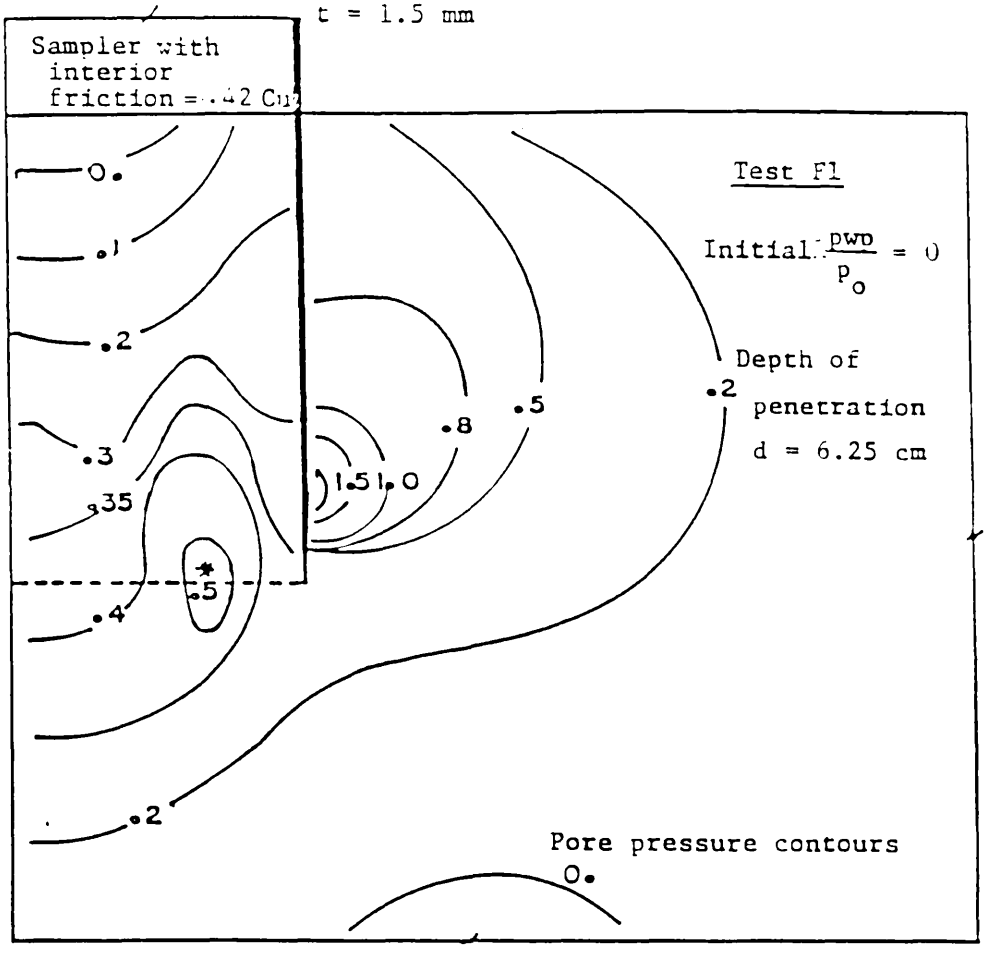

Figure 1.14 $\frac{pwp}{p_o}$ contours at the end of sampling. (32)

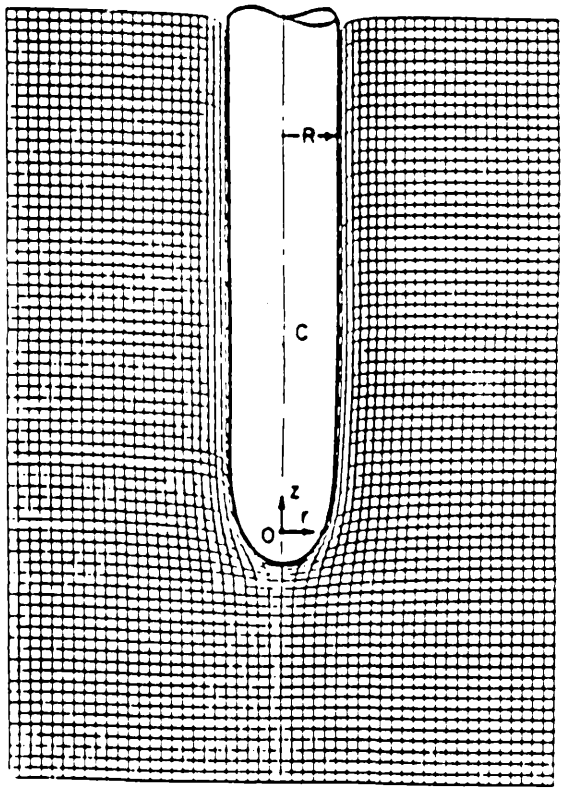

Figure 1.15 Deformation of a square grid during undrained penetration of a 'simple pile' into saturated clay (6)

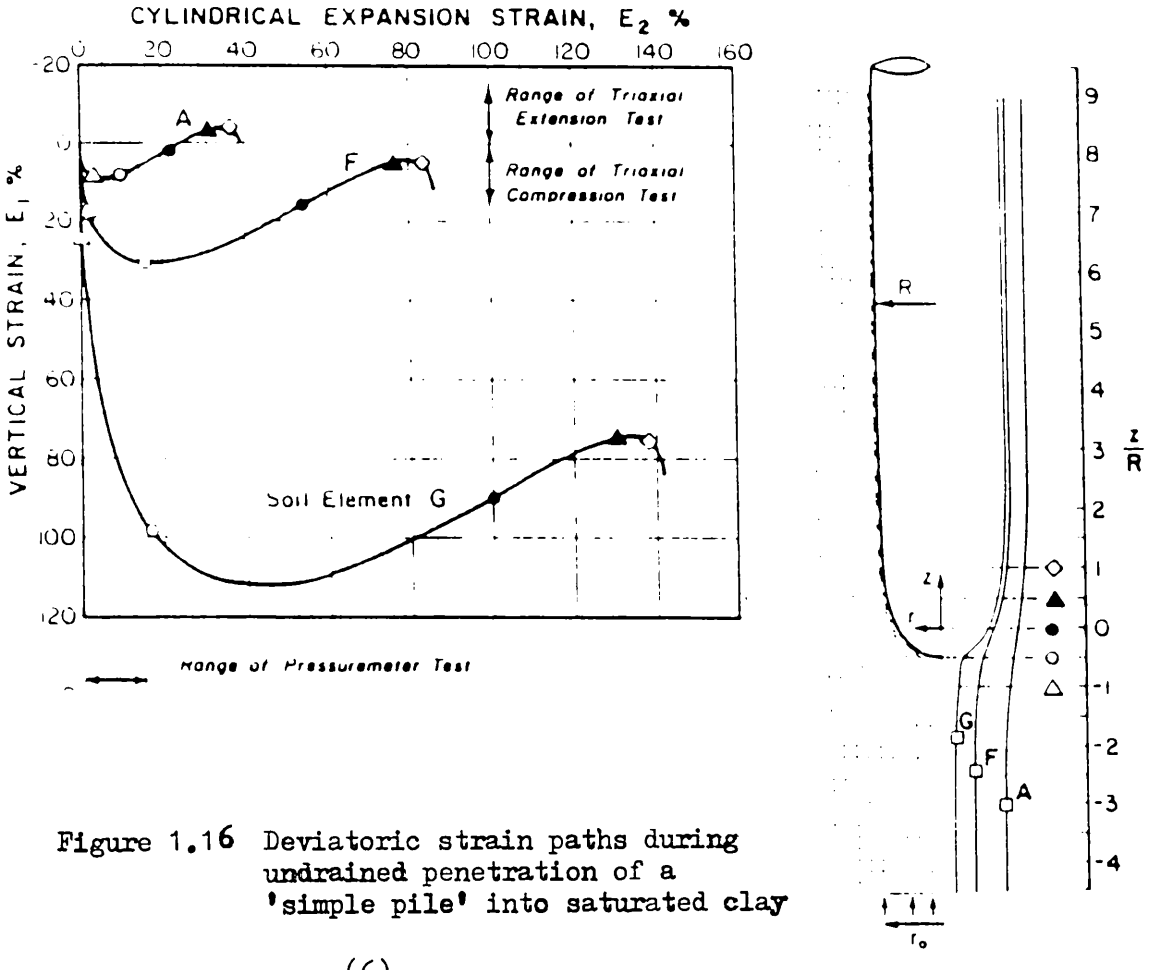

Figure 1.16 Deviatoric strain paths during undrained penetration of a 'simple pile' into saturated clay

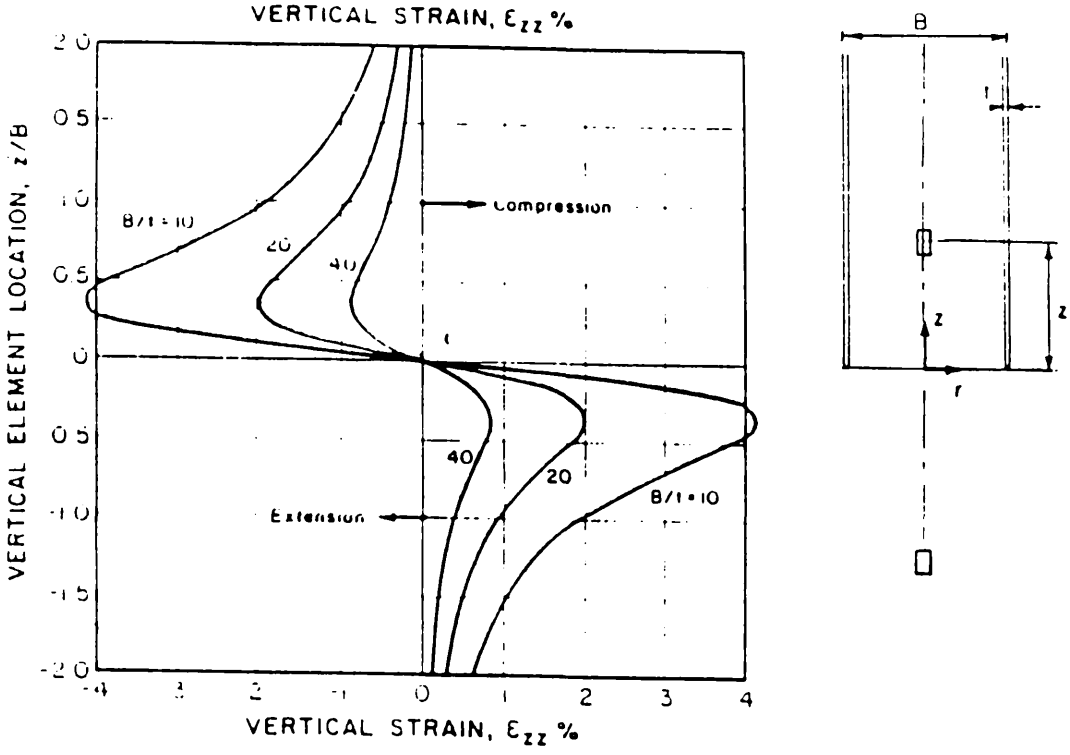

Figure 1.17 Strain history at sampler centerline (6).

CHAPTER 2

SOIL MODELS

2.1 INTRODUCTION:

A material model (constitutive law) is a mathematical model that describes the stress–strain behaviour of a material. Realistic *constitutive* (*stress–strain*) *laws* are essential if reliable results are to be obtained using numerical methods of analysis. In recent years considerable research effort has been expended on the theoretical formulation of constitutive laws and the measurement of material parameters. The former involves use of continuum mechanics whereas the latter hinges on accurate measurement of the parameters using sophisticated equipment.

The Von Mises model is often adequate for total stress analysis of soils in undrained conditions. However, for effective stress analysis, a more complex model is necessary. In this thesis, use is made of the critical state model which combines the Mohr–Coulomb criterion, dilatancy and soil stress history in a coherent model of plasticity. The model yields pore water pressure changes directly and can be used to predict changes in post–sampling strength and stiffness.

2.2 FLOW THEORY OF PLASTICITY

2.2.1 Introduction

In general, materials suffer elastic as well as plastic deformations. The

simplest (linear) constitutive law is the isotropic generalized Hooke's law characterized by an unique relationship between stresses and strains. This relationship is completely defined by two physical constants; the Poisson's ratio ν and the modulus of elasticity, E. The generalized form of Hooke's law is :

$$\begin{Bmatrix} \sigma_x \\ \sigma_y \\ \sigma_z \\ \tau_{xy} \\ \tau_{yz} \\ \tau_{zx} \end{Bmatrix} = A \begin{bmatrix} 1-\nu & \nu & \nu & 0 & 0 & 0 \\ \nu & 1-\nu & \nu & 0 & 0 & 0 \\ \nu & \nu & 1-\nu & 0 & 0 & 0 \\ 0 & 0 & 0 & 0.5-\nu & 0 & 0 \\ 0 & 0 & 0 & 0 & 0.5-\nu & 0 \\ 0 & 0 & 0 & 0 & 0 & 0.5-\nu \end{bmatrix} \begin{Bmatrix} \epsilon_x \\ \epsilon_y \\ \epsilon_z \\ \gamma_{xy} \\ \gamma_{yz} \\ \gamma_{zx} \end{Bmatrix} \qquad (2.1)$$

where $$A = E / (1-2\nu)(1+\nu) \qquad (2.2)$$

This law is valid for a very limited class of materials because many strains are nonlinear and nonrecoverable at load levels of interest. This is particularly true for soils. In consequence it is necessary to examine the more complicated theory of elastoplasticity. At the outset for simplicity, this can be at best explained by reference to the observed behaviour of metals.

A typical stress–strain curve for a metal under uniaxial tension is shown in Figure 2.1. For applied stresses less than the initial yield stress σ_y, the deformation is linearly elastic and, if the metal is unloaded, the strains caused on loading are fully recovered on unloading. However, if the metal is loaded beyond σ_y, plastic strains occur when the state of the metal might be represented by point G. When the metal is unloaded it follows path GB and some (elastic) strain is recovered. However, at B, the metal has suffered large irrecoverable plastic strain. If the metal is reloaded from B the deformation is again linearly elastic until yielding occurs at the stress level σ_g. The stresses σ_y and σ_g at which the

behaviour of the metal becomes plastic are known as yield stresses and an effect of plastic straining from Y to G is to raise the yield stress from σ_y to σ_g; this effect is known as strain hardening. If the metal is loaded beyond G it will eventually fail at F where the stress is σ_f.

It is worth noting that, firstly, yielding of metals is not influenced by mean stress. Secondly, failure is not the same as yielding, and thirdly, because the reloading paths do not follow the original loading path, the strains will be dependent on the stress history. Elastoplastic behaviour is thus characterized by history dependent deformation.

To completely describe the stress–strain relations for a simple elastoplastic material model, three different statements are required.

– A condition for yielding : yield surface

– A flow rule for the material. This specifies the relative magnitudes of the incremental plastic strains when the material is yielding, that is a relationship between the directions of the principal plastic strain increments and the principal stresses.

– A hardening law for the material. This is a relationship between the amount a material hardens and the plastic strain the material undergoes or the work that is done on the material when it is yielding.

The basic theory of elastoplasticity is reviewed in the sequel.

2.2.2 Yield Criterion / Function:

The yield criterion can be defined as the limit of elastic deformations, expressed as a function of the stress level. For a one–dimensional state of stress, the yield criterion can be easily defined in terms of the uniaxial compressive stress or uniaxial tensile stress σ_y. However, under multiaxial states of stress, a mathematical expression involving all the stress components is required.

In general, the yield function may be expressed in the form:

$$f(\underline{\sigma},R) = 0 \qquad (2.3)$$

where:

$\underline{\sigma}$ is the stress tensor,

R is the hardening parameter,

And for uniaxial loading, this simplifies to:

$$\sigma - \sigma_y(\epsilon^p) = 0 \qquad (2.4)$$

where σ and σ_y are the uniaxial stress and the yield stress, respectively.
The form of these expressions must be based on experimental observations. The hardening parameter R is usually a function of the plastic strains, that is:

$$R = R(\underline{\epsilon}^p) \qquad (2.5)$$

The yield function $f=0$ is represented, in principal stresses space, by a surface called the yield surface (Figure 2.2). When $f<0$ the behaviour of the material is elastic but when $f=0$ the behaviour of the material is elasto–plastic and the material is in a state of yield. $f>0$ is a physically inadmissible state of stress.

2.2.3 Plastic Potential, Flow Rule

It is assumed that the flow of material at yield is governed by some

function of current stresses called the plastic potential – by analogy with Newtonian potential functions. The plastic potential Q assumes a similar form to the yield function f and is expressed as:

$$Q(\underline{\sigma}) = 0 \tag{2.6}$$

The normality principle states that the plastic strain increment tensor is linearly related to the gradient of the plastic potential through the stress point, ie,

$$d\underline{\epsilon}^p = d\lambda \frac{\partial Q(\underline{\sigma})}{\partial \underline{\sigma}} \tag{2.7}$$

where $d\lambda$ is a non–negative scalar called the plasticity multiplier

The plastic potential is said to be associated when the yield function and the plastic potential are defined by the same expression ($f = Q$). In associated flow, the material satisfies the normality condition with respect to the yield surface, ie:

$$d\underline{\epsilon}^p = d\lambda \frac{\partial f}{\partial \underline{\sigma}} \tag{2.8}$$

For geological materials, the equation of the plastic potential is often different from that of yield surface; that means that the flow is non–associated. However, for simplicity associated flow is often assumed in practice.

2.2.4 Decomposition Of Strain Measures

It is assumed for analytical purposes that strains can be linearly decomposed, such that :

$$d\epsilon = d\underline{\epsilon}^e + d\underline{\epsilon}^p \tag{2.9}$$

where the subscripts e and p denote elastic and plastic components respectively.

2.2.5 Hardening Behaviour:

Hardening is said to occur when the yield stress of a material increases during elasto–plastic loading. Figure 2.3 depicts hardening, softening and ideal (elastic–perfectly plastic) material behaviour in response to uniaxial loading. Hardening can be related to the degree of plastic straining which the material has suffered (or the amount of work dissipated during this straining) in changing the state of the material. Hence, the terms "strain hardening" or "work hardening" are often used to describe this phenomenon.

For multiaxial states of stress (Figure 2.4), hardening may involve an expansion of the yield surface (isotropic hardening) or translation (kinematic hardening) or a combination of both. Kinematic hardening is necessary to describe such phenomena as the Bauschinger effect in cyclic loading.

2.2.6 Formulation of Stress–Strain Relations:

The aim of this section is to gather the threads together to obtain the relation between stress and strain increments during elasto–plastic flow. The objective is then to seek the form of D^{ep} in the equation:

$$d\underline{\sigma} = D^{ep}\, d\underline{\epsilon} \qquad (2.10)$$

where $d\underline{\sigma}$ and $d\underline{\epsilon}$ are increments of the stress and total (elastic plus plastic) strain tensors and D^{ep} is the elasto–plastic constitutive matrix. Firstly, the additivity postulate can be used to write:

$$d\underline{\epsilon} = d\underline{\epsilon}^{e} + d\underline{\epsilon}^{p} \qquad (2.11)$$

where $\underline{\epsilon}^{e}$ and $\underline{\epsilon}^{p}$ denote elastic and plastic components of strain, respectively.

Secondly, the stresses are related to the elastic components $d\underline{\epsilon}^{e}$ of the strains through an elastic matrix D^{e}, that is:

$$d\underline{\sigma} = D^{e}\, d\underline{\epsilon}^{e} \qquad (2.12)$$

Substituting (2.11) in (2.12) leads to:

$$d\underline{\sigma} = D^e \, (d\underline{\epsilon} - d\underline{\epsilon}^p) \qquad (2.13)$$

Thirdly, the plastic strain increments are related to the flow rate, ie:

$$d\underline{\epsilon}^p = d\lambda \, \frac{\partial Q}{\partial \underline{\sigma}} \qquad (2.14)$$

Fourthly, the yield function is given by:

$$f(\underline{\sigma},R) = 0 \qquad (2.15)$$

in which $R = R(\underline{\epsilon}^p)$ is the hardening parameter.

It is a fundamental assumption that during plastic yield the stress remains on the yield surface. This 'consistency condition' implies that:

$$df(\underline{\sigma},R) = 0 \qquad (2.16)$$

Expanding this relation by the chain rule yields:

$$\frac{\partial f}{\partial \underline{\sigma}}^T d\underline{\sigma} + \frac{\partial f}{\partial R} \frac{\partial R}{\partial \underline{\epsilon}^p}^T d\underline{\epsilon}^p = 0 \qquad (2.17)$$

Substituting (2.12) and (2.14) into (2.11) leads to:

$$d\underline{\epsilon} = [D^e]^{-1} \, d\underline{\sigma} + d\lambda \, \frac{\partial Q}{\partial \underline{\sigma}} \qquad (2.18)$$

Substituting (2.14) into (2.17) leads to:

$$\frac{\partial f}{\partial \underline{\sigma}}^T d\underline{\sigma} + \frac{\partial f}{\partial R} \frac{\partial R}{\partial \underline{\epsilon}^p} \, d\lambda \, \frac{\partial Q}{\partial \underline{\sigma}}^T = 0 \qquad (2.19)$$

Defining a parameter H by:

$$\frac{\partial f}{\partial \underline{\sigma}}^T d\underline{\sigma} = H \, d\lambda \qquad (2.20)$$

and substituting in (2.19) gives:

$$H = - \frac{\partial f}{\partial R} \left[\frac{\partial R}{\partial \underline{\epsilon}^p} \right]^T \frac{\partial Q}{\partial \underline{\sigma}} \qquad (2.21)$$

Multiplying equation (2.18) by $(\partial f/\partial \underline{\sigma})^T \, D^e$ and replacing the matrix product $D^e \, [D^e]^{-1}$ by the identity matrix, leads to:

$$\frac{\partial f}{\partial \underline{\sigma}}^T D^e \, d\underline{\epsilon} = \frac{\partial f}{\partial \underline{\sigma}}^T d\underline{\sigma} + \frac{\partial f}{\partial \underline{\sigma}} D^e \, d\lambda \, \frac{\partial Q}{\partial \underline{\sigma}}^T \qquad (2.22)$$

Eliminating $\frac{\partial f}{\partial \underline{\sigma}}^T d\underline{\sigma}$ by (2.20) and rearranging, gives:

$$\lambda = \frac{1}{A} \frac{\partial f}{\partial \underline{\sigma}}^T D^e \, d\underline{\epsilon} \qquad (2.23)$$

in which $$A = H + \frac{\partial f}{\partial \underline{\sigma}}^T D^e \frac{\partial Q}{\partial \underline{\sigma}} \qquad (2.24)$$

Rearranging (2.22) leads to:

$$d\underline{\sigma} = D^e \, d\underline{\epsilon} - d\lambda \, D^e \frac{\partial Q}{\partial \underline{\sigma}} \qquad (2.25)$$

Substitution of (2.23) into (2.24) gives the required relation between $d\underline{\sigma}$ and $d\underline{\epsilon}$, ie equation (2.25).

The elasto-plastic constitutive matrix D^{ep} is then:

$$D^{ep} = D^e - \frac{1}{A} D^e \frac{\partial Q}{\partial \underline{\sigma}} \frac{\partial f}{\partial \underline{\sigma}}^T D^e \qquad (2.26)$$

For associated flow, the function Q is replaced by the yield function f.

2.3 THE VON MISES MODEL

The Von Mises yield criterion is one of the most widely used in metal plasticity. It assumes that the strength of the material is independent of the first invariant of the stress tensor, i.e. the mean pressure. Therefore, the yield function for metals can be expressed in terms of the second and third invariants of the deviatoric stress tensor as :

$$f(J_2, J_3, K) = 0 \qquad (2.27)$$

where J_2 and J_3 are the second and third invariants of the deviatoric stress tensor.

$$J_2 = 1/2\ Sij\ S_{ij} \qquad (2.28)$$

$$J_3 = 1/3\ S_{ij}\ S_{jk}\ S_{ki} \qquad (2.29)$$

$$Sij = \sigma_{ij} - 1/3\ \sigma_{kk}\ \delta_{ij} \qquad (2.30)$$

Von Mises (1913) suggested that yielding occurs when the second invariant of the deviatoric stress tensor reaches a critical value . This criterion is expressed mathematically as:

$$f = J_2 - K^2 \qquad (2.31)$$

where K is a material constant to be determined from experiments. Fig. 2.5 shows the Von Mises yield surface in principal stresss space.

It is worth noting that this criterion is adequate for total stress analysis of soils in undrained conditions . In terms of principal stresses , the Von Mises yield function can be written as :

$$f = 1/6\ \left[(\sigma_1-\sigma_2)^2 + (\sigma_2-\sigma_3)^2 + (\sigma_3-\sigma_1)^2 \right] - K^2 \qquad (2.32)$$

But the maximum value of shear stress τ_{max}, ie the yield condition is

$$\tau_{max} = (\sigma_1 - \sigma_2)/2 = Cu \qquad (2.33)$$

where Cu is the undrained shear strength of soil. Thus, and assuming $\sigma_2 = \sigma_3$, the Von Mises hardening parameter becomes

$$K = 2\ Cu\ /\ \sqrt{3} \qquad (2.34)$$

2.4 THE CRITICAL STATE MODEL

2.4.1 Introduction

The critical state theories assume that "cohesive" soils are elasto–plastic materials which exhibit strain hardening (or softening) behaviour during yielding until a failure (critical) state is attained, when unconstrained plastic flow occurs. Three parameters, p, q, and V describe the state of the sample of soil during a triaxial test. These parameters are used in the development of the critical state models:

Mean effective stress

$$p = \frac{\sigma_1 + 2\sigma_3}{3} = \frac{\sigma^t_1 + 2\sigma^t_3}{3} - u \qquad (2.35)$$

Deviator stress :

$$q = \sigma_1 - \sigma_3 = \sigma^t_1 - \sigma^t_3 \qquad (2.36)$$

Specific volume

$$V = 1 + e \qquad (2.37)$$

where e is the void ratio

Corresponding to the stress parameters p, q are parameters v (volumetric strain) and ϵ (deviatoric strain)

$$\epsilon_v = \epsilon_1 + 2\epsilon_3 \qquad (2.38)$$

$$\epsilon_d = 2\,(\epsilon_1 - \epsilon_3)/3 \qquad (2.39)$$

A basic tenent of critical state theory is that if soils are continuously distorted until they flow as a frictional fluid, they will come into a critical state determined by the two equations

$$q = M\,p \qquad (2.40)$$

$$V = \Gamma - \lambda \ln p \qquad (2.41)$$

M, Γ, λ represent basic soil properties.

The first equation of the critical state determines the magnitude of the deviatoric stress q needed to keep the soil flowing continuously as the product of a frictional constant M with the effective pressure p, Fig. 2.6 . The second equation states that the specific volume occupied by unit volume of flowing particles will decrease as the effective pressure decreases.

2.4.2 Concept of Critical Void Ratio

When a loose soil sample is sheared, it passes through progressive states of yielding before reaching a state of collapse. The yielding continues until the material reaches a critical void ratio, after which the void ratio remains constant during subsequent deformation (Figure 2.7). That is, the material reaches a state in which no volume change takes place during further shearing. This state is called the critical state and the corresponding void ratio is called the critical void ratio. When a dense soil sample is sheared to failure, it reaches a peak shear stress as shown in Figure 2.7.a. Initially the material reduces in volume, and then it dilates until the volumetric strain reaches a constant value which corresponds to its critical value. A soil with a void ratio lower than the critical value (dense soil) deforms in such a manner as to increase its volume, whereas at a void ratio higher than the critical value (loose soil) the deformations will decrease the volume.

2.4.3 Associated– Modified Cam Clay:

The constitutive laws on which this model is based are very simple and, as the name suggests, involve an associated flow rule. The theory on which this model is founded is summarized in the following.

a/ Consolidation behaviour:

The elasto–plastic model is partly based on observations of consolidation and swelling behaviour . During consolidation, along AB (Figure 2.8), the void ratio of the material decreases according to the following equation:

$$e = e_1 - \lambda \ln(p/p_1) \qquad (2.42)$$

where λ, the slope of the consolidation curve, a fundamental material parameter.

p_1 is some reference stress on the consolidation curve.

If the material follows the path BC the soil swells as a consequence of reduction in the effective mean stress, and the expression for void ratio becomes:

$$e = e_0 - \kappa \ln(p/p_0) \qquad (2.43)$$

where κ, the slope of the rebound curve, is also a fundamental material parameter,and p_0 is the past maximum mean effective stress (yield stress). Void ratio changes along the swelling line are reversible, ie, elastic.

The two previous equations can be written in an incremental form:

$$de = - \lambda \, dp/p \qquad (2.44)$$

$$de^e = - \kappa \, dp/p \qquad (2.45)$$

Recalling:

$$de = de^e + de^p$$

and noting that:

$$d\epsilon_v = \frac{de}{1+e} \qquad (2.46)$$

then

$$d\epsilon_v^p = - \frac{\lambda - \kappa}{1+e} \quad \frac{dp}{p} \qquad (2.47)$$

Since p_0 takes the role of the hardening parameter the strain hardening relationship is:

$$dp_0 = - \frac{1+e}{\lambda-\kappa} d\epsilon_v^p \, p_0 \qquad (2.48)$$

b/ Yield function and plastic flow:

The form of the yield function for the associated modified Cam clay is the ellipse shown in Figure 2.9 .

$$f = p^2 - pp_0 + (q/M)^2 = 0 \qquad (2.49)$$

where M is the slope of the Mohr–Coulomb line in p–q space.
For triaxial compression ($\sigma_2 = \sigma_3$),

$$M = \frac{6 \sin\varphi}{3 - \sin\varphi} \qquad (2.50)$$

Because the failure line lies below the ellipse for overconsolidated soils, this implies softening behaviour in such soils. Of course, for associated flow, the plastic potential and the yield function are identical, ie,

$$Q = f \qquad (2.51)$$

c/ Derivatives

Before calculating any derivatives involved in the constitutive equations some parameters need to be defined for the case of axisymmetric problem. First, the mean effective stress:

$$p = \frac{\sigma_r + \sigma_\theta + \sigma_z}{3} \qquad (2.52)$$

and the deviatoric stress,

$$q = \{ \tfrac{1}{2} [(\sigma_z-\sigma_r)^2 + (\sigma_z-\sigma_\theta)^2 + (\sigma_\theta-\sigma_r)^2 + 6 \tau_{rz}^2] \}^{\frac{1}{2}} \qquad (2.53)$$

and the elastic constitutive matrix

$$[D^e] = \frac{E}{(1+\nu)(1-2\nu)} \begin{bmatrix} 1-\nu & \nu & \nu & 0 \\ & 1-\nu & \nu & 0 \\ & \text{SYM.} & 1-\nu & 0 \\ & & & \frac{1-2\nu}{2} \end{bmatrix} \quad (2.54)$$

The following derivatives are substituted into the the elasto–plastic stiffness matrix.

$$\frac{\partial f}{\partial \underline{\sigma}} = \frac{\partial f}{\partial p}\frac{\partial p}{\partial \underline{\sigma}} + \frac{\partial f}{\partial q}\frac{\partial q}{\partial \underline{\sigma}} \quad (2.55)$$

$$\frac{\partial Q}{\partial \underline{\sigma}} = \frac{\partial f}{\partial \underline{\sigma}} \quad (2.56)$$

$$\frac{\partial p}{\partial \underline{\sigma}} = \begin{bmatrix} \frac{1}{3} & \frac{1}{3} & \frac{1}{3} & 0 \end{bmatrix}^T \quad (2.57)$$

$$\frac{\partial q}{\partial \underline{\sigma}} = \frac{3}{2q} \begin{bmatrix} \sigma_z - p & \sigma_r - p & \sigma_\theta - p & 2\tau_{rz} \end{bmatrix}^T \quad (2.58)$$

$$\frac{\partial f}{\partial p} = 2p - p_0 \quad (2.59)$$

$$\frac{\partial f}{\partial q} = \frac{2q}{M^2} \quad (2.60)$$

$$\frac{\partial Q}{\partial p} = \frac{\partial f}{\partial p} \quad (2.61)$$

$$\frac{\partial Q}{\partial q} = \frac{\partial f}{\partial q} \quad (2.62)$$

$$\frac{\partial f}{\partial p_0} = -p \quad (2.63)$$

And from the flow rule we derive the following equations:

$$d\epsilon_v^p = d\lambda \frac{\partial Q}{\partial p} \quad (2.64)$$

and

$$d\epsilon_d^p = d\lambda \frac{\partial Q}{\partial q} \quad (2.65)$$

The elasto-plastic constitutive matrix is hence:

$$[D^{ep}] = [D^{e}] - \frac{[D^{e}]\frac{\partial Q}{\partial \underline{\sigma}}\frac{\partial f}{\partial \underline{\sigma}}^{T}[D^{e}]}{\frac{\partial f}{\partial \underline{\sigma}}^{T}[D^{e}]\frac{\partial Q}{\partial \underline{\sigma}} - \frac{\partial f}{\partial p_0}\frac{dp_0}{d\epsilon_v^p}\frac{\partial Q}{\partial p}} \qquad (2.66)$$

2.4.4 In Situ Stresses

In this section, we are concerned with determining the insitu stress state , i.e, the spatial distribution of effective vertical stress, σv, effective horizontal stress,σh, pore water pressure, u0, and p0 the isotropic preconsolidation pressure . The parameter p_0 is only needed where Cam clay models are used. For Cam clays it is important to try to establish the in situ stress state as accurately as possible because the displacements predicted by the model are quite sensitive to the intial conditions.

In an elastic analysis of soil (and some times in an elastic– perfectly plastic soil) it is quite common to set K_0 as ν / $(1-\nu)$. This is consistent with the condition of zero lateral strain inherent in one–dimensional elastic compression, but unfortunately measured laboratory values of ν are not consistent with the usual values of K_0 believed appropriate for the field. The elastic assumption should not be used for analysis using the critical state models, where one–dimensional compression involves plastic yielding. One of the models of determining the in situ stresses in Cam clay is Wroth's method. This method is summarized as follows:

1– Calculate σ_v from the bulk density of the soil and the position of the water table.

2– Calculate σ_{vm} (maximum effective vertical stress) from an oedometer test.

3– Use Jaky's relation ($K_{nc} = 1-\sin\Phi'$) to calculate K_{nc} and hence the horizontal effective stress acting when the maximum vertical stress (σ_{vm}) was present.

4– Calculate values of p and q corresponding to the maximum stresses found in 3. Substitute these values into the equation of Cam clay yield locus to calculate

the values of p_0.

5– Use the following formula to calculate the value of K_0 from K_{nc} and OCR (Overconsolidated Ratio). Hence the in situ horizontal effective stress :

$$K_0 = OCR.K_{nc} - \frac{\nu'}{1 - \nu'} (OCR - 1) \qquad (2.67)$$

(Elastic unloading)

Hence the in situ horizontal effective stress is :

$$\sigma_h = K_0 \sigma_v \qquad (2.68)$$

A further empirical relation between K_0 and OCR is due to Parry (1982) :

$$K_0 = K_{nc} (OCR)^{\Phi'} \quad (\Phi \text{ in radians}) \qquad (2.69)$$

This equation gives values of K_0 similar to (2.67) and its manipulation is more straightforward and consequently has been used in this study.

2.5 Conclusion

In general soil suffers elastic as well as plastic deformation during loading. Consequently, for soils, it is necessary to use elastoplastic theory because generally soils show plastic behaviour at low stress levels. The ingredients of elastoplastic models are; elastic properties, condition for yielding (yield surface), mechanism of yielding (flow rule) and finally the magnitude of plastic deformation (hardening rule).

Soil is a two–phase medium, solid and fluid. Consequently, it is necessary to distinguish between two categories of analysis: Total stress analysis and Effective stress analysis. The Von Mises model is often adequate for total stress analysis in undrained conditions whereas the Cam clay model is suitable for effective stress analysis since it is driven from effective stress changes. The Cam clay is a model behaviour which is 'simple' in the sense that the model is derived from a small

number of basic assumptions, yet the model manages to produce a useful description of soil behaviour. What really sets the critical state model apart from other attempts to formulate elasto–plastic models for soils is that it allows a consistent treatment of both drained and undrained loading.

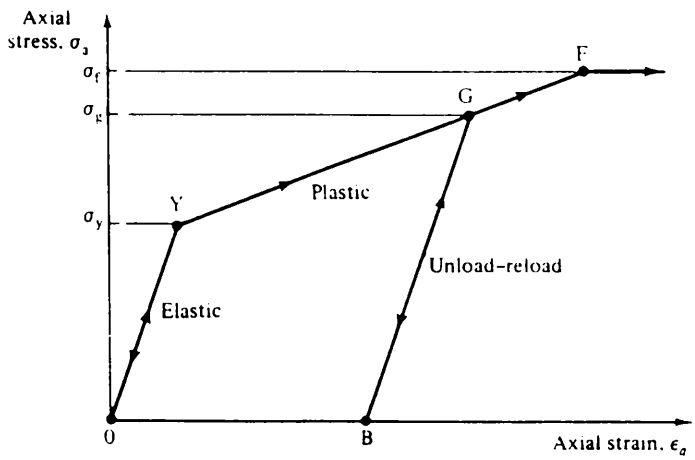

Figure 2.1 Recoverable and irrecoverable strains

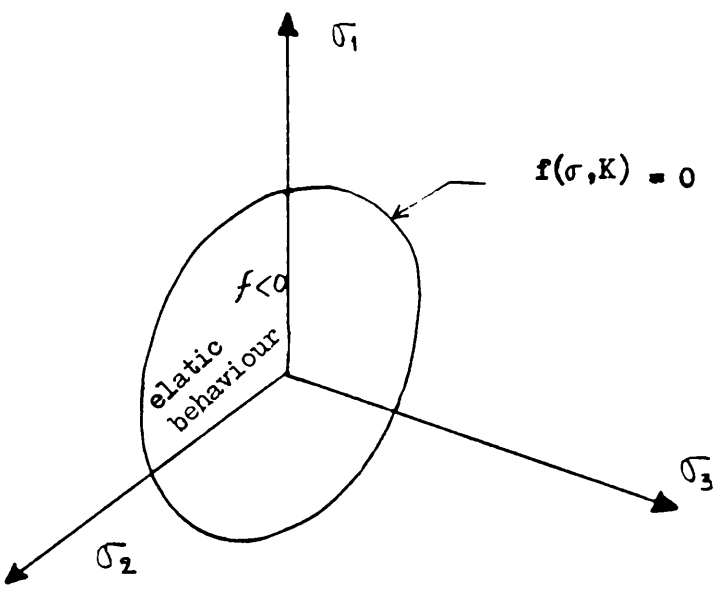

Figure 2.2 Yield function.

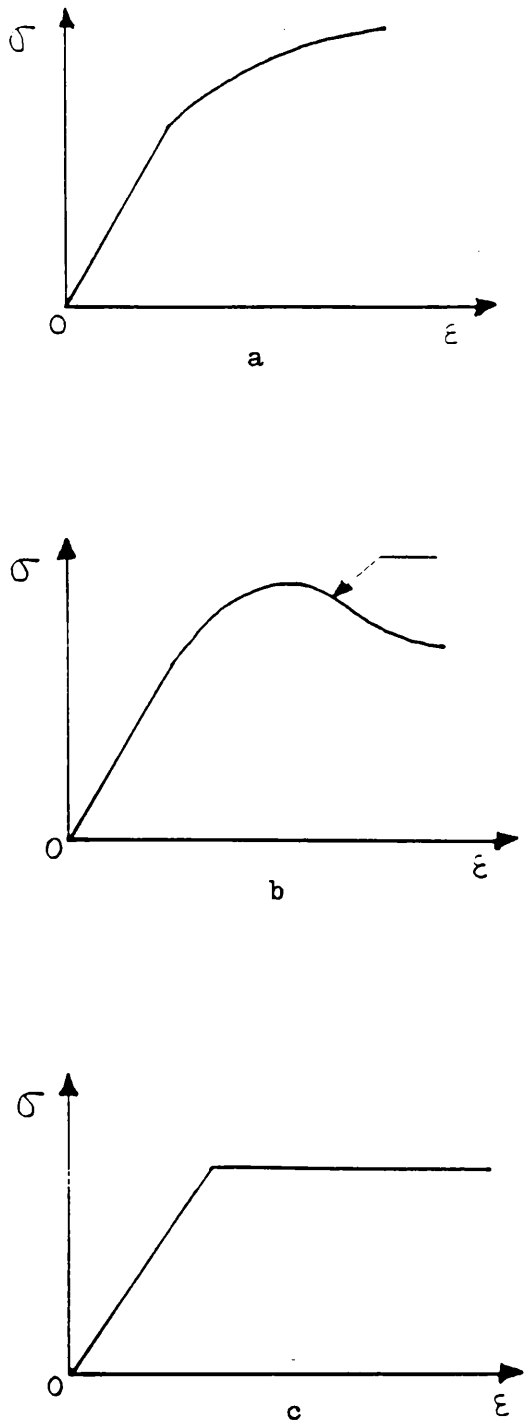

Figure 2.3 Stress-strain behaviour of
a) Hardening material
b) Softening material
c) Elastic-perfectly plastic material

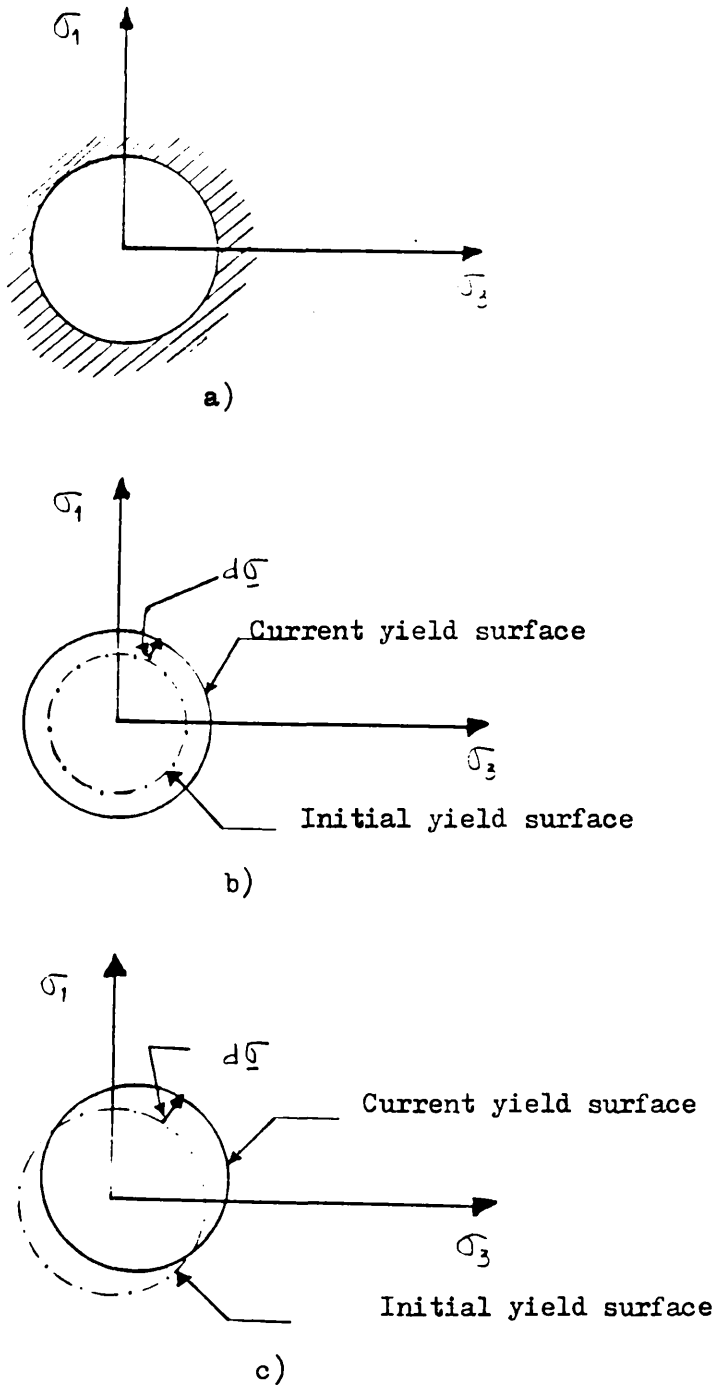

Figure 2.4 Models of strain hardening behaviour
a) Elastic-perfectly plastic
b) Isotropic strain hardening
c) Kinematic strain hardening

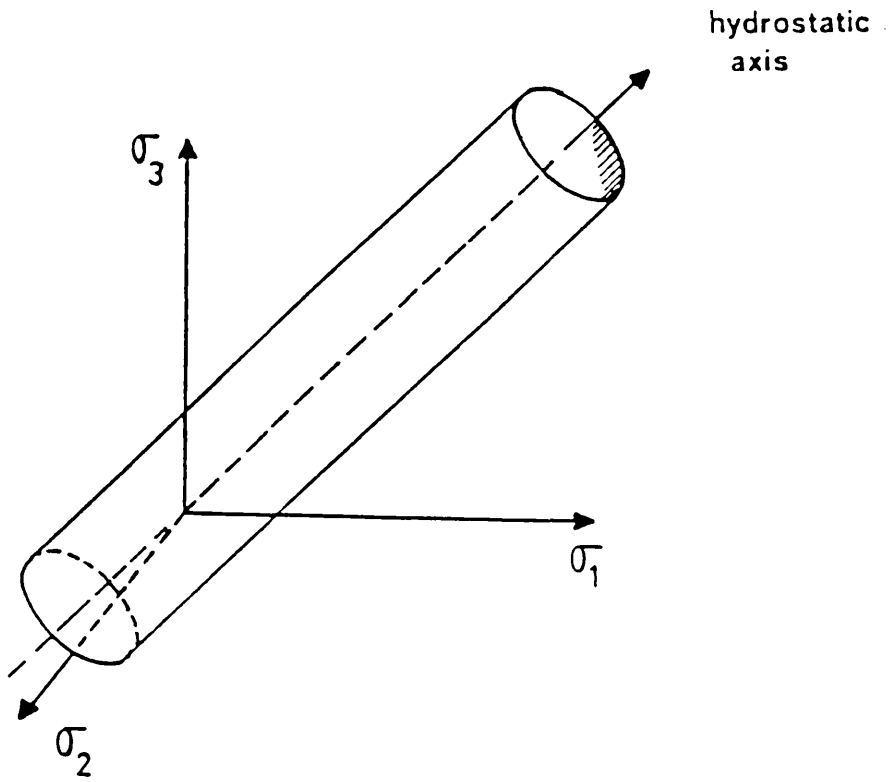

Figure 2.5 The Von Mises yield criterion

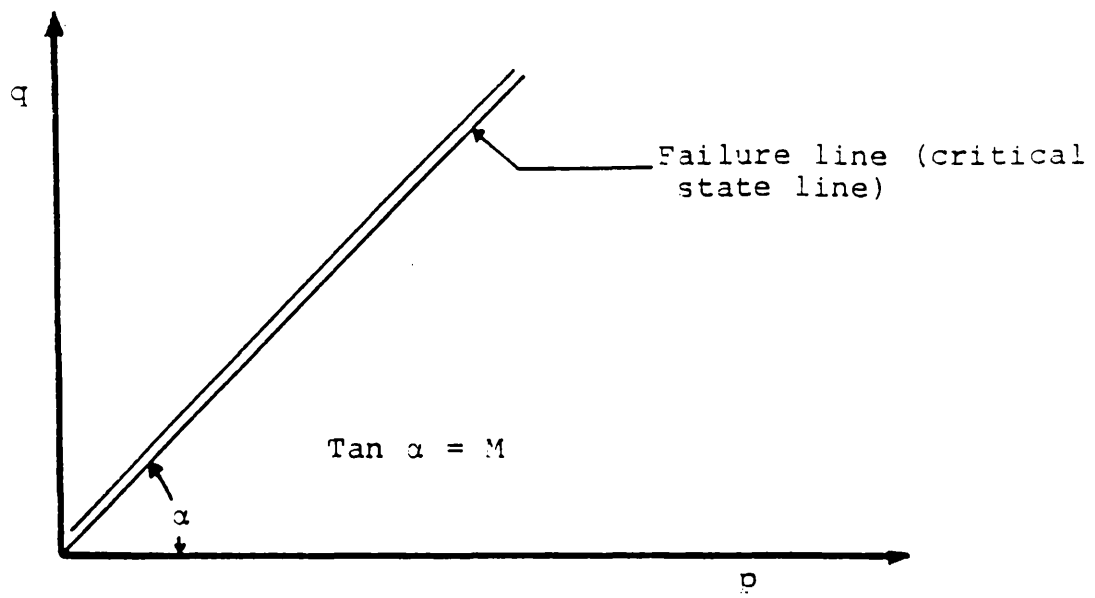

Figure 2.6 Orientation of critical state line in q-p space

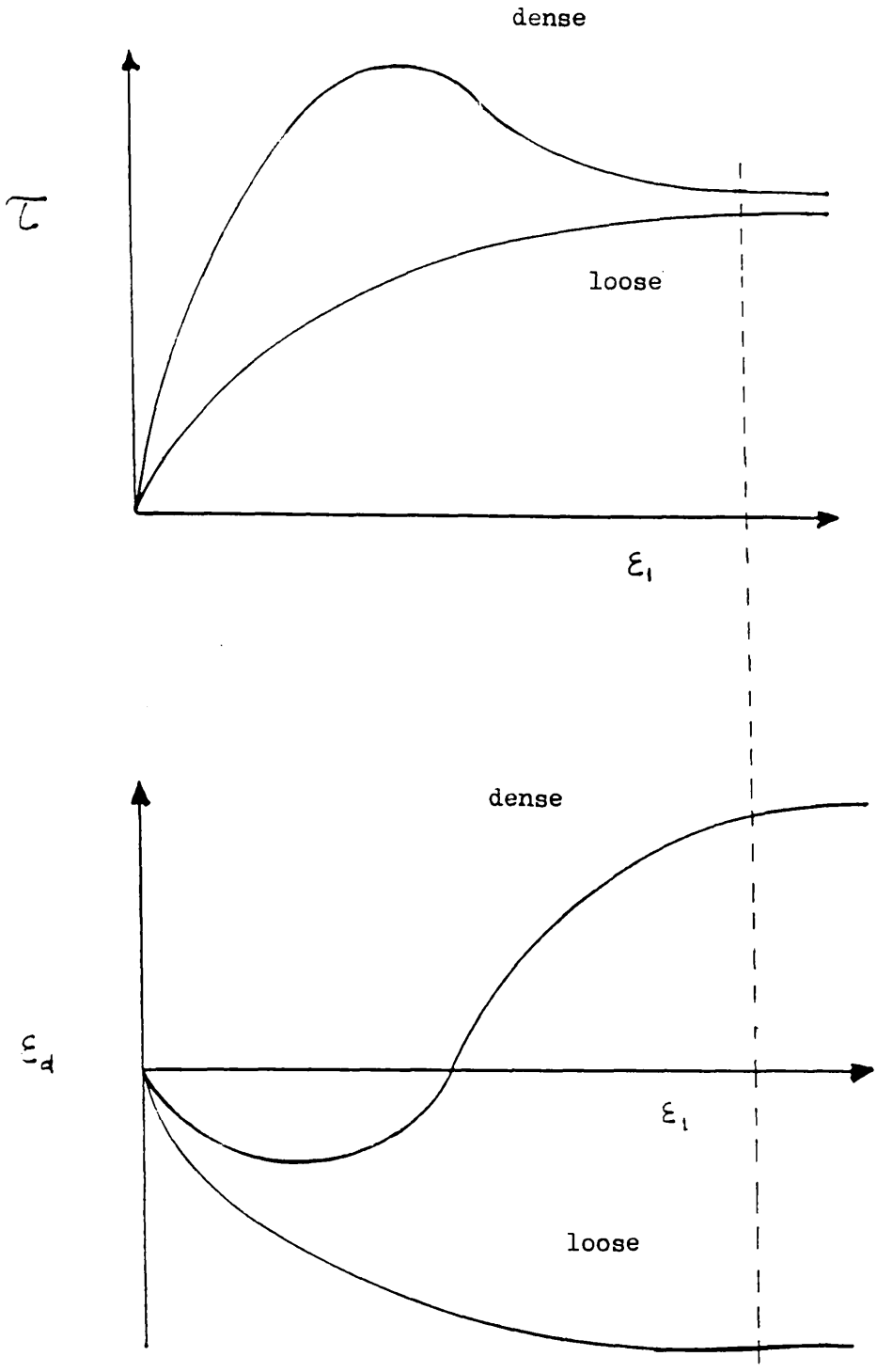

Figure 2.7 Behaviour of loose and dense soils

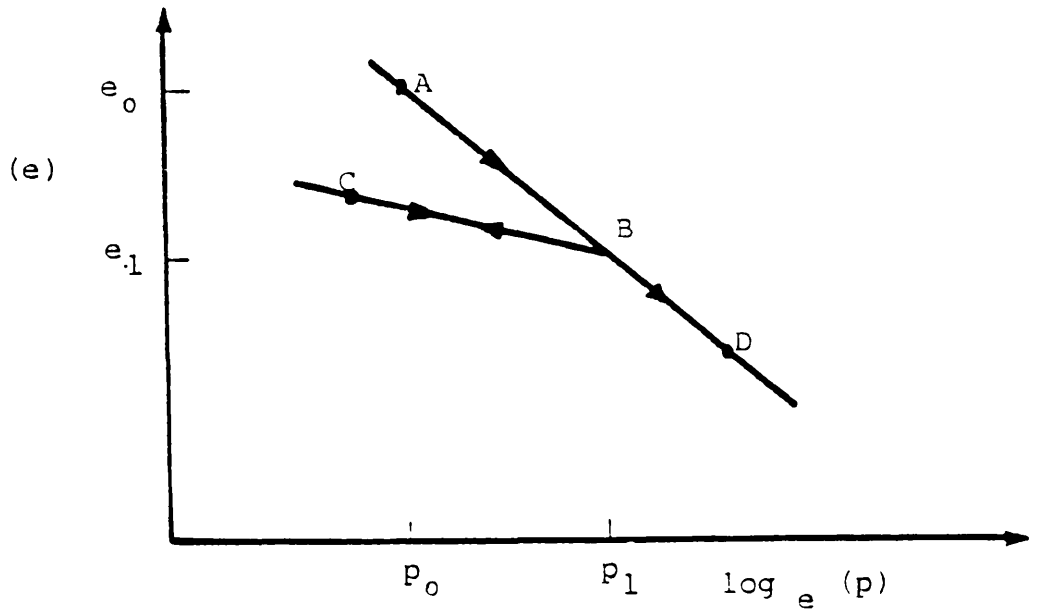

Figure 2.8 Consolidation and swelling behaviour

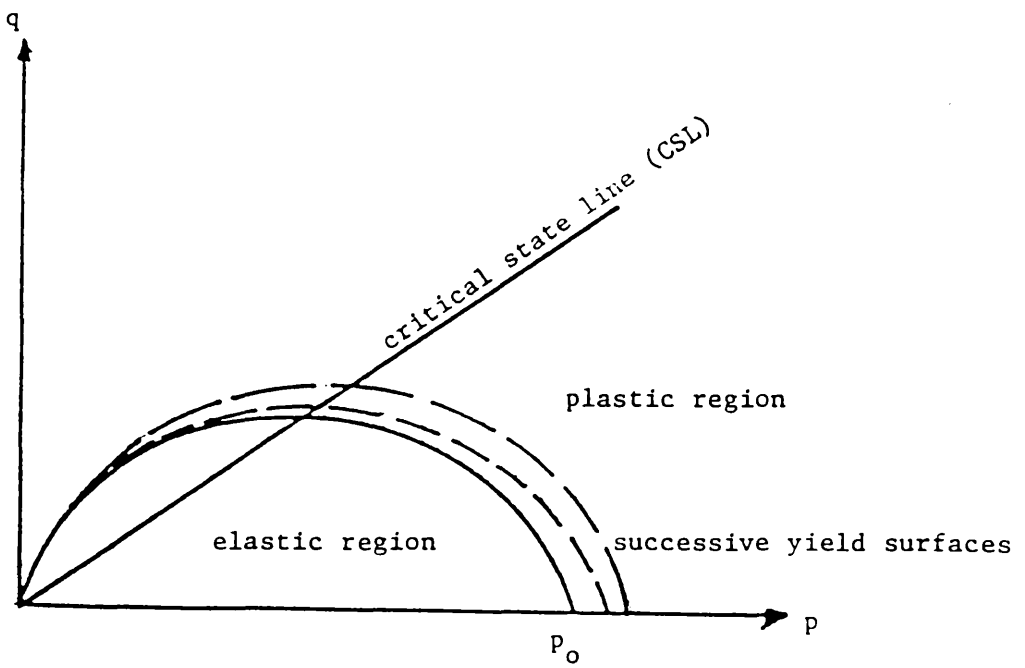

Figure 2.9 The critical state model (associated modified CAM clay model AMC)

CHAPTER 3

FINITE ELEMENT MODEL

3.1 INTRODUCTION :

In this chapter a short summary of the finite element method will be given together with a description of the computer program used in this study and the procedure used to simulate sampling disturbances in clay soils. A more complete treatment of the finite element method is given by many authors, notably Zienkiewicz[61], Naylor and Pande[45] and Owen and Hinton[25,26]. Slip elements are used to simulate the adhesion at the sampler– soil interface during the process of pushing the sampler into the soil. A review of this literature is given together with numerical example illustrating the use and performance of these slip elements.

3.2 FINITE ELEMENT METHOD:

The basis of the finite element method is the subdivision of continua into an assembly of discrete structures (finite elements) connected at their nodes. This idealisation reduces the continuum from an infinite degree of freedom system to a finite degree of freedom system, in terms of nodal quantities. The successive stages constituing the finite element algorithm are described in the following sections.

3.2.1 Discretization:

The starting point of the analysis is the division of the system into finite elements. Eight basic elements are illustrated in Fig 3.1. For geotechnical work, the triangular and quadrilateral elements for plane strain or axisymmetric analysis such as the so called 8– noded serendipity elements (Fig 3.2)are most commonly used. These elements have four corner nodes and four midside nodes. There seems to be a consensus that these so– called 'parabolic' elements which have one midside node offer the best results. These elements are termed isoparametric: that is, the equations describing the shape of their boundaries are the same as those describing the variation of the nodal unknowns (e.g. displacements) across the element. However, recent research (Sloan and Randolph[53]) has shown that in axisymmetric analyses the constraint of no volume change (which occurs in undrained situations) leads to finite element meshes 'locking up' if low– order elements are used . These problems can be avoided by using higher order elements such as cubic strain triangles. On the other hand, there are occasions where the use of a lower– order element can be advantageous: for example, situations where the mesh has irregular boundaries or contains several zones of soil of different properties. Indiscriminate use of higher order elements in these circumstances can lead to unnecessarily expensive analyses. Selection of the size and shape of elements is a matter of experience and intuition. Generally, elements should be smaller where the displacement gradients are steepest, i.e where there are rapid changes in stress and strain.

3.2.2 Shape Function:

The shape (interpolation) functions define the variation of quantities across elements in terms of the nodal values. Let V stand for the value of

the quantity at some point r, z then :

$$V = \sum_{i=1}^{n} N_i V_i \qquad (3.1)$$

where,

N_i is the shape function for node i,

n is the number of nodes in the element, and

V_i is the value of the quantity at node i.

The shape functions for the 8− node Serendipity element are shown in Fig 3.2.

for corner nodes:

$$N_i = \tfrac{1}{4}(1 + \xi\xi_i)(1 + \eta\eta_i)(\xi\xi_i + \eta\eta_i - 1) \qquad (3.2.a)$$

$$i = 1,3,5,7$$

for midside nodes:

$$N_i = \tfrac{1}{2}\xi_i^2(1 + \xi\xi_i)(1 - \eta^2) + \tfrac{1}{2}\eta_i^2(1 + \eta\eta_i)(1 - \xi^2) \qquad (3.2.b)$$

$$i = 2,4,6,8$$

where ξ and η are the intrinsic coordinates of any point within the element. By definition, ξ and η have values in the interval $[-1,+1]$.

3.2.3 Coordinate Transformation:

Transformations from local (ξ,η) to global coordinates (x,y) are necessary. These include expressions for the incremental area $dA = dr.dz$ in terms of $d\xi$ and $d\eta$, and the cartesian shape function derivatives, i.e $\partial N_i/\partial r$ and $\partial N_i/\partial z$, given $\partial N_i/\partial \xi$ and $\partial N_i/\partial \eta$.

By definition, the incremental area is:

$$dA = |J| \, d\xi . d\eta \tag{3.3}$$

where $|J|$ is the determinant of the jacobian matrix J, and :

$$J = \begin{bmatrix} \frac{\partial r}{\partial \xi} & \frac{\partial z}{\partial \xi} \\ \frac{\partial r}{\partial \eta} & \frac{\partial z}{\partial \eta} \end{bmatrix} \tag{3.4}$$

The partial derivatives $\partial r/\partial \xi$, etc... may be obtained from the shape function derivatives with respect to ξ, η and the nodal coordinates. Thus, by differentiating equation (3.1) we obtain:

$$\frac{\partial r}{\partial \xi} = \sum_{i=1}^{n} \frac{\partial N_i}{\partial \xi} . \, r_i \tag{3.5}$$

Explicit expressions for $\partial N_i/\partial \xi$ and $\partial N_i/\partial \eta$ are readily obtained by differentiating equations (3.2a) and (3.2b).

To obtain the cartesian shape function derivatives the following chain rule is needed,

$$dN_i = \frac{\partial N_i}{\partial r} \, dr + \frac{\partial N_i}{\partial z} \, dz \tag{3.6}$$

Partial differentiation of (3.6) with respect to ξ and η in turn gives the following relation :

$$\begin{bmatrix} \frac{\partial N_i}{\partial \xi} \\ \frac{\partial N_i}{\partial \eta} \end{bmatrix} = \begin{bmatrix} \frac{\partial r}{\partial \xi} & \frac{\partial z}{\partial \xi} \\ \frac{\partial r}{\partial \eta} & \frac{\partial z}{\partial \eta} \end{bmatrix} \begin{bmatrix} \frac{\partial N_i}{\partial r} \\ \frac{\partial N_i}{\partial z} \end{bmatrix} \tag{3.7}$$

Inversions gives explicit expressions for the cartesian derivatives, ie:

$$\begin{bmatrix} \frac{\partial N_i}{\partial r} \\ \frac{\partial N_i}{\partial z} \end{bmatrix} = \frac{1}{|J|} \begin{bmatrix} \frac{\partial z}{\partial \eta} & -\frac{\partial z}{\partial \xi} \\ -\frac{\partial r}{\partial \eta} & \frac{\partial r}{\partial \xi} \end{bmatrix} \begin{bmatrix} \frac{\partial N_i}{\partial \xi} \\ \frac{\partial N_i}{\partial \eta} \end{bmatrix} \qquad (3.8)$$

This expression (3.8) completes the transformations needed for axisymmetric applications.

3.2.4 Strain– Displacement Relations:

The displacements may be expressed as :

$$\underline{u} = (u,w)^T \qquad (3.9)$$

where u and w are the displacements in the r and z directions,respetively.

The components of strain are :

$$\underline{\epsilon} = (\epsilon_r, \epsilon_\theta, \epsilon_z, \gamma_{rz})^T \qquad (3.10)$$

where for small displacements, the strains are given as :

$$\begin{aligned} \epsilon_r &= \frac{\partial u}{\partial r} \\ \epsilon_\theta &= \frac{u}{r} \\ \epsilon_z &= \frac{\partial w}{\partial z} \\ \gamma_{rz} &= \frac{\partial u}{\partial z} + \frac{\partial w}{\partial r} \end{aligned} \qquad (3.11)$$

For finite element applications it is necessary to relate strains to the displacements at element nodes $\underline{\delta}^e$. Using equation (3.1) to express u and w in terms of nodal displacement gives :

$$\underline{\epsilon} = B\ \underline{\delta}^e \qquad (3.12)$$

The matrix B consists of a row of n submatrices B_i which for axisymmetric

problems take the form:

$$B = \begin{bmatrix} \frac{\partial N_i}{\partial r} & 0 \\ \frac{N_i}{r} & 0 \\ 0 & \frac{\partial N_i}{\partial z} \\ \frac{\partial N_i}{\partial z} & \frac{\partial N_i}{\partial r} \end{bmatrix} \qquad (3.13)$$

The need for the shape function cartesian derivatives is now apparent.

3.2.5 Stress–Strain Relations:

In general, the stress–strain relations can be expressed in the incremental form:

$$d\underline{\sigma} = D\ d\underline{\epsilon} \qquad (3.14)$$

where $\underline{\sigma} = (\sigma_r, \sigma_\theta, \sigma_z, \tau_{rz})^T$,in which $\sigma_r, \sigma_\theta, \sigma_z$ are the normal stresses in the r, θ and z directions and τ_{rz} is the shear stress in the rz plane. D is the constitutive matrix. Its components are constant for linear elastic materials and takes the form of equation (2.54). For nonlinear materials, the constitutive relations are stress dependent. The matrix D is symmetric for associated flow.

3.2.6 Stiffness Equations:

The global stiffness matrix equation which relates nodal forces to displacements is assembled from the individual element stiffness matrices.

Element stiffness matrices:

A typical element is assumed to be in equilibrium under a set of nodal forces $\underline{F}^e$ associated with displacements $\underline{\delta}^e$. Any external loadings are assumed to be applied at the nodes.

The use of the principle of virtual work forms the basis for the derivation of the relationship between nodal displacements and loads. A set of virtual displacements $\underline{\delta}^*$ is applied to the nodes. Let the stress at a point in the element be $\underline{\sigma}$ and the strain corresponding to the virtual displacements be $\underline{\epsilon}^*$. Equating the work done externally at the nodes to that done internally gives:

$$\underline{\delta}^{*T}.\ \underline{F}^e = \int \underline{\epsilon}^{*T}.\ \underline{\sigma}\ dV \qquad (3.15)$$

From equation (3.12), and noting the fact that (3.12) must hold true for any arbitrary virtual displacement, then:

$$\underline{F}^e = \int B^T\ \underline{\sigma}\ dV \qquad (3.16)$$

In geotechnical applications, equation (3.16) can be used to determine the equivalent nodal forces corresponding to the initial stresses.

Since the loading is applied by small increments, the relations used have an incremental form. By using the stress–strain equation (2.10), re–arranging and replacing $\underline{\epsilon}$ by (3.12) and susbtituting in (3.16) ; we obtain :

$$\underline{F}^e = \int B^T\ D\ B\ \underline{\delta}\ dV + \int B^T\ \underline{\sigma}_0\ dV \qquad (3.17)$$

And in this case $\underline{\delta}$ is the actual nodal displacement vector.

Another way to write (3.17) would be :

$$\underline{F}^e = K^e\ .\ \underline{\delta}^e + \underline{F}_{\sigma 0} \qquad (3.18)$$

where:

$K^e = \int B^T\ D\ B\ dV$ is the element stiffness matrix and

$\underline{F}_{\sigma 0} = \int B^T\ \underline{\sigma}_0\ dV$ element nodal forces due to initial stresses.

Assembly:

The global stiffness equations are obtained by superimposing the element stiffness matrices, as a consequence of the compatibility and equilibrium conditions at nodes common to adjacent elements. The global matrix K (and load vector $\underline{R}$ where $\underline{R} = \underline{F} - \underline{F}_{\sigma_0}$) is thus assembled from element matrices K^e giving the overall stiffness equation :

$$K \cdot \underline{\delta} = \underline{R} \qquad (3.19)$$

which can be solved for $\underline{\delta}$.

3.2.7 Solution Techniques for Nonlinear Problems:

The solution to nonlinear problems must proceed in an incremental manner since the solution at any stage depends not only on the current displacements of the structure but also on the previous loading history.

Tangential stiffness method:

In this method, the stiffness matrix $K(\delta)$ is assembled at the beginning of each increment of load. The load increments should, in theory, be infinitesimally small. However, with finite increments, at the end of the increment, equilibrium conditions will not be satisfied, and :

$$K(\underline{\delta}) \cdot \Delta\underline{\delta} - \Delta\underline{R} = \underline{\Psi}(\underline{\delta}) \neq 0 \qquad (3.20)$$

where $\underline{\Psi}(\underline{\delta})$ is the residual load vector.

Iterations may be applied within load increments with the aim to make $\underline{\Psi}(\underline{\delta})$ tend to zero, and element stiffnesses are recomputed during each iteration of each load increment. The technique is illustrated schematically in Fig 3.3 for a one–dimensional problem. The use of this method in strain softening

situations, where the tangent stiffness is negative, may lead to numerical instability.

Initial stiffness method:

If the stiffness matrix is not updated and instead the original (elastic) stiffness matrix is used, complete reduction of the stiffness matrix at each step can be avoided. In this case, complete equation solution need only be performed for the first iteration and subsequent approximations to the nonlinear solution obtained, via the expression

$$K \cdot \Delta\underline{\delta} - \Delta\underline{R} = \underline{\Psi}(\underline{\delta}) \qquad (3.21)$$

Since the same stiffness matrix K is employed at each stage, the reduced matrix can be stored and subsequent solutions merely necessitate the reduction of the right hand side $\underline{\Psi}(\underline{\delta})$ terms. This has the immediate advantage of significantly reducing the computing cost per iteration but reduces the convergence rate as can be seen in Fig 3.4. This method is said to be unconditionally convergent and can be employed (with care) for strain softening materials.

For the analysis of sampling disturbances in clays, the tangential stiffness method was used.

3.3 MODELLING OF THE SAMPLING PROCESS

The modelling of the sampling process is done by means of the finite element mesh shown in Fig. 3.19 . Only part of the domain is analysed due to the axisymmetry about the Z− axis. The location of the sampling tube section within the soil is indicated by the nodal points (ABCD). The line (AE) is, by symmetry frictionless in the Z direction and fixed in the r direction. Surface (EF) is fully fixed whereas the surface (FG) may be

assumed to be smooth or fixed. The sampling tube itself is given prescribed vertically downwards displacements, Figure. 3.20 . The main advantages for imposing displacement control on the sampling tube are :

– The incremental process is stabilised.

– The ill–conditioning problems arising from large differences between the values of the Young's modulus of steel (tube) and soil is avoided.

Frictional behaviour at the sampler wall is simulated by inside and outside slip elements (See section 3.4) which allow for localised slip. It should be noted that the sampling tube is already installed in the soil before being advanced and the soil is modelled variously as a Von Mises material as well as a critical state elasto–plastic material.

3.4 SLIP ELEMENTS

3.4.1 Introduction

In many engineering problems, discontinuities such as joints, faults and regional interfaces are embedded in continua. Since the finite element method presumes continuity between adjacents elements, such discontinuities must be introduced into the mesh by special slip elements which allow for slip at the interface between two dissimilar media. The term slip defines the relative motions between the two solid elements.

Slip elements can be used in a wide range of geotechnical problems. In Rock Mechanics, Goodman et al [21] proposed the use of slip elements to simulate rotations as well the sliding of rock masses, Fig.3.5 . In Soil Mechanics, Desai et al [17] suggest the use of joint (interface) elements in soil–structure interaction such as soil–foundation (deep/shallow) interfaces , Fig.3.6, soil–retaining wall interfaces,.. ..etc.

3.4.2 Literature Review

In the 1960's, Goodman et al [21] introduced the idea of representing joints by simple, rectangular, two dimensional elements with eight degrees of freedom, Fig.3.7.a . With this element, due to its zero thickness, adjacents blocks of continuous elements can penetrate each other. Zienkiewicz et al used a six noded paralinear (no midside nodes in the thickness direction) joint element, Fig.3.7.b, assuming uniform strain in the thickness direction. However, that though the thickness of the joint element may be very small, sharp variations in the strains of adjacent continuum elements can take place and a linear interpolation of strains may be preferable. Ghaboussi et al [20] pointed out that numerical difficulties may arise from ill–conditioning of the stiffness matrix due to very large off–diagonal terms and very small diagonal terms which are generated by these elements in certain cases. They proposed a new joint element that uses relative displacements as independent degrees of freedom. The displacement degrees of freedom of one side of the slip surface are transformed into the relative displacements between the two sides of the slip surface. Ghaboussi et al [20] stated that this joint element avoids the drawbacks of other elements. They presented exact explicit stiffness matrices for the two dimensional case.

Inspired by their idea, Pande et al [48] developed and programmed an eight (8) noded parabolic isoparametric interface element based on relative displacements as an independent parameter, Fig.3.7.c. Numerical experiments have, however, shown that on accurate modern machines the differences in the results obtained from (a) conventional isoparametric parabolic (CIP) elements and (b) isoparametric parabolic elements based on relative displacements (RDIP) are insignificant even for extremely small aspect ratios (thickness/length).

Ill-conditioning of the stiffness matrices was evaluated in terms of 'conditioning number' K [48] which is defined as :

$$K = \frac{\text{Largest eigenvalue of the stiffness matrix}}{\text{Smallest eigenvalue of the stiffness matrix}} \qquad (3.22)$$

The conditioning number K for the stiffness matrices obtained by CIP and RDIP are not significantly different; the ratio being 1.4 : 1, indicating that the relative displacement formulation improves the conditioning only very slightly. Pande et al [48] pointed out that the ill-conditioning may occur if very thin interface element are used.

Desai et al [15,17] introduced the idea of using a thin solid element , called a thin-layer element, to simulate interfaces between the two dissimilar media. The quality of simulation of the interface behaviour will depend on a number of factors such as physical and geometrical properties of the surrounding media, nonlinear material behaviour and the thickness of the thin-layer element. If the thickness is too large in comparison with the length of surrounding elements, Fig.3.8, then the thin-layer element will behave essentially as a solid element. If it is too small, computational difficulties may arise. The choice of thickness can, therefore, be an important question but this can be resolved by performing parametric studies and Desai et al [17] carried out such a study into the effects of varying the thickness of the interface element. Fig.3.9 shows a schematic diagram of a direct shear test device in which the bottom half is in concrete and the top half contains soil. A series of tests were performed with a concret/sand interface under normal loads. Fig.3.10 shows typical test results for the sand (with relative density around 80%) for two normal loads. The thickness, t, of the interface

Table 3.1 Distribution of shear stress in interface element at integration points

σ_n = 4.77 Kg/cm^2

t/B	Integration points 1	2	3	4	Average
1.0	2.3939	3.6034	2.1203	3.8771	2.9987
0.1	2.7390	3.2602	2.7049	3.2940	2.9996
0.01	3.0022	2.9975	2.9975	3.0022	2.9999
0.001	2.9967	3.0021	2.9964	3.0025	2.9994

σ_n = 9.55 Kg/cm^2

t/B	Integration points 1	2	3	4	Average
1.0	3.7868	6.2084	3.239	6.7562	4.9976
0.1	4.4778	5.521	4.4093	5.5895	4.9994
0.01	5.0044	4.9950	4.9950	5.0044	4.9997
0.001	4.9914	5.0065	4.9905	5.0075	4.9990

element was varied such that the ratio t/B was 0.001, 0.01, 0.1 and 1.0. The computed results in terms of (relative) displacement, u_r, and the ratio t/B for applied shear stress τ = 3.0 Kg/cm^2 , σ_n = 4.77 Kg/cm^2 , and τ = 5.0 Kg/cm^2 for σ_n = 9.55 Kg/cm^2 are plotted in Fig.3.11 . The computed displacements show wide variations as the thickness is changed. However, the results for t/B values in the range of 0.01 and 0.1 show satisfactory agreement with the observed values of 0.032 cm and 0.034 cm for the tests with 4.77 Kg/cm^2 and 9.55 Kg/cm^2, respectively, Fig.3.10 . Note that for higher and lower values of t/B than this range, the computed displacements are significantly different from the measured values. Table 3.1 shows computed values of shear stresses in the interface element. It can be seen that the best correlation between computed and applied stresses of τ = 3.0 Kg/cm^2 and 5.0 Kg/cm^2 is obtained for a t/B ratio in the range of 0.01 and 0.1 . Although the average values of the computed stresses are not significantly different for a wide range of t/B values, more uniform stress values are obtained t/B ratios smaller than 0.1 . In conclusion, Desai et al [17] stated that satisfactory

simulation of interface behaviour can be obtained for t/B ratios in the range from 0.01 to 0.1 .

Griffiths [22] carried out similar numerical experiments. He analysed the simple problem shown in Fig. 3.12 in which the column contains an inclined interface of weak material, and an axial force (P) is increased until irreversible slippage occurs. He carried out a finite element analysis using the mesh shown in Fig. 3.13 on the effects of variations in interface thickness, material properties and inclination. From the results shown in Fig. 3.14, it can be concluded that for small aspect ratios (up to 1/100) slippage was modelled quite accurately. This conclusion confirms Desai's findings that , for a good simulation of of the interface between two dissimilar media, the thickness of the slip element shall be such that the ratio of thickness to the

length is in the range of 0.01 to 0.1

3.4.3 Numerical Example

Desai and Griffiths stated that an ordinary element of small aspect ratio can be used as an interface element. As an illustration of the use and performance of these slip elements, we consider the problem depicted in Fig. 3.15 . The compressible material is loaded by a uniform pressure P in a rough walled rigid container. Plane strain conditions are assumed. We consider three cases :

i) smooth walls

ii) fully bonded walls

iii) Rough walls, described by an adhesion factor

i) smooth walls

Since this is a linear elastic problem, Fig.3.16.a, there is no problem of convergence and a single element mesh gives the correct results. After loading the compressible material, the top surface displaces downwards uniformly to a depth of 1.48E−5 m which can be confirmed by elastic theory as follows :

$$\delta = \frac{LP}{E}\left[\frac{(1+\nu)(1-2\nu)}{(1-\nu)}\right] \qquad (3.23)$$

$L = 10$ m $\quad \nu = 0.3 \quad E = 1E+6$ KN/m^2 $\quad P = 2$ KN/m^2

Equation (3.23) gives $\delta = 1.48E-5$ m .

− The stress field is uniform everywhere.

ii) Fully bonded walls

This is an elastic case but the stress state developed is complex because of the boundary conditions, Fig. 3.16.b. . Refinement of the mesh was necessary to obtain an accuracy of 1% in the displacement. The computed displacement of the centre of the top surface was 1.05E−5 m. This value is about 67% of the displacement obtained previously. Fig. 3,17 shows the vertical stress contours whithin the compressible material. It can be seen that the vertical stress varies in the material and falls to 30% of the surface pressure at the bottom boundary. This is clearly different from the smooth−walled case where the stress field was uniform.

iii) Rough Walls

The adhesion between wall and soil is assumed to be 10% of the shear strength of the soil , i.e,

$$Cu_{se} = \alpha\, Cu \qquad (3.24)$$

where α = Adhesion factor (taken equal to 0.1 for this example).

Cu_{se} = Undrained shear strength of the slip elements.

Cu = Undrained shear strength of the soil.

The soil is assumed to be elastic−perfectly plastic and modelled by Von Mises criterion.

From prior studies and in confirmity with Desai [17] and Griffiths's [22] findings, an aspect ratio of 1/30 for the slip elements was used, Fig. 3.16.c . The computed displacement of the centre of the top surface was 1.06E−5 m. Fig.3.18 shows the stress field through the body. Further refinement of the mesh was required to obtain these results. The vertical stress falls to only 20% of the surface pressure at the lower boundary (which is lower than the case of fully bonded walls) and the form of the stress fiel is different. In the

case of fully bonded walls, the contours of constant stress tend to be flatter near the vertical boundary than this case.

Based on the foregoing results, it can be seen that the solution for rough walls lies between that obtained for the smooth and fully bonded walls.

3.4.4 Conclusion

In this section, an insight into the use and performance of slip elements has been given. It appears that slip elements are a good tool of modelling relative movements between two adjacent dissimilar media, provided that appropriate parameters for these elements are chosen. From the literature review and from the example studied herein, simple rectangular elements included in the finite element mesh, of aspect ratio (thickness/length) varying between 0.01 and 0.1 can quite accurately model the interface between two dissimilar media. The undrained shear strength of the slip elements should be a fraction of the undrained shear strength of the soil in order to simulate the adhesive strength of the interface.

Finally, these slip elements are used in this study to model the friction which develops during the process of sampler penetration into soils.

3.5 COMPUTER PROGRAM :

The finite element program used in this study is the CRISP (CRitical State Program) program developed by research workers in the Cambridge University Soil Mechanics Group. The CRISP program is based on continuum mechanics, critical state soil mechanics and finite element techniques. It is a robust program, reliable and widely used. Elastoplastic material models using Von Mises, Tresca, Mohr– Coulomb, Drucker– Prager yield criteria are

available and element sides can be given prescribed incremental values of displacements , loads or excess pore water pressures. Loading can be applied as nodal loads or pressure loads on element sides . The nonlinear solution technique used in this program is the incremental (tangent stiffness) approach with and options for updating nodal coordinates as deformation proceeds.

3.6 CONCLUSION

The main stages constituting the general finite element algorithm have been described for the particular case of axisymmetry. This was followed by a review of the literature on slip elements as well as an example illustrating their use and performance. Slip elements are modelled by simple rectangular finite elements of aspect ratio (thickness/length) varying between 0.01 and 0.1 . In later work, slip elements of aspect ratio of 1/30 have been used to model the friction occuring at the soil/sampler interface during sampling.

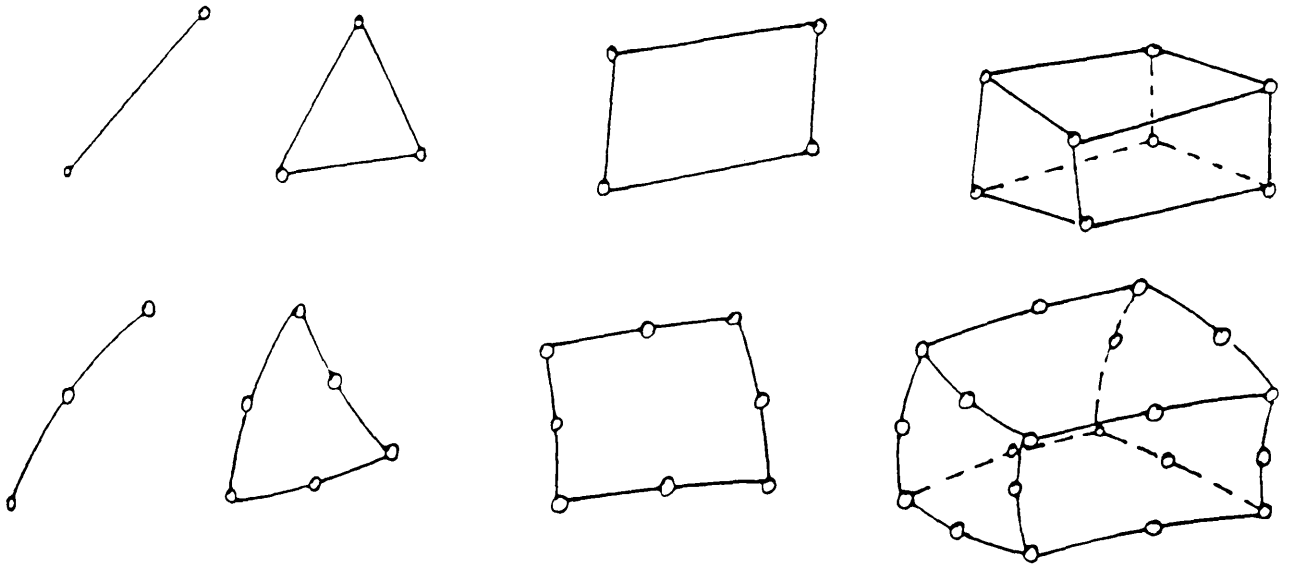

Figure 3.1 Some basic finite elements.

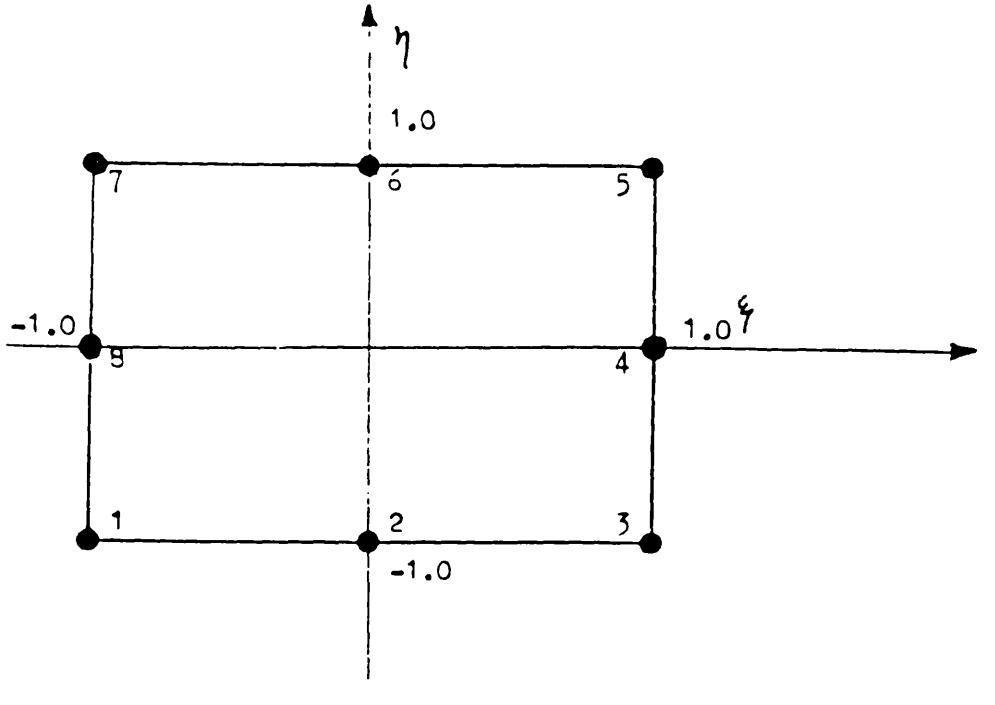

Figure 3.2 Eight-node Serendipity element.

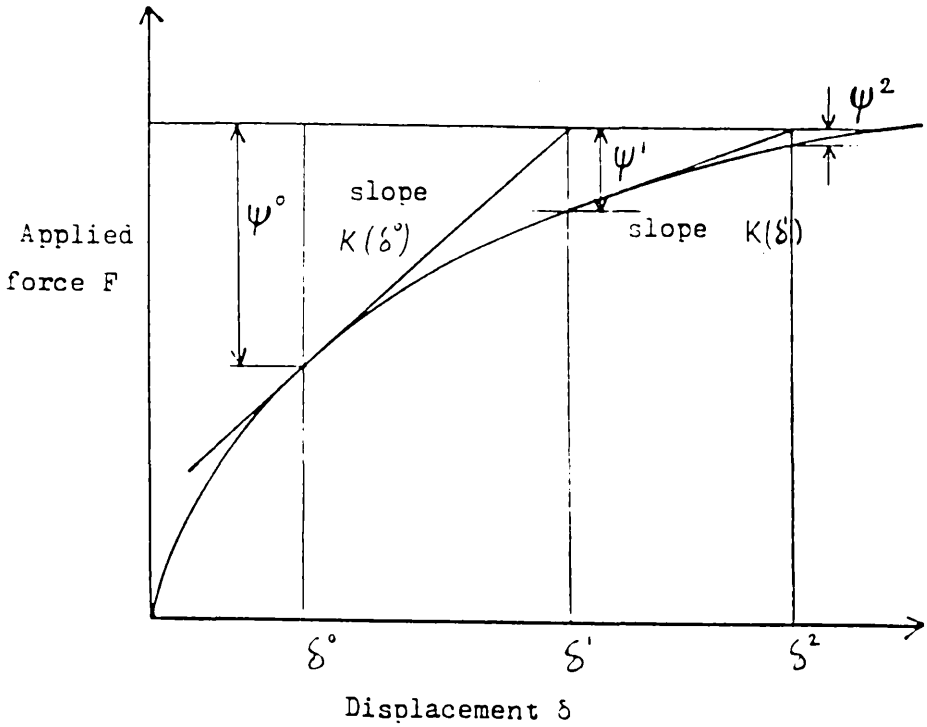

Figure 3.3 Tangential stiffness solution algorithm for a single degree of freedom.

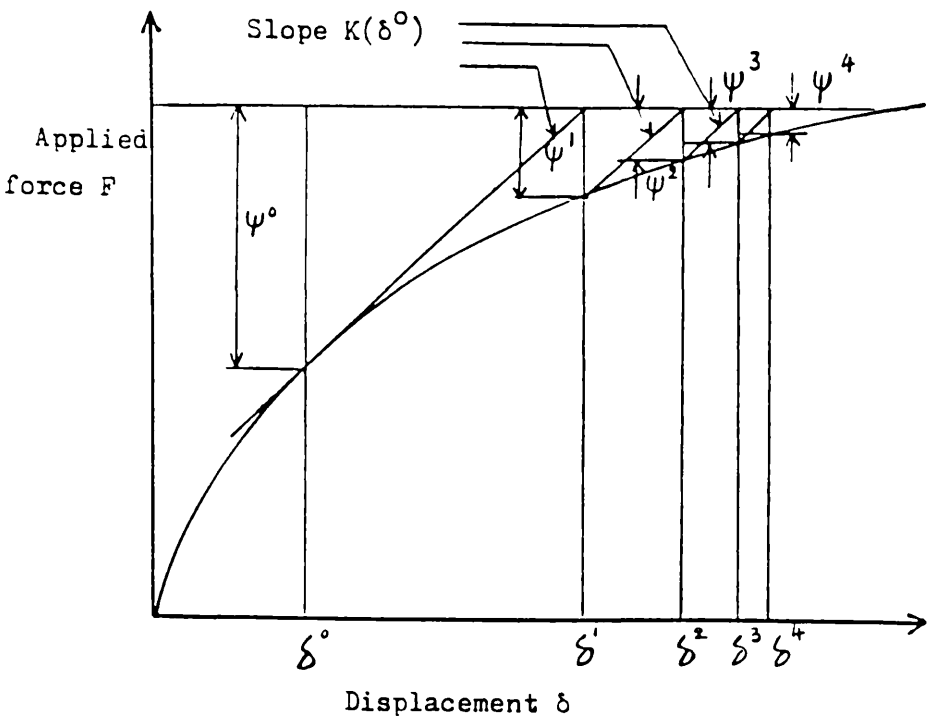

Figure 3.4 Initial stiffness solution algorithm for a single degree of freedom.

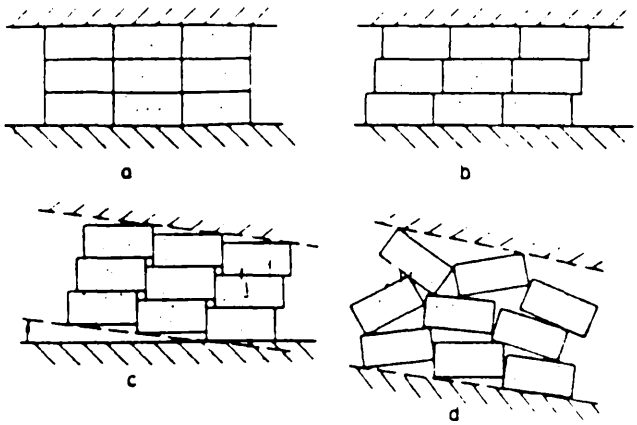

Figure 3.5 Deformation of jointed rock masses
a) Initial state
b) Shearing along one joint set
c) Shearing along two sets
d) Shearing and rotations

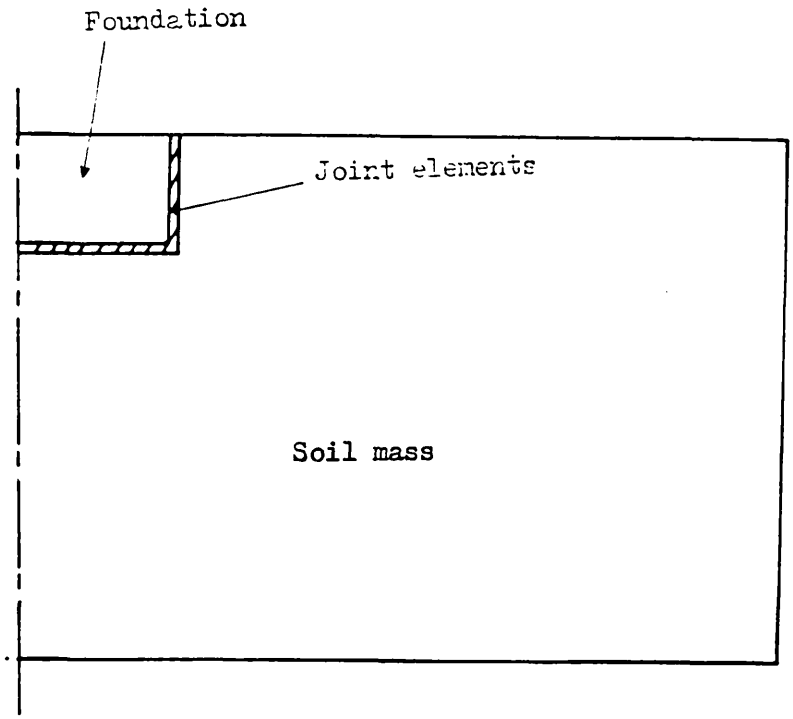

Figure 3.6 Soil-foundation interface

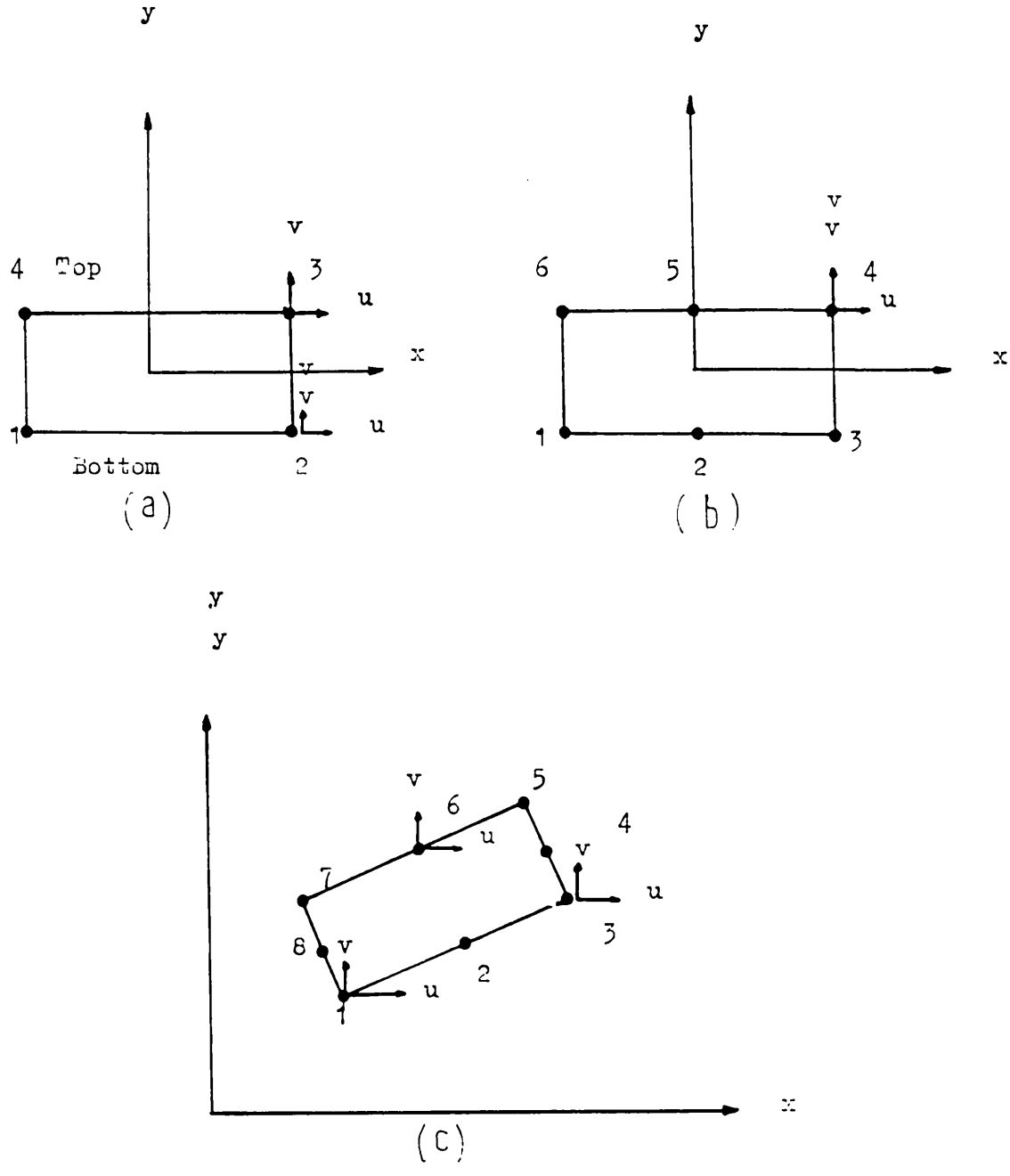

Figure 3.7 Joint elements used by different authors.

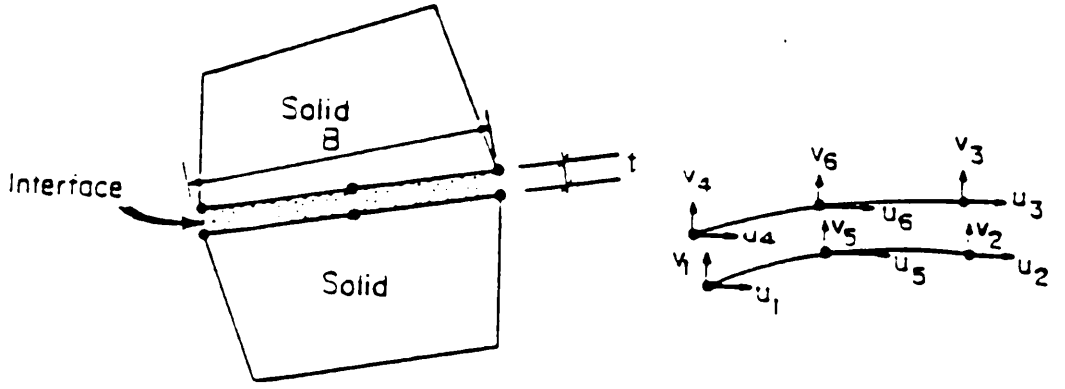

(a) Two-dimensional

B = (average) contact dimension

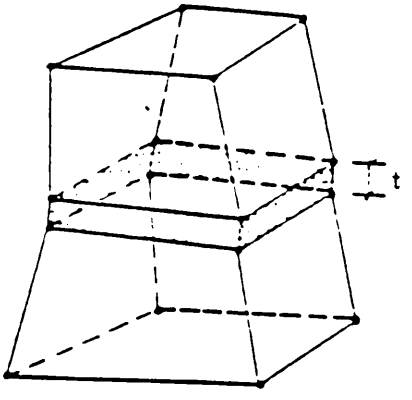

(b) Three-dimensional

Figure 3.8 Thin-layer interface element (17)

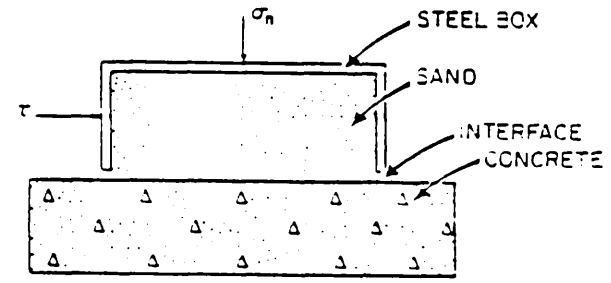

(a) Direct Shear Test for Concrete-Soil Interface

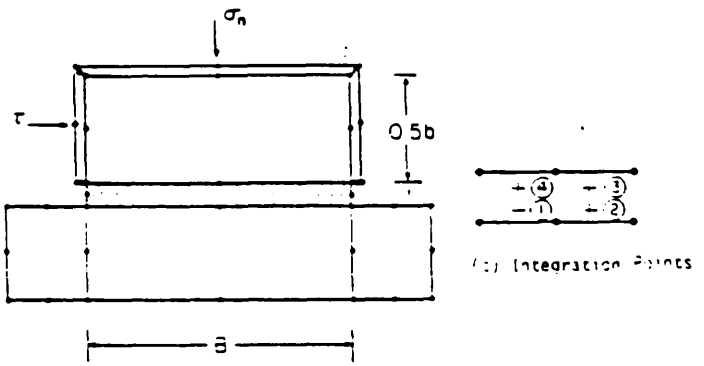

(b) Finite Element Mesh

(c) Integration Points

Figure 3.9 Analysis of direct shear test for choice of thickness

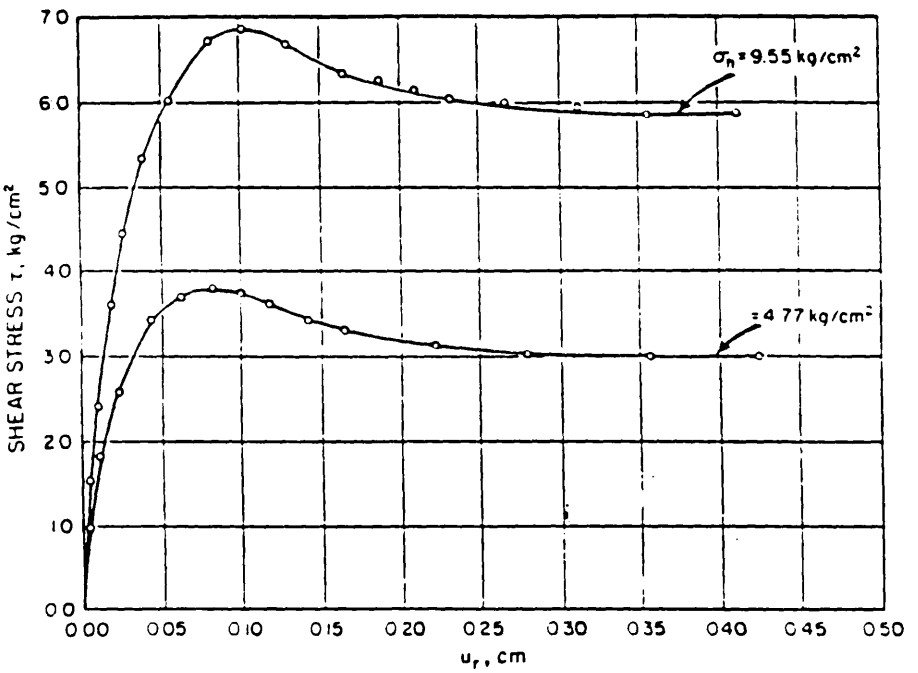

Figure 3.10 Typical direct shear test results, Dr = 80 percent (17)

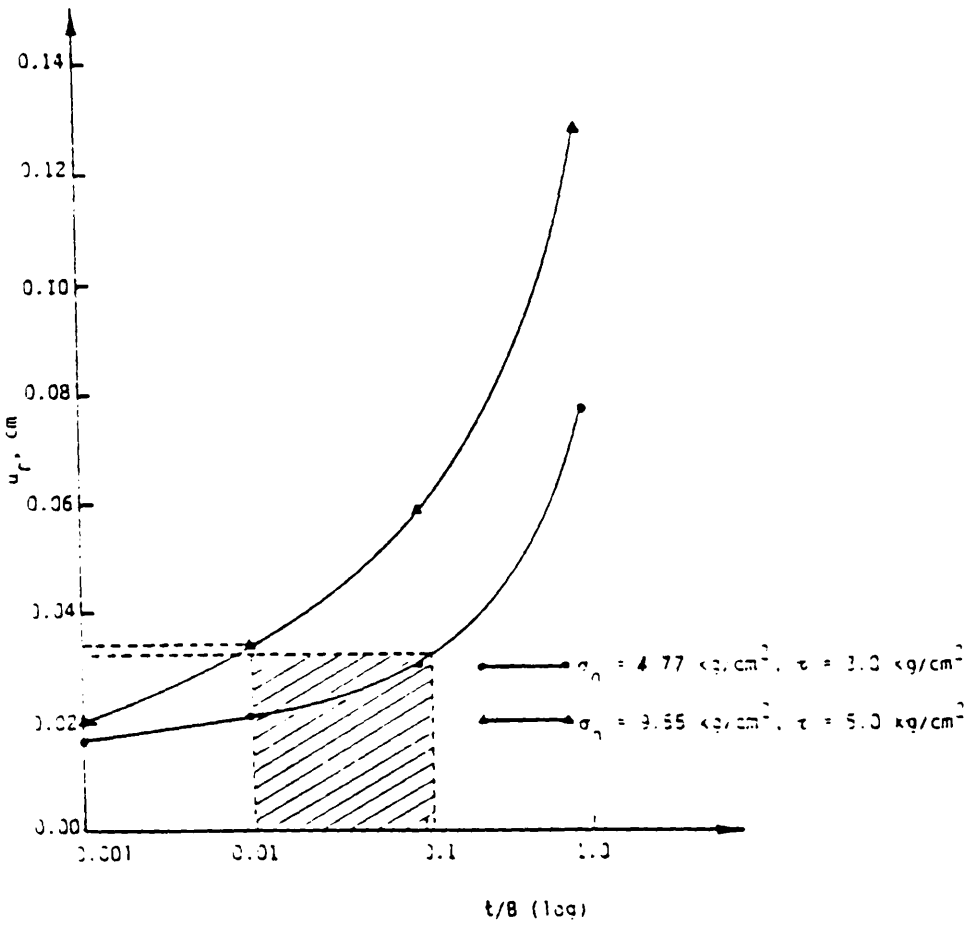

Figure 3.11 Effect of thickness of interface element. (17).

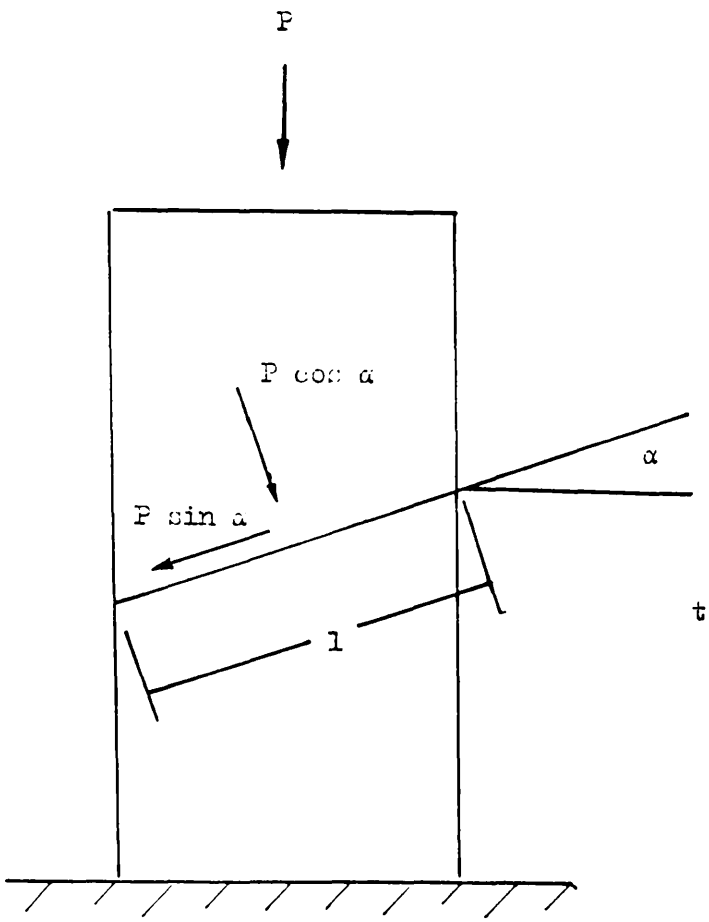

Figure 3.12 Axially loaded column

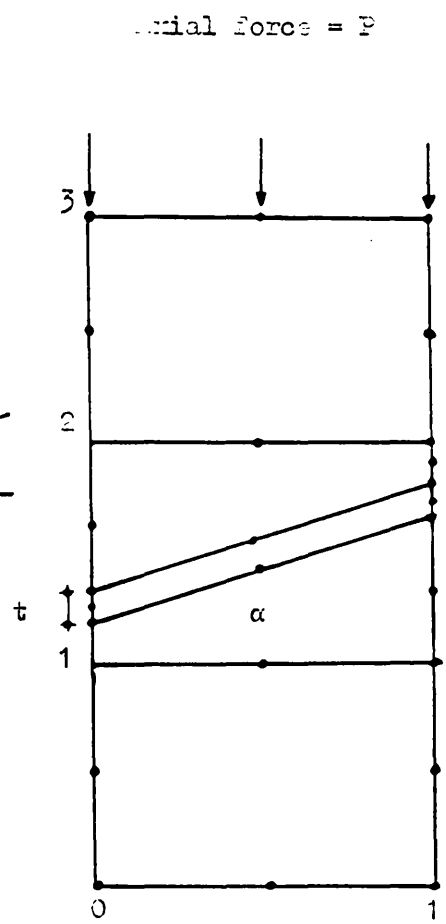

Figure 3.13 Mesh of 8-noded elements for study of inclined interfaces

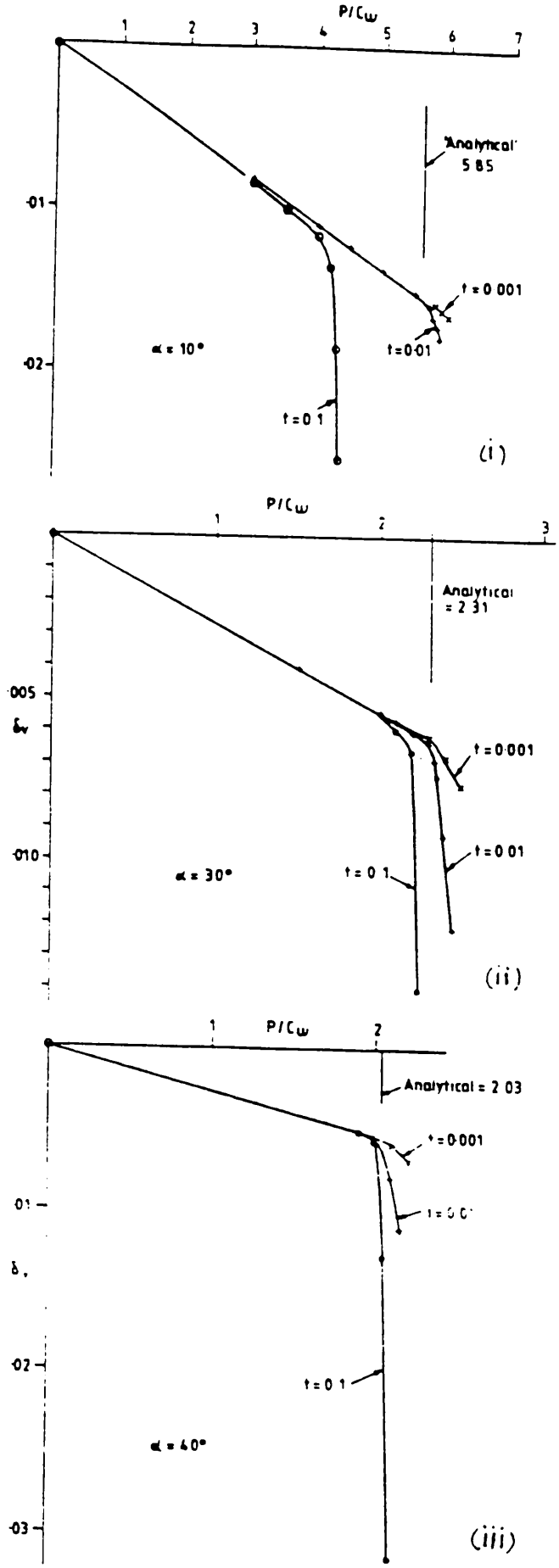

Figure 4.17 Computed force-displacement for different values of α (22).

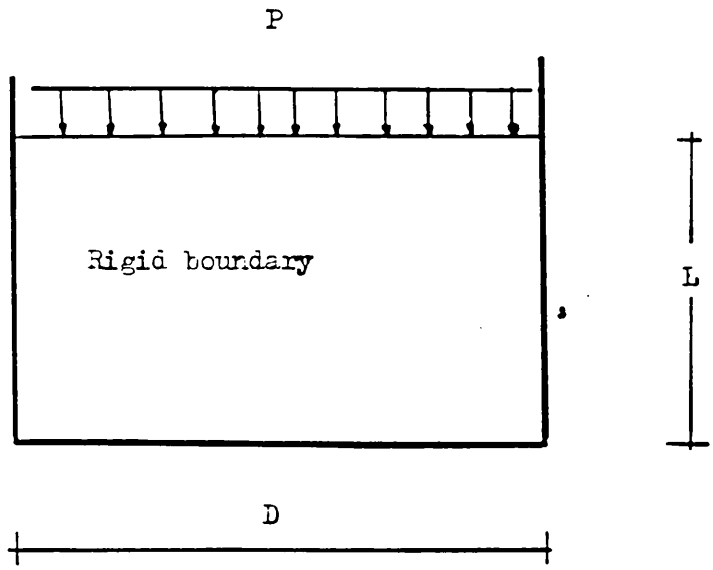

Figure 3.15 Presentation of the problem

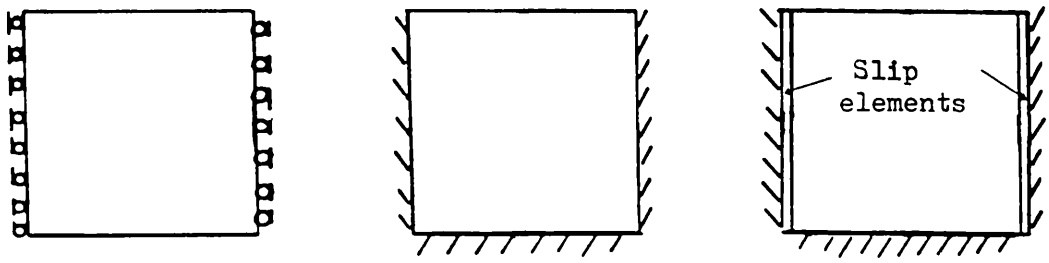

Figure 3.16 Presentation of the boundary conditions.

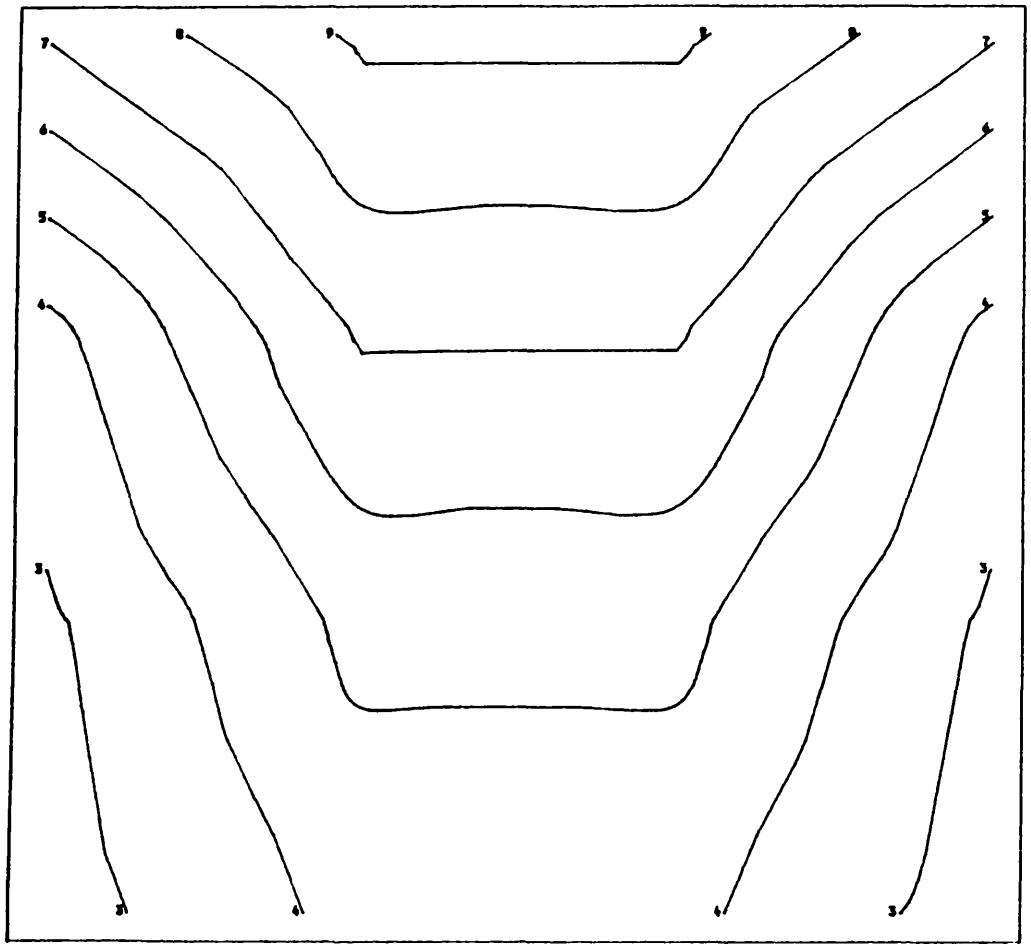

LEVELS	SIGY/P
1	0.100
2	0.200
3	0.300
4	0.400
5	0.500
6	0.600
7	0.700
8	0.800
9	0.900
10	1.000

FIGURE 3.17 VERTICAL STRESS CONTOURS (NO SLIP ELEMENTS)

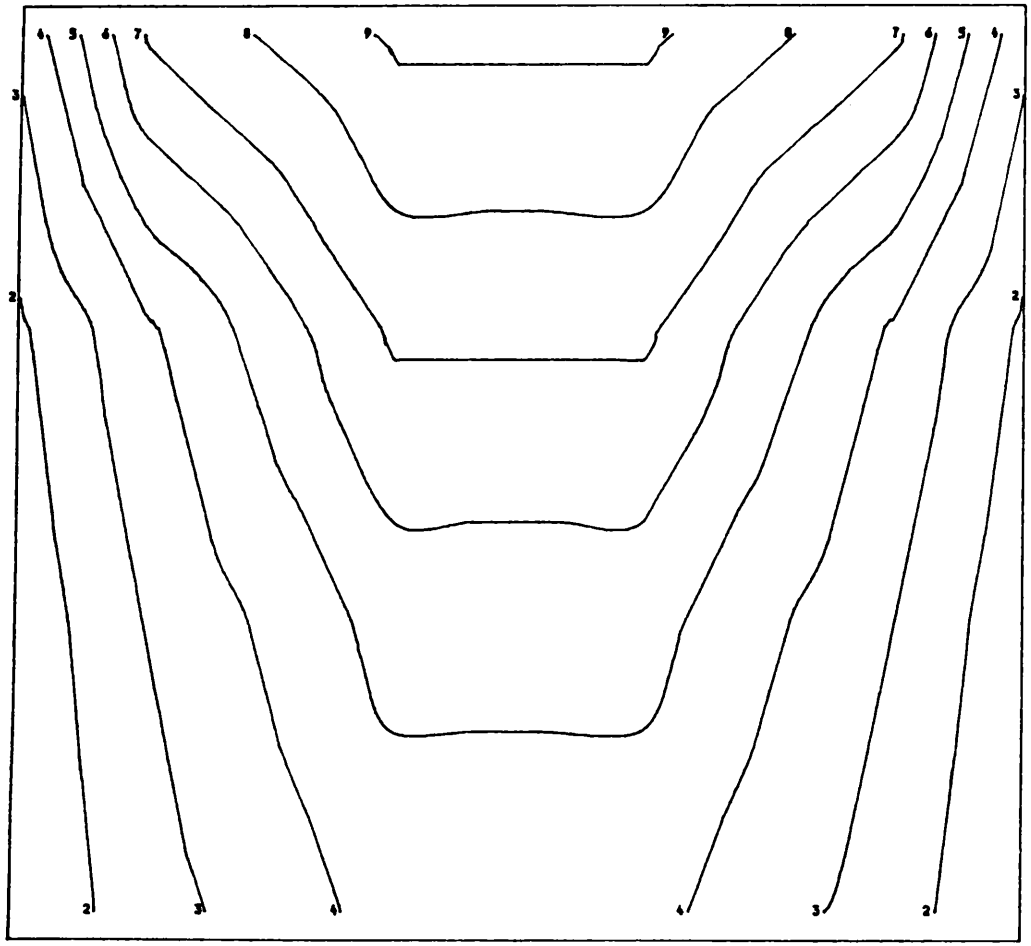

LEVELS	SIGY/P
1	0.100
2	0.200
3	0.300
4	0.400
5	0.500
6	0.600
7	0.700
8	0.800
9	0.900
10	1.000

FIGURE 3.18 VERTICAL STRESS CONTOURS USING SLIP ELEMENTS

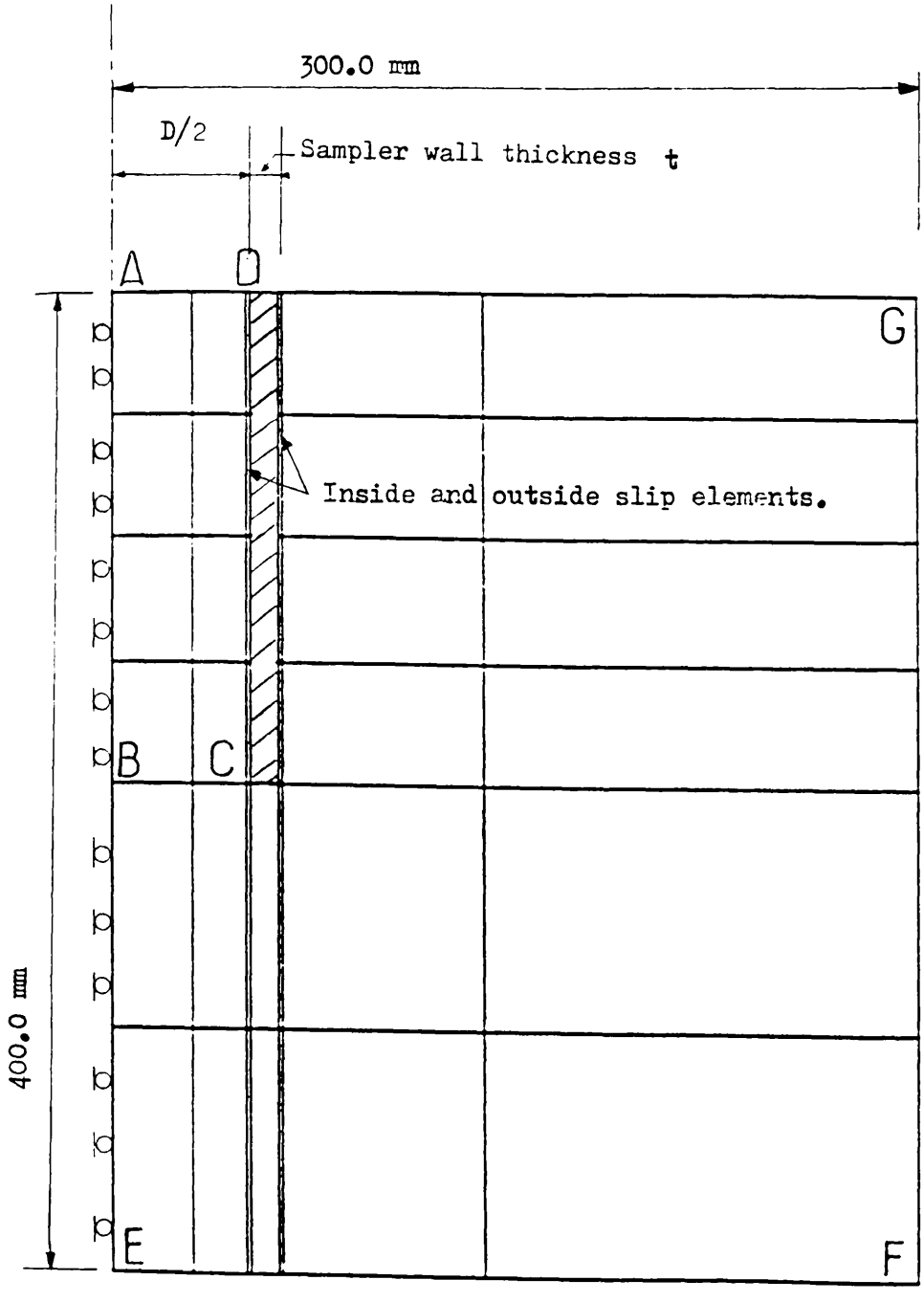

Figure 3.19 Finite element mesh for the sampling problem.

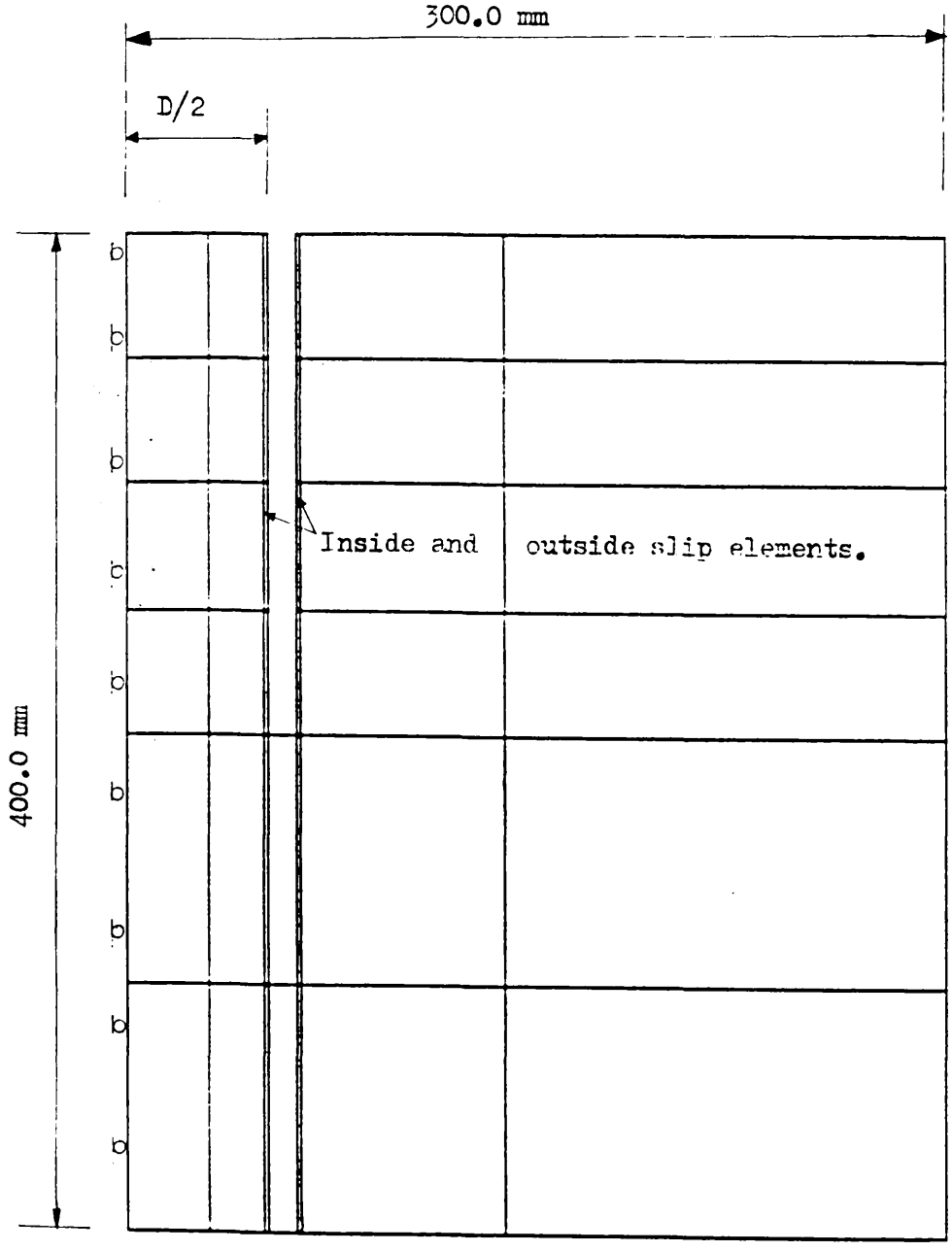

Figure 3.20 Finite element mesh of the sampling problem without the representation of the sampling tube.

CHAPTER 4

RESULTS

4.1 INTRODUCTION

The sensitivity of the numerical solutions obtained here to mesh size, boundary conditions, increment size etc has been investigated by means of a convergence study. Attention is then focussed on those parameters having the greatest effect on sampling disturbance; namely, sampler geometry, (diameter to thickness ratio, D/t, angle of cutting shoe etc), roughness of the sampling tube, and soil properties. A total stress analysis is carried out using the Von Mises criterion, followed by a more realistic effective stress analysis using the critical state elastoplastic model.

4.2 CONVERGENCE STUDY.

The aim of this part of the work is to obtain optimum values of mesh geometry, element type, size of increment, etc. In this study, the soil was modelled as a Von Mises elastoplastic material. The soil characteristics used are :

$E = 100$ N/mm2 $\quad Cu = 0.1$ N/mm2 $\quad Cu_{se} = 0.05$ N/mm2 $\quad \nu = 0.48$

where Cu and Cu_{se} are the undrained shear strengths of the soil and slip elements, respectively. A high value of E was used in order to avoid numerical difficulties associated with large deformations. Consequently, the results obtained here are most relevant to highly overconsolidated soils. Secondly, the assumption of elastic– perfectly plastic behaviour (the Von Mises model) is better suited to stiff clays than to soft clays.

Mesh geometry.

Fig. 4.3 depicts the load applied on the sampling tube versus the corresponding vertical tube displacement for the 38–, 52–, 86– and 125– element meshes shown in Fig. 4.1 and 4.2 . The number of elements in the meshes was increased where concentration of stress was expected. In general elements were added inside and below the sampling tube. Fig. 4.3 shows that the mesh geometry has very little effect on the soil response in the linear part of the curve. However, when the material behaviour becomes elastoplastic, the effect of mesh geometry becoms significant. The curves show that meshes with fewer elements offer stiffer responses to loading. The failure load decreases significantly when the number of elements in the mesh increases until a stable plateau of the load deflection curve was obtained. For instance, when the number of elements in the mesh increases from 52 to 86 elements, the load decreases (for a tube displacement of 2mm)from about 17.5 KN to 13.5 KN, which represents a variation of about 30 %. When the number of elements increases again from 86 to 125 elements, the load decreases about 13.5 KN to about 13 KN. Consequently, the 86 element mesh was adopted to model the problem of sampling operation during the course of this study.

Types of elements.

Recent research (Sloan and Randolph[53]) has shown that in axisymmetric analyses the constraint of no volume change (which occurs in undrained conditions) leads to finite element meshes 'locking up' if low order elements (such as linear strain triangles,LST, linear strain quadrilaterals, LSQ) are used. Accordingly two runs were carried out in order to see the effect of using high order elements (cubic strain triangles, CuST) on the load deflection curves of the sampling tube. Twenty six CuST and fifty two CuST element

meshes were used (Fig. 4.4) and and the corresponding load deflection curves for the sampling tube were recorded. Fig. 4.5 shows that the failure load obtained for the 52 CuST elements and 86 LSQ elements differs by only 3%. Consequently 86 LSQ elements was adopted since use of higher–order elements can lead to unnecessarily expensive analyses. Moreover, some investigators (10) have pointed out that there are occasions where the uses of lower–order elements can be advantageous: for example, situations where the mesh has irregular boundaries or contains several zones of soil with different properties.

Increment size.

The CRISP program uses the incremental or tangential stiffness approach: the total load acting is divided into a number of small increments and the program applies each of these incremental loads in turn. During each increment, the stiffness properties for the current stress levels are used in the calculations. If only a few increments are used, this method produces a solution which tends to drift away from the true or exact solution. This means a stiffer response results for a strain hardening model. This approach is in contrast to that adopted in the elastoplastic programs used in the analysis of mechanical engineering components or steel structures (Hinton and Owen (26), 1980). In these applications it is usual to use a large size of increment and to correct for the error by performing iterations within each increment until convergence to the non–linear load–displacement curve is obtained. Some claim to have applied the technique with the critical state models with no particular difficulty (Zienckiewicz (1975), Potts (1980)), but others Naylor (1975), Britto (1984) stated that sometimes there can be problem with convergence.

In the present study, the sampling tube was given a total prescribed vertical displacement of 2 mm. This displacement was divided into 70, 100, 200 and 400 equal increments corresponding to size increments of 0.03, 0.02, 0.01

and 0.005 mm respectively, and the load–displacement curve was recorded for each case. the soil characteristics are:

E = 100 N/mm2 Cu = 0.1 N/mm2 Cu_{se} = 0.05 N/mm2 ν = 0.48

where Cu and Cu_{se} are the undrained shear strengths of the soil and the slip elements, respectively.

Fig. 4.6 shows that up to 0.6 mm displacement of the sampling tube, the incremental size has a little effect on the soil response. From there on, for the case of 70 increments (size increment = 0.03 mm), the load–displacement curve obtained was unstable and had to be smoothed. Consequently, smaller increments of displacements (0.02mm, 0.01mm and 0.005mm) were used and practically the same smooth load–displacement curve was obtained in each case.

Boundary conditions.

The distance from the sampling tube to the bottom and lateral boundaries of the finite element mesh should be large enough to ensure that these boundaries will not have any significant effect on the response of the soil when subjected to the penetration of the sampling tube. To verify this, a finite element mesh with two different boundary conditions ((a) smooth and (b) rigid) was analysed. Results as shown in Fig. 4.8 indicate that with the ratios r/r_0 (radius of the soil from the centerline to the lateral boundary / radius of the sample) and H/D (depth of the soil / length of the sample) equal to 6 and 2, respectively, the load–displacement curves for the sampling tube coincide. Therefore, with these mesh dimensions, the boundary conditions do not have a significant effect on the response of the soil during sampling.

Updating nodal coordinates.

The nodal coordinates may be updated after each increment of the analysis by adding to the coordinates the displacements undergone by the nodes during the increment. The stiffness matrix of the continuum is then calculated with respect to these new coordinates during the next analysis increment. The intention of this process is that at the end of the analysis equilibrium will be satisfied in the final (deformed) configuration. Britto (10) stated out that although this approach would seem to be intuitively more appropriate when there are significant deformations it should be noted that it does not constitue a rigorous treatement of the large strain / displacement behaviour for which use of strain and stress tensors appropriate to large deformations and strains are required. Carter (12) examined the importance of non– linear geometric effects in geotechnical analysis and found that ' the linear assumption ' of small strains and small displacements is usually satisfactory in the solution of geotechnical problems. He concluded that for most geotechnical analyses, non– linearity arising from material behaviour is of more importance than non– linearity from geometrical effects. He added that in most situations use of updated coordinates leads to a stiffer load– deflection response near failure.

In the present study two runs were carried out using both updated and non– updated coordinates and the load– displacement curves recorded. Fig.4.9 shows that up to a displacement of the sampling tube of 1.0 mm,
the the load– displacement curves coincide. After that, the use of updated coordinates offers a stiffer response to loading. The option to use updated coordinates has not been used in this study because this small error tends to cancel out any errors in using only a finite number of finite elements.

4.3 PARAMETRIC STUDY.

This section is divided into two parts. The first part is a record of the results of total stress analysis and the second part concerns an effective stress analysis. These analyses shed light on the stress and pore water water pressure changes which occur during sampling as well as the progressive mechanism of failure and distortions which occur in soil samples.

4.3.1 Total stress analysis.

The Von Mises model has often been used for total stress analysis under undrained conditions and is adopted for this purpose here.

The material properties used for the clay are:

- Young's modulus: E = 100N/mm2
- Poisson's ratio: ν = 0.48

In undrained deformations, the deformation is assumed to take place so quickly that the water does not have time to flow out of the pores, i.e the soil behaves essentially as an incompressible material. The correct value of Poisson's ratio ν would therefore be 0.5. However, the use of this value in finite element program causes numerical problems since the bulk modulus ($K = E / 3 (1-2\nu)$) becomes infinite. In practice, this problem is circumvented by using a value of Poisson's ratio close to 0.5. Therefore a value of ν of 0.48 was used in this section.

The undrained shear strength of the soil, Cu, is assumed to be equal to 0.1 N/mm2. The values of the material parameters for the slip elements are similar to those of the surrounding soil except for the undrained shear strength which is related to the undrained shear strength of the soil by the equation :

$$Cu_{se} = \alpha \, Cu \qquad (4.1)$$

where

Cu_{se} : undrained shear strength of the slip elements.

Cu : undrained shear strength of the soil.

α : adhesion factor, $0 \leq \alpha \leq 1$.

The numerical tests.

Four series of numerical tests were run using the CRISP program. In the first series (TS1), the diameter to thickness ratio (D/t) of the sampler was varied whereas the length of the sampler, the geometry of the cutting shoe (i.e flat edged sampler) and the adhesion soil/sampler were kept constant. In the second series (TS2), the frictional behaviour at the sampler wall, simulated by inside and outside slip elements, was varied while everything else remained constant. In the third series (TS3), the values of length to diameter of sample (L/D) was varied from 1 to 4 while all other parameters remaining constant. In the fourth series (TS4), only the value of the tip angle of the sampler was varied in order to compare results between flat and sharp edged samplers. The two values used were 90° (flat edge) and 20° (sharp edge). Smaller values than 20° were not considered in order to avoid severe distortions of the finite elements surrounding the tip of the sampler.

Although the primary concern was with events taking place within the sampling tube, it is of interest to observe how these events relate to changes occuring outside the sample and the mechanism of transfer between the two regions. For this reason the plots are shown for a section of the domain larger than the sample, where failure zones, displacements, stresses and pore water pressure variations are given. Plots are generally given at the elastic as well as the plastic stages.

TEST SERIES TS1

Effect of D/t (diameter to thickness of the sampling tube)

Fig. 4.10 shows the load– displacement curves for the sampling tube using three different values of D/t : a thick tube (D/t= 10) and thinner tubes (D/t= 20 and 40). It should be noted that the diameter of the sampling tube has been kept constant (D= 100 mm) during this study whereas the thickness of the tube was varied. The plots show that D/t has a very little effect on the soil response in the linear part of the curves. However, when the soil yields, the effect of D/t becoms significant. For instance, when the thickness of the tube decreases from 10 mm to 5 mm (D/t increases from 10 to 20), the load decreases (for a tube displacement of 2 mm) from about 13 KN to 11.5 KN, which represents a variation of about 13%. When the thickness decreases again from 5 mm to 2.5 mm (D/t increases from 20 to 40), the load decreases from 11.5 KN to about 10 KN, representing a variation of 15%. This is due to the fact that the load necessary to push the sampler into the ground is increased if the bearing area at the base of the sampler is increased.

Displacement field

Fig. 4.11 shows the displacement field in the region of the sampling tube at the elastic state. The pattern of deformation shown represents the difference between the initial and the final position of the sampling tube. In general it was found that the displacement fields in the vicinity of the sampler are similar for all values of D/t in the elastic state (corresponding to a tube displacement of 0.1 mm) and consequently, no significant effect of D/t is apparent. These plots show that the top surface of the sample displaces downwards by about 0.1 mm remaining horizontal whereas for the soil outside the sampling tube, hardly any

movement takes place. In the plastic stage, Fig. 4.12 and 4.13 , distortions occur along the wall inside and outside the sampler. The top surface of the sample is slightly inclined resulting from the fact that downward displacement along the wall are slightly larger than those of the centerline. The greatest downwards displacement occurs for the thickest tube (D/t= 10).

Growth of failure zones.

In Fig. 4.14 to 4.16 , the mechanism of growth of the zones of failure are shown. The dots in the figures are are the corner nodes of elements forming the mesh. Generally, the zones of failure initiate close to the edge of the sampler at the outside slip elements and are dragged down with the tube. For D/t = 20 and 40, failure occurs in all outside slip elements at early stages of penetration of the sampling tube (d = 0.3 mm) whereas for D/t = 10, the failure of all outside slip elements occurs at a vertical displacement of the tube of 0.6 mm. Similarly, zones of failure propagate into the inside slip elements and the soil directly below the sampler. The rate of propagation of these zones of failure in the inside slip elements is similar for all D/t values and is complete at d = 0.6 mm. However, in the soil below the sampler, zones of failure reach the central part of the sample at earlier stages of penetration of the tube for the case of D/t= 10 than for the cases D/t= 20 and 40. This suggests that soil is disturbed even before entering the sampling tube and, an increase of the area ratio Ar (defined as $(De^2 - Di^2)/Di^2$ where D is the diameter of the sampler and subscripts (i) and (e) refer respectively to the internal and external diameters of the sampler) results in further disturbance of the soil. For instance, for D/t= 20 and 40 corresponding to Ar = 19% and 10%, respectively, the growth of zones of failure is similar, whereas for D/t= 10 (thickest tube) with Ar = 36%, the growth of the zones of failure occurs at earlier stages of penetration of the sampling tube

and affects larger areas than in the previous cases.

Vertical stress contours.

Fig. 4.17 to 4.19 show the vertical stress distribution in the elastic state (displacement = 0.1 mm corresponding to load level of about 6 KN, Fig. 4.10). The vertical stresses inside the tubes are practically constant accross the width of the tube. The vertical stress increases smoothly along the axis of the tube, reaching a maximum just below the tip of the tube. The maximum values of the stresses on the centroidal axis are 0.09 N/mm2 for the thick tube (D/t= 10) and 0.08 N/mm2 for the other tubes (D/t= 20 and 40). The vertical stresses fall off monotonically with distance below the tube. Outside the tube (excluding the soil beneath the sampler) the rise in vertical stress is small.

In the ultimate state (corresponding to a load level of 12 KN for a tube displacement of 2 mm), Fig. 4.20 to 4.22 show high vertical stress gradient normal to the wall over a short distance (about 8 mm). Thereafter, the vertical stresses inside the tubes are practically constant accross the width of the tube. The vertical stresses increase along the axis of the tube reaching the maximum just below the tip of the tube. The maximum values of the vertical stresses on the centroidal axis is 0.4 N/mm2. Very substantial increases in vertical stress occur just below the cutting shoe of the sampling tube and the area of the stress concentration increases with increasing tube thickness. Outside the sample and the soil beneath it, the rise in vertical stress is small.

Maximum shear stress contours.

Fig. 4.23 to 4.25 show the maximum shear stress contours

$(\sigma 1 - \sigma 3)/2Cu$ at the elastic state. The plots show that D/t has no effect on on the maximum shear stress at this stage. The value of $(\sigma 1 - \sigma 3)/2Cu$ increases along the axis reaching 0.3 at the bottom of the sample whereas its value is 1.0 in the narrow area (about 10 mm width) along the outer side of the sampler indicating that this part of the soil has already reached the state of failure. Outside the tube (excluding the volume of soil beneath the sampler) the maximum shear stress decreases smoothly reducing to zero at about 130 mm away from the sampler wall. However, Fig. 4.26 to 4.28 show that at the ultimate state (corresponding to a load level of about 12 KN), most of the soil below the sampler, the outer third of the sample and along the outer side of the wall over a short distance (about 10 mm) has reached the state of failure. It should be noted however, that zones of failure undeneath the sampler are larger for the thickest tube (D/t= 10). Consequently, disturbances of soil increase with increasing tube thickness.

Mean effective stress contours.

Fig. 4.32 to 4.34 show the mean effective stress contours at the ultimate state (displacement d = 1.5 mm). The curves show high pore water pressure gradients normal to the wall over a very short distance (about 5 mm) thereafter the pore water pressures inside the tubes are practically constant across the width of the tube. Pore water pressure increases smoothly along the axis of the tube, reaching a maximum just below the tip of the tube. This maximum appears to occur at grater depths in thick walled tubes (D/t= 10). For thin walled tubes (D/t= 40), the maximum occurs almost at the same level as the tip. There is a substantial increase in pore water pressure below the tube but these fall off monotonically with distance below the tube. The maximum values of pore water pressure on the centroidal axis is about 0.45 N/mm2 for the thickest tube

(D/t= 10) and 0.40 N/mm2 for thinner tubes (D/t = 20 and 40). It should be noted however that very substantial increases in in pore water pressure occur just below the cutting shoe of the sampling tube, although these are fairly localised. Outside the tube (excluding the volume of soil beneath the sampler) the rise in pore water pressure is small. In a continuous sampling operation therefore, it seems that a rise in pore water pressure of 0.4 N/mm2 can be expected in the soil samples over most of the volume. The high pore water presure gradients at the sample edges has significant consequences because of pore water migration and consolidation during storage and the inevitable delays before testing can commence.

TEST SERIES TS2 : ROUGHNESS OF THE SAMPLER.

In this second test series (TS2), the friction specified to the inner and outer side of the sampler is varied by specification of an adhesion factor α where :

$$Cu_{se} = \alpha \, Cu \qquad (4.2)$$

Cu_{se} : undrained shear strength of the slip elements.

Cu : undrained shear strength of the soil.

α : adhesion factor, $0 < \alpha < 1$.

All other parameters (diameter, thickness and length of the sampling tube) were kept constant as well as the angle of cutting edge of the sampler.

Load– displacement relationship.

Fig. 4.35 depicts the load displacement curve showing the effect of

roughness of the sampling tube. Fig. 4.35 shows the results for four cases : smooth sampler, smooth at inner side and rough at outer side (Outside Slip Elements, OSE), rough at inner side and smooth at outer side (Inside Slip Elements, ISE), and, finally, rough sampler (slip elements at both sides ISE and OSE).

Friction specified in all these cases is specified to be equal to 0.5 Cu (α = 0.5) since our concern here is just to see the effect of using or not using slip elements on the load–dislacement curve. It is worth noting that failure loads for rough samplers are approximately twice those for smooth samplers.

Displacement field in the vicinity of the sampler.

Fig. 4.11 shows the displacement field in the vicinity of the sampler at the elastic state (the load level is about 4 KN). Generally it was found that at this stage hardly any distortion takes place and the effect of roughness of the sampler on the soil response is not visible. In the ultimate state, Fig. 4.36 to 4.39 where the load level was about 11 KN, it can be seen that when soil–sampling tube interface is smooth, soil is dragged down very little and the displacement close to the sampler wall is similar to that at the centerline. The top surface of the sample remains horizontal. However, when the sampler wall is rough, the amount of soil that is dragged down with the sampler is very dependent on the degree of friction specified and the top surface of the sample is no longer horizontal. The largest downward displacement of the sample occurs when the inner side of the sampler wall is perfectly rough; that is α = 1.0 . But in this case (Cu_{se} = Cu) the top surface of the sample remains horizontal (the displacements at the centerline and close to the sampler wall are similar and are nearly equal to the displacement prescribed to the sampler (1.5 mm)). However, with α = 0.5, downward displacements are smaller than the previous case but the top surface is no longer horizontal. This is due to the fact that downward displacements close

to the sampler wall are larger than those at the centerline. Moreover, the curvature of the top surface is more pronounced close to the sampler wall than at the centerline . For the outer side of the tube, when α = 0.0 very little downward displacement of the soil outside the sampler takes place, but in all other cases (α = 0.5 and 1.0) soil in the vicinity of the sampler is displaced downwards close to the sampler wall. Far from the sampling tube (about 130 mm), the soil does not move significantly.

Growth of zones of failure.

Fig. 4.40 to 4.45 show the growth of failure zones at various stages of penetration of the sampling tube into soil. The propagation of failure zones depends on the friction being specified at the soil–sampling tube interface. For a perfectly smooth sampler, zones of failure propagate from the edge of the sampling tube and develop ahead of the sampler. The rate of propagation is slow and at a displacement of 1.5 mm, the zones of failure are localised just underneath the sampler wall and do not reach the centerline. For the rough sampler, six cases were studied depending on the degree of friction being specified at either inner or outer side of the sampler. We distinguish between the frictional constants for the inner and outer surfaces by the use of subscripts i and o, respectively.

In the first case (αi = 0.5, αo = 0.0) zones of failure initiate at the inside slip elements and the region close to the tip of the sampler and are generally dragged down with the tube until all the slip elements fail as well as the soil ahead of the sampler (at a vertical displacement of the tube of 1.0 mm). Zones of failure reach the central part of the sample at very early stages of penetration (d= 0.3 mm). It is worth noting that in this case the soil outside the sampling tube remais largely constant.

In the second case (αi = 0.0 and αo = 0.5) the outside slip elements start to fail first followed by the area underneath the sampling tube. At a tube displacement of 1.5 mm, the area affected by the zones of failure is smaller than the previous case even at d=1.0 mm. The zone of failure does not reach the central part of the sample.

In the third case (αi = αo = 0.5) where some friction is specified at both inner and outer sides of the sampling tube, the rate of propagation of zones of failure is similar to the first case (αi = 0.5 and αo = 0.0).

In the fourth case (αi = αo = 1.0) which represents the perfectly rough sampling tube, it can be seen that, at d=1.5mm, the zones of failure occupy the largest area among all other cases. Failure occurs in whole region underneath the sample and reaches the centerline into the sampler, and also the domain outside the sampler. It is worth noting that in this case the inside slip elements do not all fail during the process of pushing the sampling tube.

The fifth (αi = 1.0 and αo = 0.5) and the sixth (αi = 0.5 and αo = 1.) cases are similar to the previous case but the regions where failure occurs are smaller.

In conclusion, it is worth noting that the propagation of zones of failure depends greatly on the friction developed at the sampler–soil interface. The largest zones of failure occur for the roughe tubes. As might be expected, friction at the inner side of the sampler largely governs failure in the sample and directly below the sampler whereas friction at the outer side affects the soil outside the sampler.

Maximum shear stress contours.

Fig. 4.52 to 4.57 show the maximum shear stress contours at the ultimate state (d=1.5 mm, F=12 KN). The value of $(\sigma_1 - \sigma_3)/2Cu$ decreases across the width of the tube from the sampler wall to the middle third of the sample, reducing from 1.0 to 0.5 (in cases where αi or αo are greater than zero) and

from 1.0 to 0.2 in all other cases (αi or αo $\leq$ 0.5). Similarly, the value of $(\sigma_1 - \sigma_3)/2Cu$ is equal to 1.0 in the soil directly below the sampler. This zone of failure tends to extend to the bottom of the sample when α increses from 0.0 to 1.0 and, in general, zones of failure are larger in the sample amd the soil below the sampler for the perfectly roughe tube. Outside the sampler (excluding the volume of the soil beneath the sampler) it can be seen that zones of failure initiate close to the edge of the sampler and extend to the area along the the outer side of the sampling tube when α is increased from 0.0 to 1.0. The maximum shear stress contours decrease smoothly away from the sampling tube reducing to 0.2 at 160 mm from the sampler for αo = 0.0, 190 mm for αo = 0.5 and, finally, 200 mm for αo = 1.0

Mean effective stress contours.

Fig. 4.58 to 4.63 depict the mean effective stress contours at the elastic state (d= 0.1mm). Pore water pressures inside the tube are practically constant across the width of the tube. They increase smoothly along the axis reaching a maximum of 0.1 N/mm2 at the bottom of the sample, except for two cases (where no inside slip elements are used, i.e α = 0.0) where pore water pressures are concentrated in a narrow area at the bottom of the sample reaching a maximum of 0.08 N/mm2. Outside the sampler, the rise in pore water pressure is small.

Fig. 4.64 to 4.69 show the mean effective stress contours at the ultimate state (d= 1.5mm). The curves show high pore water pressure gradients normal to the wall over a short distance (about 5 mm) in the cases where αi = 0.5 . Inside this zone, the pore water pressures inside the tube are practically constant across the width of the tube. Pore water pressure increases along the axis of the tube reaching the maximum at the bottom of the sample in rough tubes. However, for

frictionless samplers, pore water pressures rise only at the bottom of the sample at the same level as the cutting shoe. The maximum of the pore water pressures on the centroidal axis is about 0.3 N/mm2 for the smooth tube and 0.5 N/mm2 for the roughe tube. It should be noted however that substantial increases in pore water pressures occur just below the cutting shoe of the sampling tube reaching a maximum value of -1.0 N/mm2. Outside the sample, no significant rise in pore water pressure takes place.

TS3: THE LENGTH TO DIAMETER RATIO (L/D) OF THE SAMPLING TUBE

Displacement field

Fig. 4.70 shows the displacement field in the vicinity of the sampling tube at the ultimate state (d=1.5mm). It can be seen that the soil displacement increases as the length of the tube increases . For instance, when the sampling tube is pushed downwards by 1.5 mm, the soil sample is dragged down by 0.7 mm for the shortest tube (L=100mm = D), 0.8 mm for L =200 mm (L/D = 2) and 1.45 mm for L = 400 mm (L/D = 4). The plots show also high gradients of displacement normal to the wall over a very short distance. These high gradients of displacement tend to decrease as L/D ratio increases.

Growth of zones of failure.

Fig. 4.71 and 4.72 show the growth of zones of failure at various stages of penetration of the sampling tube. Generally zones of failure initiate close to the outside tip of the tube and are dragged down with the sampler. For the

outside slip elements, the growth of zones of failure is similar for all L/D values and is complete at a tube displacement of 0.2 mm. However, for the inside slip elements, the zones of failure grow quite differently for different L/D values. For instance, failure zone is complete at d = 0.2 mm for L/D =1, at d = 0.5 mm for L/D = 2 and at d = 1.45 mm for L/D = 4. Consequently, disturbances in the outer third of the sample increase as L/D ratio decreases.

Vertical stress contours.

Fig. 4.73 and 4.79 show the vertical stress distribution in the elastic state (d= 0.1 mm corresponding to a load level of 6 KN). The vertical stresses inside the tube are practically constant across the width of the tube. Vertical stresses increase along the axis of the tube, reaching a maximum just below the tip of the tube. The maximum values of the vertical stresses on the centroidal axis are 0.1 N/mm2 for L/D = 1 and 0.08 N/mm2 for L/D = 2 and 4. The vertical stress fall off monotonically with distance below the tube. Outside the tube, the rise in vertical stresses is small. In the ultimate state (at d=1.5 mm and a load level of 12 KN), Fig. 4.74 and 4.80 show high vertical stress gradients normal to the wall over a short distance for L/D = 1 and 2 whereas these high gradients of vertical stresses do not appear for L/D = 4. The maximum values of vertical stresses along the axis of the tube are 0.2 N/mm2 for the shortest tube (L/D= 1), 0.4 N/mm2 for L/D = 2 and finally 0.5 N/mm2 for L/D =4. Again, outside the sampler, the rise in vertical stress is small.

Mean effective stress contours.

Fig. 4.77 and 4.83 show the mean effective stress contours in the elastic state. Pore water pressures are constant across the width of the tube and increase along the centroidal axis reaching a maximum at the bottom of the sample. In the ultimate state, Fig. 4.78 and 4.84 , the values of pore water pressure

increase with increasing length of tube. For L/D = 1, the maximum pore water pressure is 0.3 N/mm2 and for L/D = 4, the maximum pore water pressure is 0.5 N/mm2.

TS4: CUTTING SHOE ANGLE.

The effect of the cutting shoe angle is investigated in this section. The values of the cutting shoe angle used are α = 90° (flat edge) and 20° (sharp edge). Smaller values for α were not considered in order to avoid the severe distortions that may arise in the finite elements surrounding the tip of the sampler during loading, due to their very small aspect ratio (thickness /length). The main results (Fig. 4.85 to 4.92) show that the differences in soil behaviour using flat and sharp edges are localised in the area surrounding the tip of the sampler. They are summarised as follows:

- Zones of failure are larger for the flat edged sampler than sharp edged samplers.
- The maximum value of vertical stress is 0.8 N/mm2 for the flat edged sampler and 0.6 N/mm2 for the sharp edged sampler.
- The maximum pore water pressure is 1.0 N/mm2 for the flat edged sampler and 0.6 N/mm2 for the sharp edged sampler.

Consequently, it can be seen that a sharper cutting shoe angle reduces soil disturbance.

Discussion of the results:

The parameters having the greatest effect on sampling disturbance of clay samples during sampling operation have been investigated . It was found that an

increase of effective vertical stress along the centroidal axis of the sample of 0.1 N/mm2 (1 Cu) for the smooth sampler and 0.4 N/mm2 (4 Cu) for the perfectly rough sampler. The effective vertical stresses tend to increase from 4Cu with a sampler length of 200 mm (L/D = 2, D = 100 mm) to 5 Cu with a sampler length of 400 mm (L/D = 4). In the area just below the tip of the sampler, there is a substantial increase in effective vertical stresses due to the thickness and geometry of the cutting shoe showing clearly their effect on sampling disturbance during the process of pushing the tube into the soil.

Soil disturbance, as described by the maximum shear stress decreases towards the centre of the sample showing the effect of friction developed at the soil/sampler interface. This friction results in severe shearing of the outer third of the sample. The largest sheared zones are produced by the roughest tubes which verifies Hvorslev's statement that " the inside wall friction is the most important single source of disturbance during the sampling operation [27]".

Analyses conducted on samplers with flat edged tubes and sharp edged tubes indicated no significant effect of the cutting shoe on the stress or pore water pressure changes at the centerline.

Pore water pressure increases with depth in the central part of the sample reaching the value of 0.45 N/mm2 (4.5 Cu) at the bottom of the rough sampler and 0.4 N/mm2 (4 Cu) for the smooth sampler. High pore water pressure gradients develop close to the sampler wall over a short distance . Pore water pressure tends to decrease from the sides to the central portion of the sample. The high pore water pressures at the sampler edges may have significant consequences because of pore water migration and swelling during storage and other delays before laboratory testing. The failure zones within the sample initiate generally close to the edge and are gradually dragged down with the tube. Friction simulation tests reveal a tendency for the failure zones to approach the middle of the sample at early stages of penetration for rough tubes. Generally,the results show that the highest degree of disturbance occurs with rough thick

tubes.

4.3.2 Effective stress analysis

This section is concerned with the effect of the stress history of clay soils, modelled as associated modified Cam clays, on sampling disturbance. In all cases, the diameter to thickness ratio (D/t) of the sampling tube is assumed to be 20. The fundamental parameters of the clay analysed in these examples are as follows:

$\lambda = 0.2 \quad \kappa = 0.05 \quad \nu = 0.3 \quad e = 1.0 \quad M = 1.0$ (for the soil)

$M = 0.5$ (for the slip elements)

The in situ stresses are:

Initial pore water pressure $u_0 = -0.1$ N/mm2

$\sigma_z = \sigma_r = \sigma_\theta = 0.1$ N/mm2

The stresses are constant throughout the domain surrounding the sampling tube.

Discussion of the results.

Two analyses of soils subjected to sampling were carried out using the CRISP program. The sampling tube was pushed into two clays having different overconsolidation ratios (OCR = 1.5 and OCR = 10.0).

Until yielding occurs (during the process of pushing the sampler into the clay soil) the soil history, as expected, has no effect on the soil response.

Effective vertical stress contours.

Figs 4.93 and 4.99 show the effective vertical stress contours at the elastic state. It can be seen that the effective vertical stress remains at 0.1 N/mm2 over the volume of the sample but increases rapidly to 0.14 N/mm2 at the sampler tip level. This increase of effective vertical stress falls off below the sampler .

Pore water pressure contours.

Figs 4.95 4.101 show the pore water pressure contours at the elastic state. The pore water pressure increases smoothly along the centroidal axis of the sampler reaching the value of -0.02 N/mm2 ($0.2\ u_0$) at the same level as the tip of the sampler. This value of pore water pressure appears to be constant ahead of the sampler. Just below the tip of the sampler, a decrease of pore water pressure takes place reaching the value of -0.2 N/mm2 ($2\ u_0$). Outside the sampler, the rise in pore water pressure is small.

Deviator stress contours.

Figs 4.97 and 4.103 show that a deviator stress concentration of clay occurs in the area just below the tip of the sampler where the deviator stress is equal to the mean efective stress p (0.1 N/mm2). Elsewhere, the value of the deviator stress is is 0.02 N/mm2 throughout the volume of the sample although it increases to 0.05 N/mm2 in the soil ahead of the sampler.

Effect of soil history in the plastic state.

In the plastic state, after extensive yielding of the soil takes place, the

soil history has a significant effect on the soil response.

Effective stress contours.

Figs 4.94 and 4.100 show that the value of the effective vertical stress (σ_z) over the volume of the sample remains equal to 0.1 N/mm2 (the initial effective vertical stress) for both lightly overconsolidated and highly overconsolidated clay samples. Effective vertical stress increases rapidly at the bottom of the sample reaching 0.14 N/mm2 for the lightly overconsolidated soil but remaining reasonably constant ahead of the sampler whereas it reaches 0.5 N/mm2 for the highly overconsolidated sample but falls off with distance below the sampler. The curves show high effective stress gradients along the outer side of the sampling tube. The maximum value of effective vertical stress reached in this zone is 0.19 N/mm2 for the lightly overconsolidated clay and 0.65 N/mm2 for the highly overconsolidated clay sample.

Pore water pressure contours.

Figs 4.96 and 4.102 show that for the lightly overconsolidated clay, the pore water pressure increases along the centroidal axis of the sampler down to the middle of the sample reaching the value of 0.1 N/mm2 (u_0) and then remains constant in the lower half of the sample and for a distance of about D/2 below the sampler. However, for the overconsolidated clay sample, the pore water increases smoothly along the axis of the sample reaching the maximum of 0.4 N/mm2 (4 u_0) almost at the same level as the tip of the sampler. The pore water pressure falls off with distance below the sampler. A very large negative pore water pressure develops locally just below the edge of the sampler reaching the value of of -1.3 N/mm2 (13 u_0) for the overconsolidated clay sample. These large negative pore water pressures are a result of severe shearing of the

clay soil.

Deviator stress contours.

Figs 4.98 and 4.104 depict the deviator stress contours of lightly consolidated and overconsolidated clay soil at the plastic state. The deviator stress q is 0.07 N/mm2 in the sample for the lightly overconsolidated clay whereas it is 0.1 N/mm2 for an overconsolidated clay. For the lightly overconsolidated soil, at the bottom of the sample, the value of q is 0.08 N/mm2 . The deviator stress increases to 0.3 N/mm2 remaining constant for a distance of about D/2 ahead of the sampler for the overconsolidated soil. The maximum shear stress occurs on the outer side of the sampler where q is 0.1 N/mm2 for the lightly overconsolidated sample and 0.35 N/mm2 for the overconsolidated sample.

Growth of zones of failure.

Figs 4.105 and 4.106 show that, in general, the zones of failure within the sample initiate close to the sampler tip and propagate along both sides of the sampling tube and into the soil below the sampler. The zones of failure reach the central part of the sample at earlier stages of penetration of the tube (d = 4.0 mm) for lightly overconsolidated clay sample than for the highly overconsolidated clay (d = 10.0 mm). This is due to the fact that the yield stress of a highly overconsolidated soil is much higher than that of a lightly overconsolidated soil with the same value of initial stress.

Total and effective stress paths

The effective and total stress paths of 3 successive elements (elements

47,57 and 67, Figs 4.2) near the bottom of the sampler along the centroidal axis are shown in Figs 4.107 to 4.112 in (q − p) space for the two cases of lightly overconsolidated and highly overconsolidated clay samples. These plots show that these 3 elements behave similarly and hence only the results for element 47 are discussed.

Highly overconsolidated clay sample.

Fig. 4.107 shows the effective and total stress paths followed by a highly overconsolidated (OCR = 10) clay sample during the sampling operation. The total stress path shows that the deviator stress q increases during loading of the sample reaching a maximum value of 0.35 N/mm2. The effective stress path is vertical at the begining (elastic behaviour) until it intersects the yield surface. The path then passes through successive states of yielding until reaching a peak (q = 0.37 N/mm2) then continuous contraction of the yield surface (softening) occurs until the critical state line is attained.

Lightly overconsolidated clay sample.

Fig. 4.108 shows the effective and total stress paths followed by a lightly overconsolidated clay sample (OCR =1.5) during the sampling operation. The total stress path shows that the deviator stress increases during loading until it reaches a maximum value of about 0.08 N/mm2. The effective stress path is vertical at the begining (elastic state) until it intersects the yield surface. The path then passes through successive states of yielding before it attains the failure state represented in Fig. 4.108 by the critical state line of slope M. The clay hardens in this case. The hardening behaviour of lightly overconsolidated clay sample is characterised by continuous expansion of the yield surfaces up to collapse.

Effect of disturbance on soil behaviour.

The effect of sampling disturbance of these samples on their subsequent stress– strain behaviour and pore water pressure response to loading is investigated in this section by analysing their behaviour in their original states and in their disturbed states.

In this analysis, once the sampling simulation is finished, it is assumed that no further disturbance occurs except that the insitu shear stresses are removed. The samples theoretical response to conventional triaxial testing in compression (by means of a computer program listed in appendix) is then determined. This response is compared with that predicted for the sample in its original state. It should be noted, Fig. 4.117, that an ideal unloading of the sample has been considered in this section; that is the mean effective stress at the end of the sampling operation is assumed to be the actual mean stress of the sample (minimum disturbed state) before the start of the triaxial test. However, in practice, the mean stress decreases due to storage, transportation, etc before any testing commences.

Highly overconsolidated clay sample.

Stress– strain relationship.

Fig. 4.115 shows the stress– strain behaviour of a highly overconsolidated clay sample at its original state (OCR = 10) and after sampling. It can be seen that the stiffness of the sample in its disturbed state is 2.5 times that of its original state. This is due to the fact that during sampling the mean effective stress increases as the sample is sheared and hence the subsequent stiffness of the highly overconsolidated clay sample increases. This result does not accord with

practical experience and the discrepency may be attribute to several causes including the reduction in effective stress which normally occurs during the delay between sampling and testing and the destruction of the fabric of real soils during shearing.

Pore water pressure response.

The pore water pressure predicted during undrained triaxial compression of a disturbed sample also differs from that for the soil in its original state (OCR = 10), Fig. 4.116 . For instance, for the highly overconsolidated clay, the pore pressure increases up to a peak (u = 0.09 N/mm2) then decreases until reaching a constant negative value (u = −0.11 N/mm2), ie the values of the pore water pressure coefficient at failure A_f are −0.3 (u= −0.11) and 0.26 (u = 0.09), respectively . A negative value of A_f means that the tendency to dilate is strong enough to reduce the pore pressure to a level below that at the start of the compression test. However, after the sampling operation and testing of the sample in the compression test, a rather different pore water pressure response is obtained, Fig. 4.116 . The pore water pressure is now similar to that of a lightly overconsolidated clay sample where the pore pressure increases continuously up to a peak value and the pore pressure coefficient at failure A_f is 0.31.

Lightly overconsolidated clay sample.

Stress− strain relationship.

Fig. 4.113 shows the stress− strain behaviour of the clay in its original state (OCR = 1.5) and after sampling. Fig. 4.113 shows that the deviator

stress increases continuously up to failure reaching the value of 0.08 N/mm2 . This means that the soil hardens. The plots show also a slight decrease in the stiffness of the disturbed soil.

Pore water pressure response.

Fig. 4.114 shows that the the pore water pressure increases continuously during loading for both cases (original and disturbed states) . The difference between the two cases is that the maximum value of the pore water pressure for the original sample is 0.05 N/mm2 (A_f = 0.6) whereas it is only 0.03 N/mm2 (A_f = 0.38) for the disturbed sample.

4.4 CONCLUSION

In this section, an investigation into the parameters having the greatest effects on sampling disturbance of clays during the sampling operation has been carried out. The numerical results are presented in two stages; first, a detailed study of the convergence of the solution process was carried out. Secondly, a parametric study which included the effects of sampler geometry (Diameter to thickness ratio (D/t), angle of cutting shoe, etc), roughness of the sampling tube and the soil history on the degree of disturbance was described . Observation of the propagation of yielding in clay samples during the process of pushing the sampler into soil has been helpful for the undcrstanding of failure mechanisms. Contours of the stress components and stress invariants in the soil mass were also plotted in elastic and plastic states. Soil disturbance, as described by the maximum shear stress, decreases towards the centre of the sample. Friction simulation tests by means of the so–called slip elements show that the highest degree of disturbance occurs for the roughest tubes. This agrees well with Hvorslev's statement that " The inside wall friction is the most single source of

disturbance during the sampling operation " (27).

Pore water pressure increases with depth along the centroidal axis of the sampler reaching an average of 4 Cu. The maximum pore water pressures develop close to the tip and this suggests that during storage water would migrate from the sides (disturbed) to the central portion of the sample (relatively undisturbed). Negative pore water pressures occur in some soils as a result of severe shearing of the soil during the sampling operation but the highest pore water pressures are generated if thick rough sampling tubes are used.

Using the simple associated Cam clay model, it was found that highly overconsolidated soils are particularly susceptible to the effects of sampling disturbance although even lightly overconsolidated soils are not immune to disturbance.

38 elements

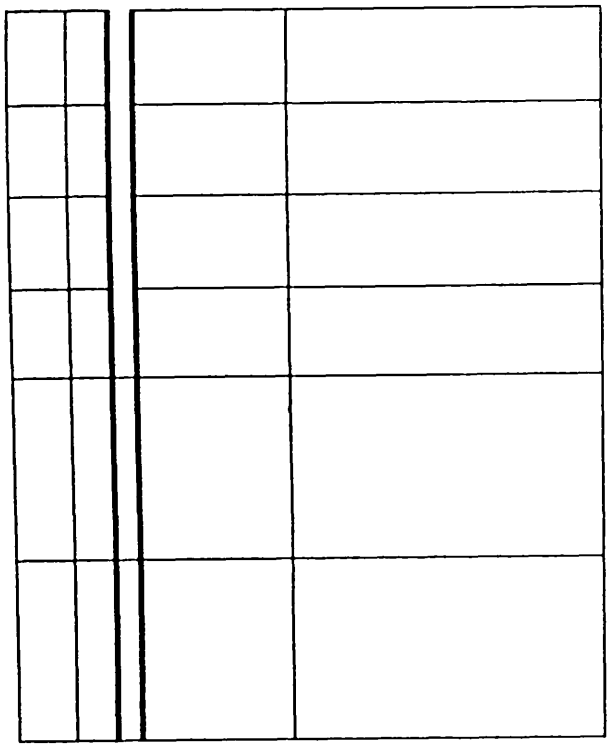

52 elements

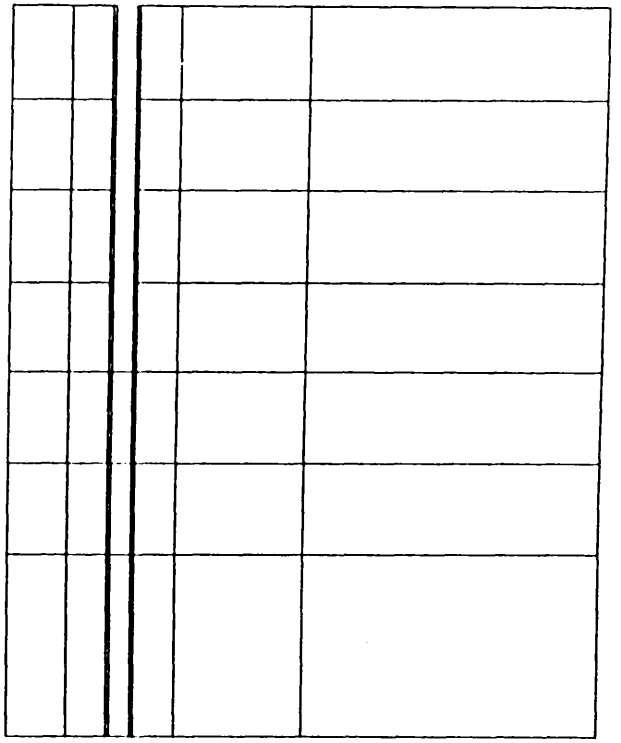

Figure 4.1 Finite element meshes for the sampling problem.

86 elements

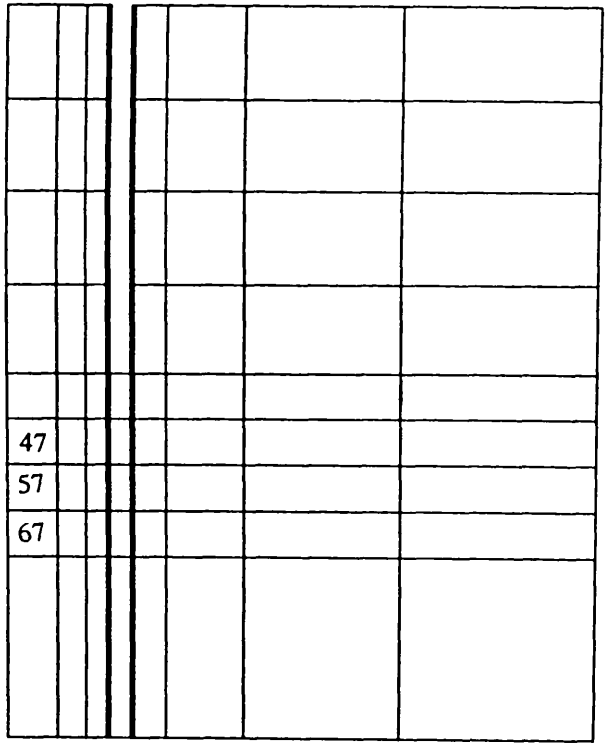

125 elements

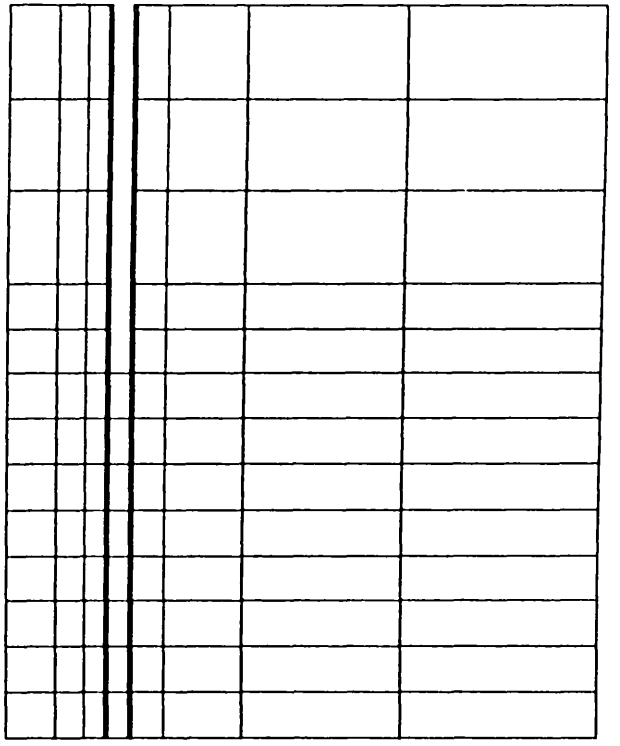

Figure 4.2 Finite element meshes for the sampling problem.

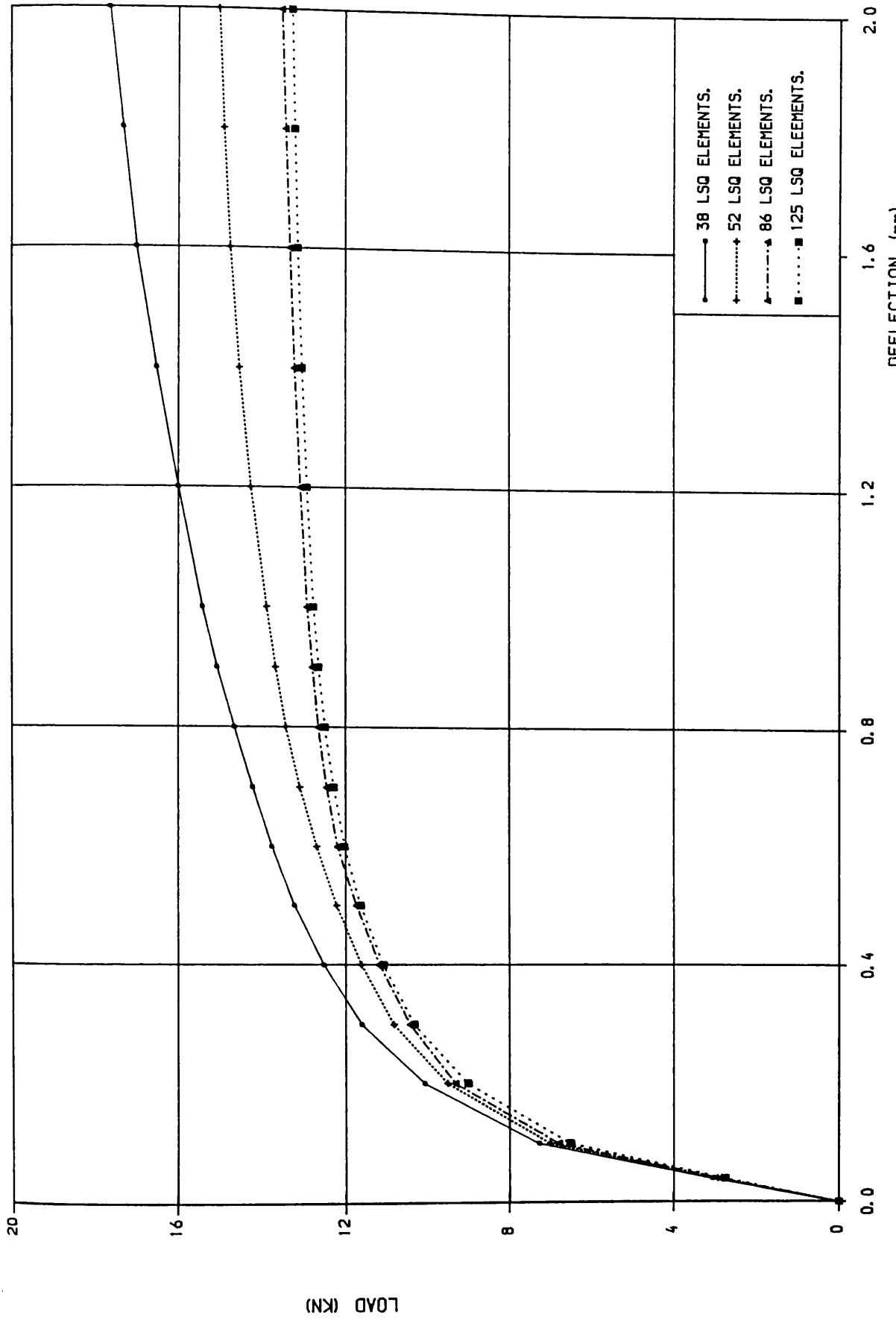

FIG. 4.3 LOAD DEFLECTION CURVES , EFFECT OF MESH GEOMETRY.

26 CuST elements

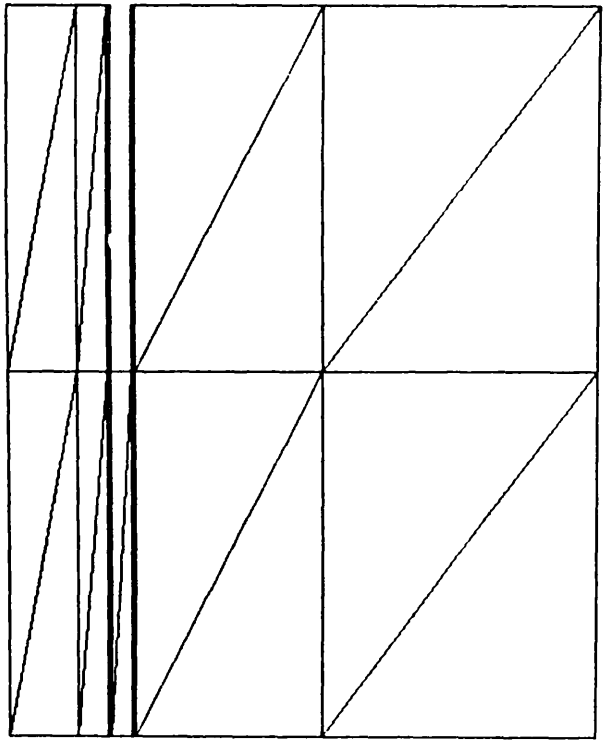

52 CuST elements.

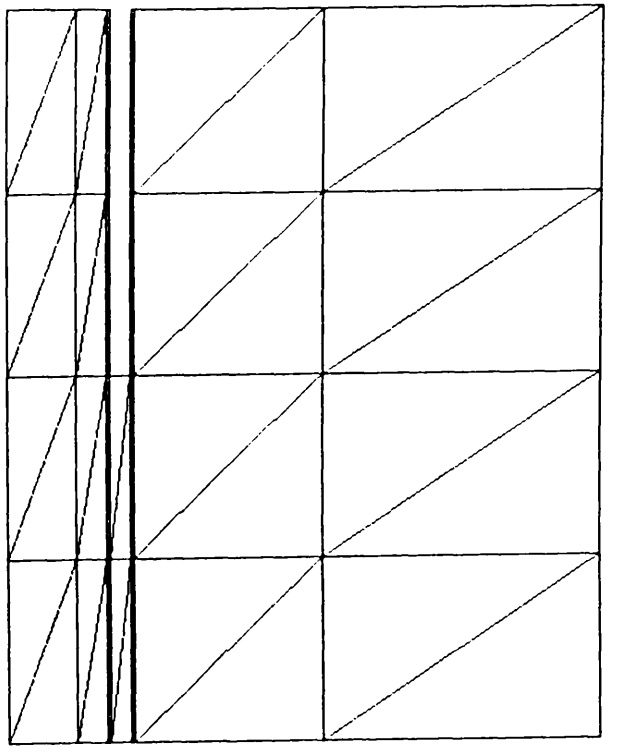

Figure 4.4 Finite element meshes for the sampling problem using CuST elements.

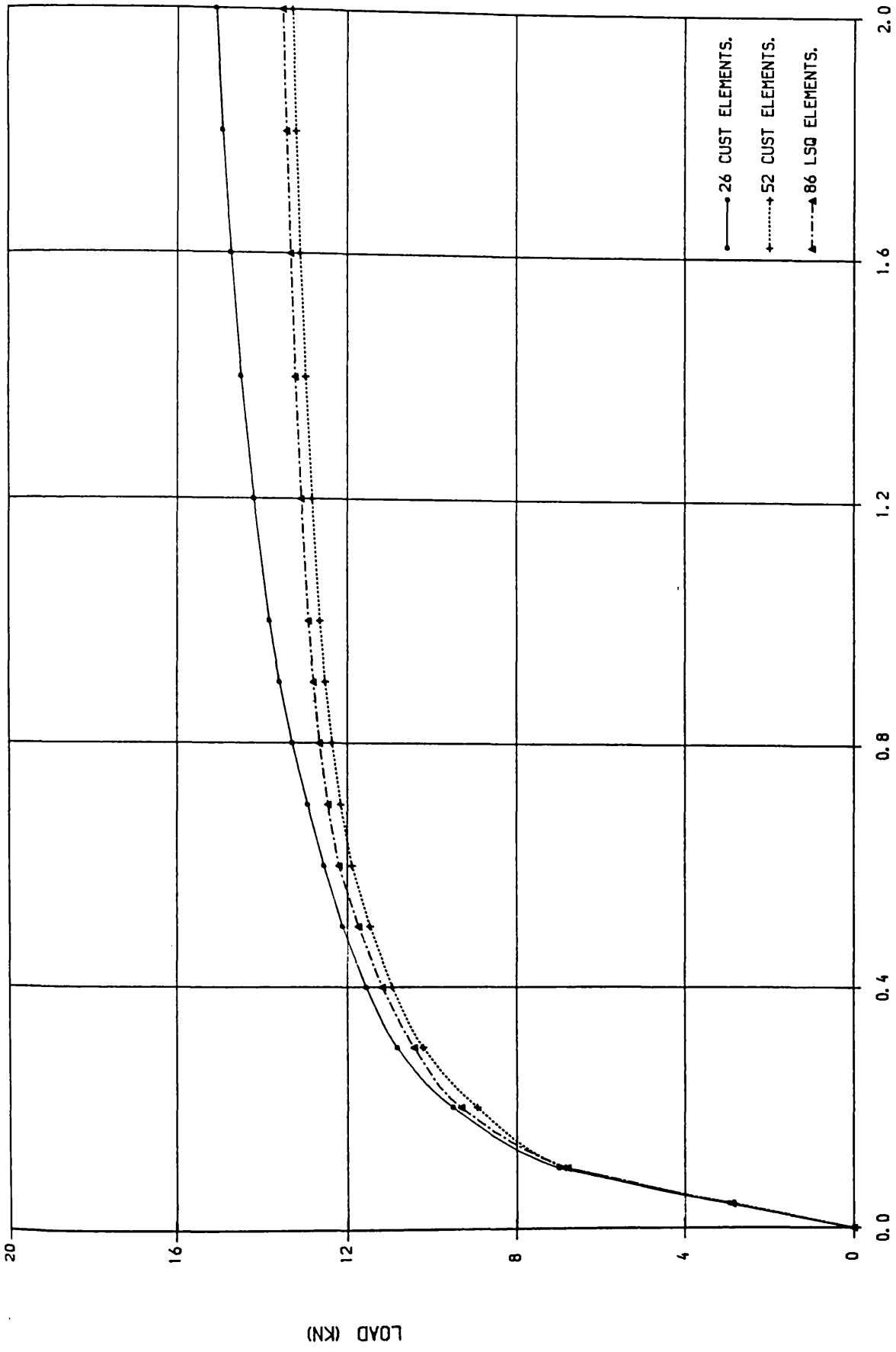

FIG. 4.5 LOAD DEFLECTION CURVES, EFFECT OF ELEMENT TYPE.

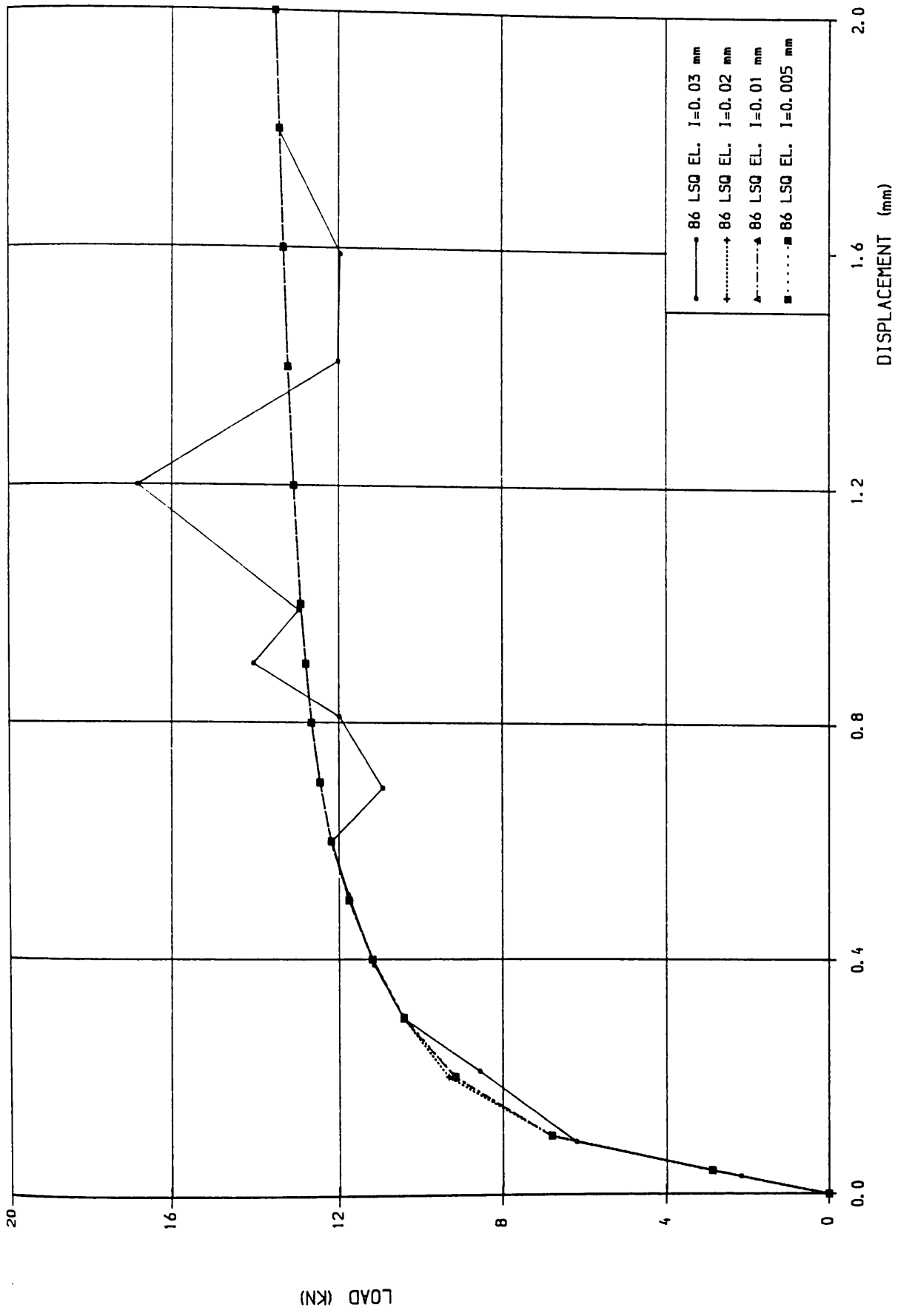

FIG. 4.6 LOAD DEFLECTION CURVES , EFFECT OF SIZE INCREMENT

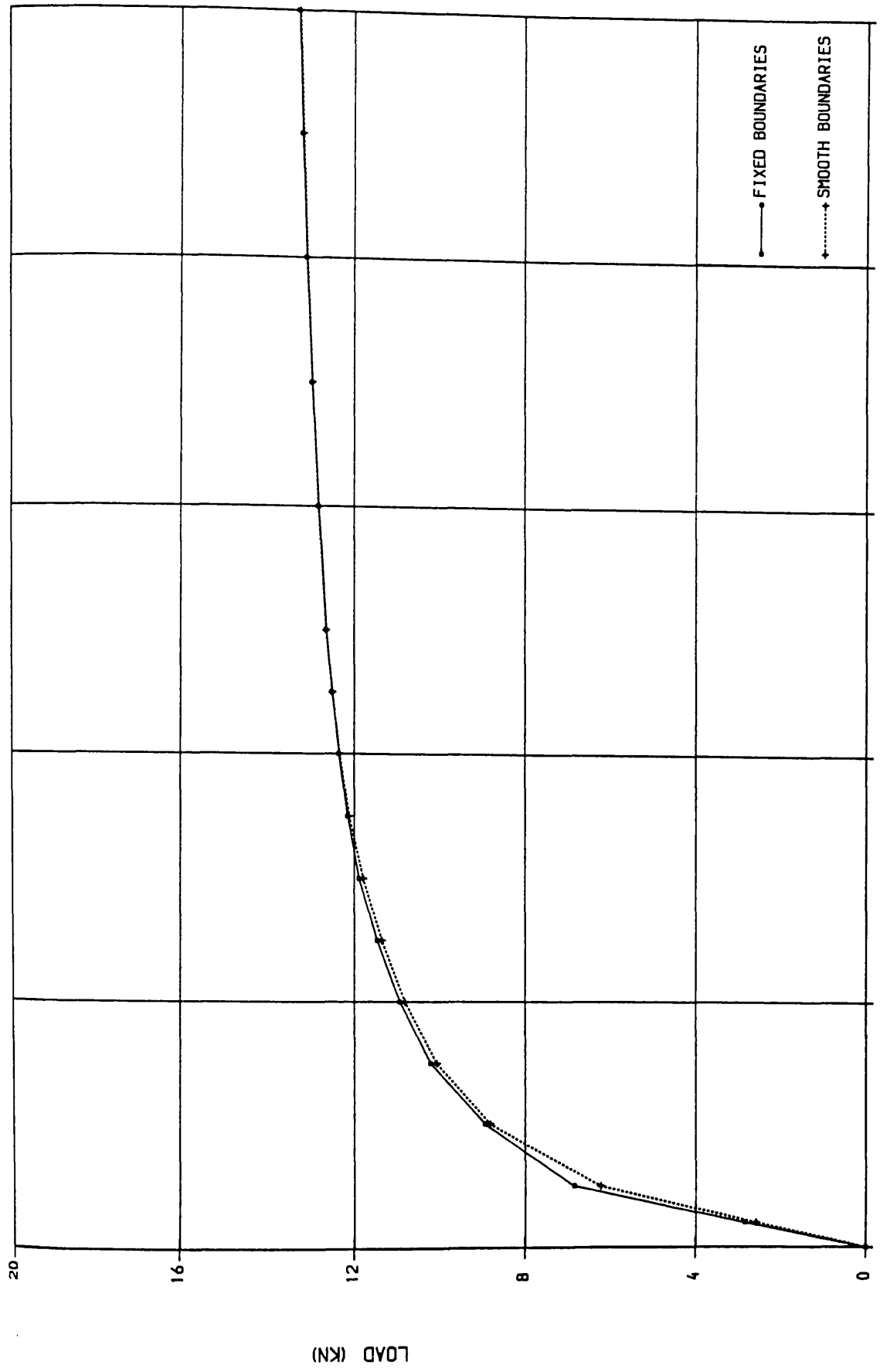

FIG. 4.8 LOAD DEFLECTION CURVES, EFFECT OF BOUNDARY CONDITIONS

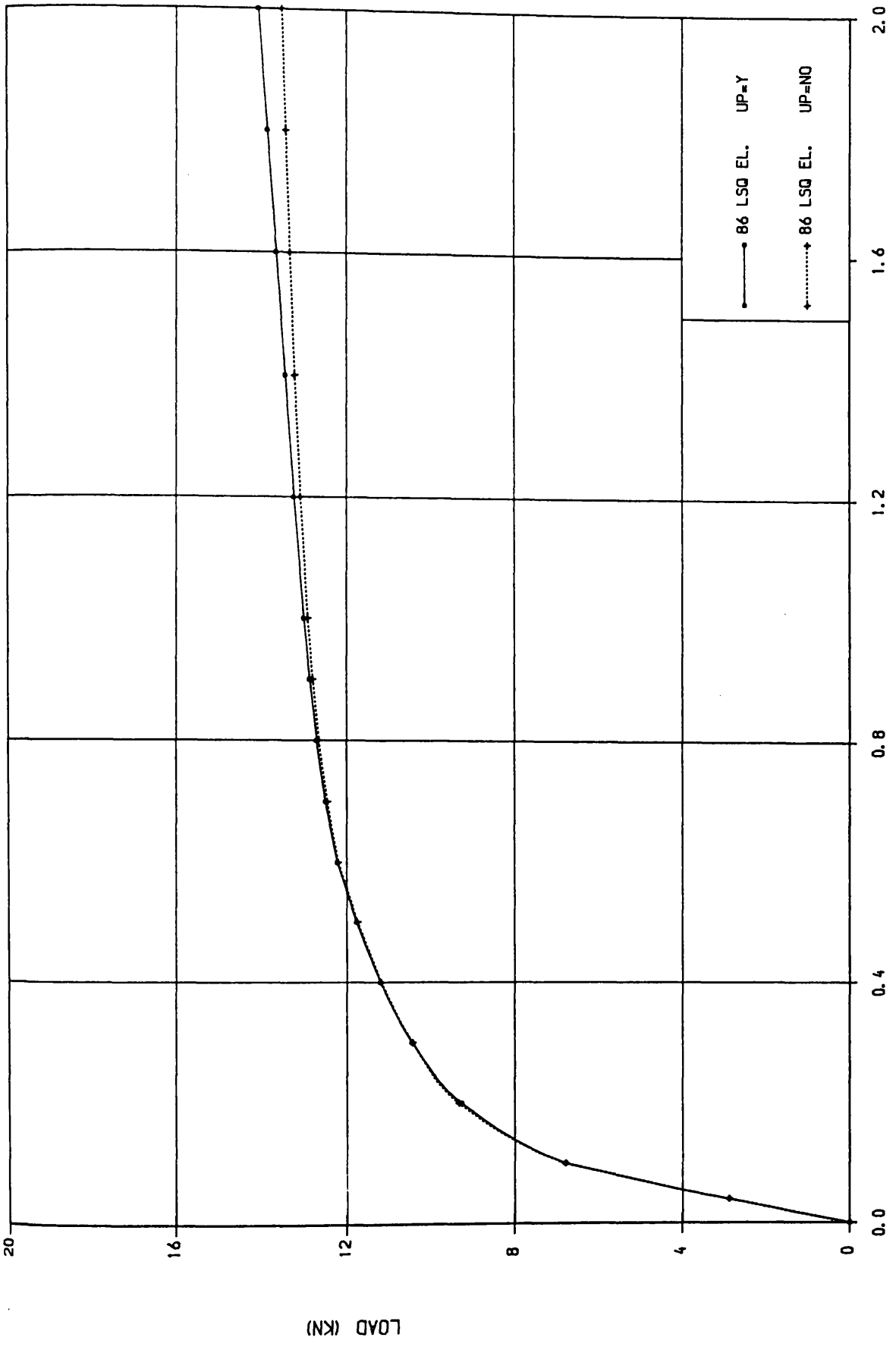

FIG. 4.9 LOAD DEFLECTION CURVES , EFFECT OF UPDATING COORDINATES

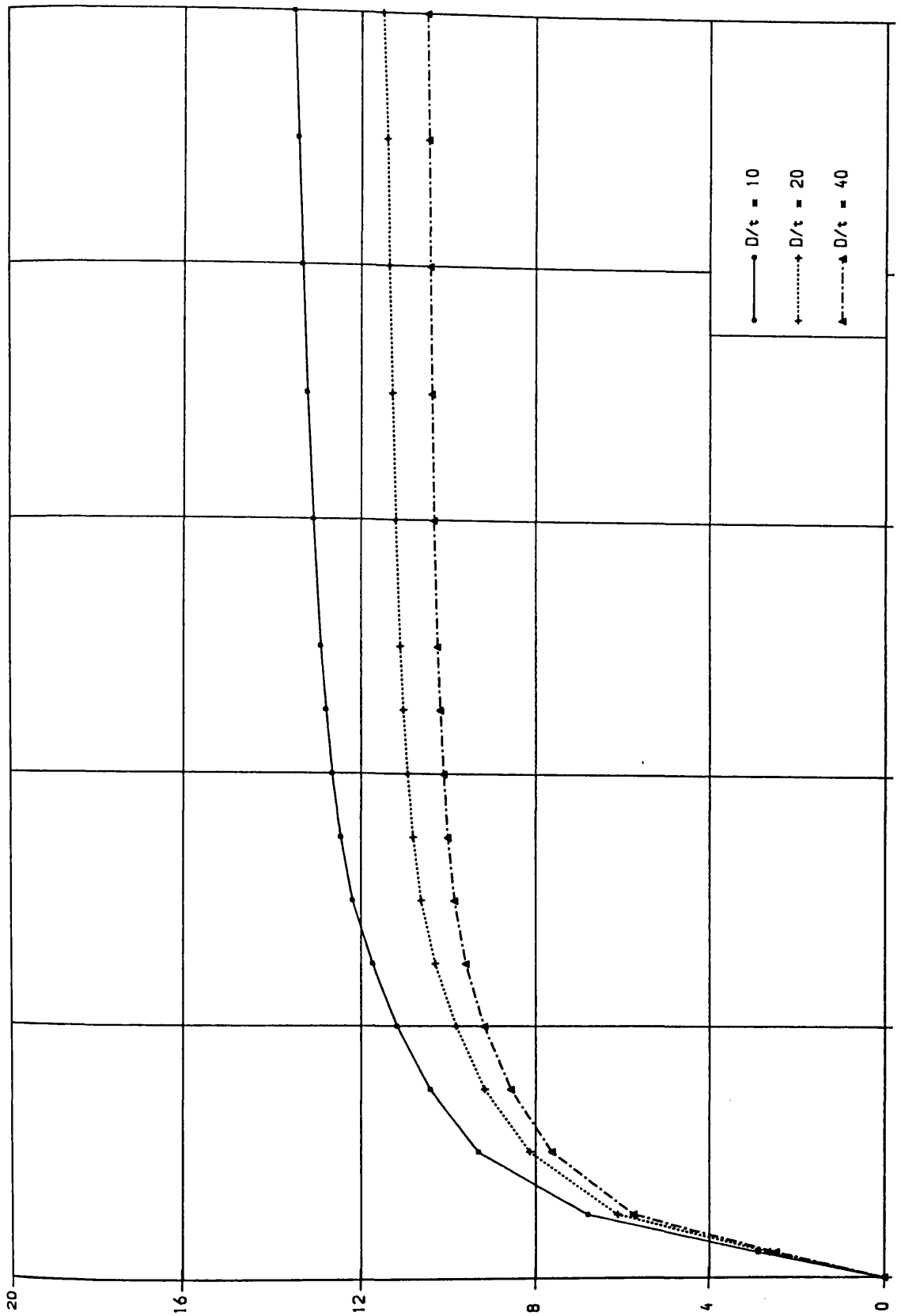

FIG. 4.10 LOAD DEFLECTION CURVES , EFFECT OF D/t

(only displacement field is drawn to scale)

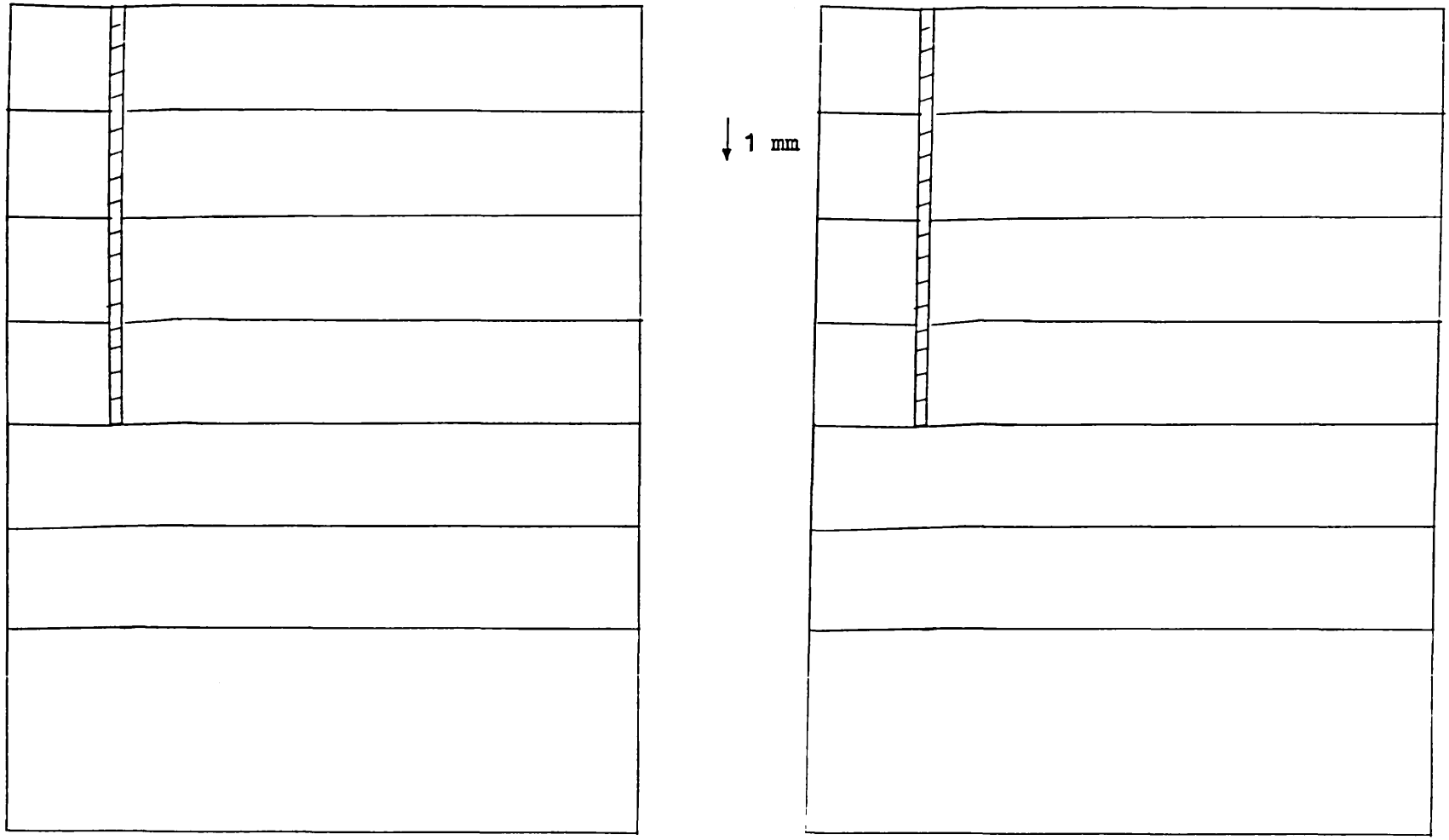

Fig. 4.11 Displacement field in the vicinity of the sampling tube

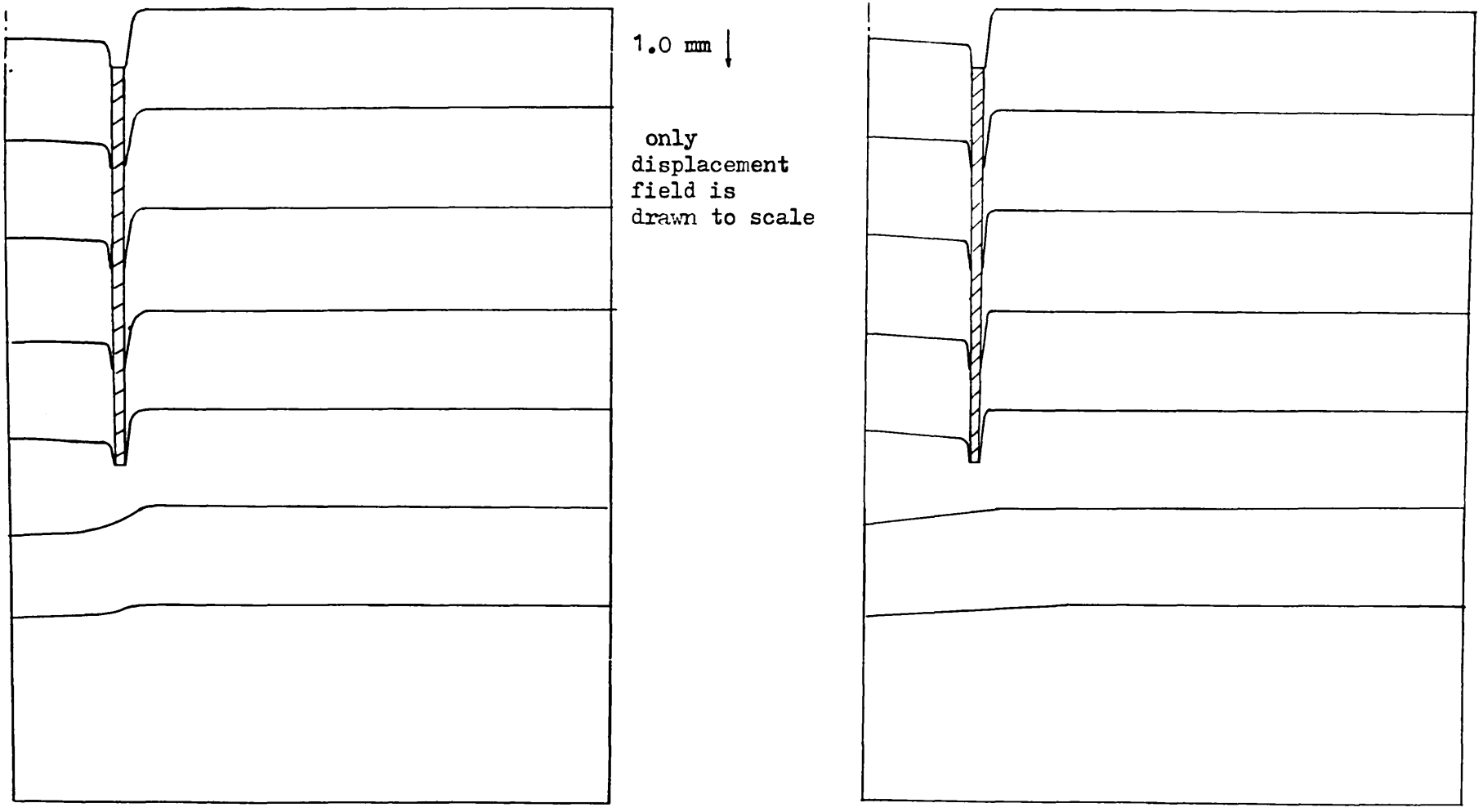

Fig. 4.12 Displacement field in the vicinity of the sampling tube

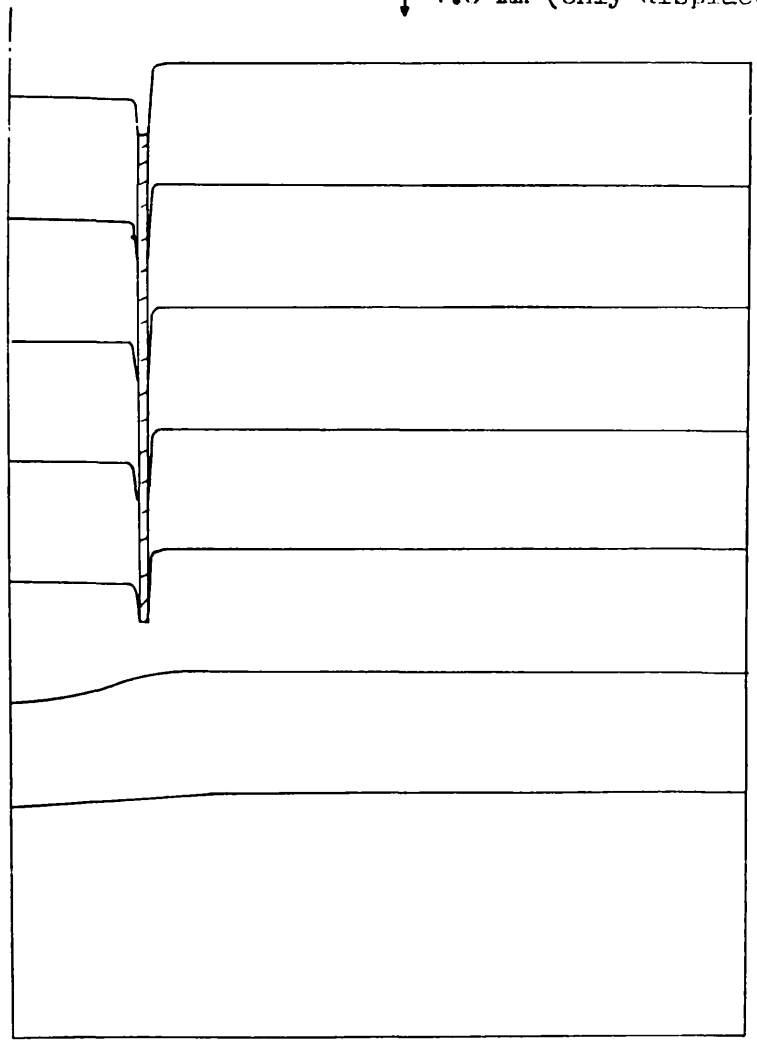

d = 1.5 mm D/t = 40

FIG. 4.13 Displacement field in the vicinity of the sampling tube

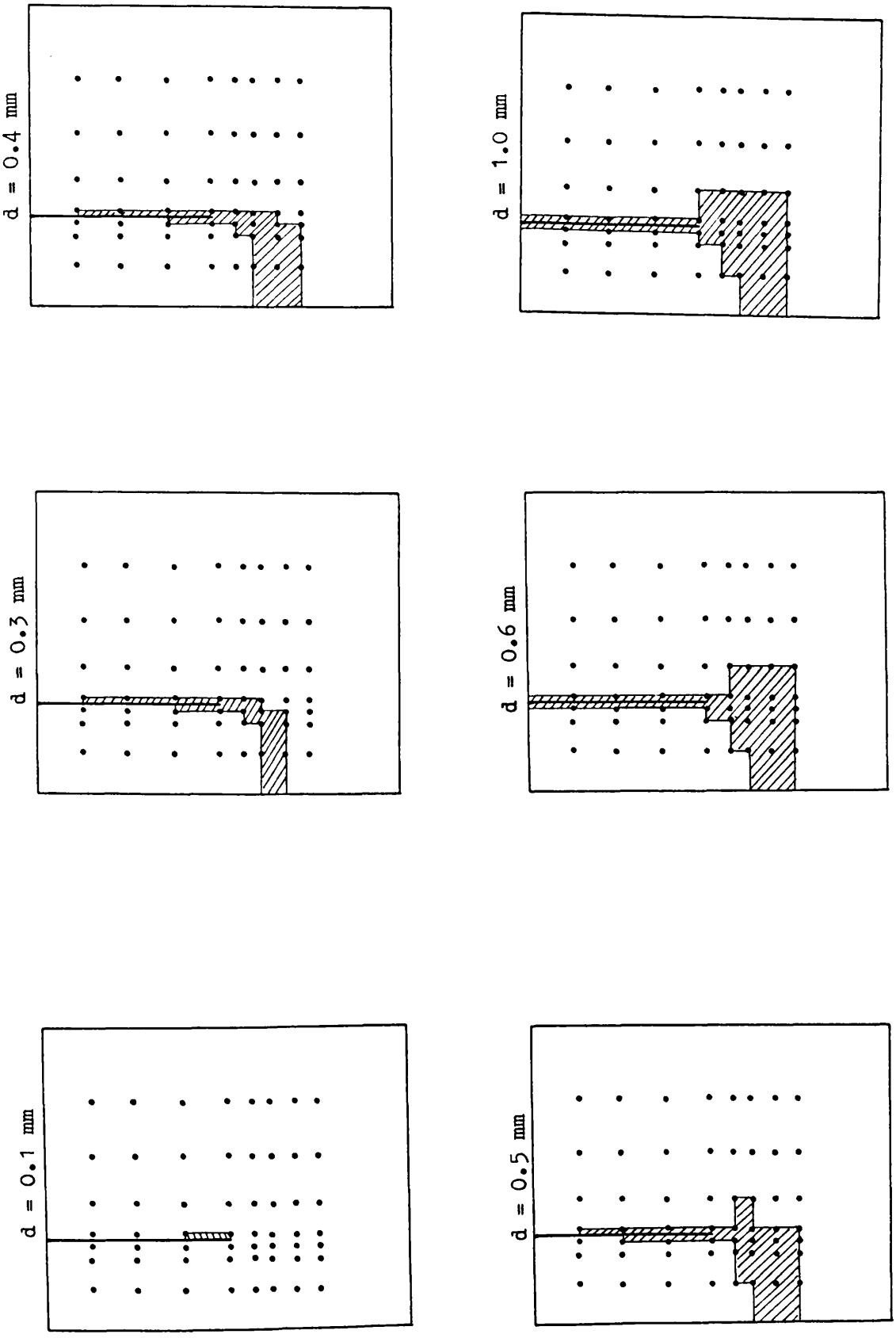

Fig. 4.14 Growth of failure zones at various stages of penetration , D/t = 10

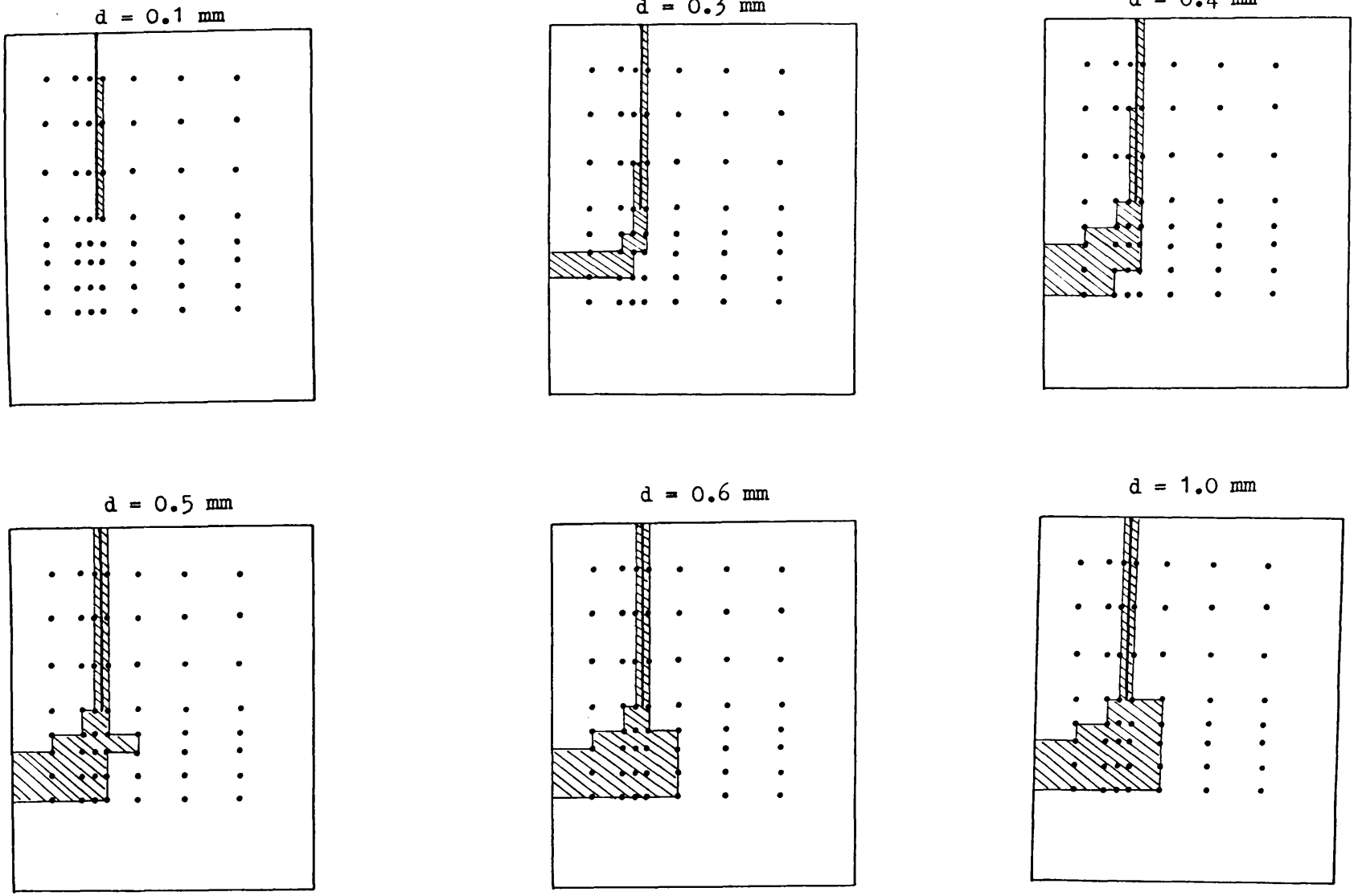

Fig. 4.15 Growth of failure zones at various stages of penetration , D/t = 20

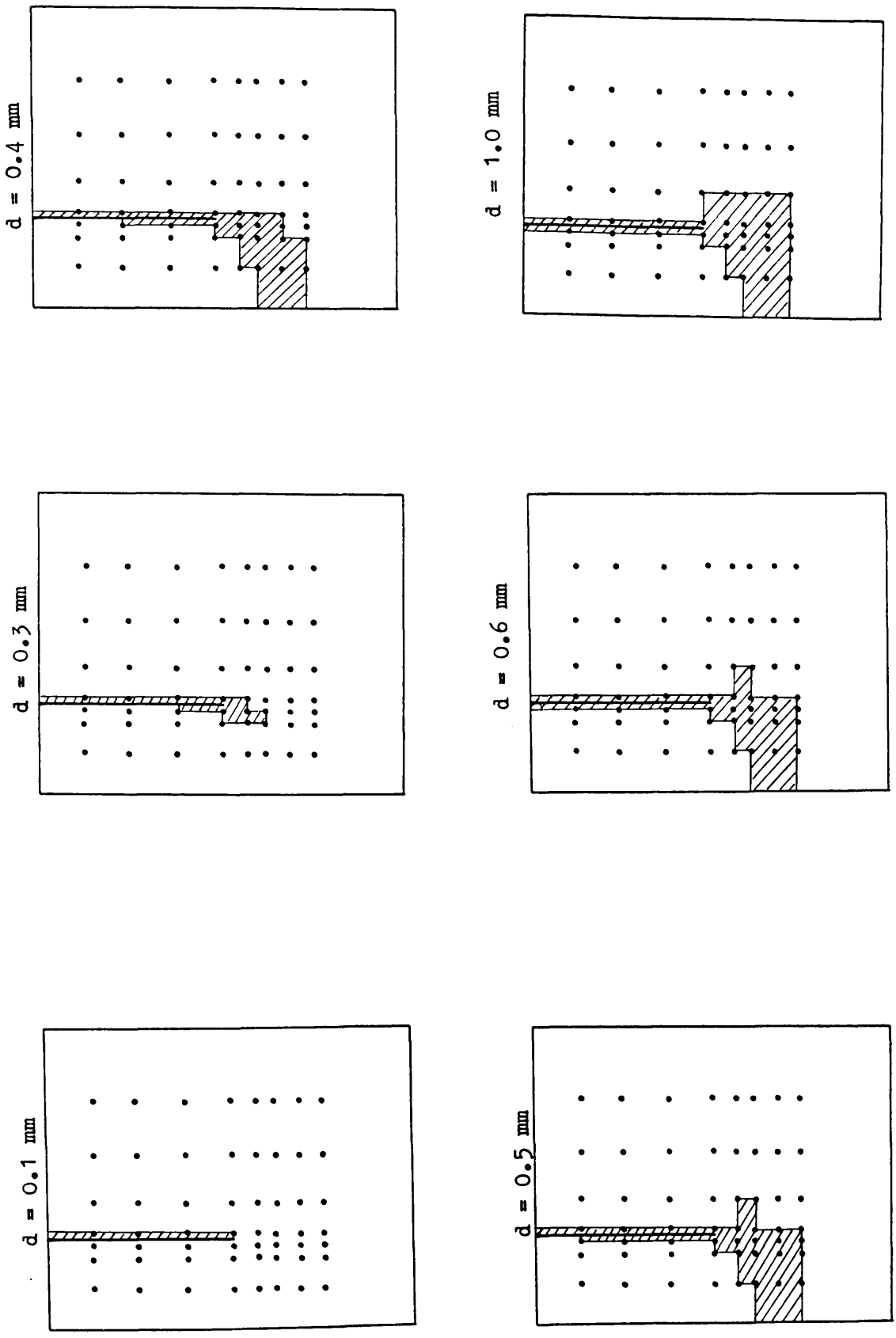

Fig. 4.16 Growth of failure zones at various stages of penetration , D/t = 40

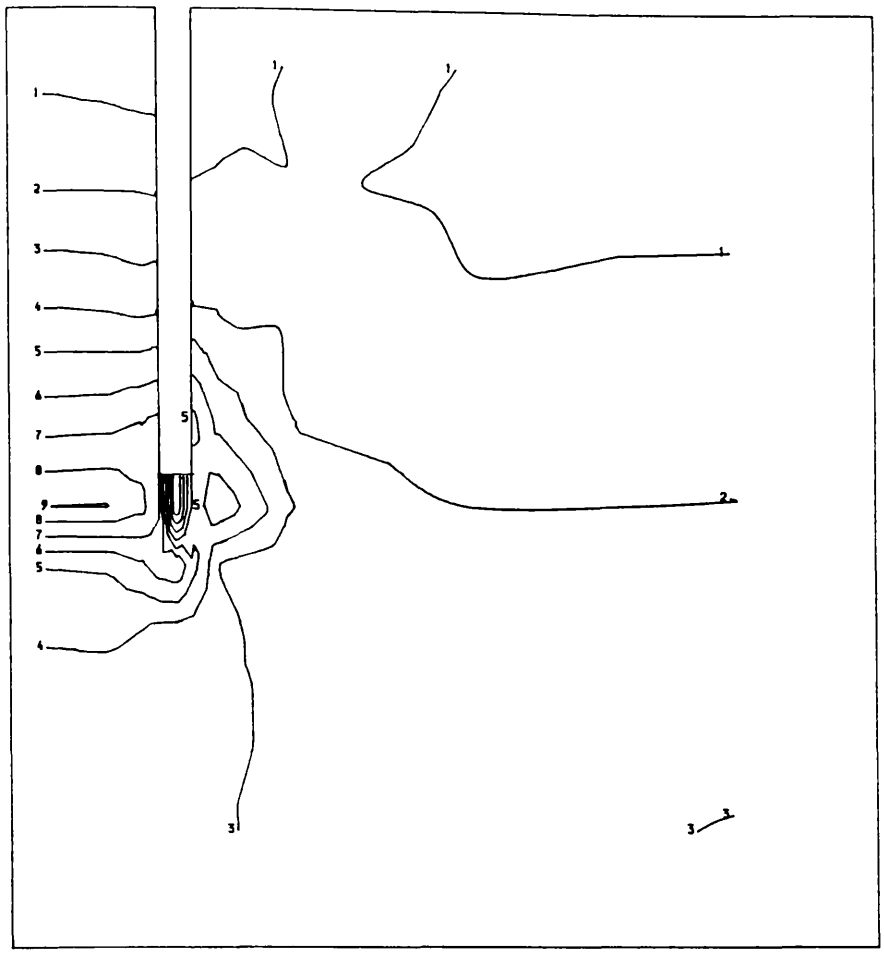

Fig. 4.17
Vertical stress contours in elastic state (d=0.1mm), D/t = 10

Key:		
1	0.01	N/mm2
2	0.02	
3	0.03	
4	0.04	
5	0.05	
6	0.06	
7	0.07	
8	0.08	
9	0.09	
10	0.1	

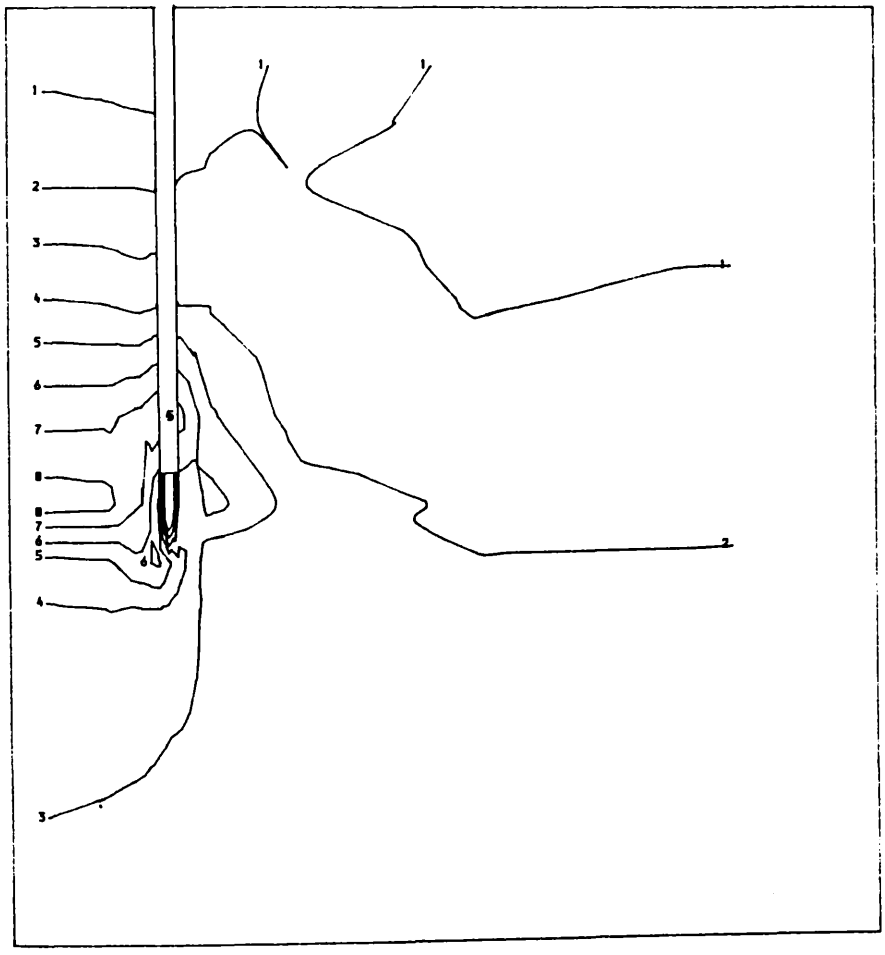

Fig. 4.18
Vertical stress contours in elatic state (d=0.1mm), D/t = 20

Key:		
1	0.01	N/mm2
2	0.02	
3	0.03	
4	0.04	
5	0.05	
6	0.06	
7	0.07	
8	0.08	
9	0.09	
10	0.1	

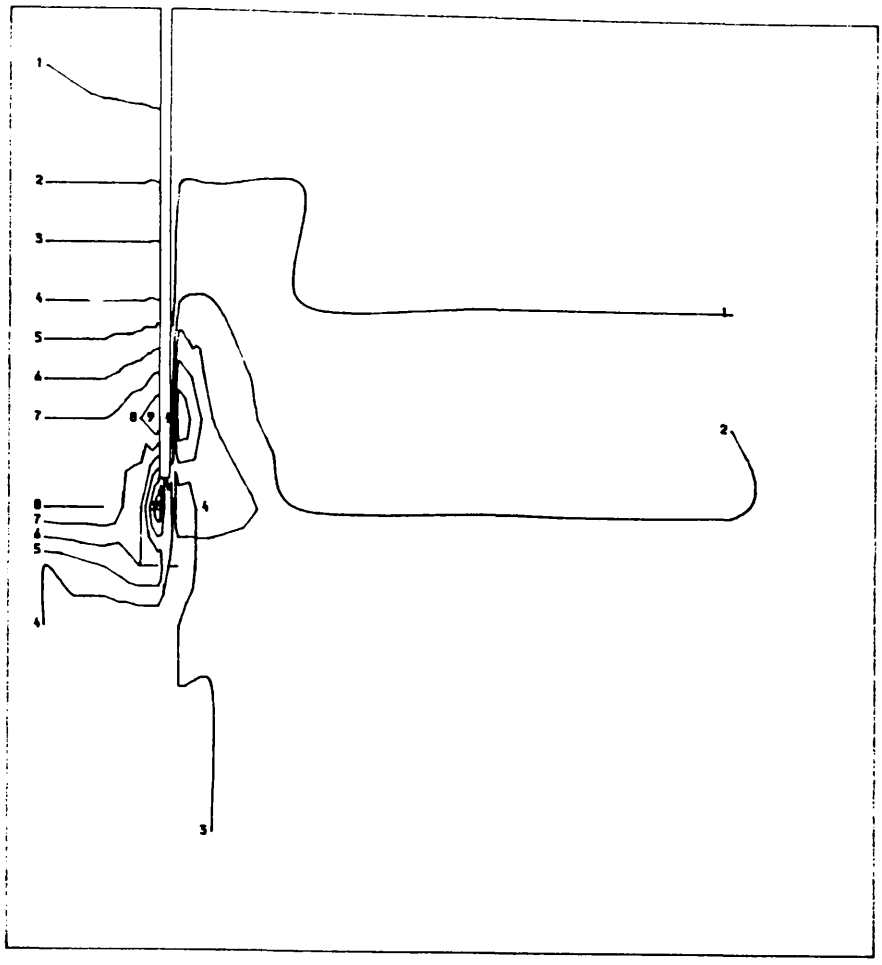

Fig. 4.19
Vertical stress contours in elastic state (d=0.1mm) D/t = 40

Key:		
1	0.01	N/mm2
2	0.02	
3	0.03	
4	0.04	
5	0.05	
6	0.06	
7	0.07	
8	0.08	
9	0.09	
10	0.1	

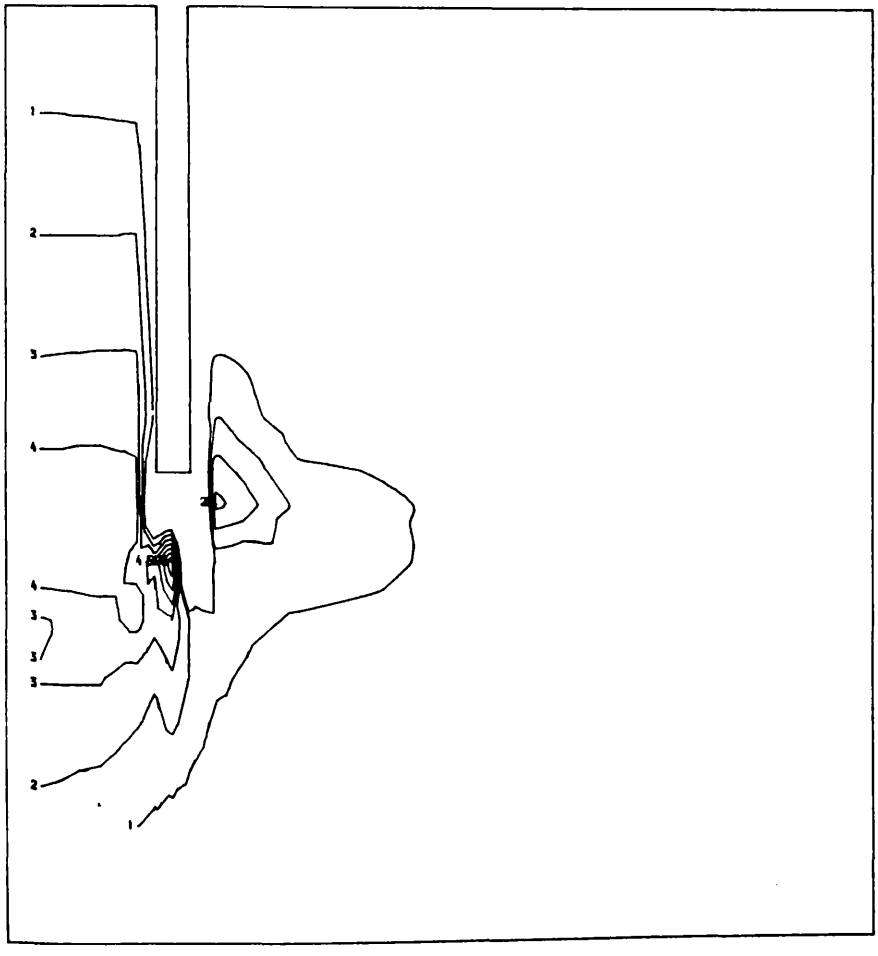

Fig. 4.20
Vertical stress contours at ultimate state (d=1.5mm), D/t = 10

Key:		
1	0.1	N/mm2
2	0.2	
3	0.3	
4	0.4	
5	0.5	
6	0.6	
7	0.7	
8	0.8	
9	0.9	
10	1.0	

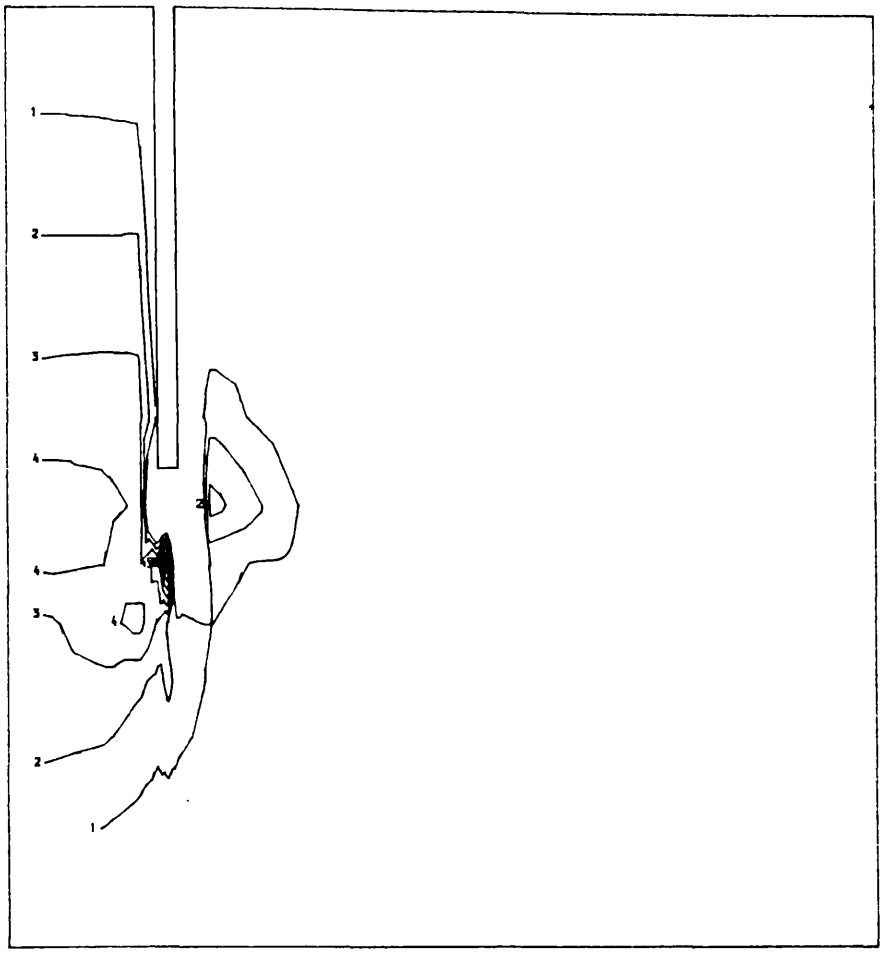

Fig. 4.21
Vertical stress contours at ultimate state (d=1.5mm), D/t = 20

Key:		
1	0.1	N/mm2
2	0.2	
3	0.3	
4	0.4	
5	0.5	
6	0.6	
7	0.7	
8	0.8	
9	0.9	
10	1.0	

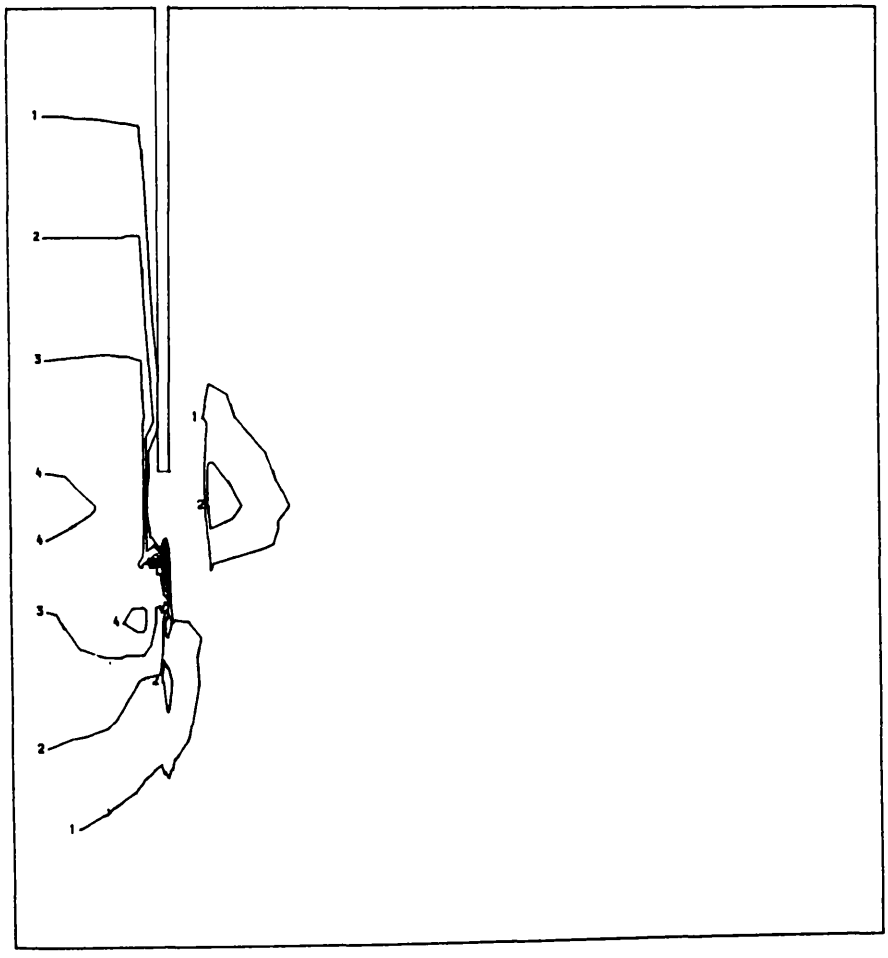

Fig. 4.22
Vertical stress contours at ultimate state (d=1.5 mm), D/t = 40

Key:		
1	0.1	N/mm2
2	0.2	
3	0.3	
4	0.4	
5	0.5	
6	0.6	
7	0.7	
8	0.8	
9	0.9	
10	1.0	

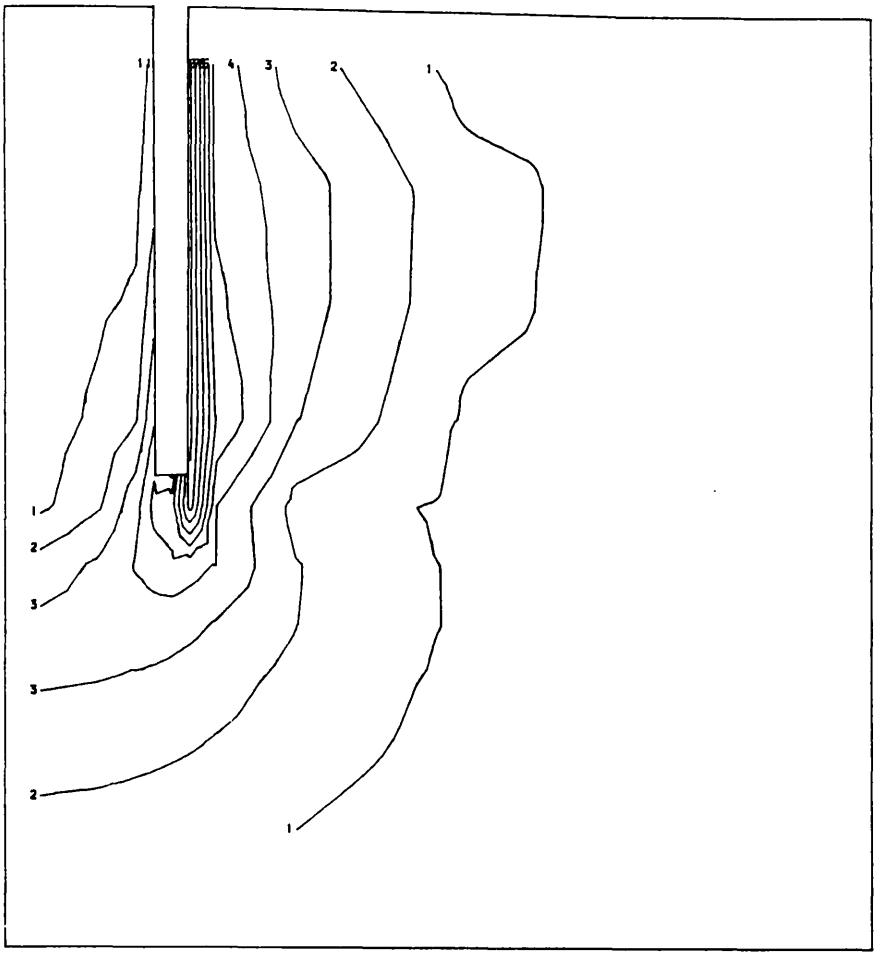

Fig. 4.23
$(\sigma 1-\sigma 3)/2Cu$ contours in elastic state (d=0.1mm), D/t = 10

Key:	
1	0.1
2	0.2
3	0.3
4	0.4
5	0.5
6	0.6
7	0.7
8	0.8
9	0.9
10	1.0

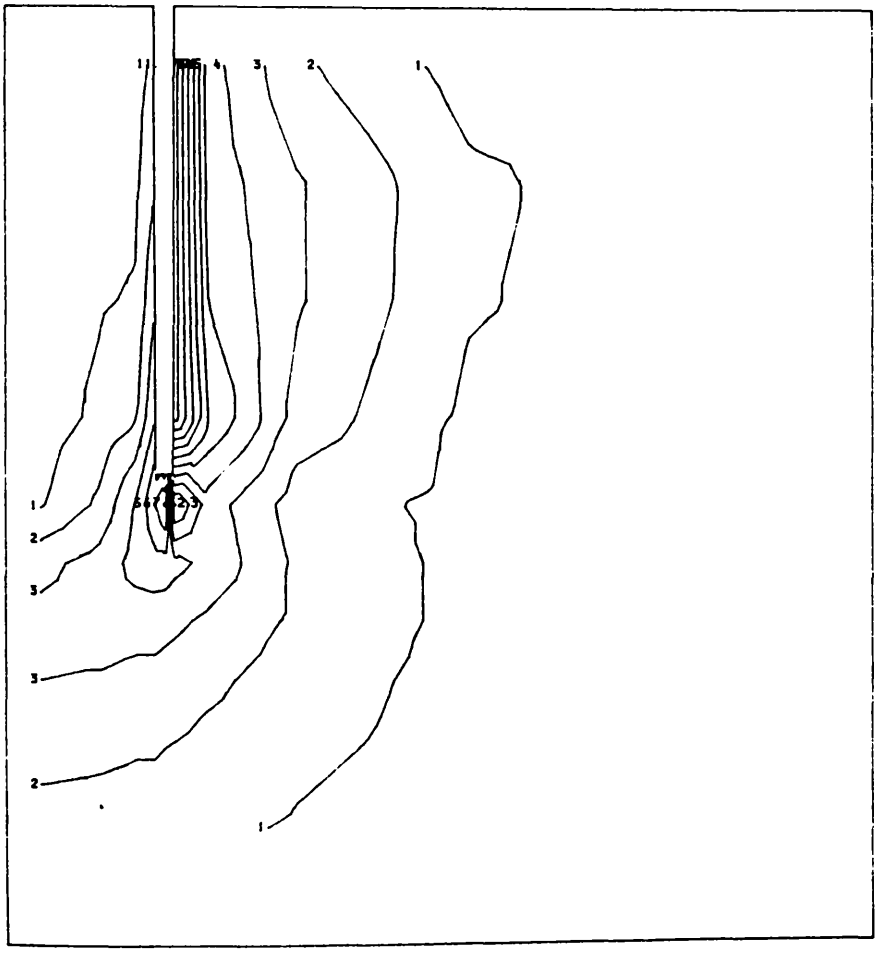

Fig. 4.24
$(\sigma 1-\sigma_3)/2Cu$ contours at ultimate state (d=0.1mm), D/t= 20

Key:	
1	0.1
2	0.2
3	0.3
4	0.4
5	0.5
6	0.6
7	0.7
8	0.8
9	0.9
10	1.0

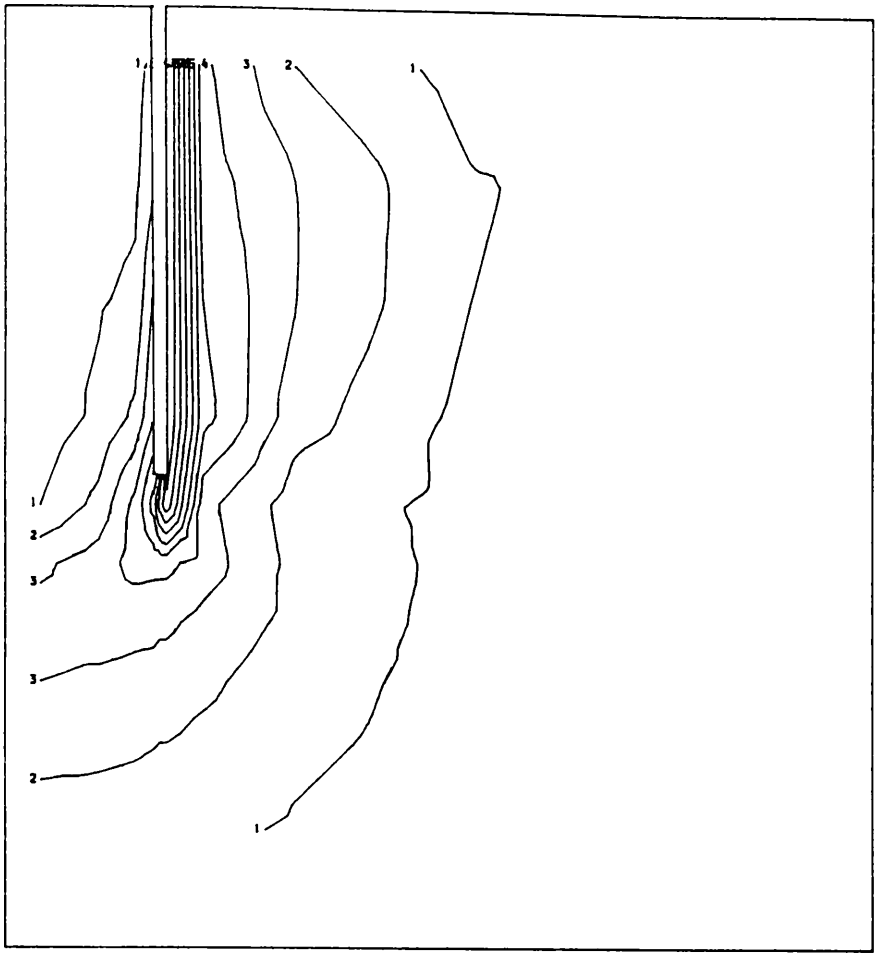

Fig. 4.25
($\sigma 1-\sigma_3$) contours
in elastic state
(d=0.1mm), D/t =40

Key:	
1	0.1
2	0.2
3	0.3
4	0.4
5	0.5
6	0.6
7	0.7
8	0.8
9	0.9
10	1.0

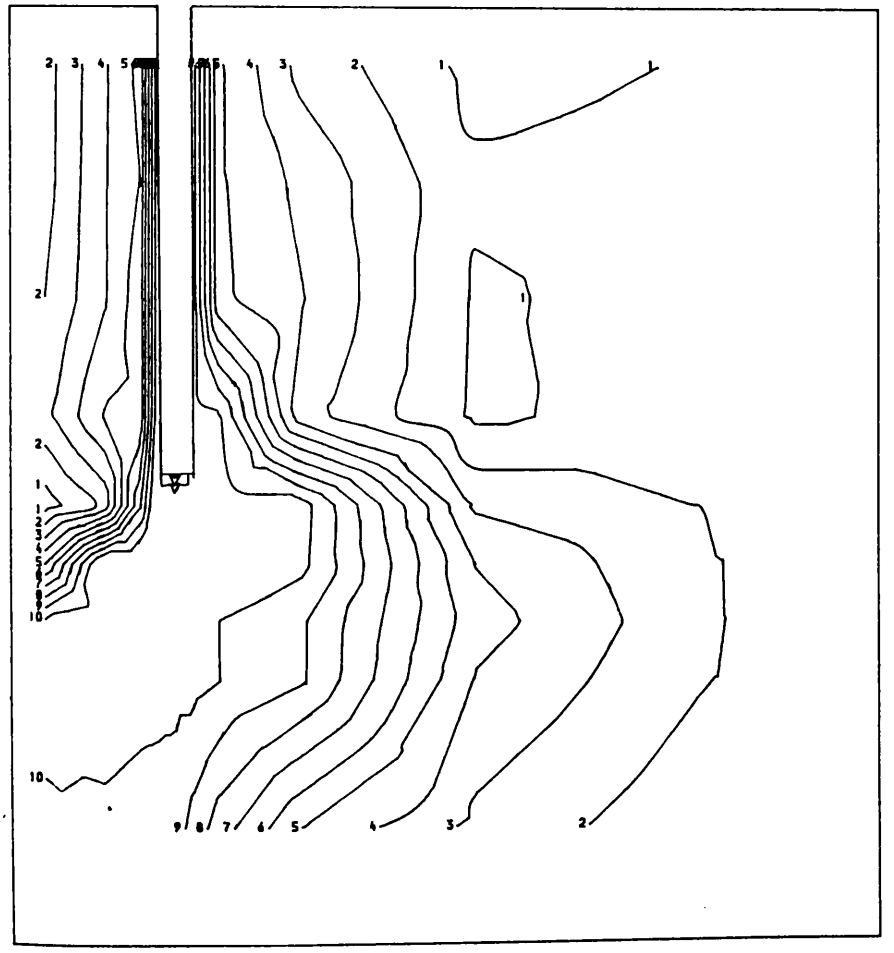

Fig. 4.26
($\sigma 1-\sigma_3$)/2Cu contours
at ultimate state
(d=1.5mm), D/t = 10

Key:	
1	0.1
2	0.2
3	0.3
4	0.4
5	0.5
6	0.6
7	0.7
8	0.8
9	0.9
10	1.0

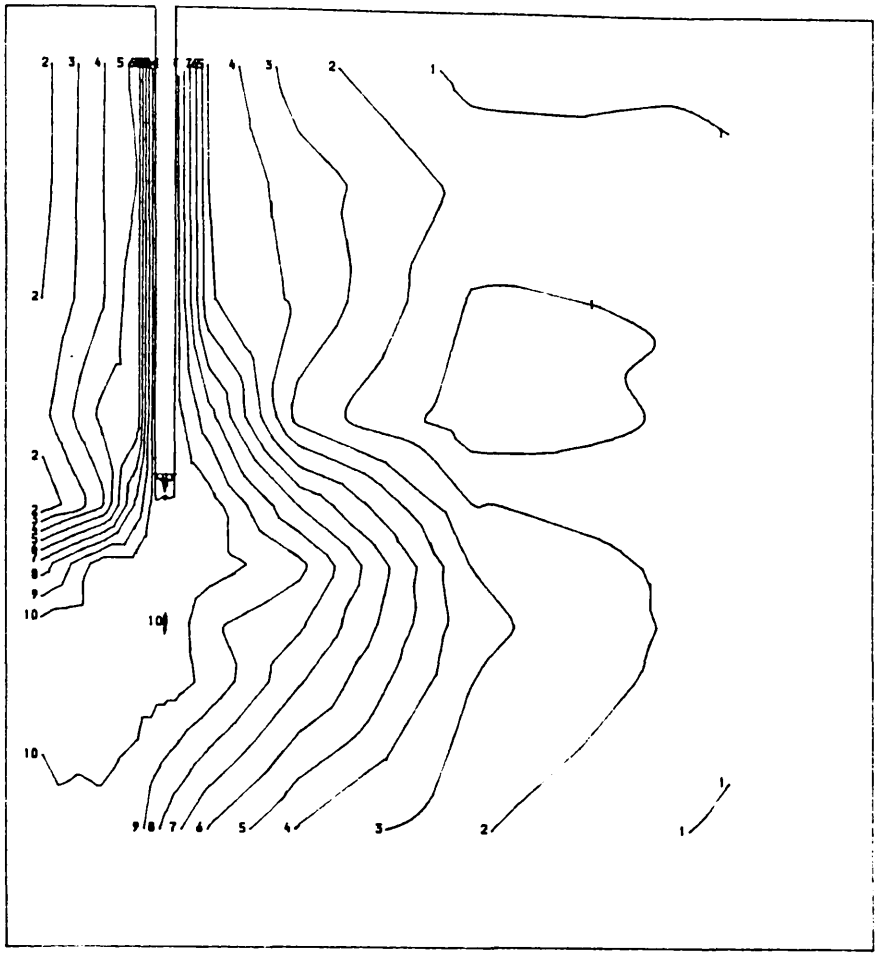

Fig. 4.27
$(\sigma 1-\sigma_3)/2Cu$ contours at ultimate state (d=1.5mm), D/t = 20

Key:	
1	0.1
2	0.2
3	0.3
4	0.4
5	0.5
6	0.6
7	0.7
8	0.8
9	0.9
10	1.0

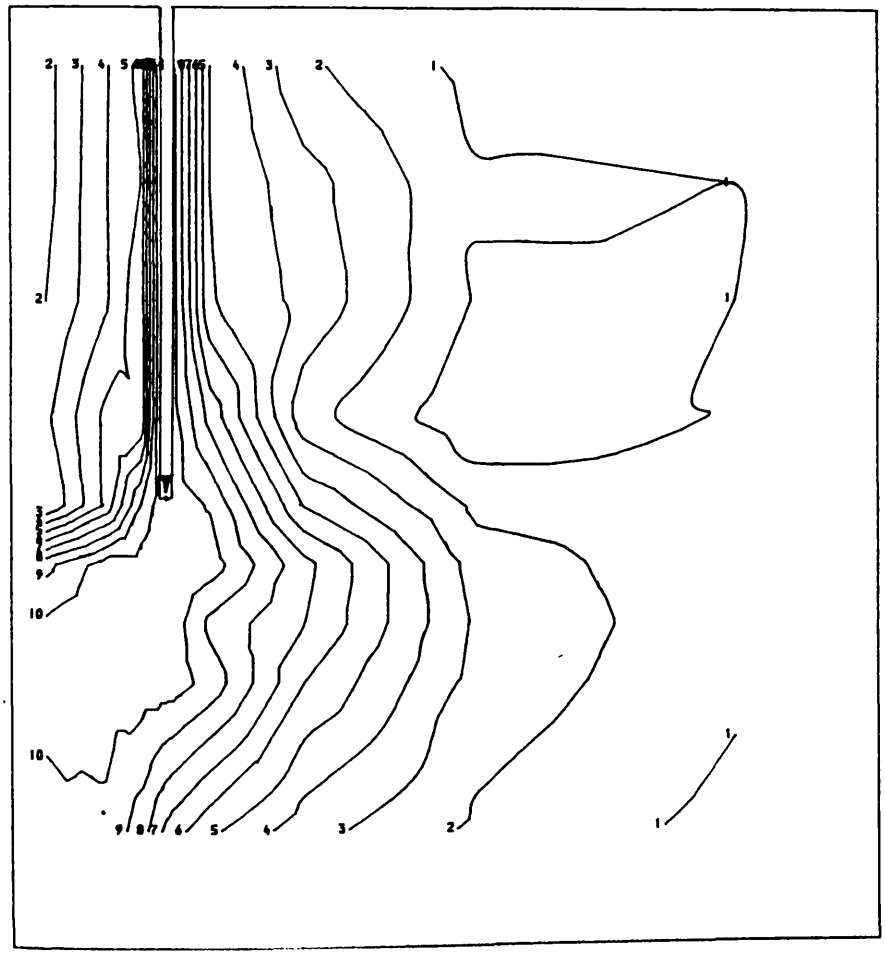

Fig. 4.28
$(\sigma 1-\sigma_3)/2Cu$ contours at ultimate state (d=1.5mm), D/t = 40

Key:	
1	0.1
2	0.2
3	0.3
4	0.4
5	0.5
6	0.6
7	0.7
8	0.8
9	0.9
10	1.0

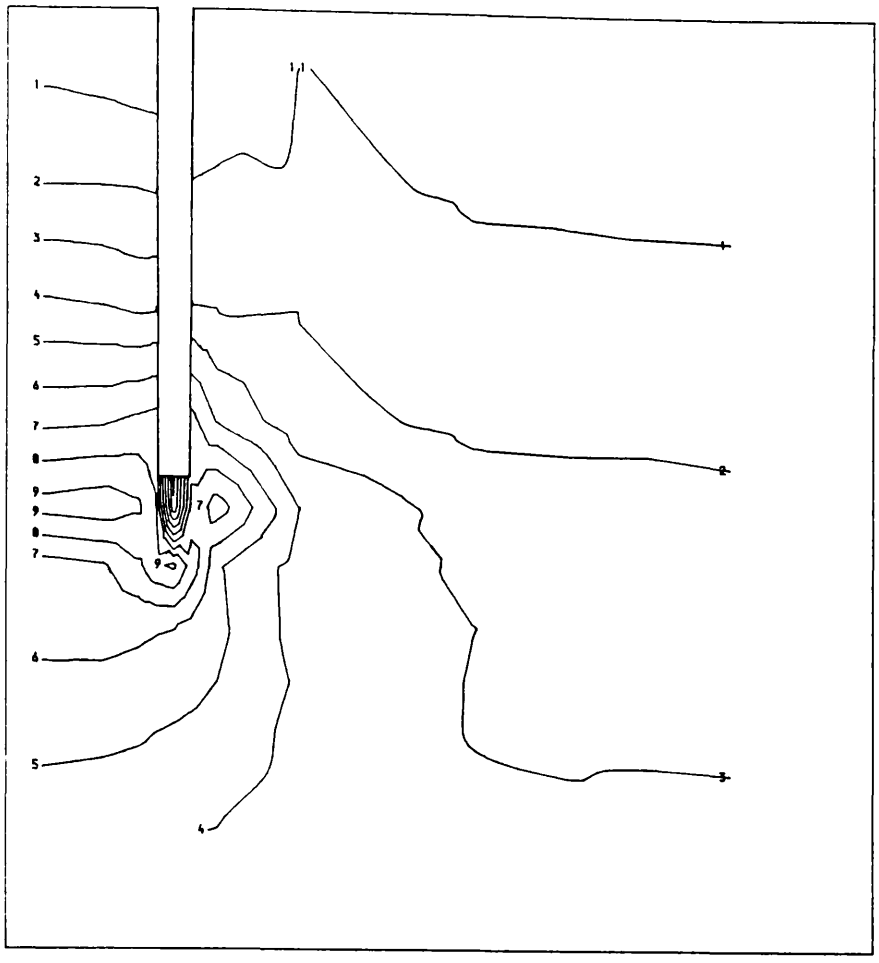

Fig. 4.29
Mean effective stress contours in elastic state (d=0.1mm), D/t = 10

Key:		
1	0.01	N/mm2
2	0.02	
3	0.03	
4	0.04	
5	0.05	
6	0.06	
7	0.07	
8	0.08	
9	0.09	
10	0.1	

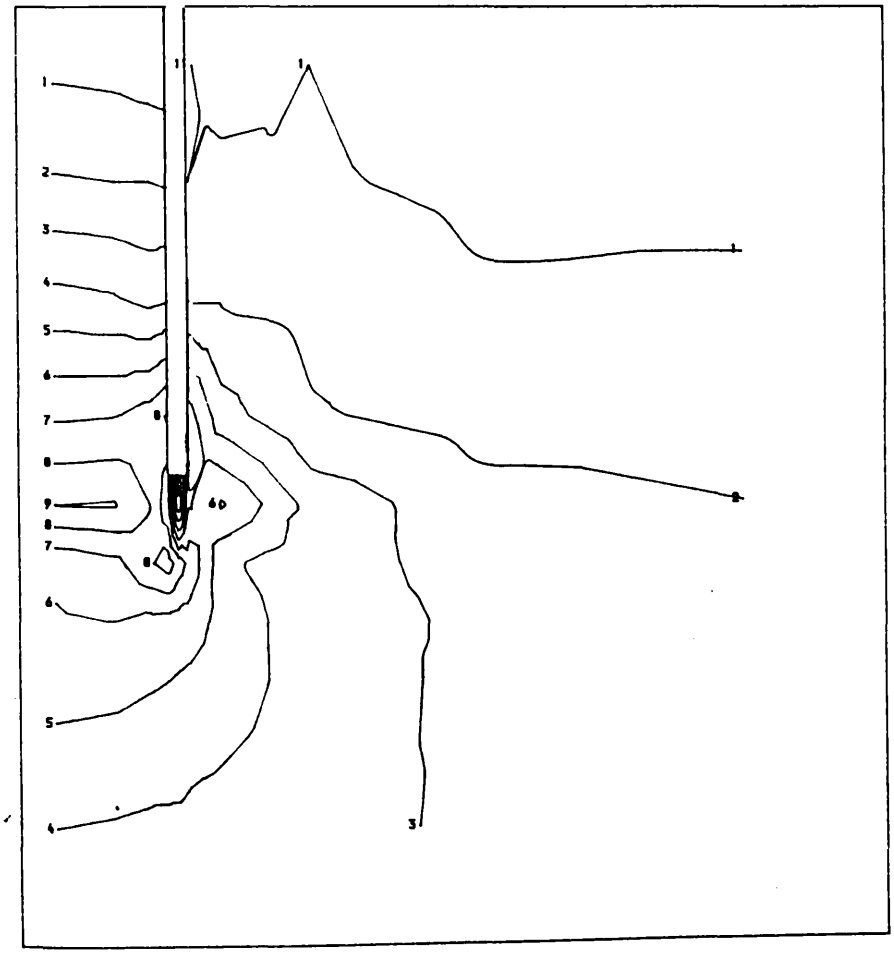

Fig. 4.30
Mean effective stress contours in elastic state (d=0.1mm), D/t = 20

Key:		
1	0.01	N/mm2
2	0.02	
3	0.03	
4	0.04	
5	0.05	
6	0.06	
7	0.07	
8	0.08	
9	0.09	
10	0.1	

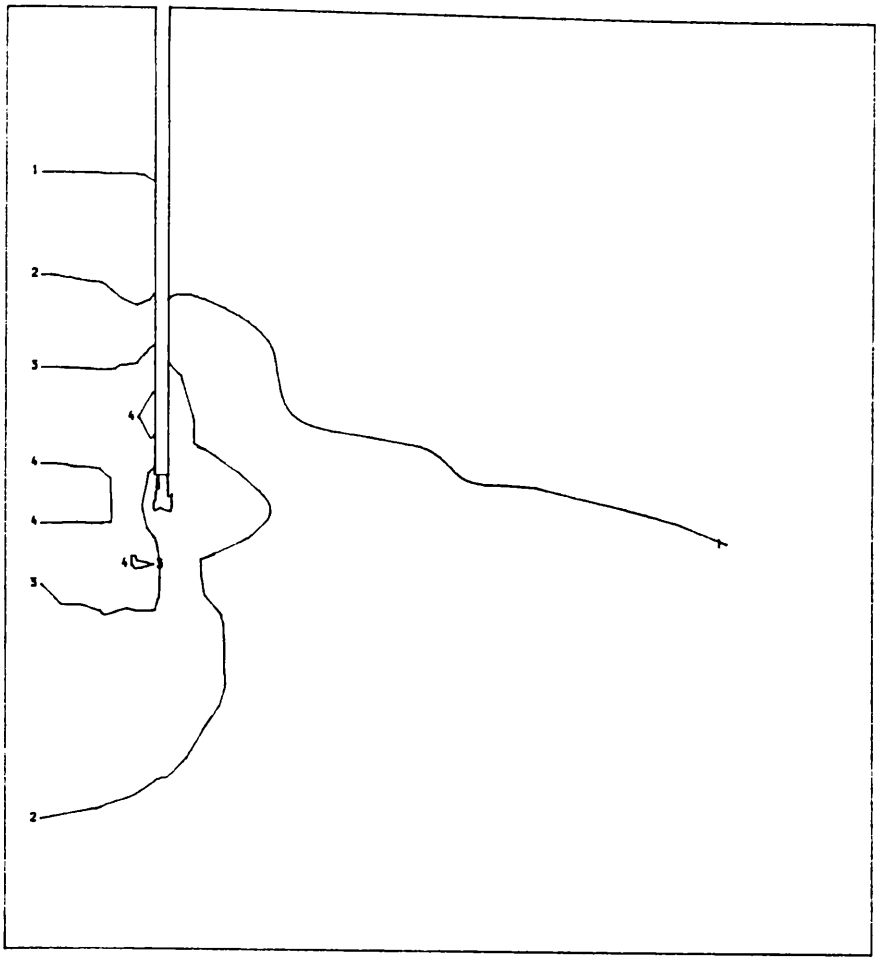

Fig. 4.31
Mean effective stress contours in elastic state (d=0.1mm), D/t = 40

Key:		
1	0.02	N/mm2
2	0.04	
3	0.06	
4	0.08	
5	0.10	

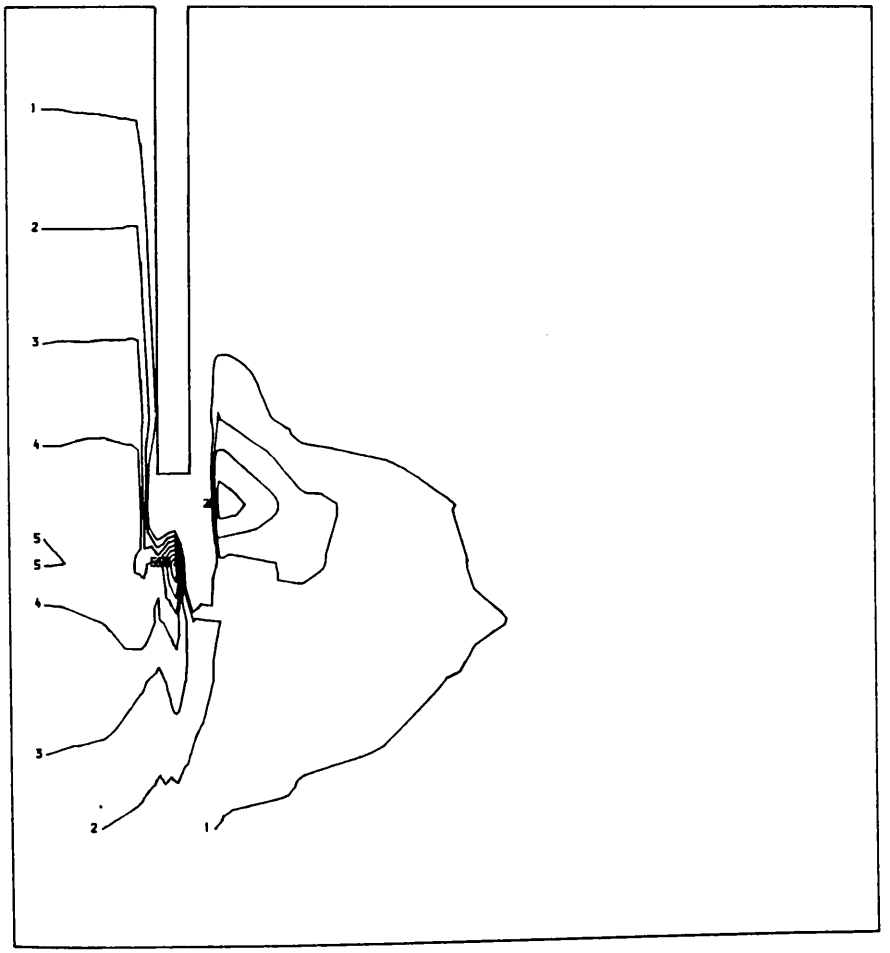

Fig. 4.32
Mean effective stress contours at ultimate state (d=1.5mm), D/t = 10

Key:		
1	0.1	N/mm2
2	0.2	
3	0.3	
4	0.4	
5	0.5	
6	0.6	
7	0.7	
8	0.8	
9	0.9	
10	1.0	

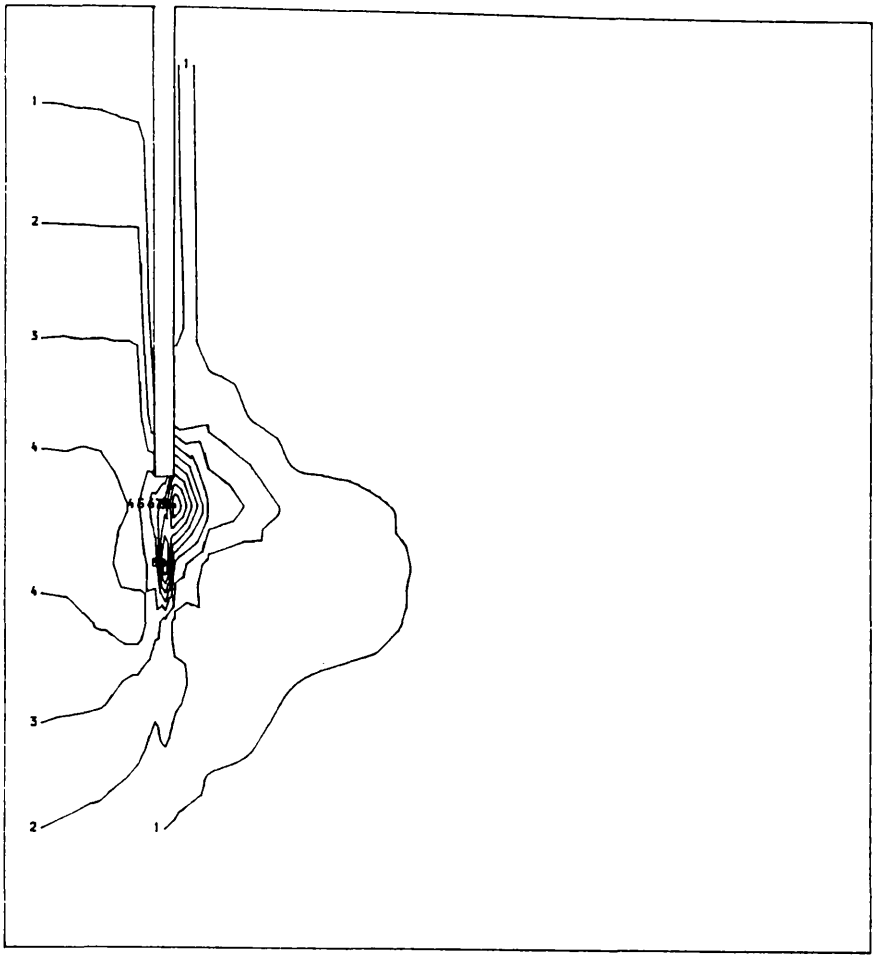

Fig. 4.33
Mean effective stress contours at ultimate state
(d=1.5mm), D/t = 20

Key:	
1	0.1 N/mm2
2	0.2
3	0.3
4	0.4
5	0.5
6	0.6
7	0.7
8	0.8
9	0.9
10	1.0

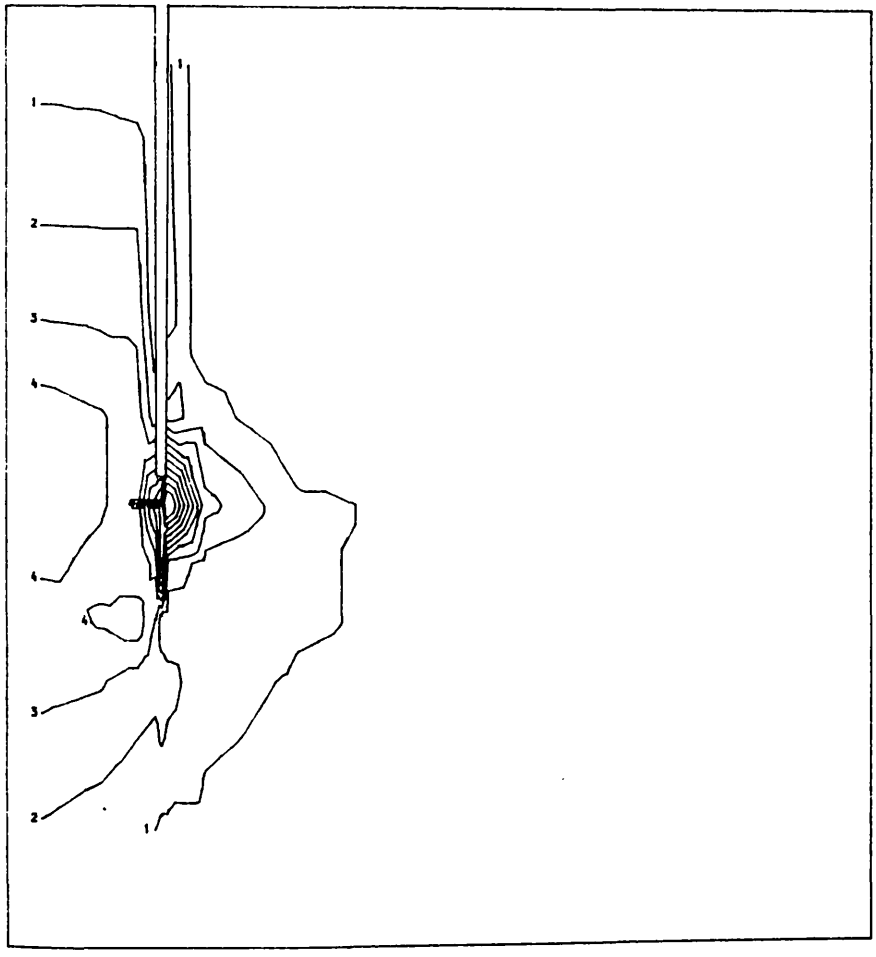

Fig. 4.34
Mean effective stress contours at ultimate state
(d=1.5mm), D/t = 40

Key:	
1	0.1 N/mm2
2	0.2
3	0.3
4	0.4
5	0.5
6	0.6
7	0.7
8	0.8
9	0.9
10	1.0

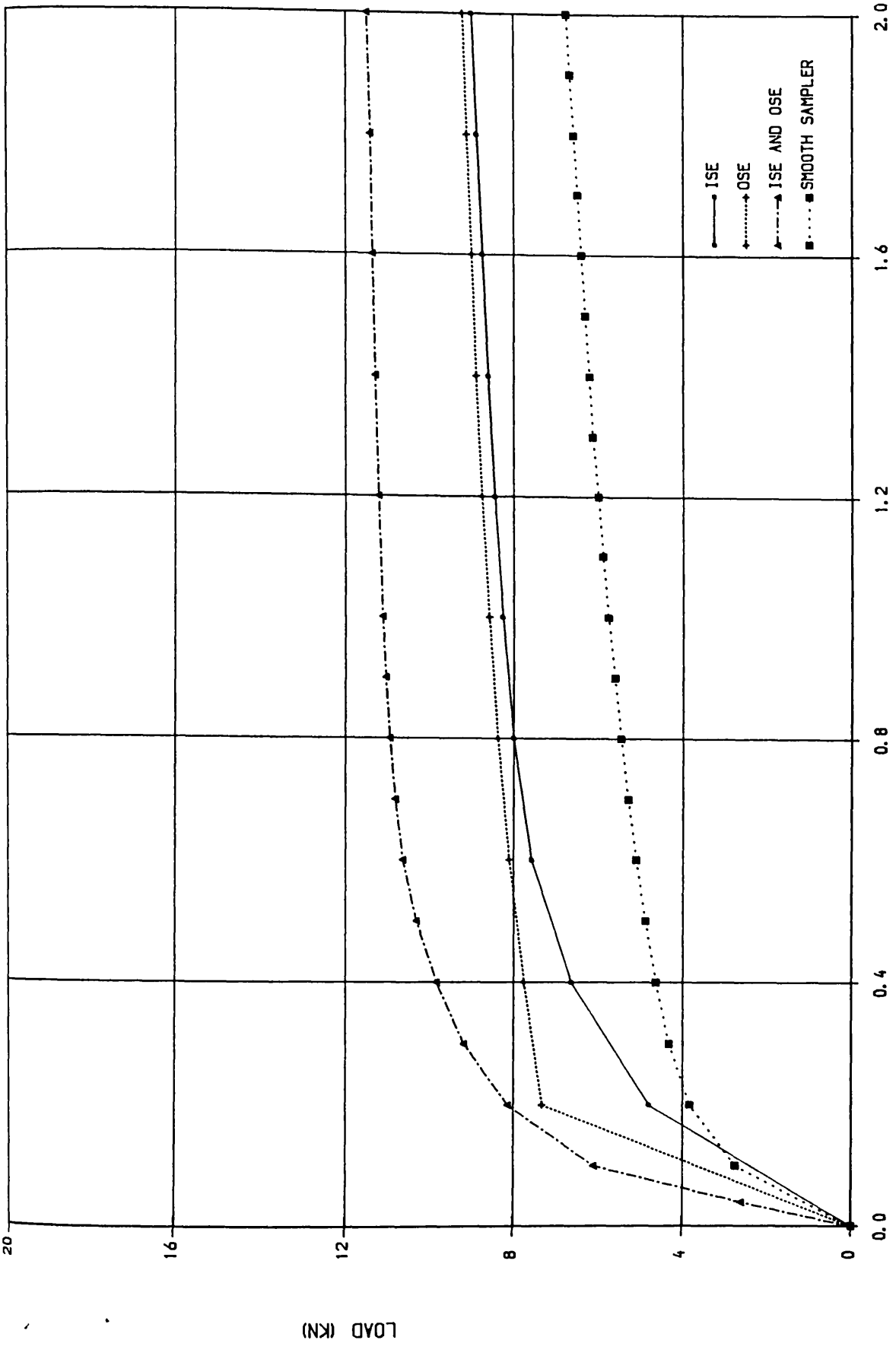

FIG. 4.35 LOAD DISPLACEMENT CURVES, EFFECT OF ROUGHNESS OF SAMPLER

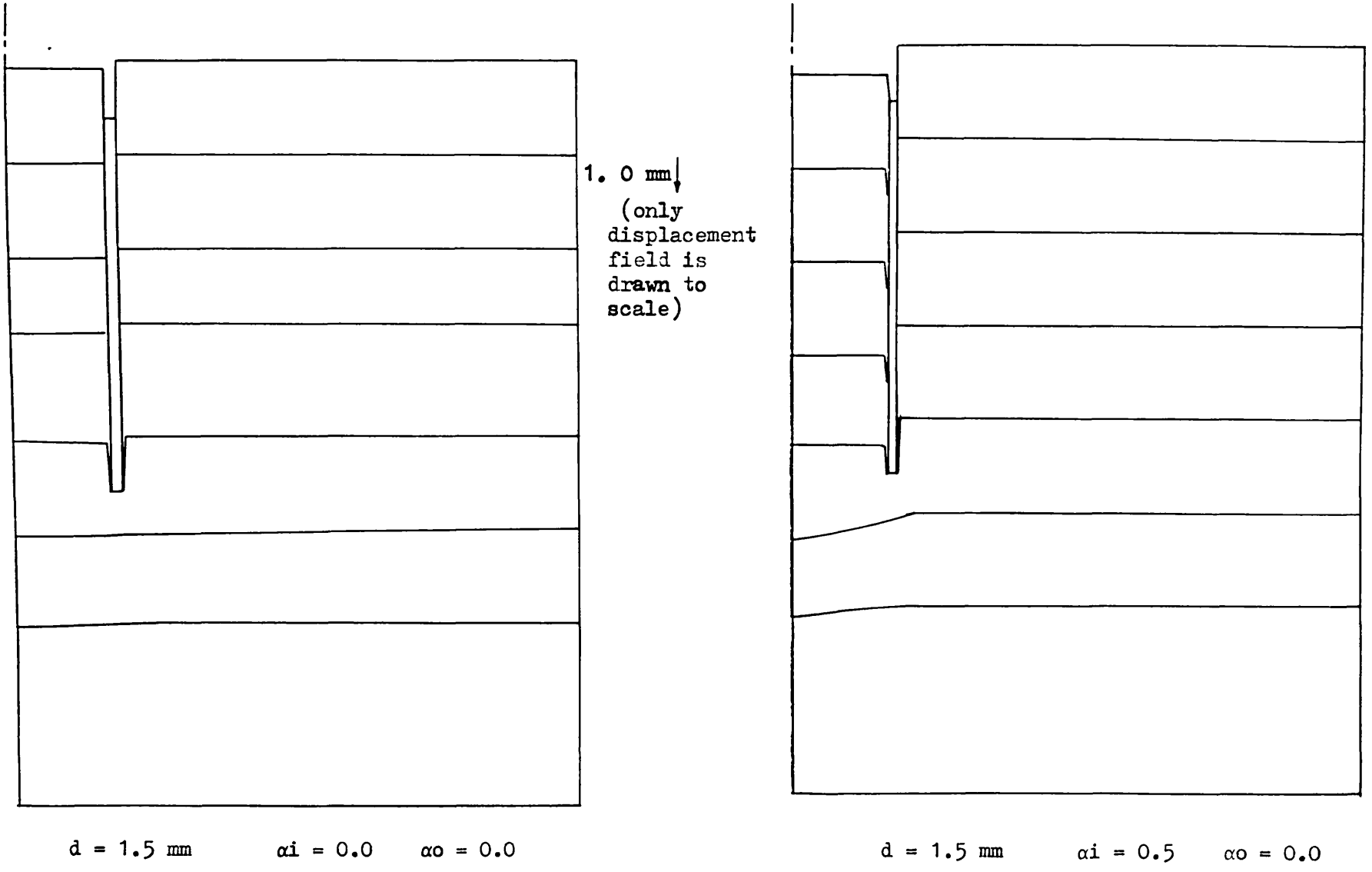

Fig. 4.36 Displacement field in the vicinity of the sampling tube

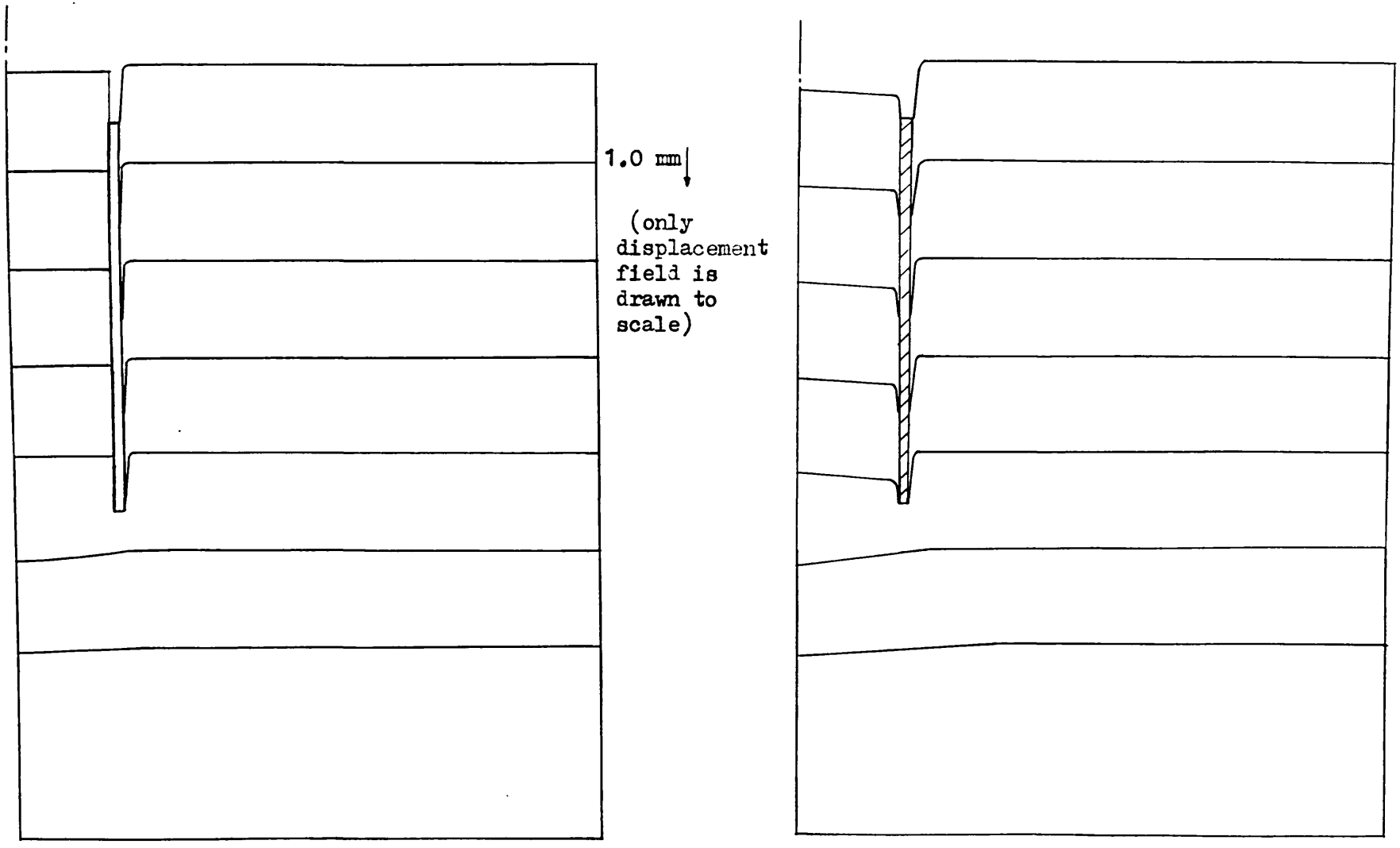

Fig. 4.37 Displacement field in the vicinity of the sampling tube

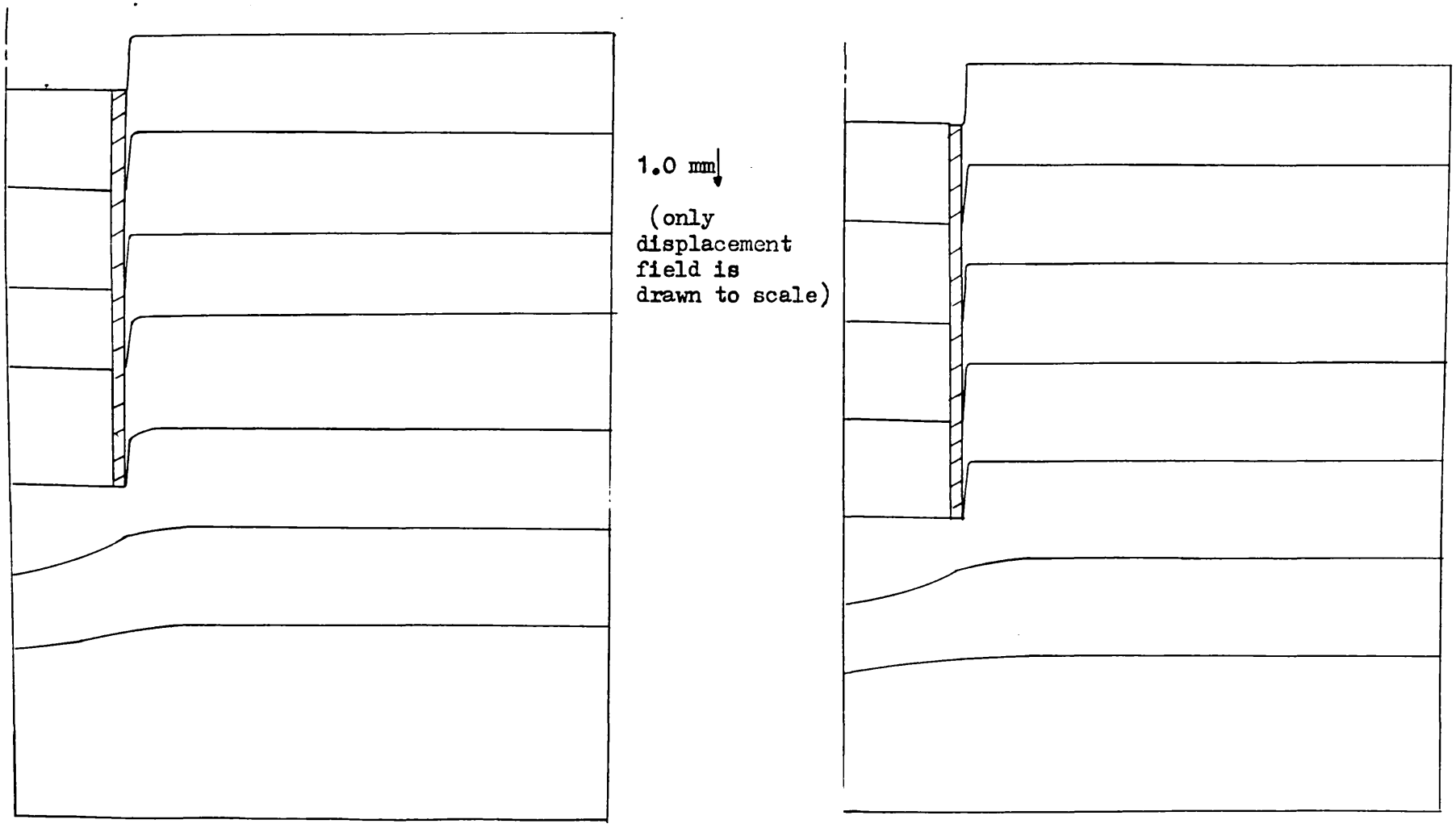

d = 1.5 mm αi = 1.0 αo = 1.0

d = 1.5 mm αi = 1.0 αo = 0.5

Fig. 4.38 Displacement field in the vicinity of the sampling tube

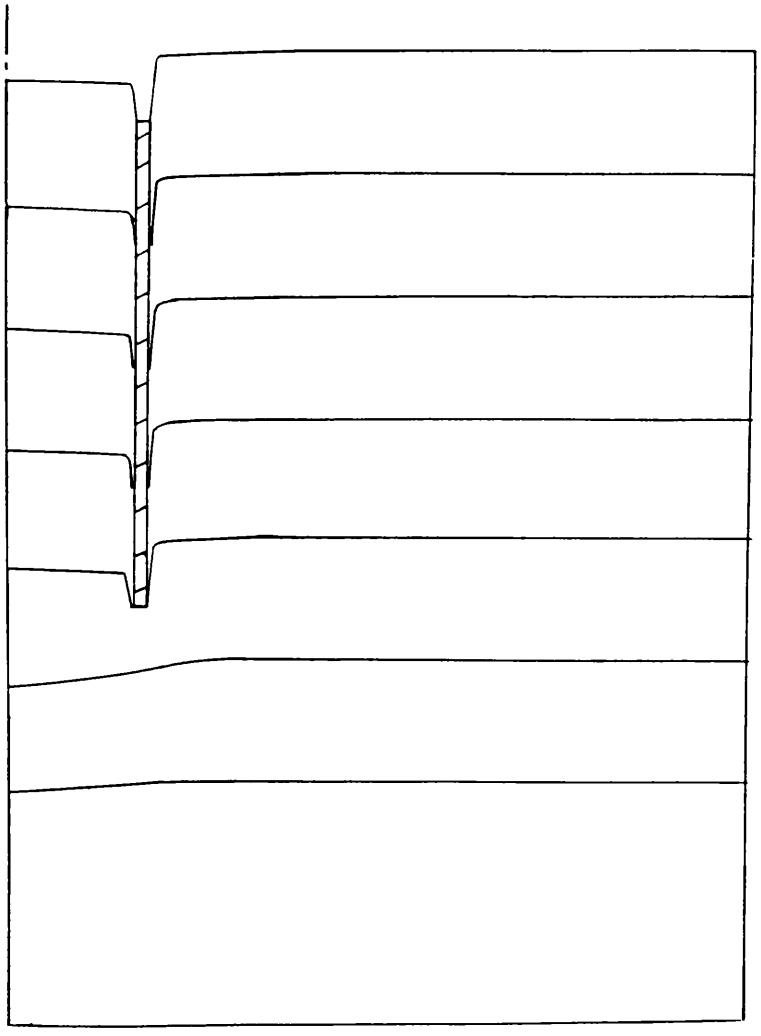

1.0 mm

(only displacement field is drawn to scale)

d = 1.5 mm αi = 0.5 αo = 1.0

Fig. 4.39 Displacement field in the vicinity of the samplig tube

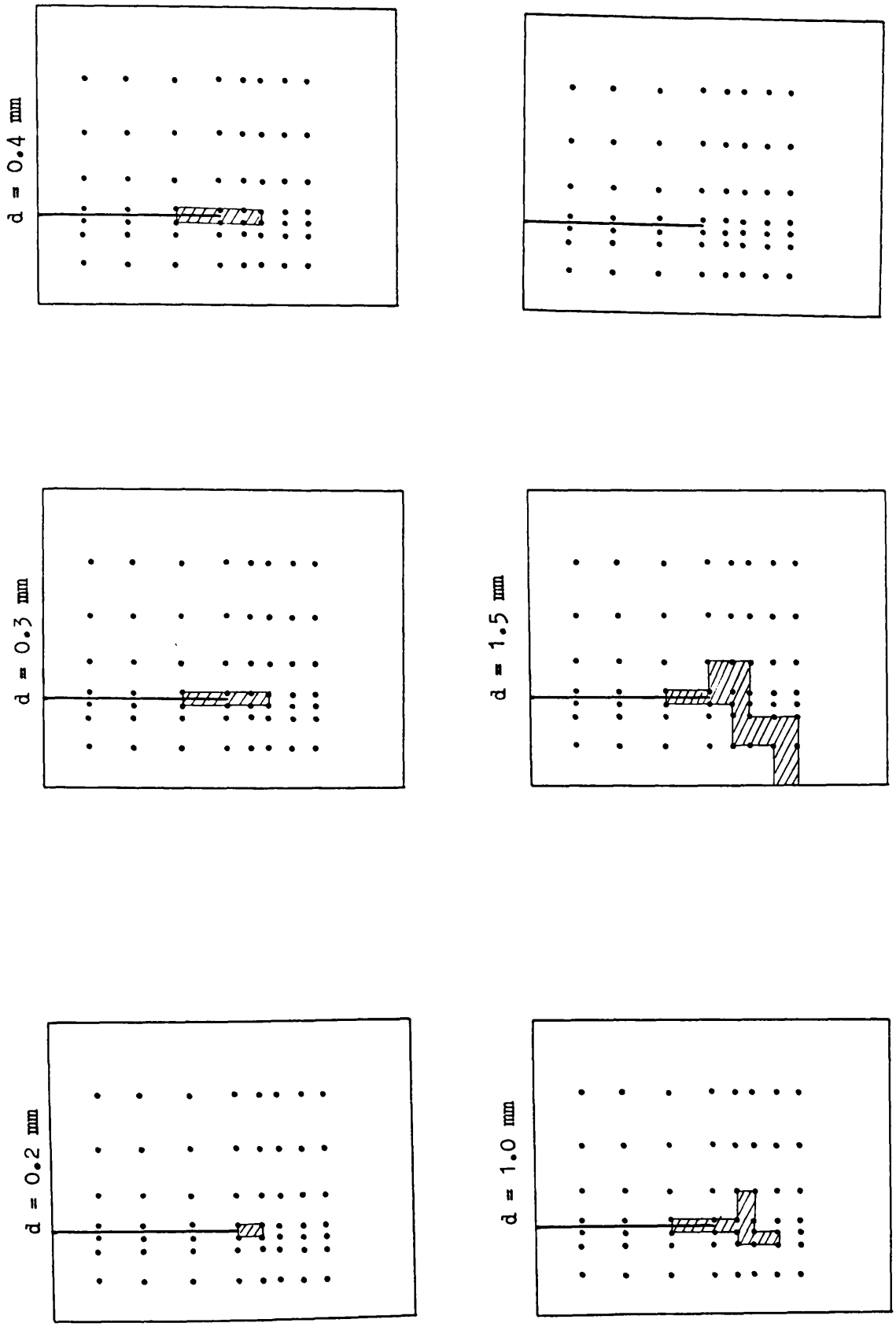

Fig. 4.40 Growth of failure zones at various stages of penetration , $\alpha_i = 0.0$ $\alpha_o = 0.0$

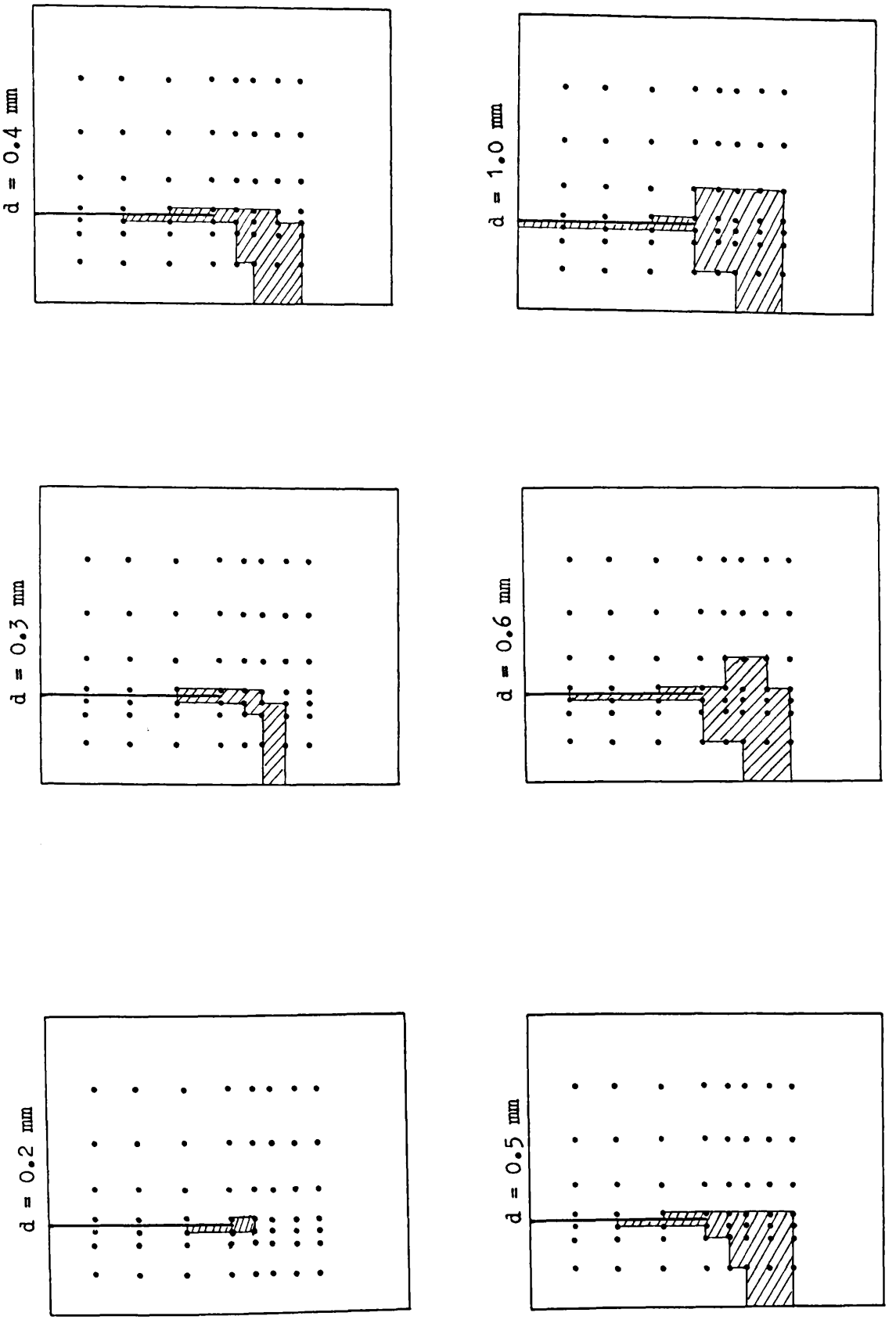

Fig. 4.41 Growth of failure zones at various stages of penetration , $\alpha i = 0.5$ $\alpha o = 0.0$

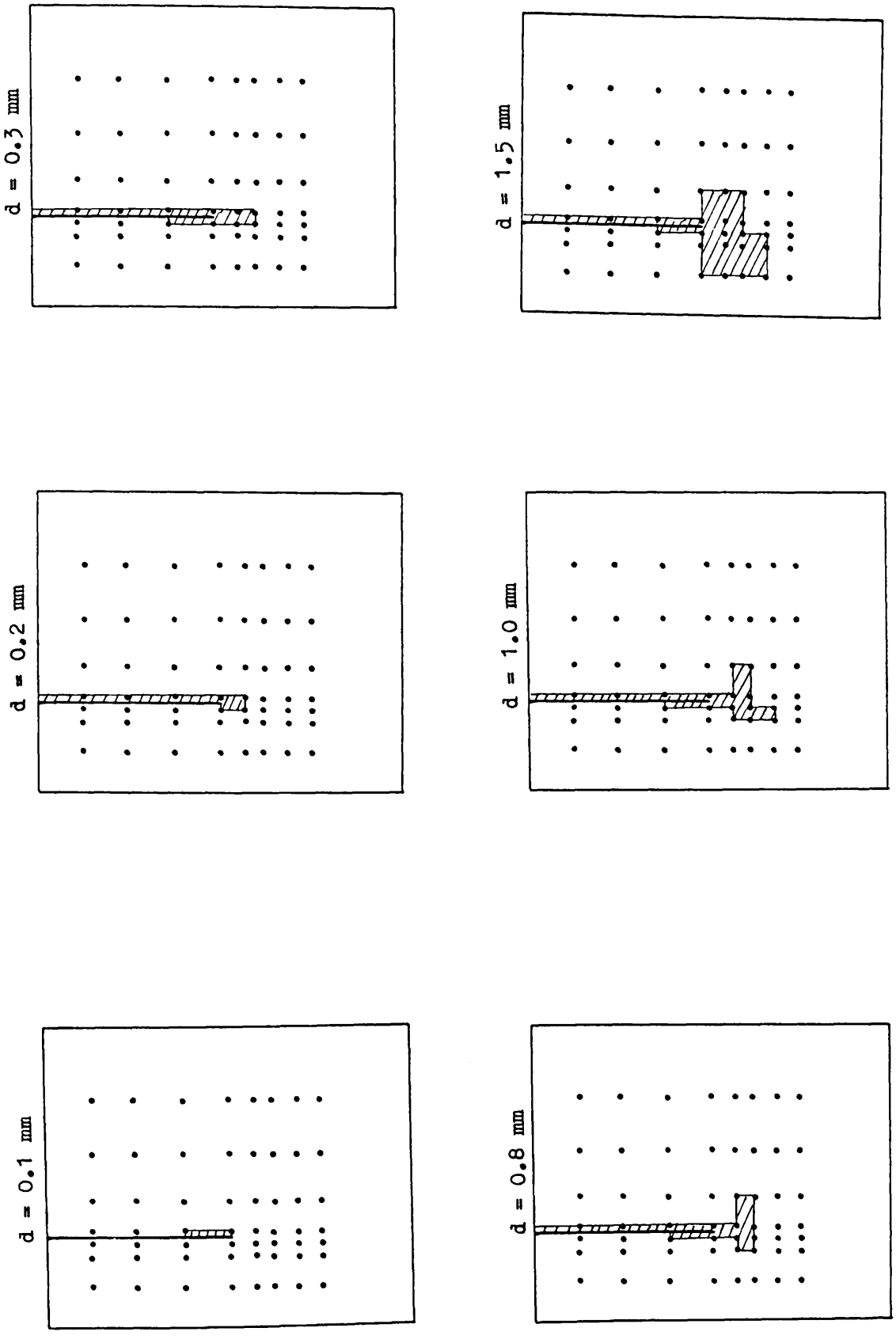

Fig. 4.42 Growth of failure zones at various stages of penetration , $\alpha_1 = 0.0$ $\alpha_0 = 0.5$

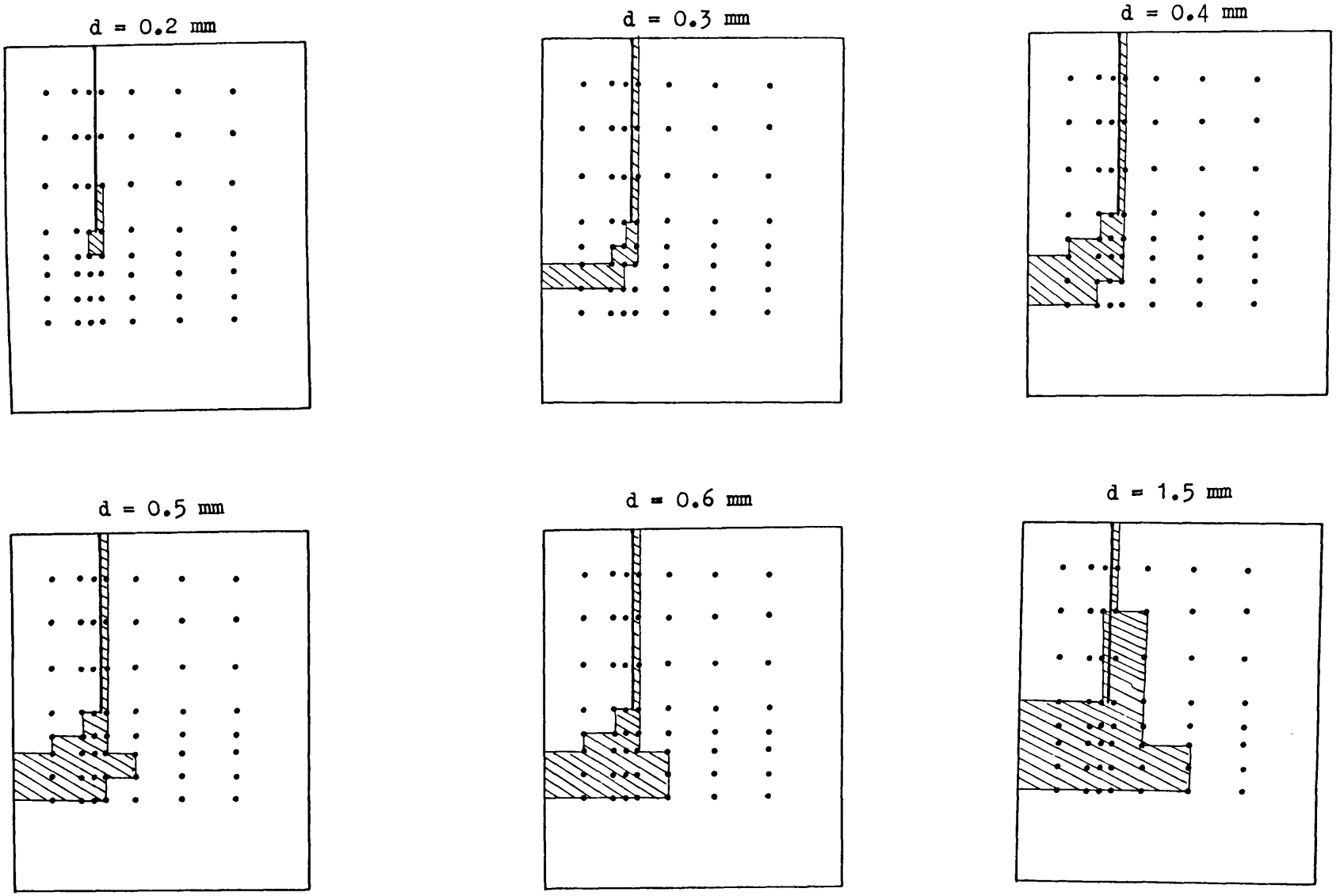

Fig. 4.43 Growth of failure zones at various stages of penetration , $\alpha i = 1.0$ $\alpha o = 1.0$

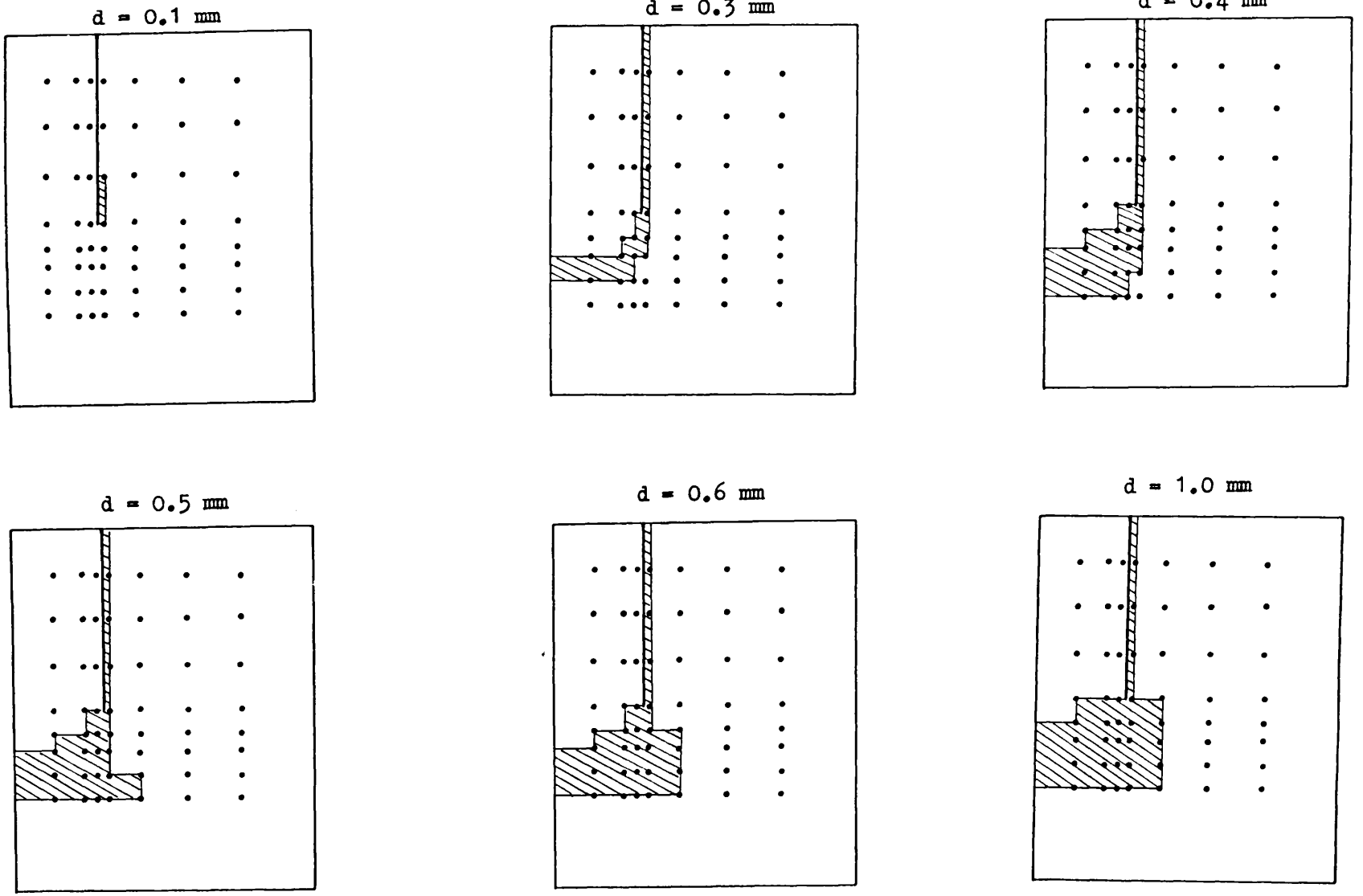

Fig. 4.44 Growth of failure zones at various stages of penetration , $\alpha i = 1.0$ $\alpha o = 0.5$

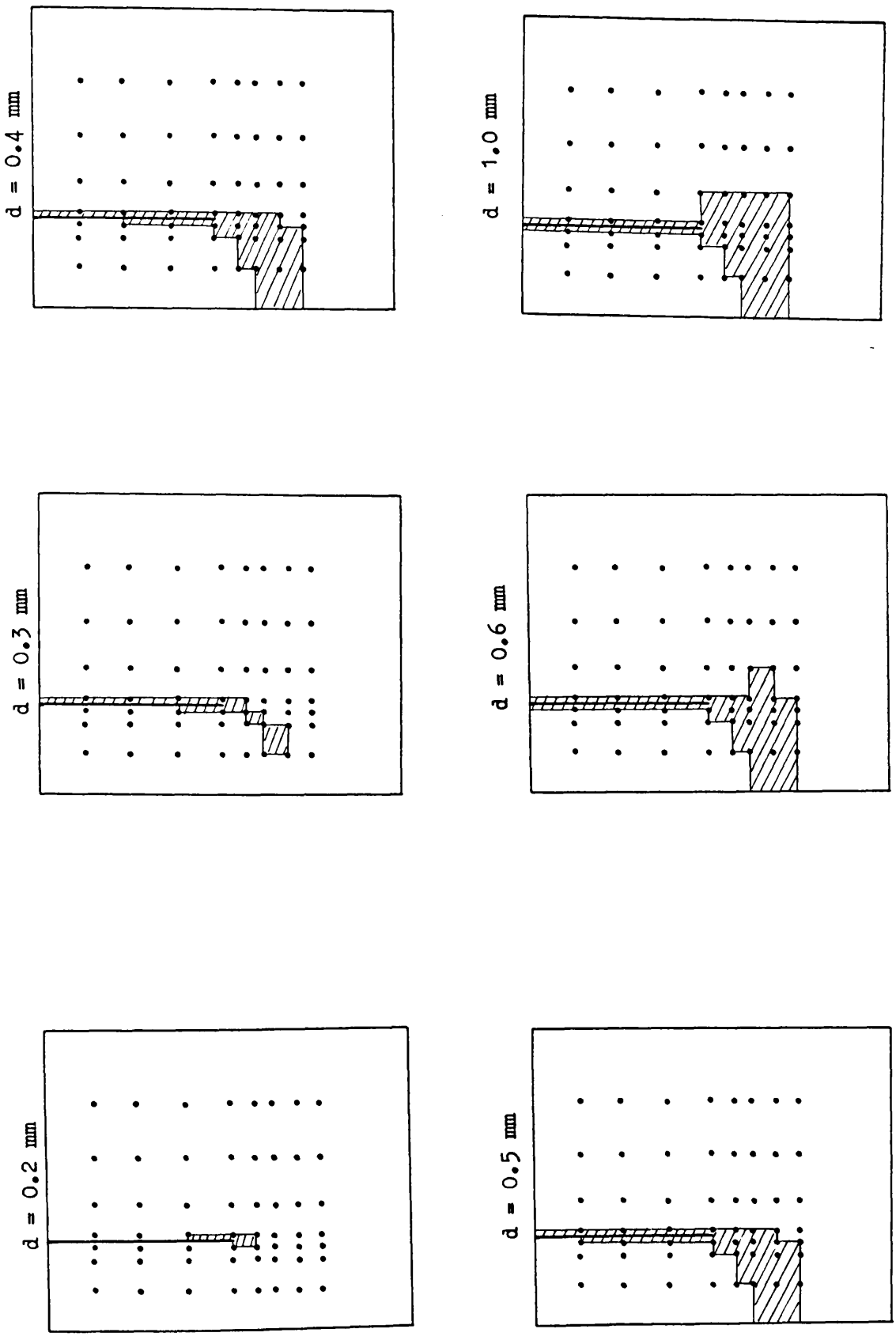

Fig. 4.45 Growth of failure zones at various stages of penetration , $\alpha i = 0.5$ $\alpha o = 1.0$

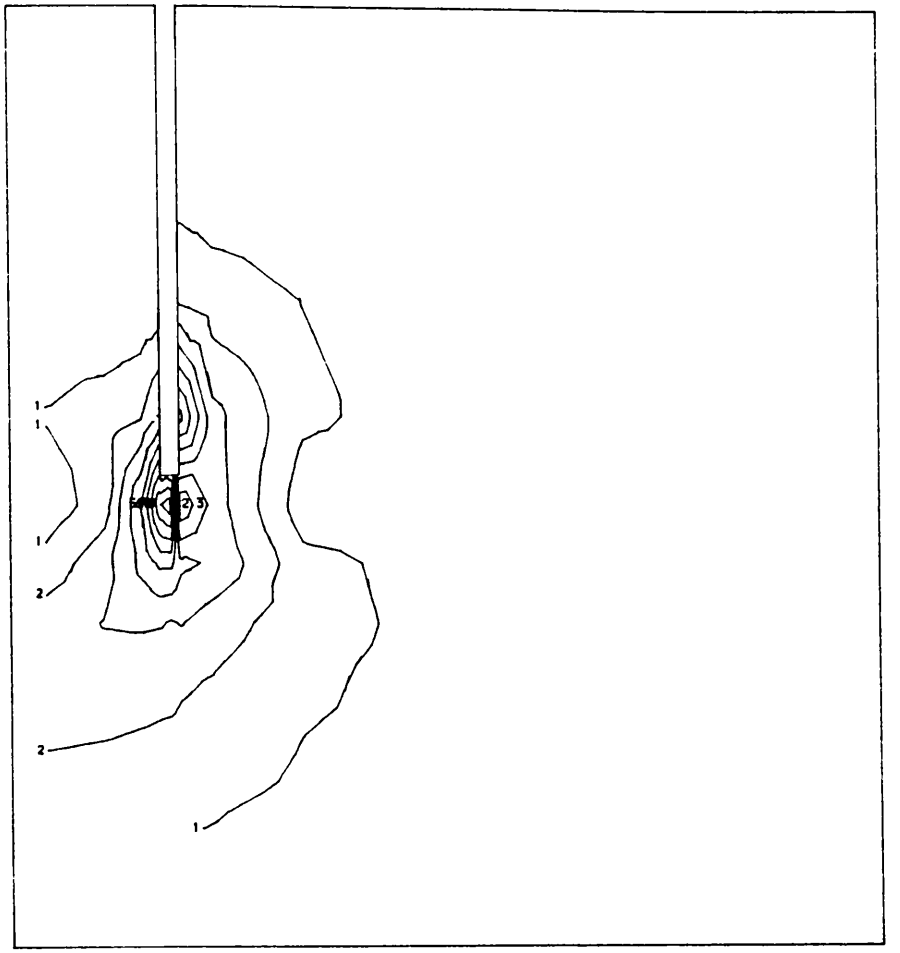

Fig. 4.46
$(\sigma 1-\sigma_3)/2Cu$ contours
in elastic state
(d=0.1mm), αi=0.0 αo=0.0

Key:	
1	0.1
2	0.2
3	0.3
4	0.4
5	0.5
6	0.6
7	0.7
8	0.8
9	0.9
10	1.0

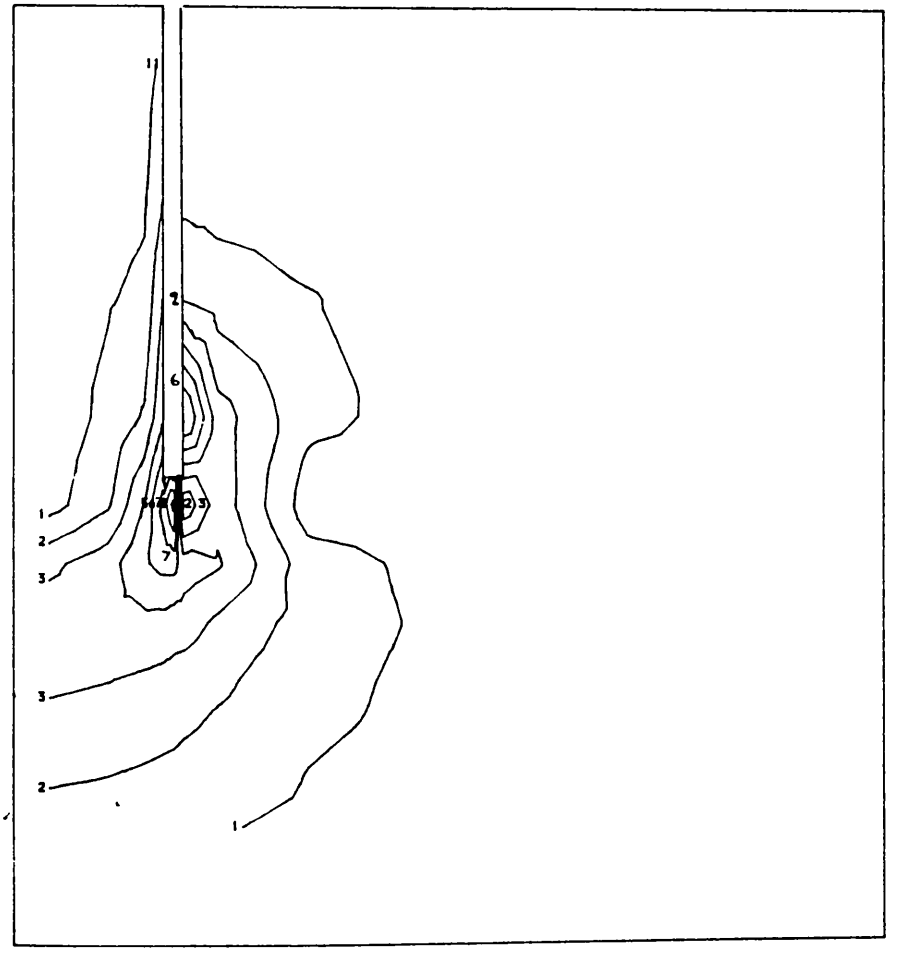

Fig. 4.47
$(\sigma 1-\sigma_3)/2Cu$ contours
in elastic state
(d=0.1mm)
αi = 0.5 αo = 0.0

Key:	
1	0.1
2	0.2
3	0.3
4	0.4
5	0.5
6	0.6
7	0.7
8	0.8
9	0.9
10	1.0

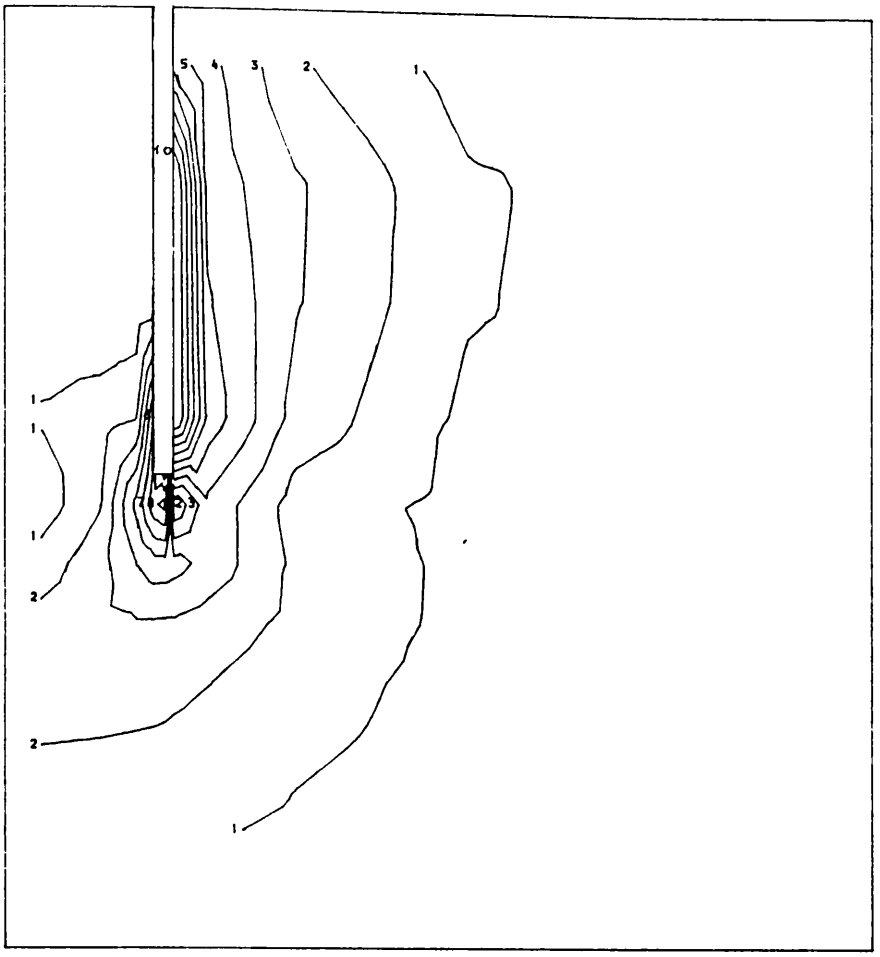

Fig. 4.48
$(\sigma 1-\sigma_3)/2Cu$ contours
in elastic state
(d=0.1mm)
$\alpha i = 0.0 \quad \alpha o = 0.5$

Key:	
1	0.1
2	0.2
3	0.3
4	0.4
5	0.5
6	0.6
7	0.7
8	0.8
9	0.9
10	1.0

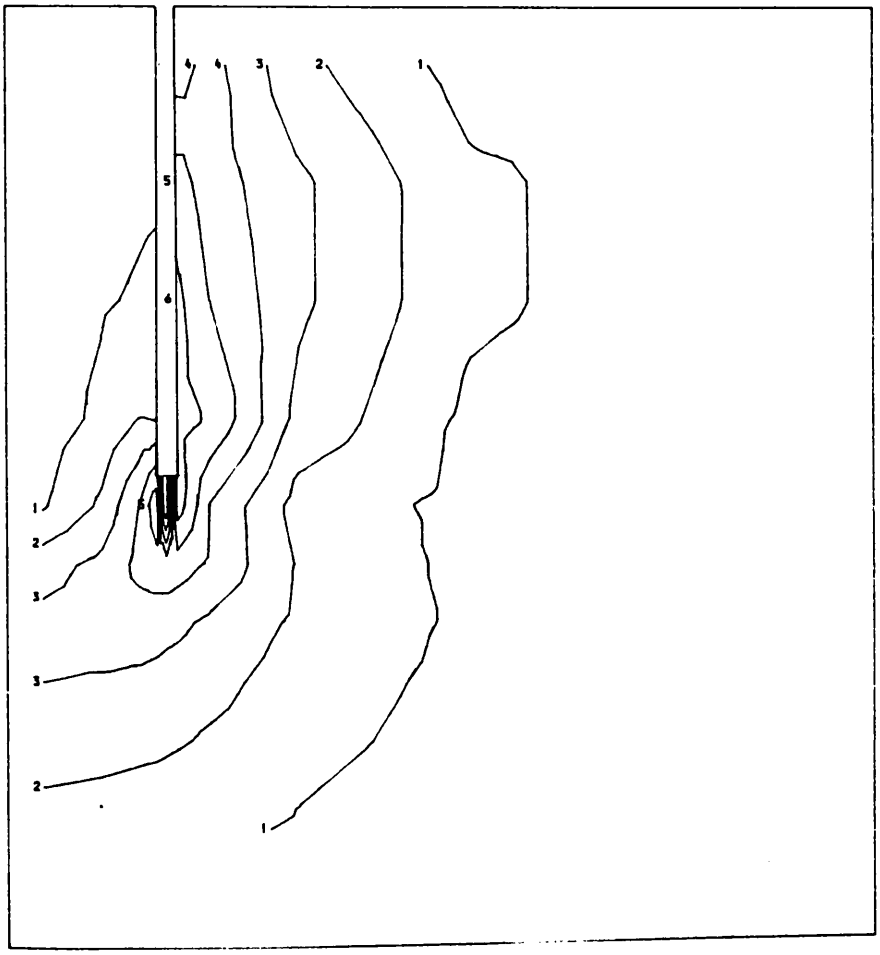

Fig. 4.49
$(\sigma 1-\sigma_3)/2C_u$ contours
in elastic state
(d=0.1mm)
$\alpha i = 1.0 \quad \alpha o = 1.0$

Key:	
1	0.1
2	0.2
3	0.3
4	0.4
5	0.5
6	0.6
7	0.7
8	0.8
9	0.9
10	1.0

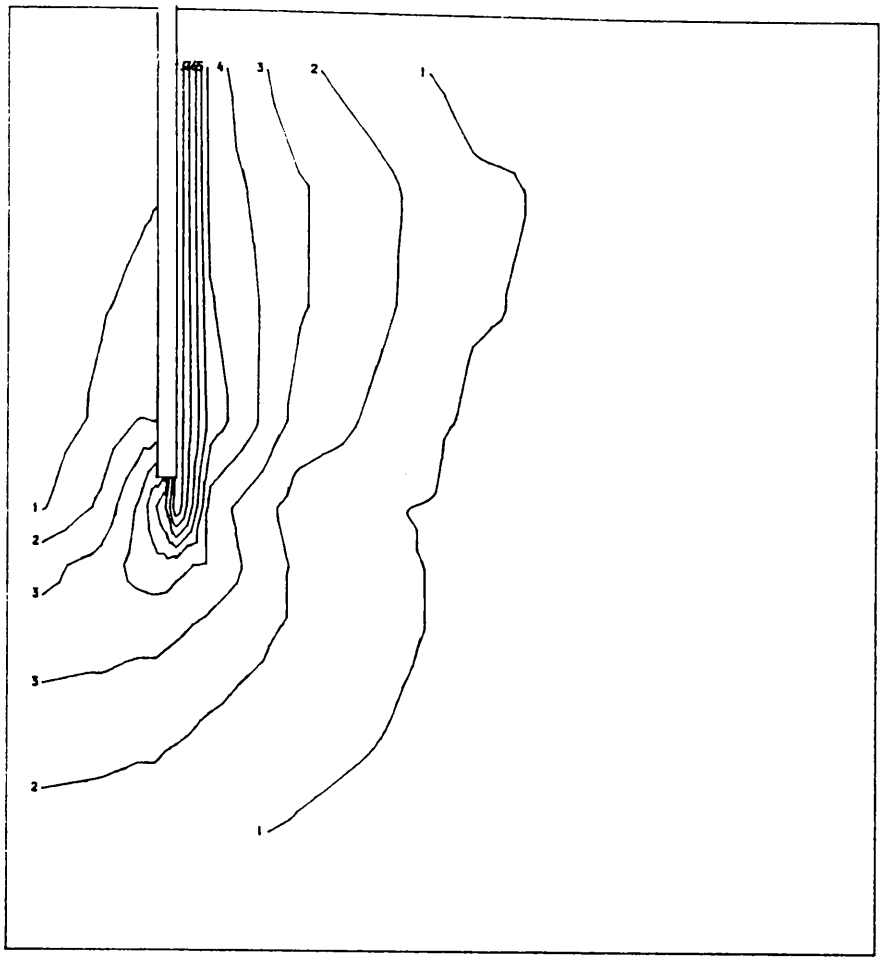

Fig. 4.50
$(\sigma 1-\sigma_3)/2Cu$ contours
in elastic state
(d=0.1mm)
$\alpha i = 1.0 \quad \alpha o = 0.5$

Key:	
1	0.1
2	0.2
3	0.3
4	0.4
5	0.5
6	0.6
7	0.7
8	0.8
9	0.9
10	1.0

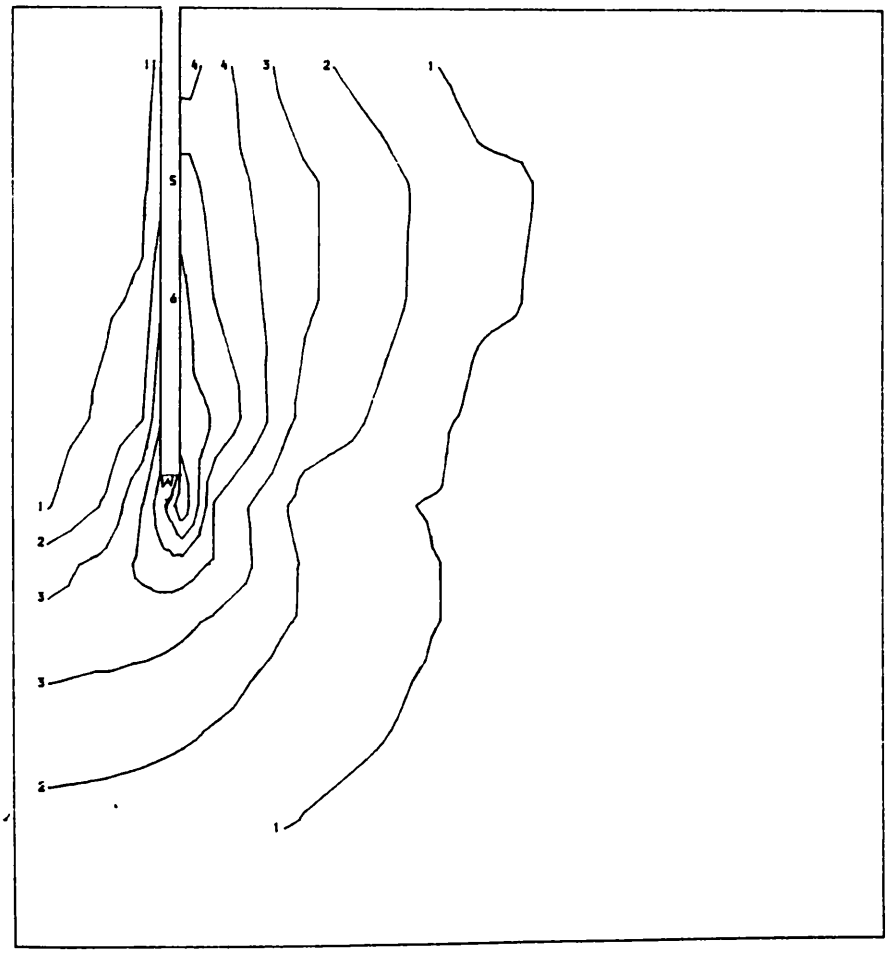

Fig. 4.51
$(\sigma 1-\sigma_3)/2Cu$ contours
in elastic state
(d=0.1mm)
$\alpha i = 0.5 \quad \alpha o = 1.0$

Key:	
1	0.1
2	0.2
3	0.3
4	0.4
5	0.5
6	0.6
7	0.7
8	0.8
9	0.9
10	1.0

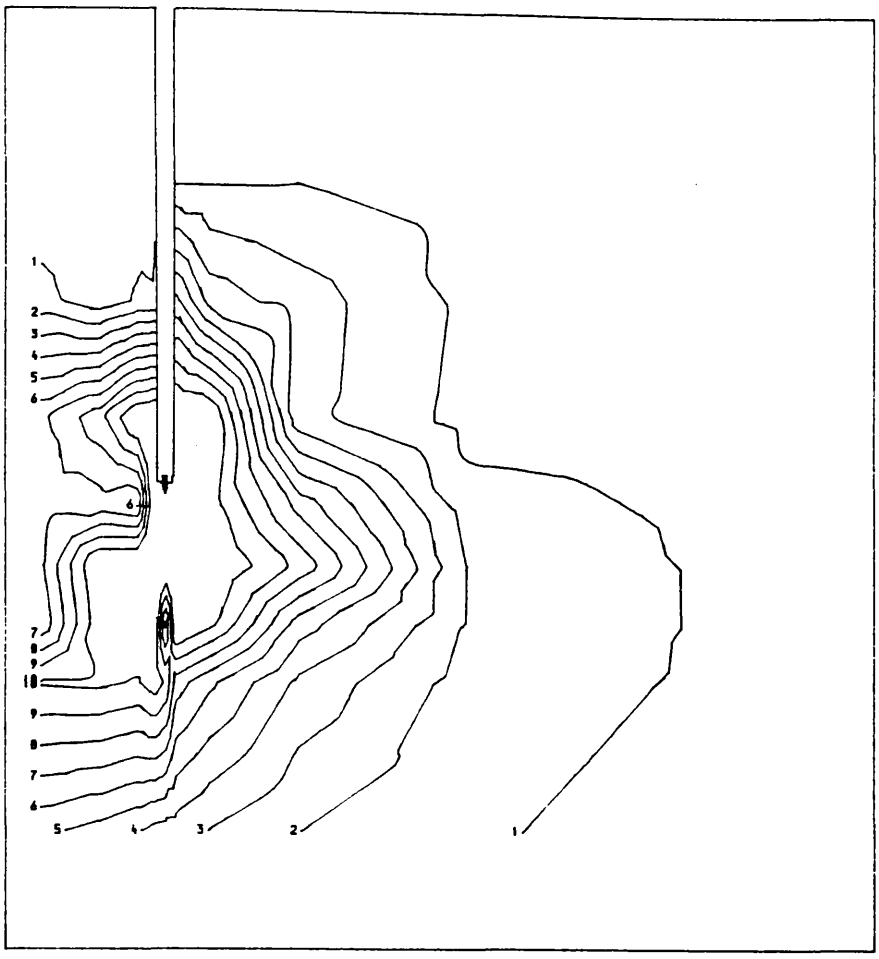

Fig. 4.52
$(\sigma 1-\sigma_3)/2Cu$ contours
at ultimate state
(d=1.5mm)
$\alpha i = 0.0 \quad \alpha o = 0.0$

Key:	
1	0.1
2	0.2
3	0.3
4	0.4
5	0.5
6	0.6
7	0.7
8	0.8
9	0.9
10	1.0

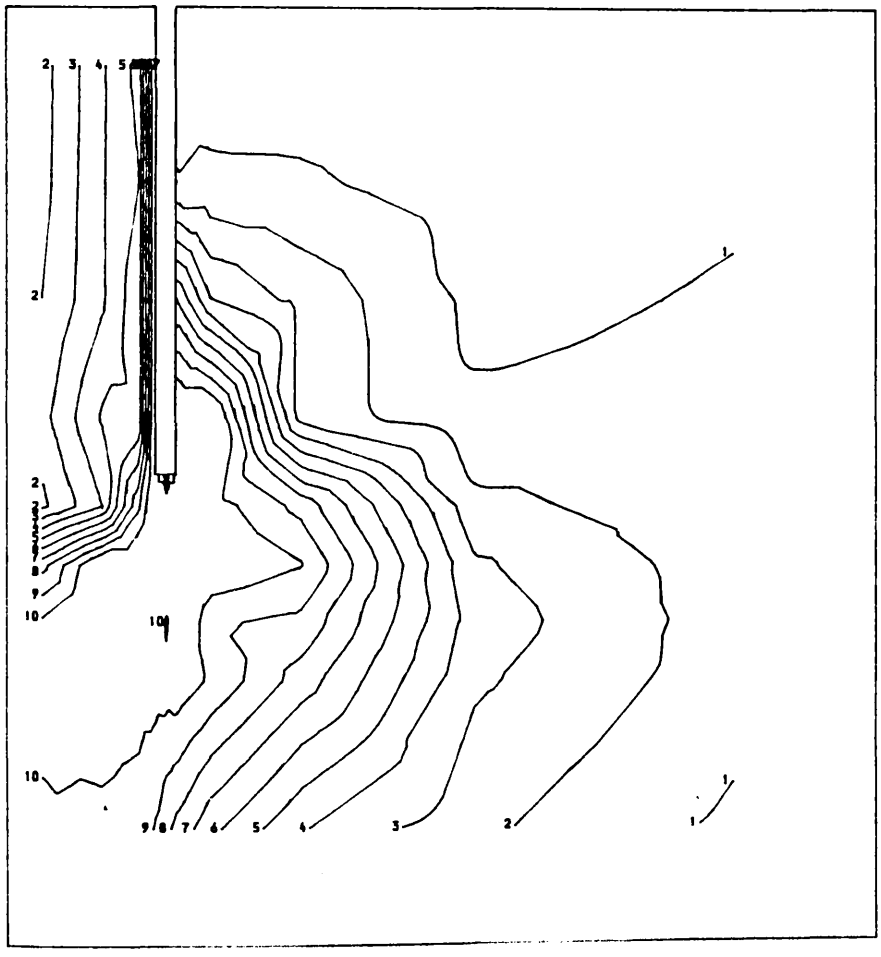

Fig. 4.53
$(\sigma 1-\sigma_3)/2Cu$ contours
at ultimate state
(d=1.5mm)
$\alpha i = 0.5 \quad \alpha o = 0.0$

Key:	
1	0.1
2	0.2
3	0.3
4	0.4
5	0.5
6	0.6
7	0.7
8	0.8
9	0.9
10	1.0

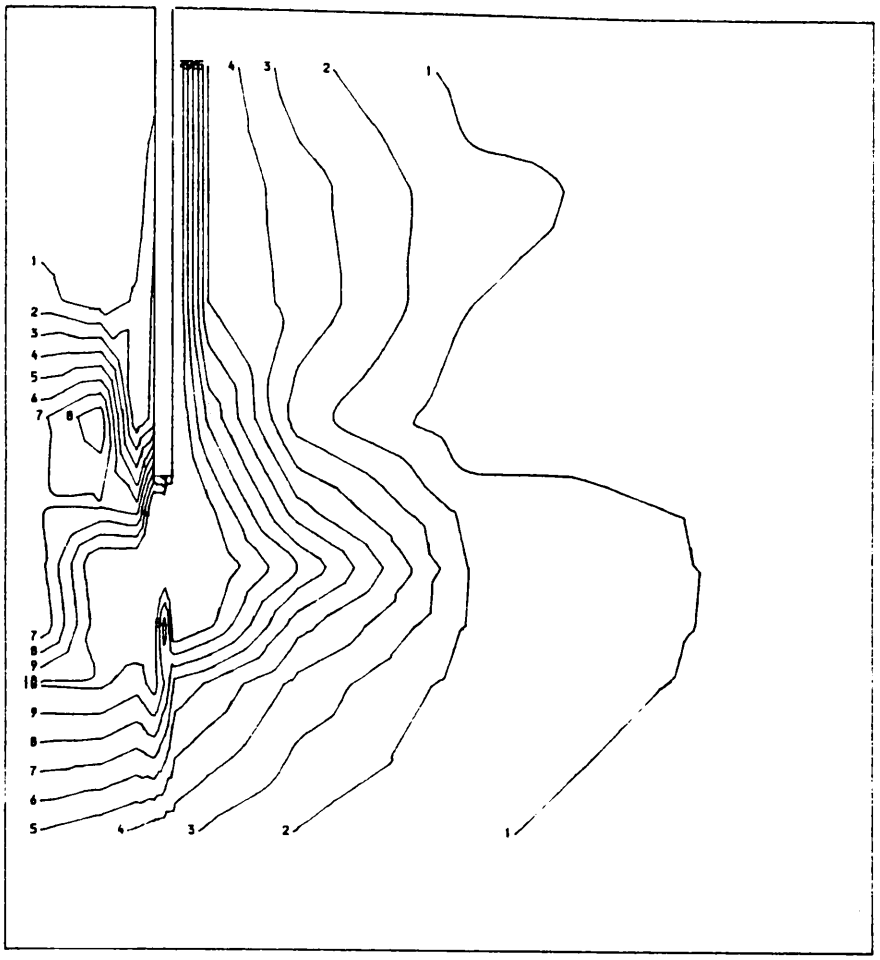

Fig. 4.54
$(\sigma 1-\sigma 3)/2Cu$ contours
at ultimate state
(d=1.5mm)
$\alpha i = 0.0 \quad \alpha o = 0.5$

Key:	
1	0.1
2	0.2
3	0.3
4	0.4
5	0.5
6	0.6
7	0.7
8	0.8
9	0.9
10	1.0

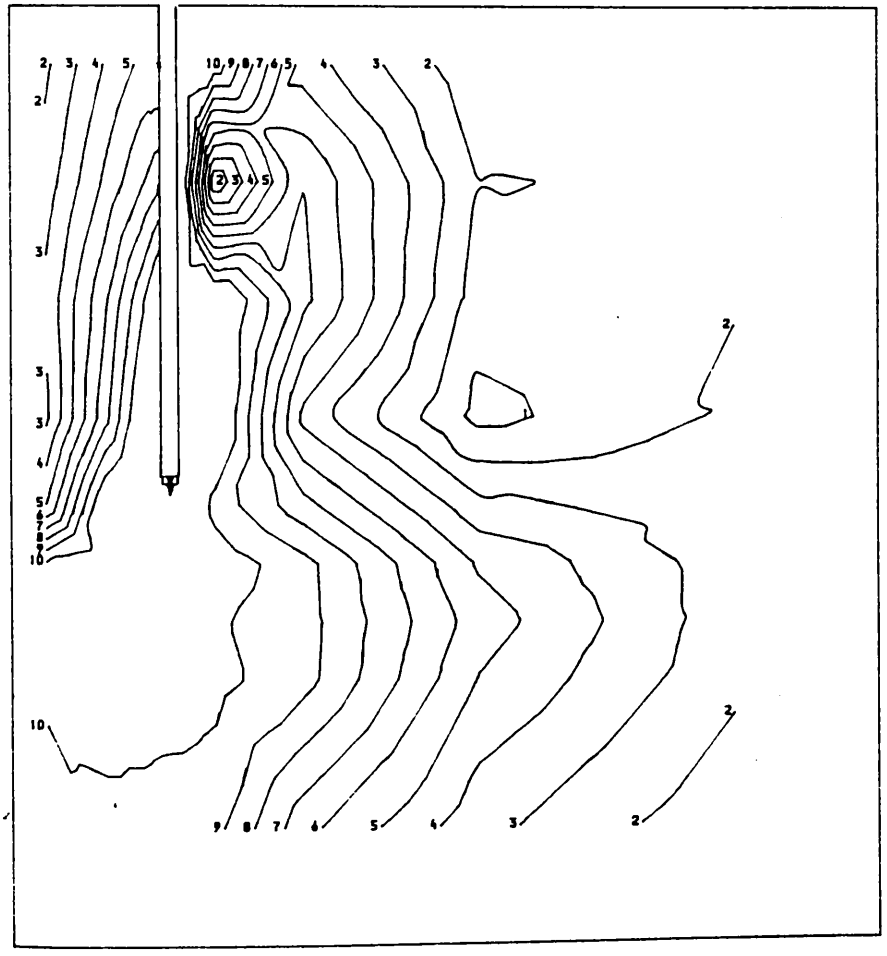

Fig. 4.55
$(\sigma 1-\sigma 3)/2Cu$ contours
at ultimate state
(d=1.5mm)
$\alpha i = 1.0 \quad \alpha o = 1.0$

Key:	
1	0.1
2	0.2
3	0.3
4	0.4
5	0.5
6	0.6
7	0.7
8	0.8
9	0.9
10	1.0

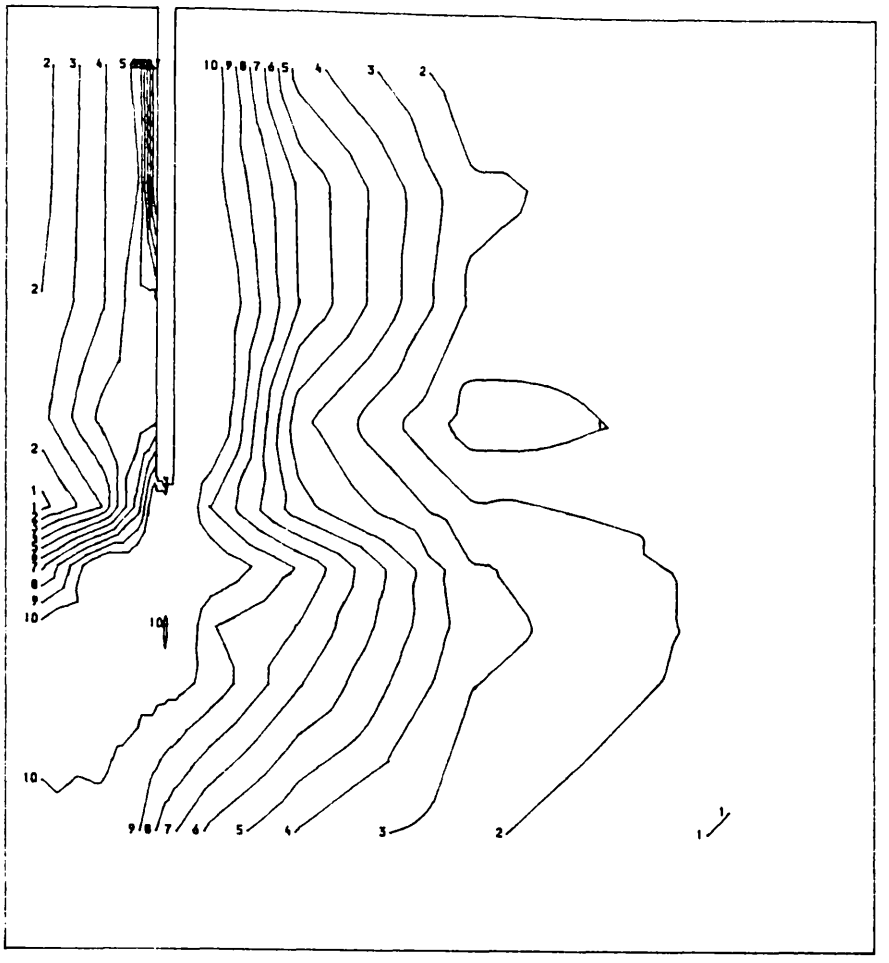

Fig. 4.56
$(\sigma 1-\sigma_3)/2Cu$ contours
at ultimate state
(d=1.5mm)
$\alpha i = 0.5 \quad \alpha o = 1.0$

Key:	
1	0.1
2	0.2
3	0.3
4	0.4
5	0.5
6	0.6
7	0.7
8	0.8
9	0.9
10	1.0

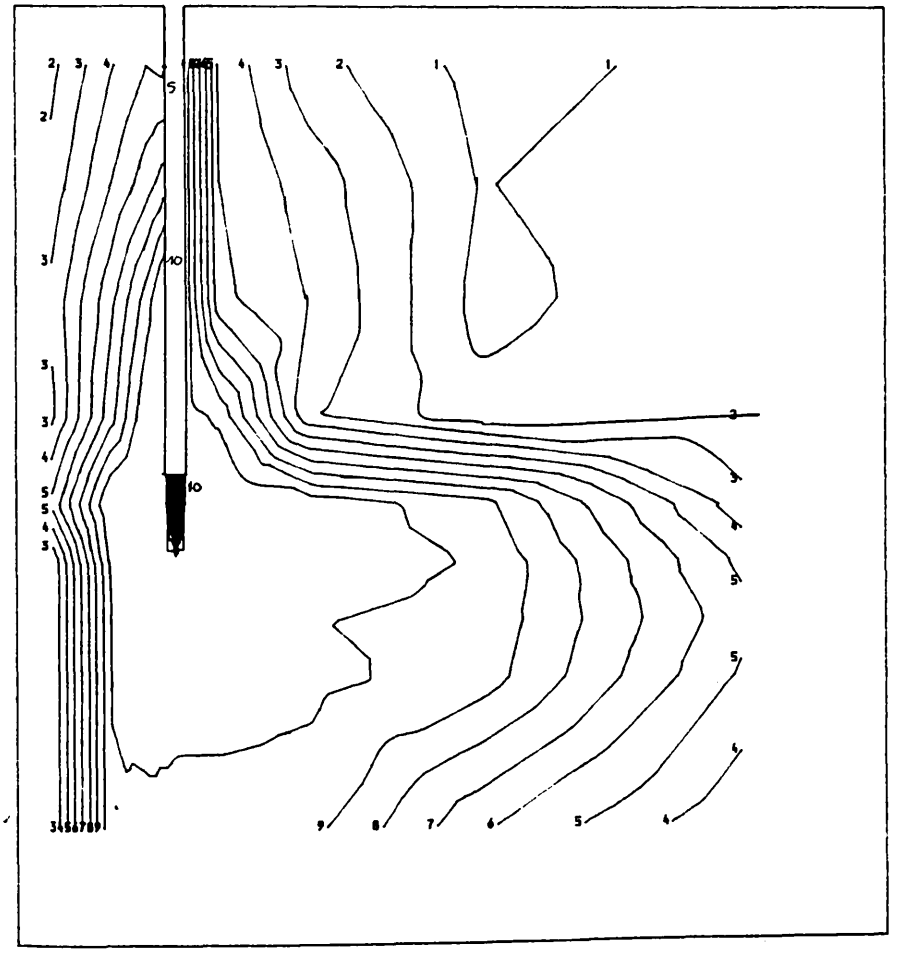

Fig. 4.57
$(\sigma 1-\sigma_3)/2Cu$ contours
at ultimate state
(d=1.5mm)
$\alpha i = 1.0 \quad \alpha o = 0.5$

Key:	
1	0.1
2	0.2
3	0.3
4	0.4
5	0.5
6	0.6
7	0.7
8	0.8
9	0.9
10	1.0

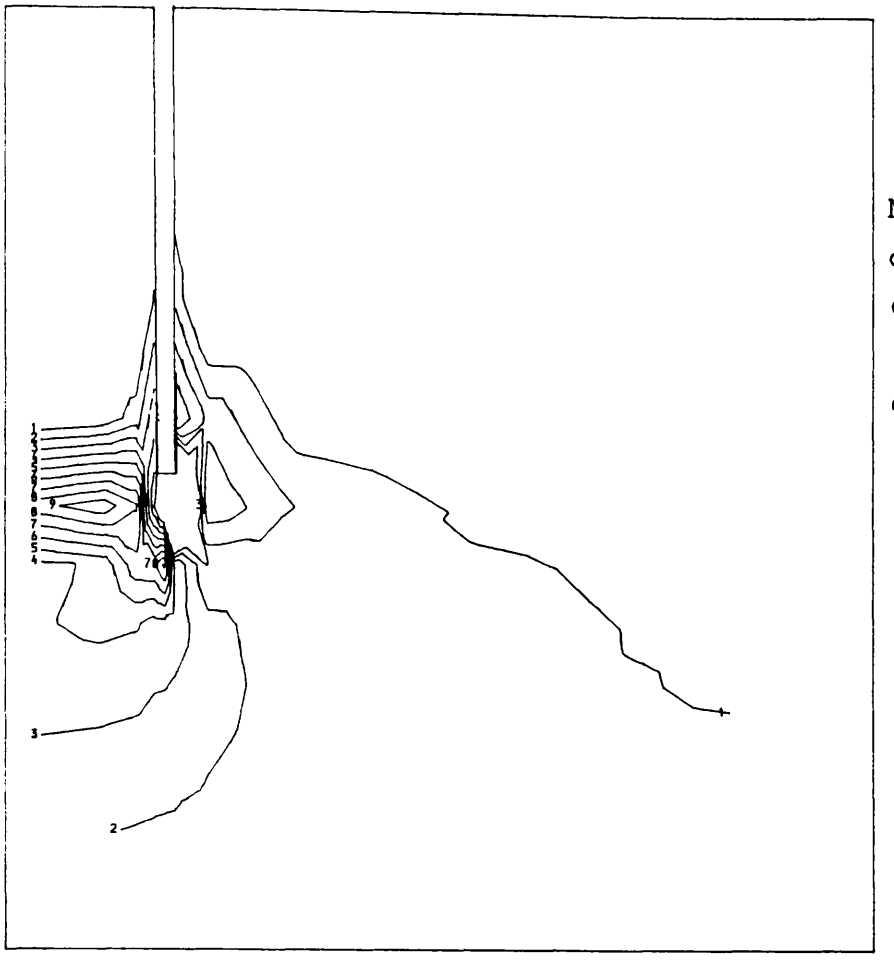

Fig. 4.58
Mean effective stress contours in elastic state (d=0.1mm)
αi = 0.0 αo = 0.0

Key:		
1	0.01	N/mm2
2	0.02	
3	0.03	
4	0.04	
5	0.05	
6	0.06	
7	0.07	
8	0.08	
9	0.09	
10	0.1	

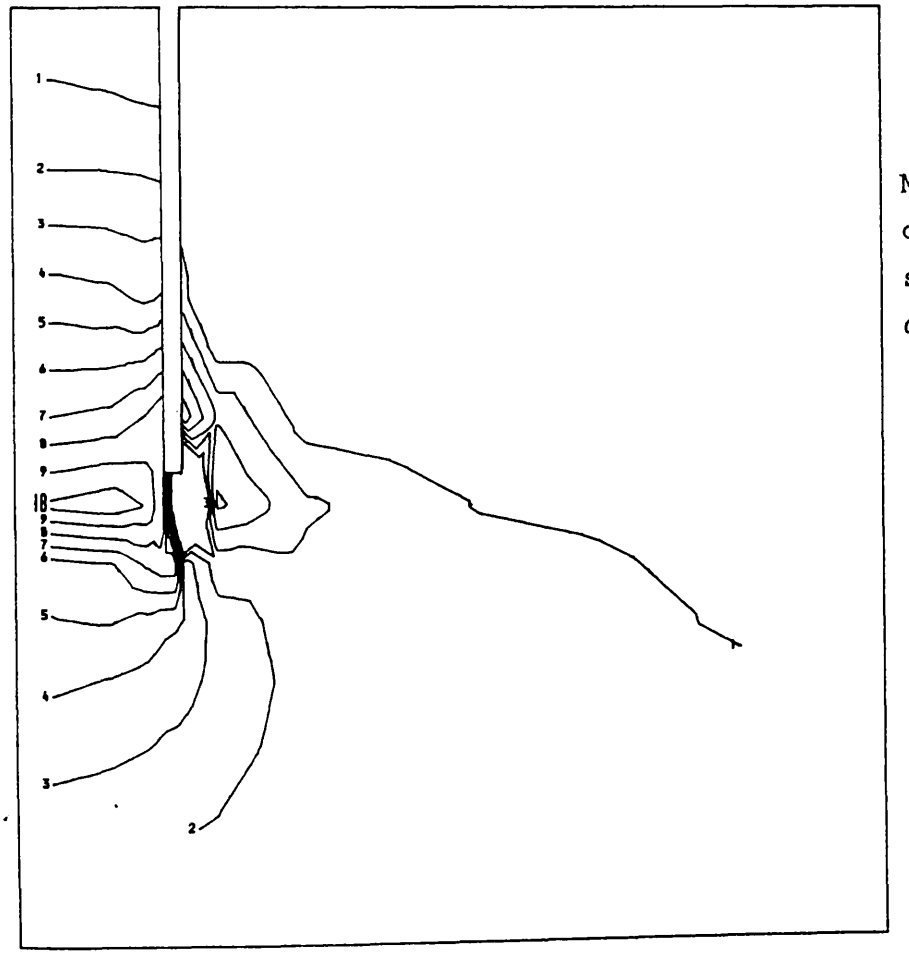

Fig. 4.59
Mean effective stress contours in elastic state (d=0.1mm)
αi = 0.5 αo = 0.0

Key:		
1	0.01	N/mm2
2	0.02	
3	0.03	
4	0.04	
5	0.05	
6	0.06	
7	0.07	
8	0.08	
9	0.09	
10	0.1	

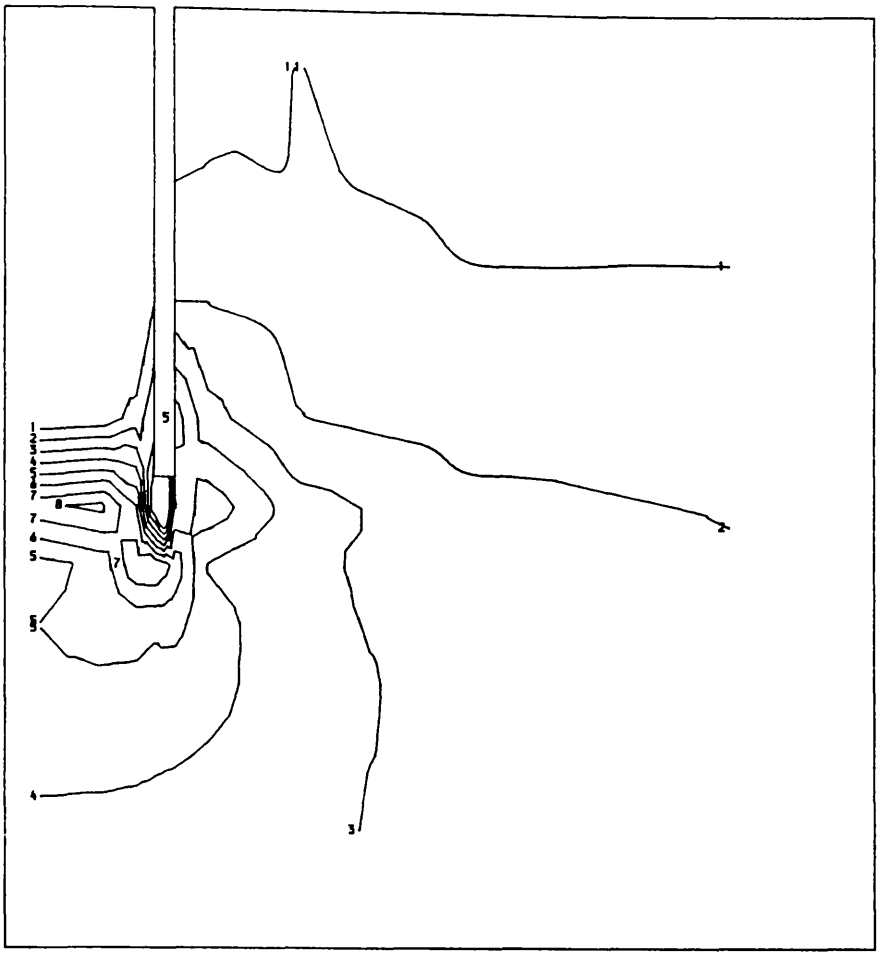

Fig. 4.60
Mean effective stress contours in elastic state (d=0.1mm)
αi = 0.0 αo = 0.5

Key:		
1	0.01	N/mm2
2	0.02	
3	0.03	
4	0.04	
5	0.05	
6	0.06	
7	0.07	
8	0.08	
9	0.09	
10	0.1	

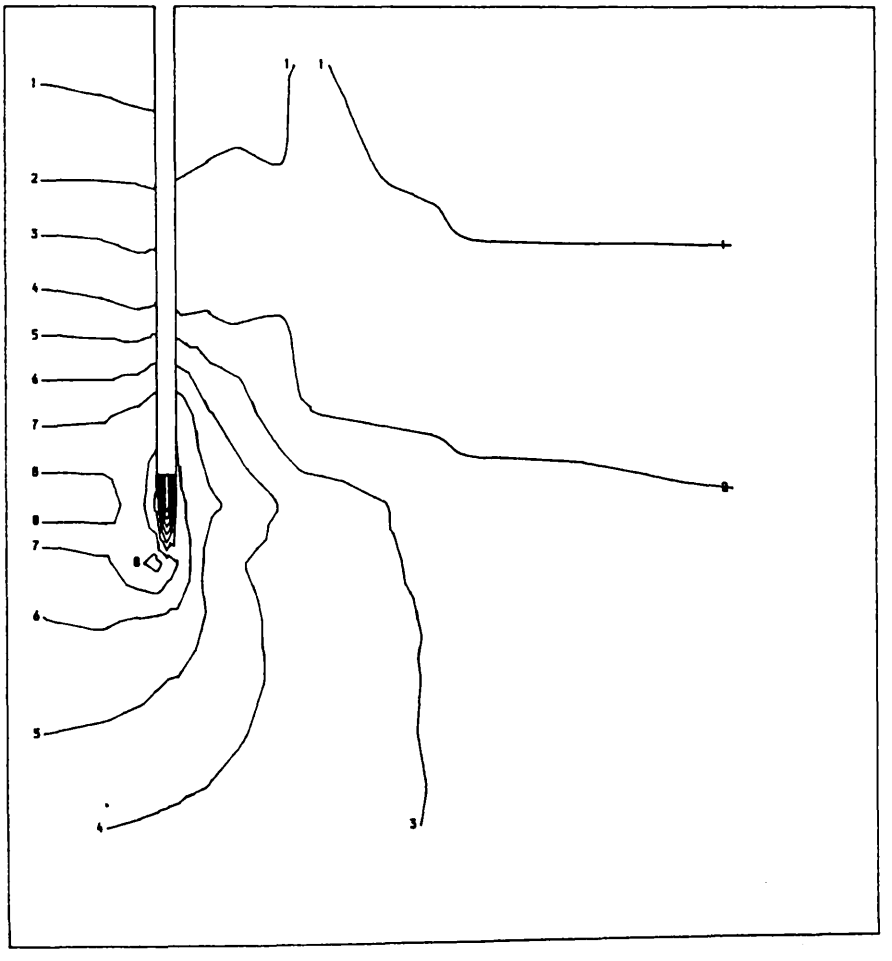

Fig. 4.61
Mean effective stress contours in elastic state (d=0.1mm)
αi = 1.0 αo = 1.0

Key:		
1	0.01	N/mm2
2	0.02	
3	0.03	
4	0.04	
5	0.05	
6	0.06	
7	0.07	
8	0.08	
9	0.09	
10	0.1	

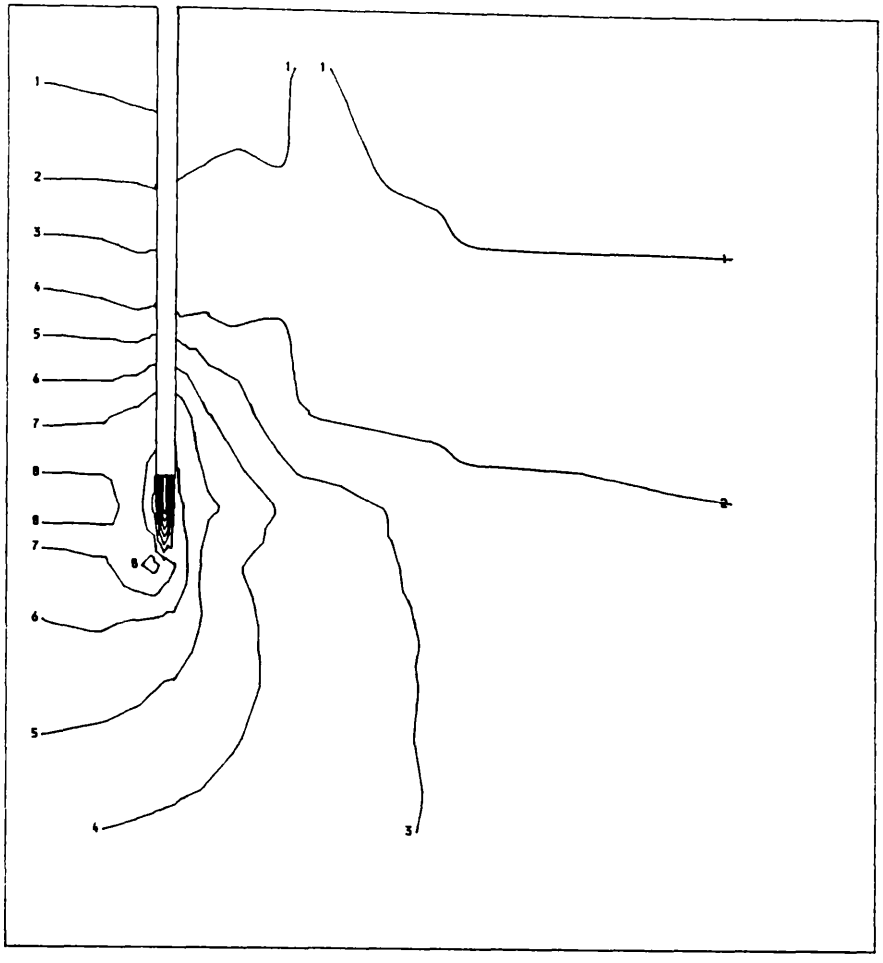

Fig. 4.62
Mean effective stress contours in elastic state (d=0.1mm)
αi = 0.5 αo = 1.0

Key:		
1	0.01	N/mm2
2	0.02	
3	0.03	
4	0.04	
5	0.05	
6	0.06	
7	0.07	
8	0.08	
9	0.09	
10	0.1	

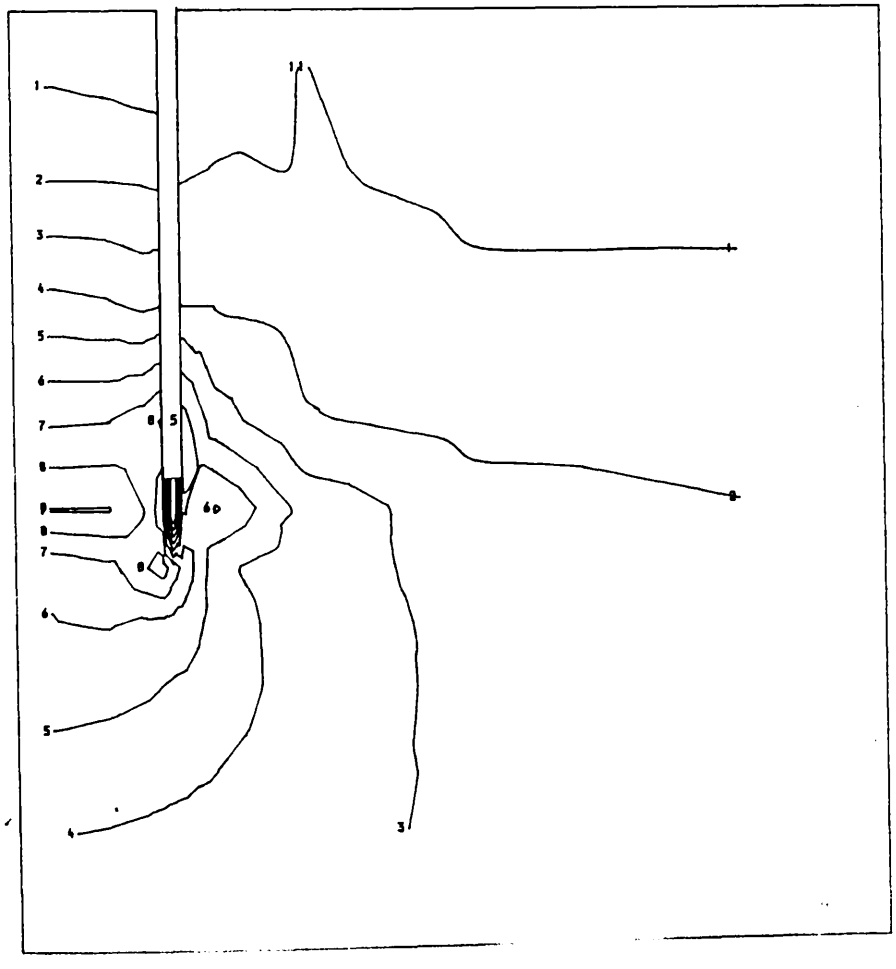

Fig. 4.63
Mean effective stress contours in elastic state (d=0.1mm)
αi = 1.0 αo = 0.5

Key:		
1	0.01	N/mm2
2	0.02	
3	0.03	
4	0.04	
5	0.05	
6	0.06	
7	0.07	
8	0.08	
9	0.09	
10	0.1	

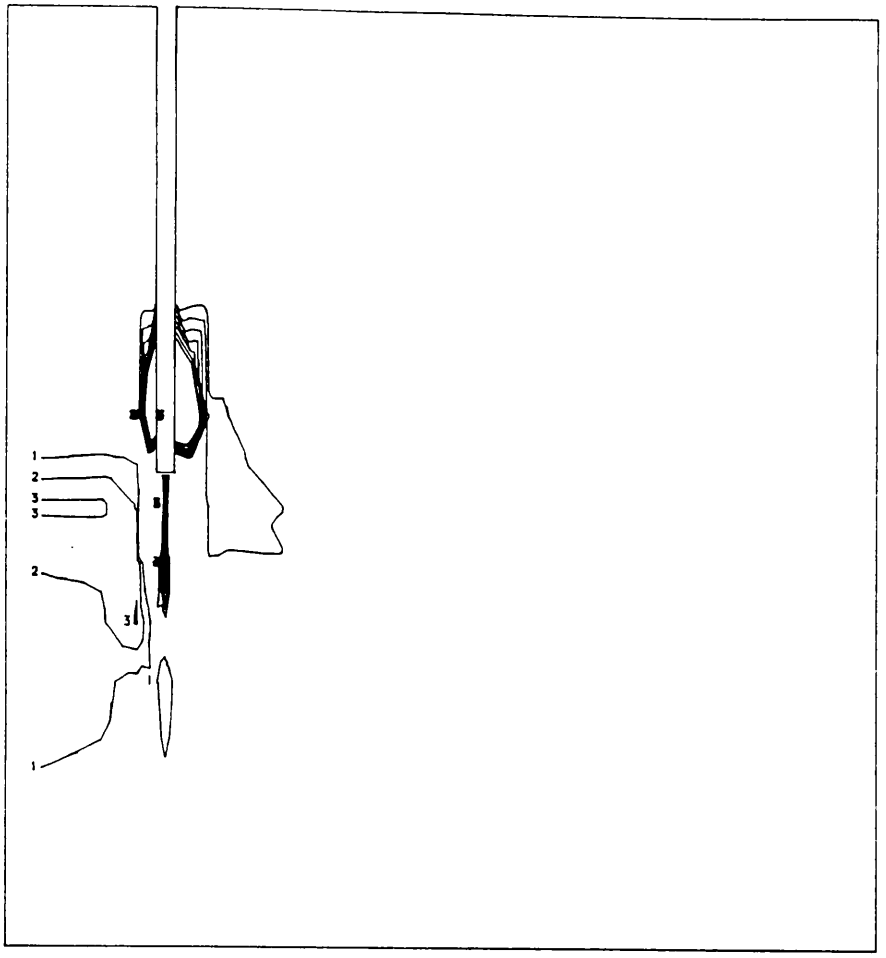

Fig. 4.64
Mean effective stress contours at ultimate state (d=1.5mm)
αi = 0.0 αo = 0.0

Key:		
1	0.1	N/mm2
2	0.2	
3	0.3	
4	0.4	
5	0.5	
6	0.6	
7	0.7	

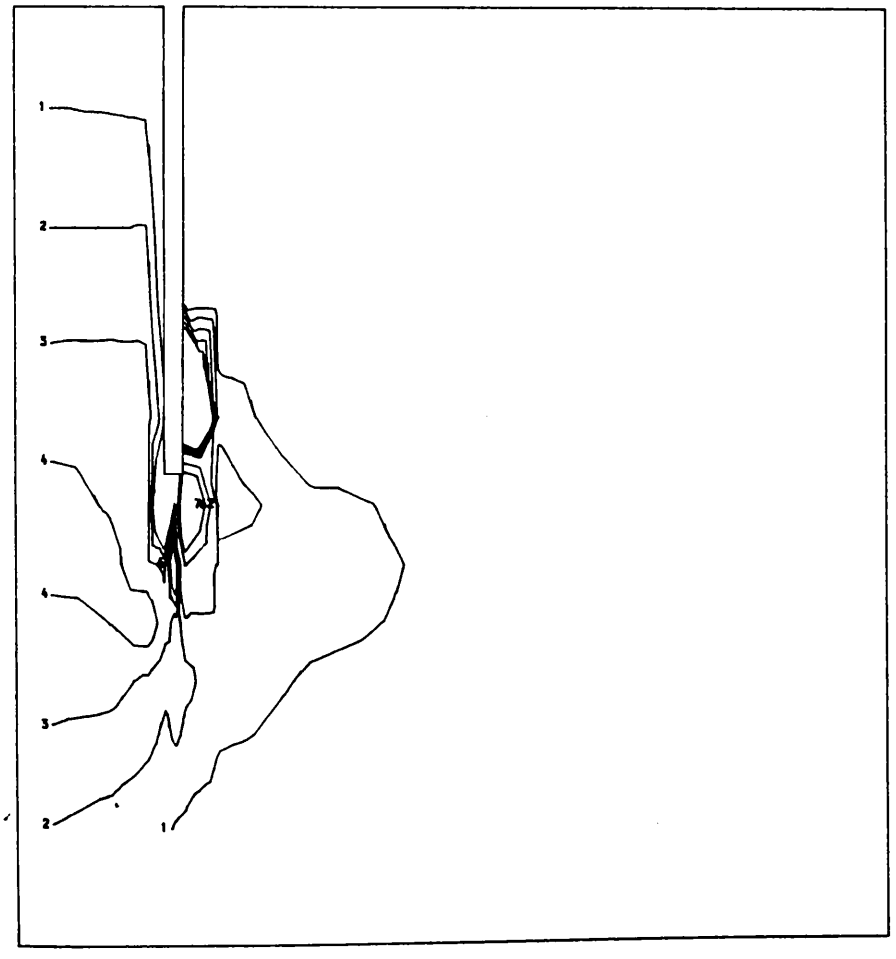

Fig. 4.65
Mean effective stress contours at ultimate state (d=1.5mm)
αi = 0.5 αo = 0.0

Key:		
1	0.1	N/mm2
2	0.2	
3	0.3	
4	0.4	
5	0.5	
6	-0.5	
7	-1.0	

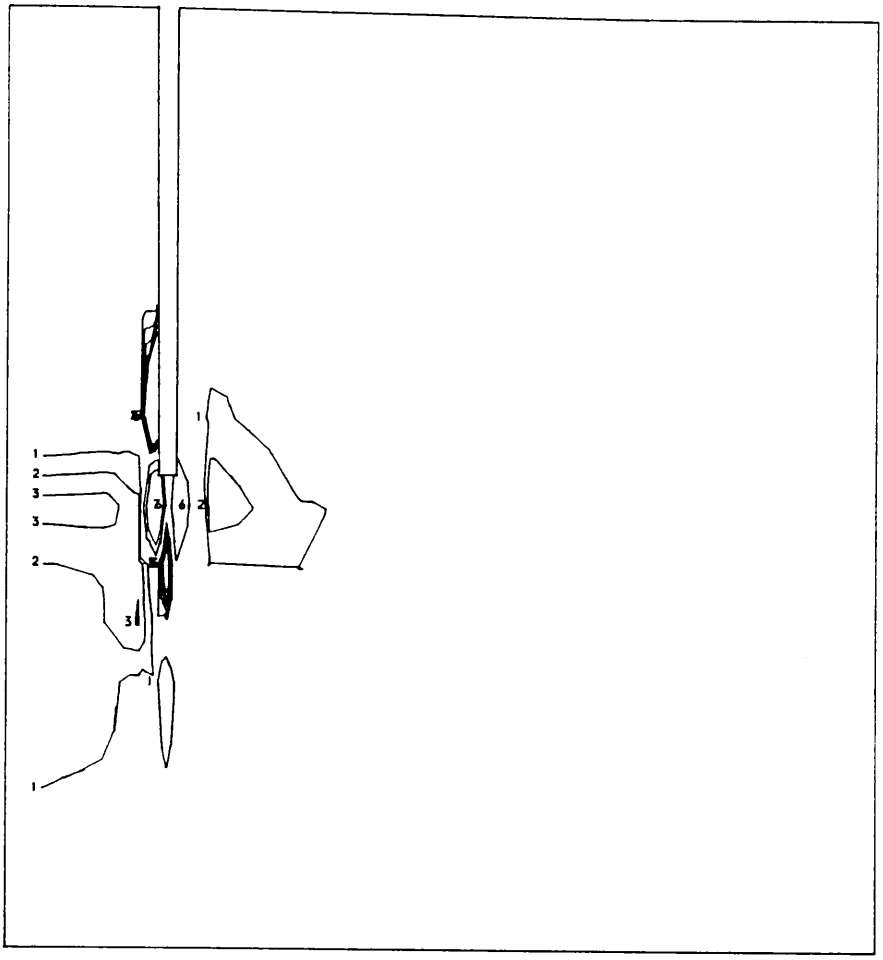

Fig. 4.66
Mean effective stress contours at ultimate state (d=1.5mm)
αi = 0.0 αo = 0.5

Key:	
1	0.1 N/mm2
2	0.2
3	0.3
4	0.4
5	0.5
6	-0.5
7	-1.0

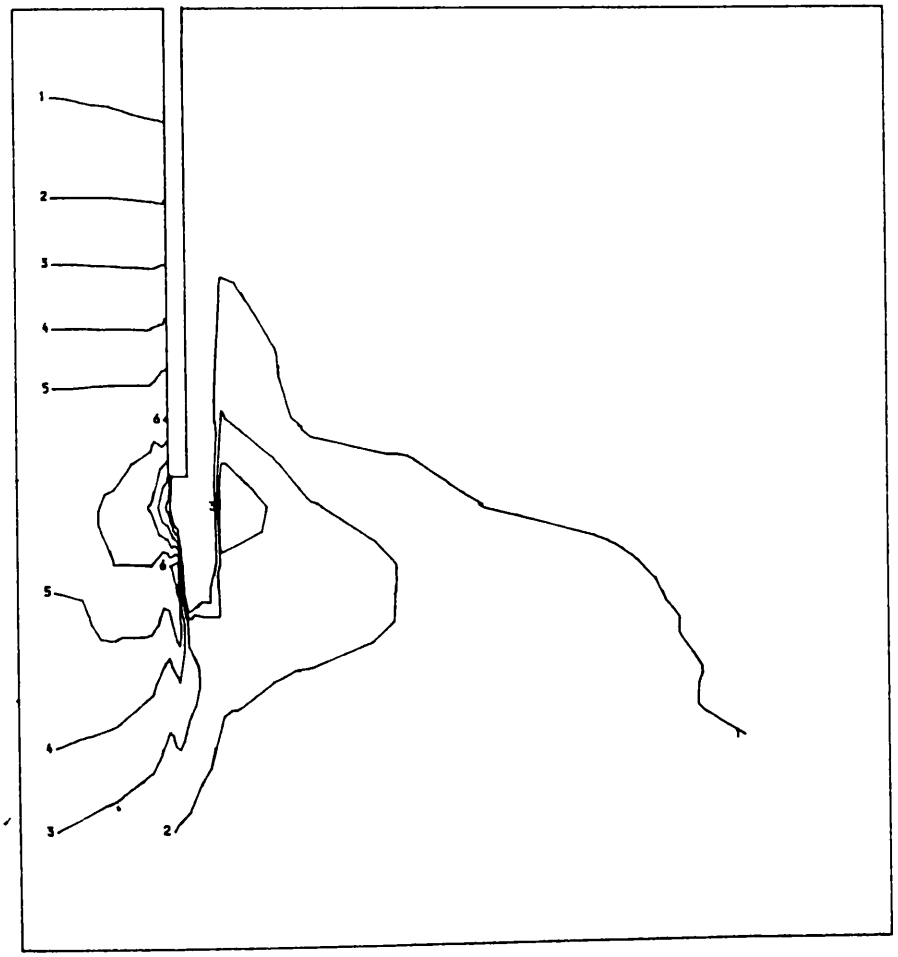

Fig. 4.67
Mean effective stress contours at ultimate state (d=1.5mm)
αi = 1.0 αo = 1.0

Key:	
1	0.1 N/mm2
2	0.2
3	0.3
4	0.4
5	0.5
6	0.6
7	0.7
8	0.8
9	0.9
10	1.0

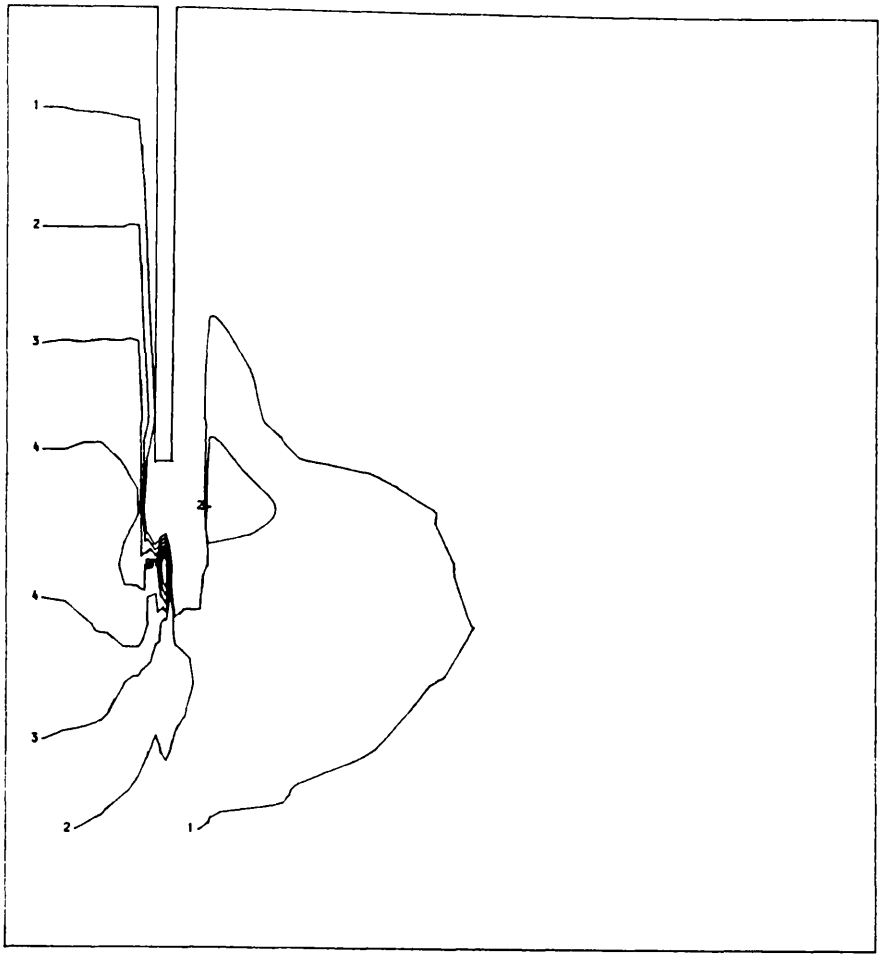

Fig. 4.68
Mean effective stress contours at ultimate state (d=1.5mm)
αi = 0.5 αo = 1.0

Key:		
1	0.1	N/mm2
2	0.2	
3	0.3	
4	0.4	
5	0.5	
6	0.6	
7	0.7	
8	0.8	
9	0.9	
10	1.0	

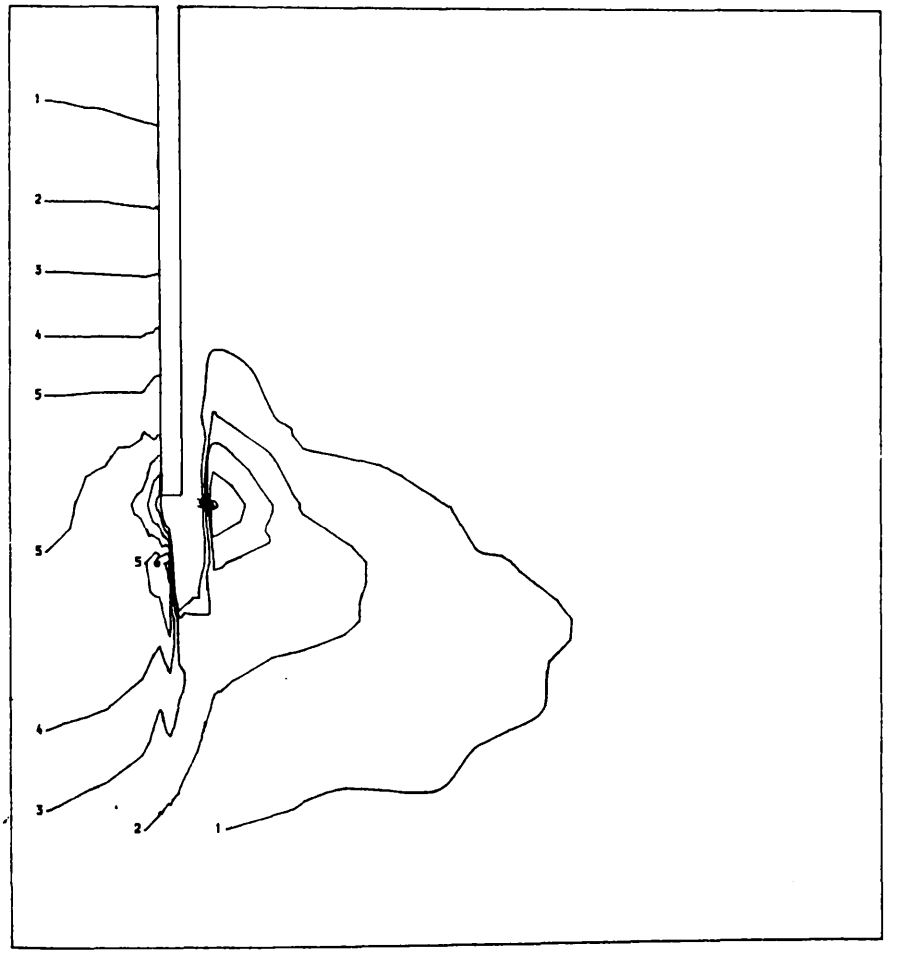

Fig. 4.69
Mean effective stress contours at ultimate state (d=1.5mm)
αi = 1.0 αo = 0.5

Key:		
1	0.1	N/mm2
2	0.2	
3	0.3	
4	0.4	
5	0.5	
6	0.6	
7	0.7	
8	0.8	
9	0.9	
10	1.0	

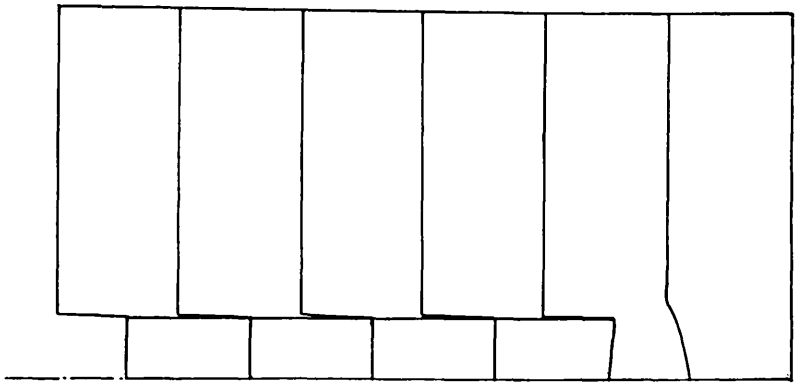

d = 1.5 mm L/D = 4

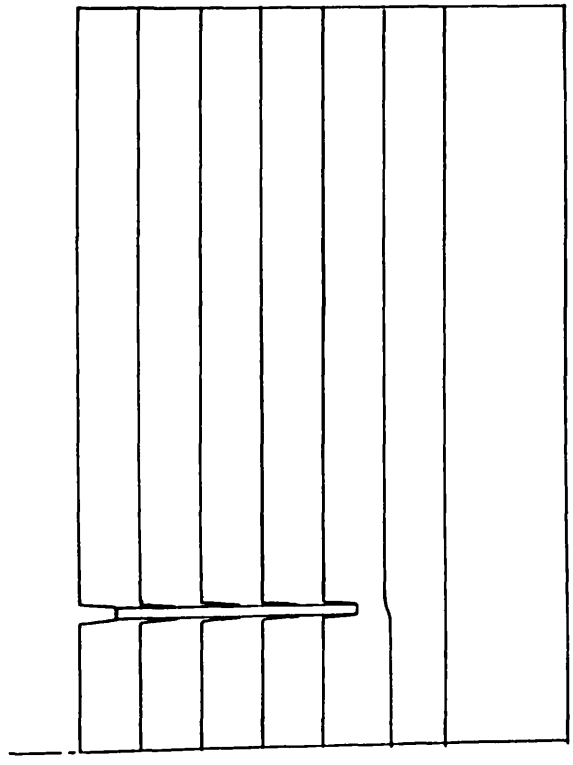

d = 1.5 mm L/D = 1

Fig. 4.70 Displacement field in the vicinity of the sampling tube

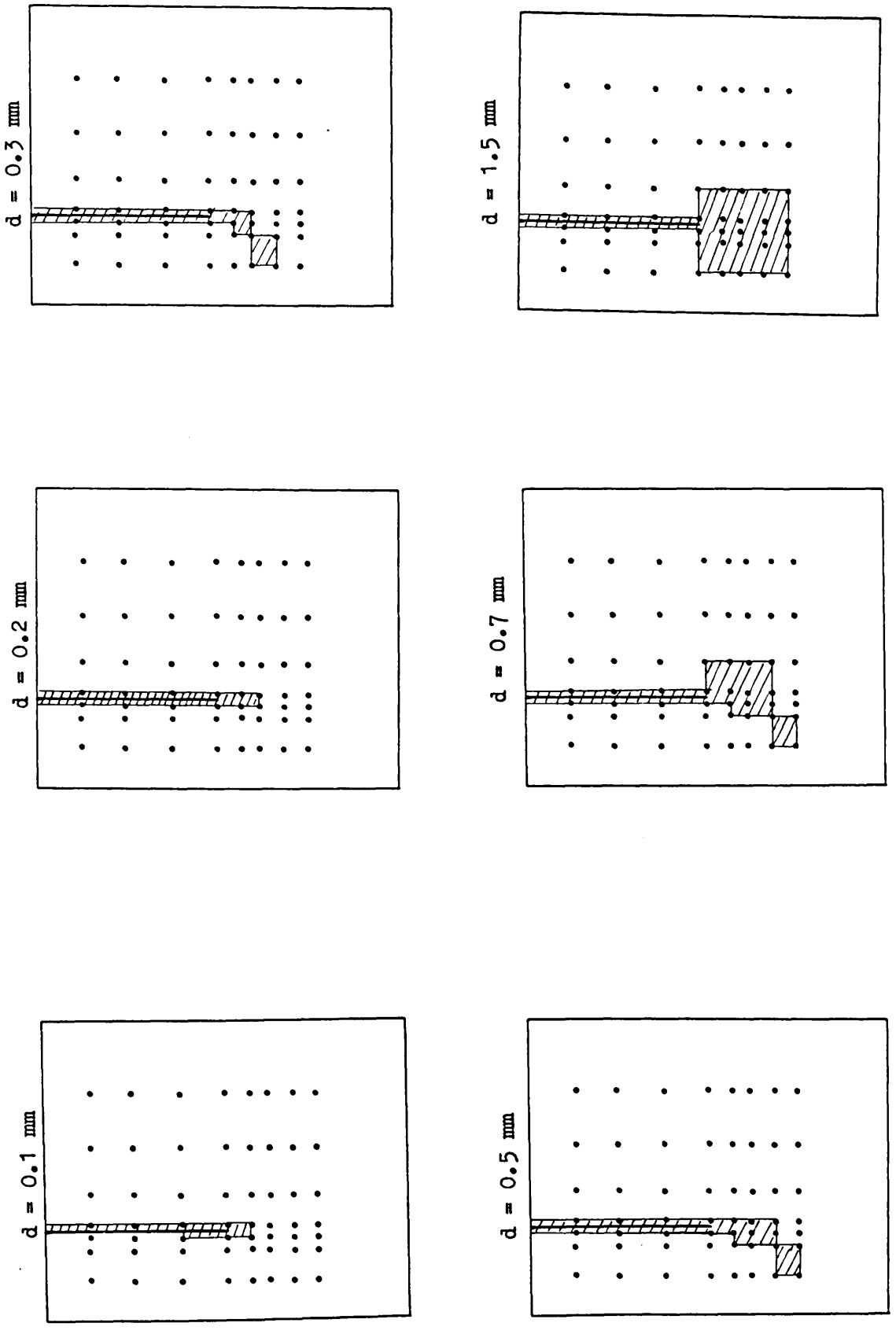

Fig. 4.71 Growth of failure zones at various stages of penetration , L/D = 1

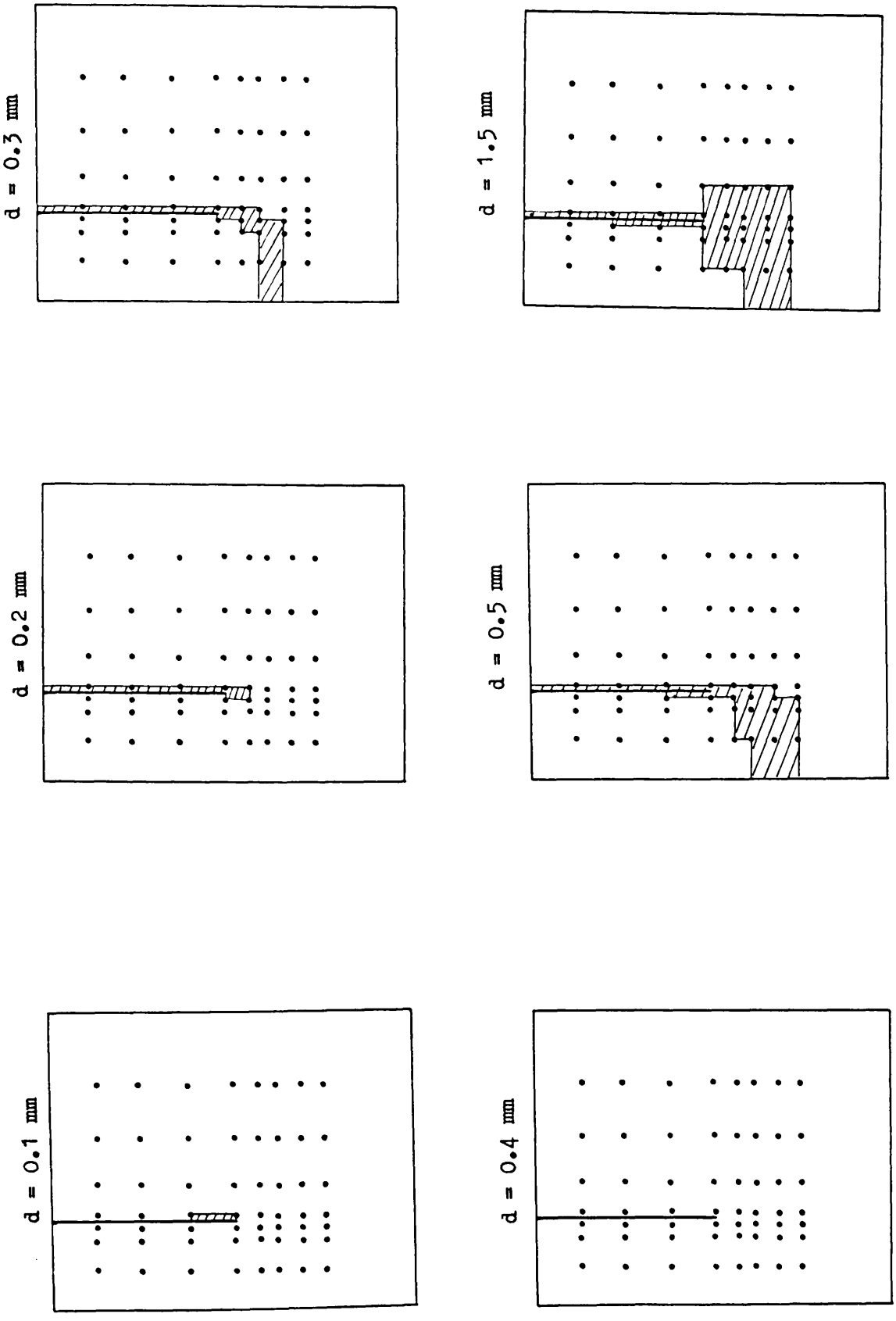

Fig. 4.72 Growth of failure zones at various stages of penetration , L/D = 4

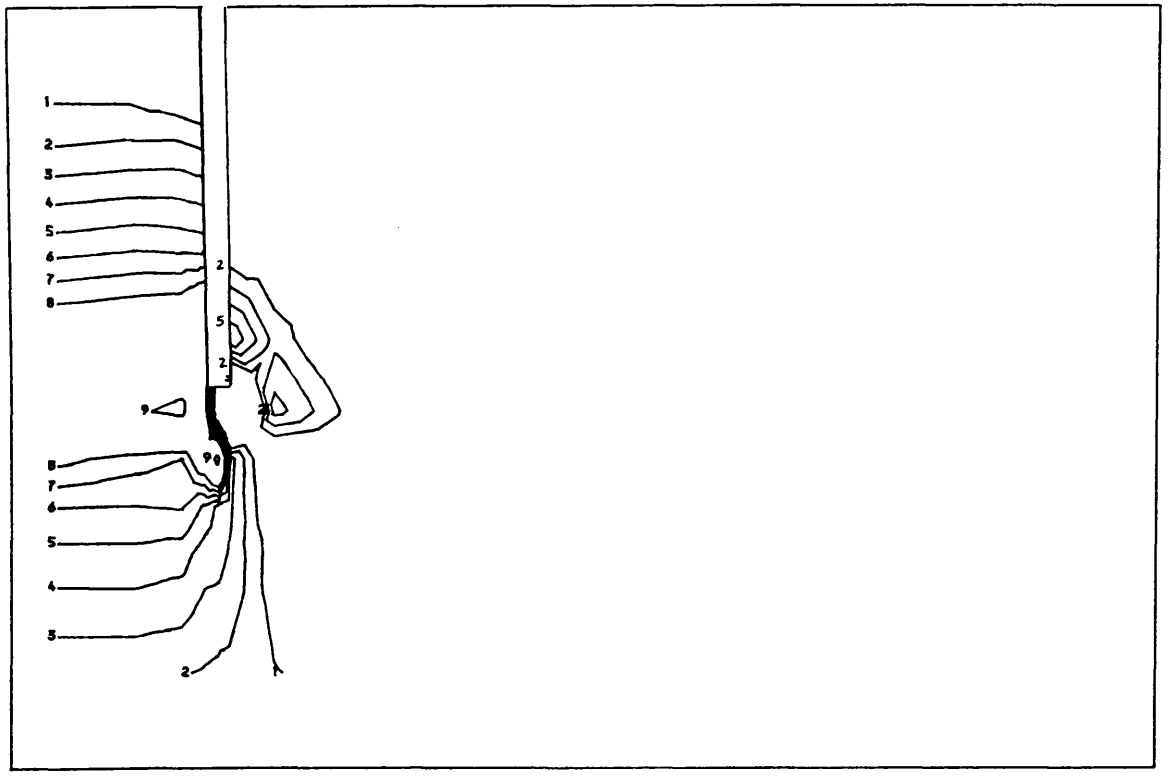

Key	N/mm2
1	0.030
2	0.040
3	0.050
4	0.060
5	0.070
6	0.080
7	0.090
8	0.100
9	0.150
10	0.200

FIG. 4.73 VERTICAL STRESS CONTOURS, L/D=1, Elastic state (d=0.1 mm).

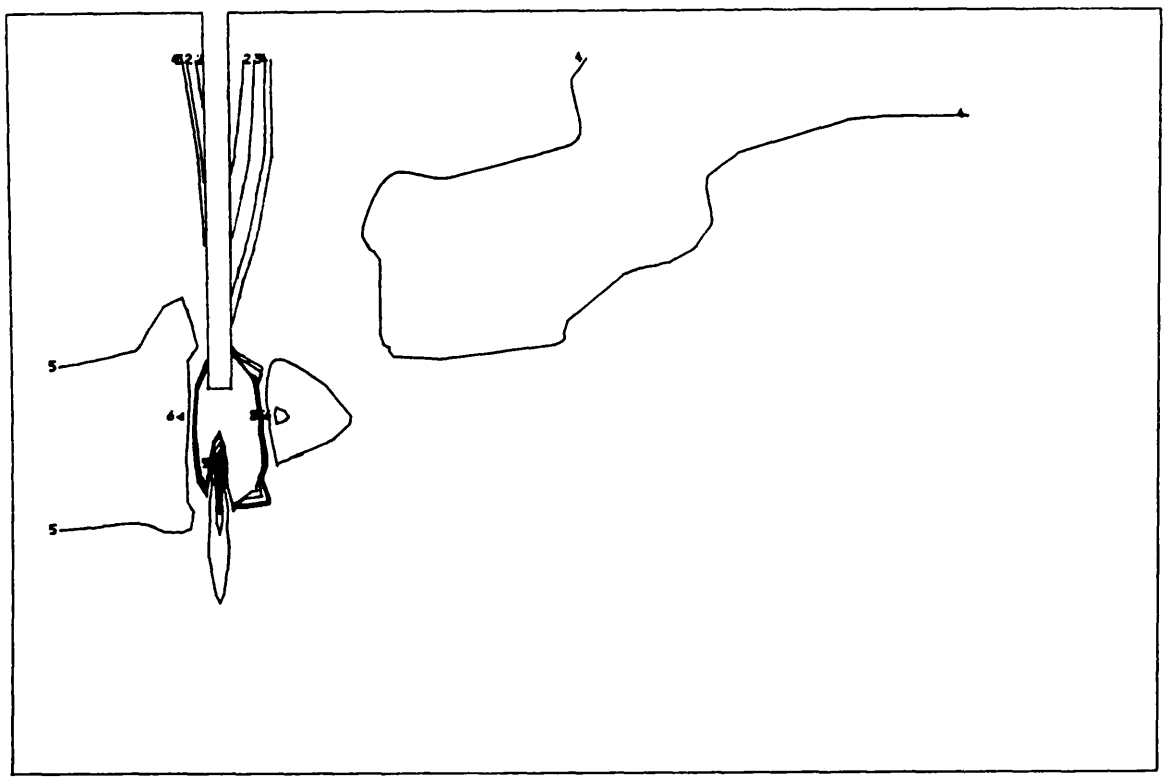

Key	N/mm2
1	-0.100
2	-0.060
3	-0.020
4	0.000
5	0.200
6	0.400
7	0.500
8	0.600
9	0.700
10	0.800

FIG. 4.74 VERTICAL STRESS CONTOURS, L/D=1, Plastic state (d=1.5mm).

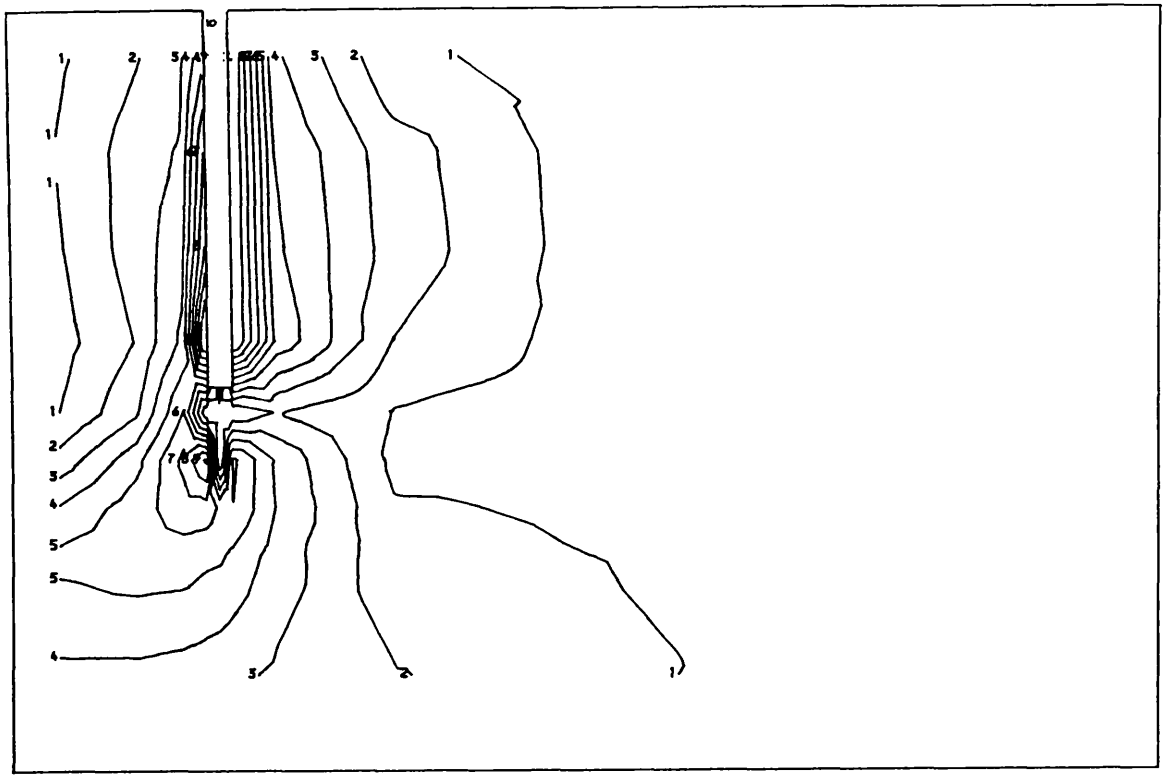

Key	
1	0. 100
2	0. 200
3	0. 300
4	0. 400
5	0. 500
6	0. 600
7	0. 700
8	0. 800
9	0. 900
10	1. 000

FIG. 4.75 (SIG1-SIG3)/2Cu CONTOURS, L/D=1, Elastic state (d=0.1mm).

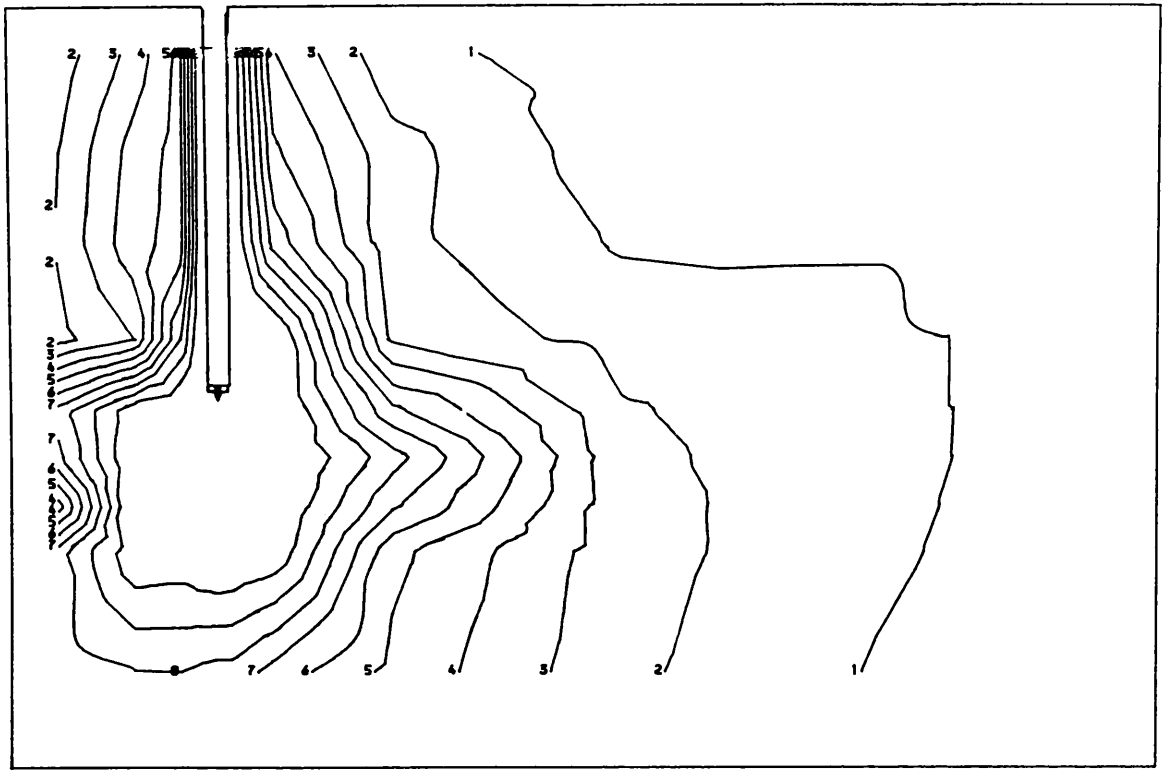

Key	
1	0.100
2	0.200
3	0.300
4	0.400
5	0.500
6	0.600
7	0.700
8	0.800
9	0.900
10	1.000

FIG. 4.76 (SIG1-SIG3)/2Cu CONTOURS, L/D=1, Plastic state (d=1.5mm).

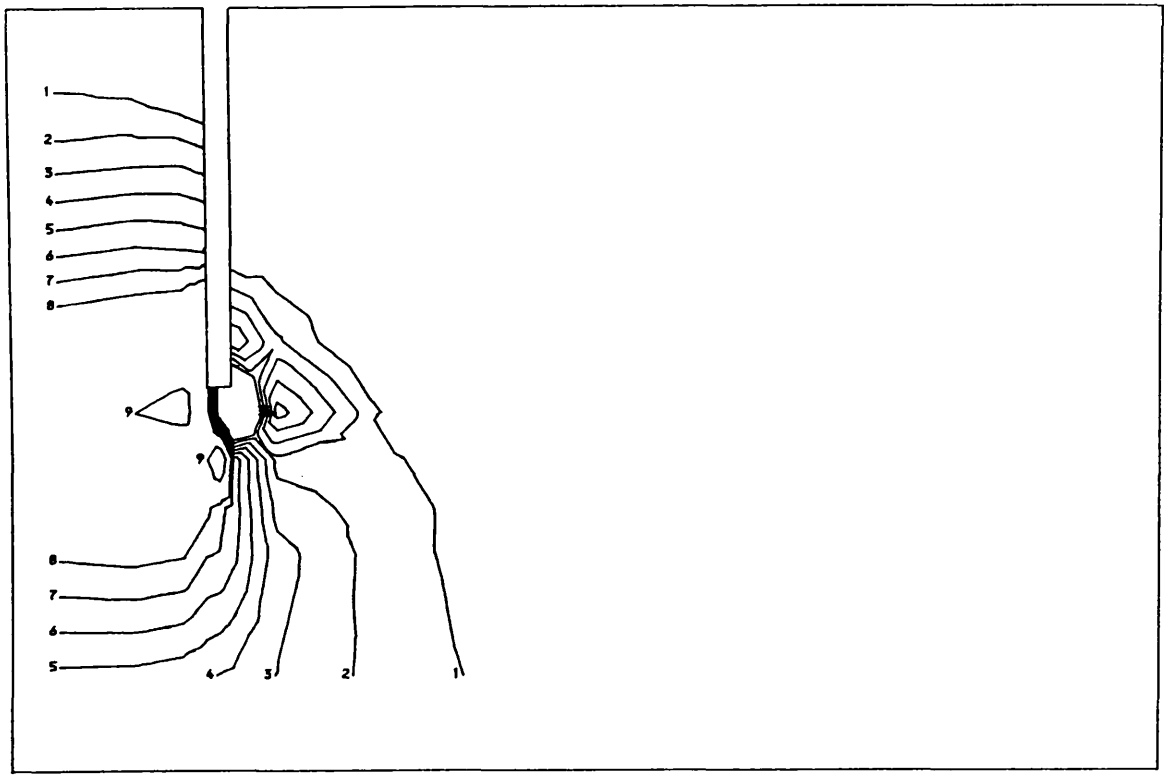

Key	N/mm2
1	0.030
2	0.040
3	0.050
4	0.060
5	0.070
6	0.080
7	0.090
8	0.100
9	0.150
10	0.200

FIG. 4.77 MEAN EFFECTIVE STRESS CONTOURS, L/D=1, Elastic state (d=0.1mm).

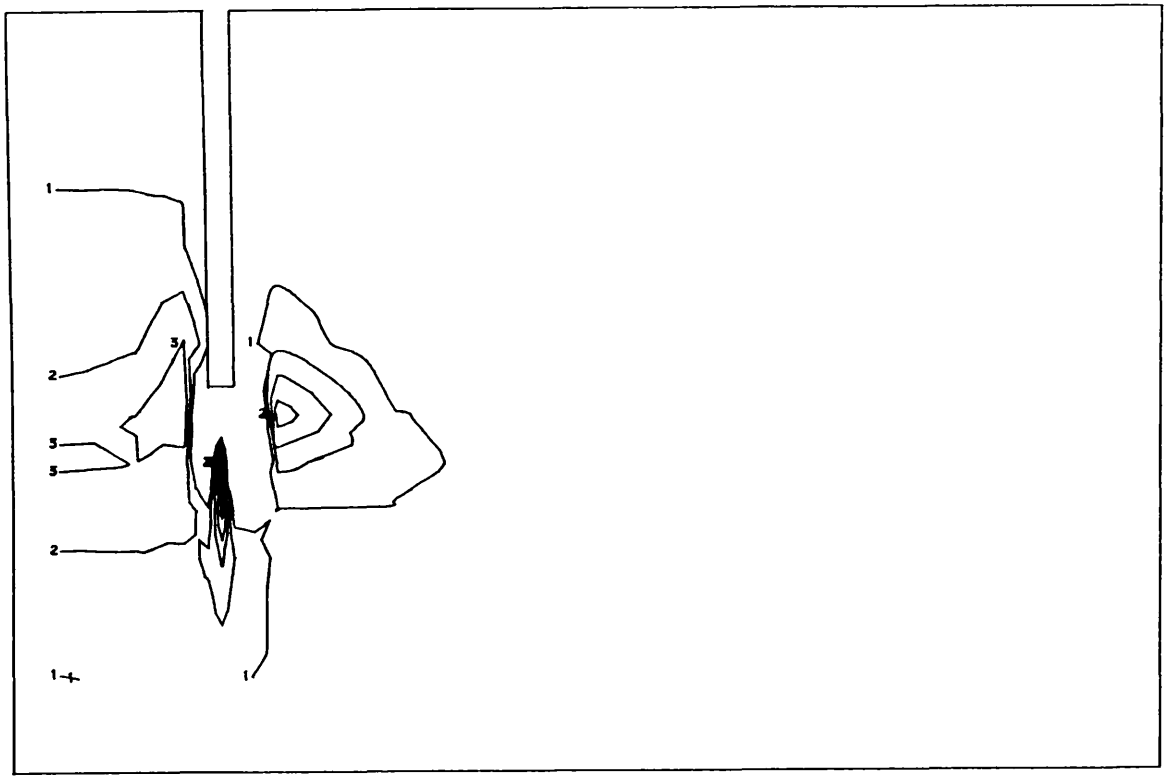

Key	N/mm2
1	0. 100
2	0. 200
3	0. 300
4	0. 400
5	0. 500
6	0. 600
7	0. 700
8	0. 800

FIG. 4.78 MEAN EFFECTIVE STRESS CONTOURS, L/D=1, Plastic stage (d=1.5mm).

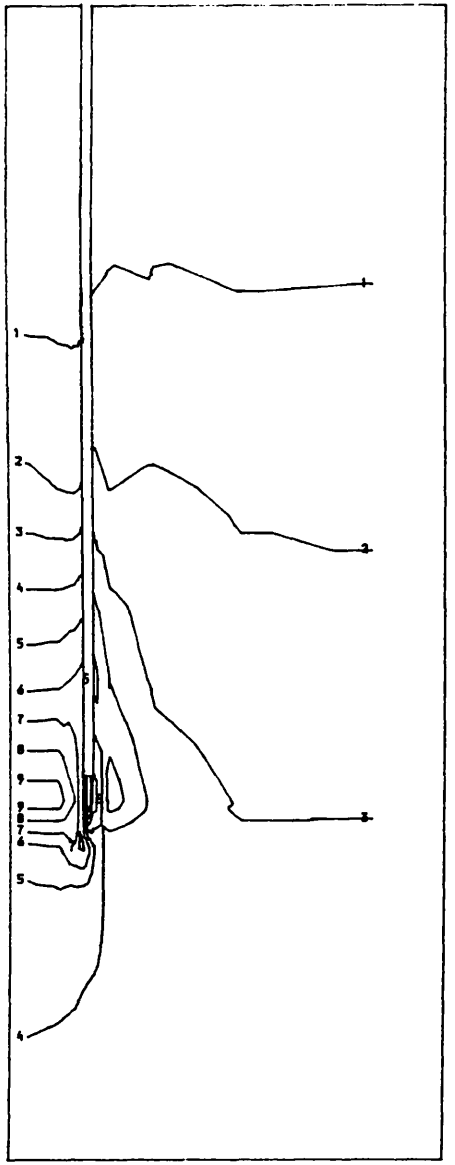

Fig. 4.79
Vertical stress contours
in elastic state (d=0.1mm)
L/D = 4

Key	N/mm2
1	0. 010
2	0. 020
3	0. 030
4	0. 040
5	0. 050
6	0. 060
7	0. 070
8	0. 080
9	0. 090
10	0. 100

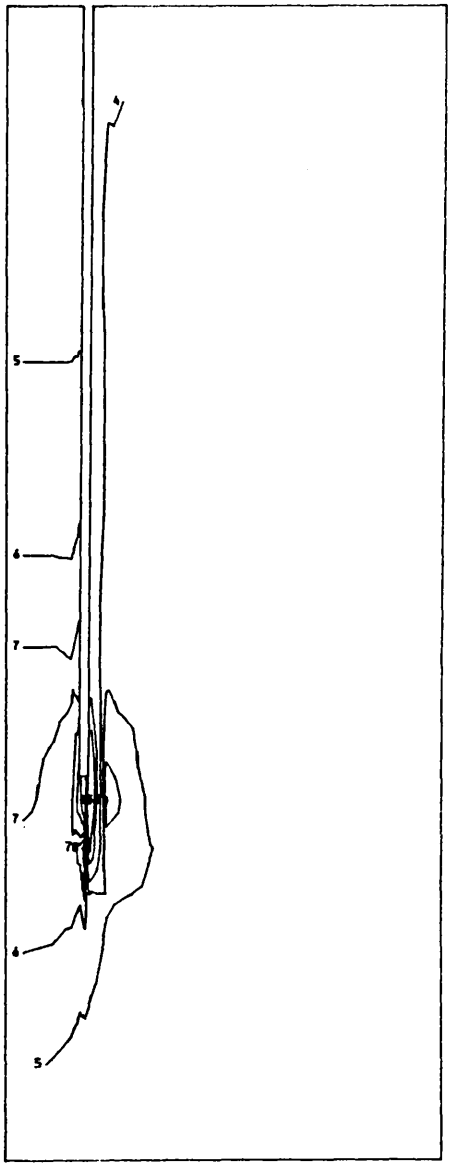

Fig. 4.80
Vertical stress contours
at ultimate state (d=1.5mm)
L/D = 4

Key	N/mm2
1	-0. 900
2	-0. 500
3	-0. 300
4	0. 000
5	0. 200
6	0. 400
7	0. 500
8	0. 600
9	0. 700
10	0. 800

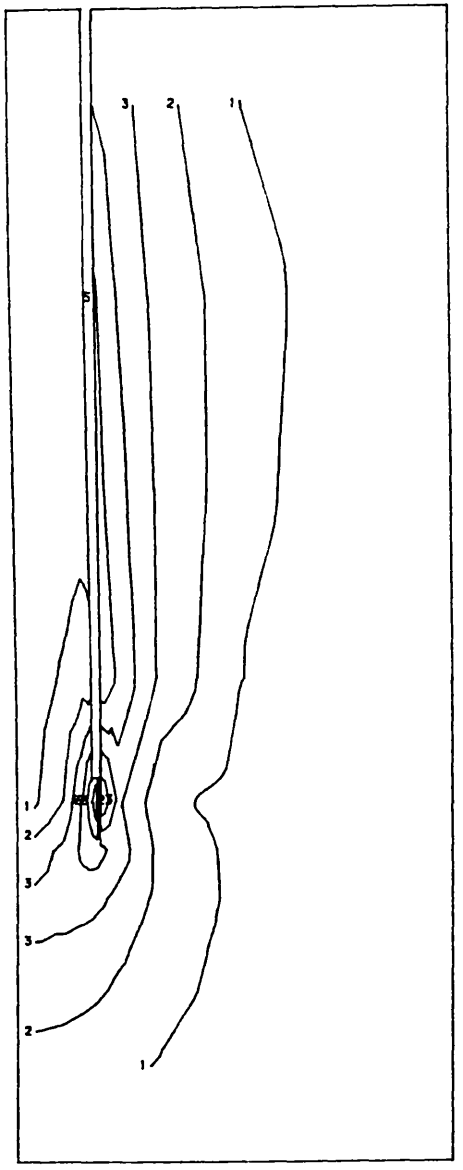

Fig. 4.81
$(\sigma 1-\sigma_3)/2Cu$ contours
in elastic state (d=0.1mm)
L/D = 4

Key	
1	0.100
2	0.200
3	0.300
4	0.400
5	0.500
6	0.600
7	0.700
8	0.800
9	0.900
10	1.000

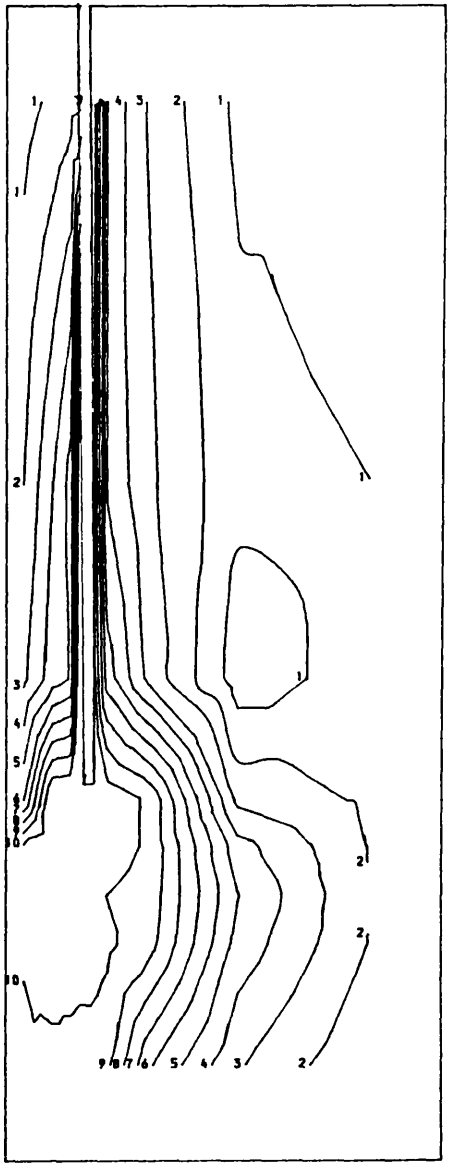

Fig. 4.82
$(\sigma 1-\sigma_3)/2Cu$ contours
at ultimate state (d=1.5mm)
L/D = 4

Key	
1	0.100
2	0.200
3	0.300
4	0.400
5	0.500
6	0.600
7	0.700
8	0.800
9	0.900
10	1.000

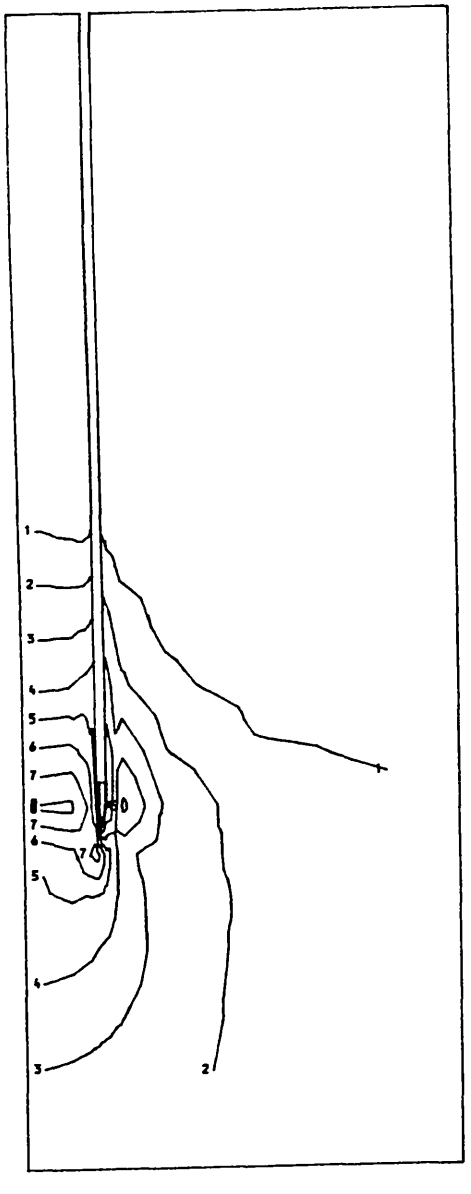

Fig. 4.83
Mean effective stress contours in elastic state (d=0.1mm)
L/D = 4

Key	N/mm2
1	0.030
2	0.040
3	0.050
4	0.060
5	0.070
6	0.080
7	0.090
8	0.100

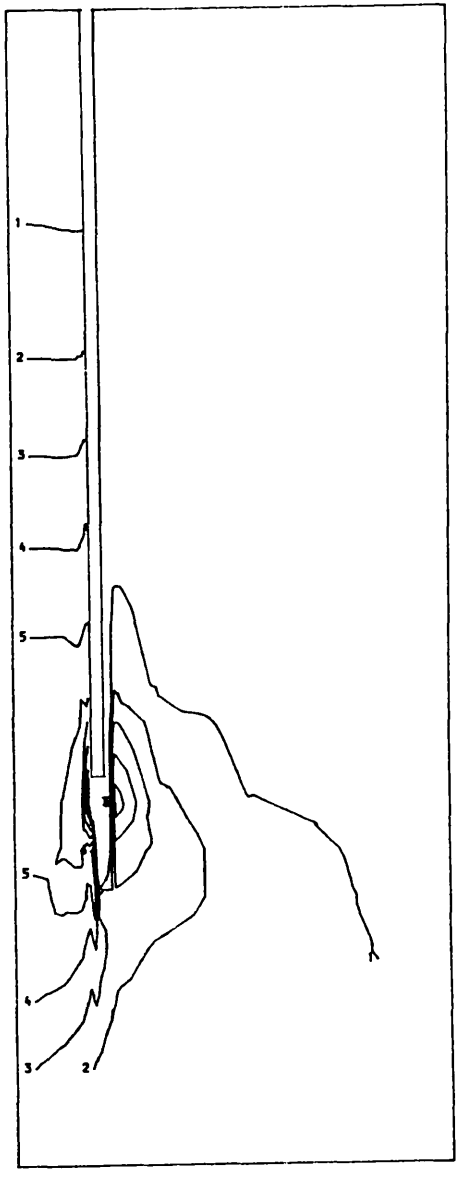

Fig. 4.84
Mean effective stress contours at ultimate state (d=1.5mm)
L/D = 4

Key	N/mm2
1	0.100
2	0.200
3	0.300
4	0.400
5	0.500
6	0.600
7	0.700
8	0.800

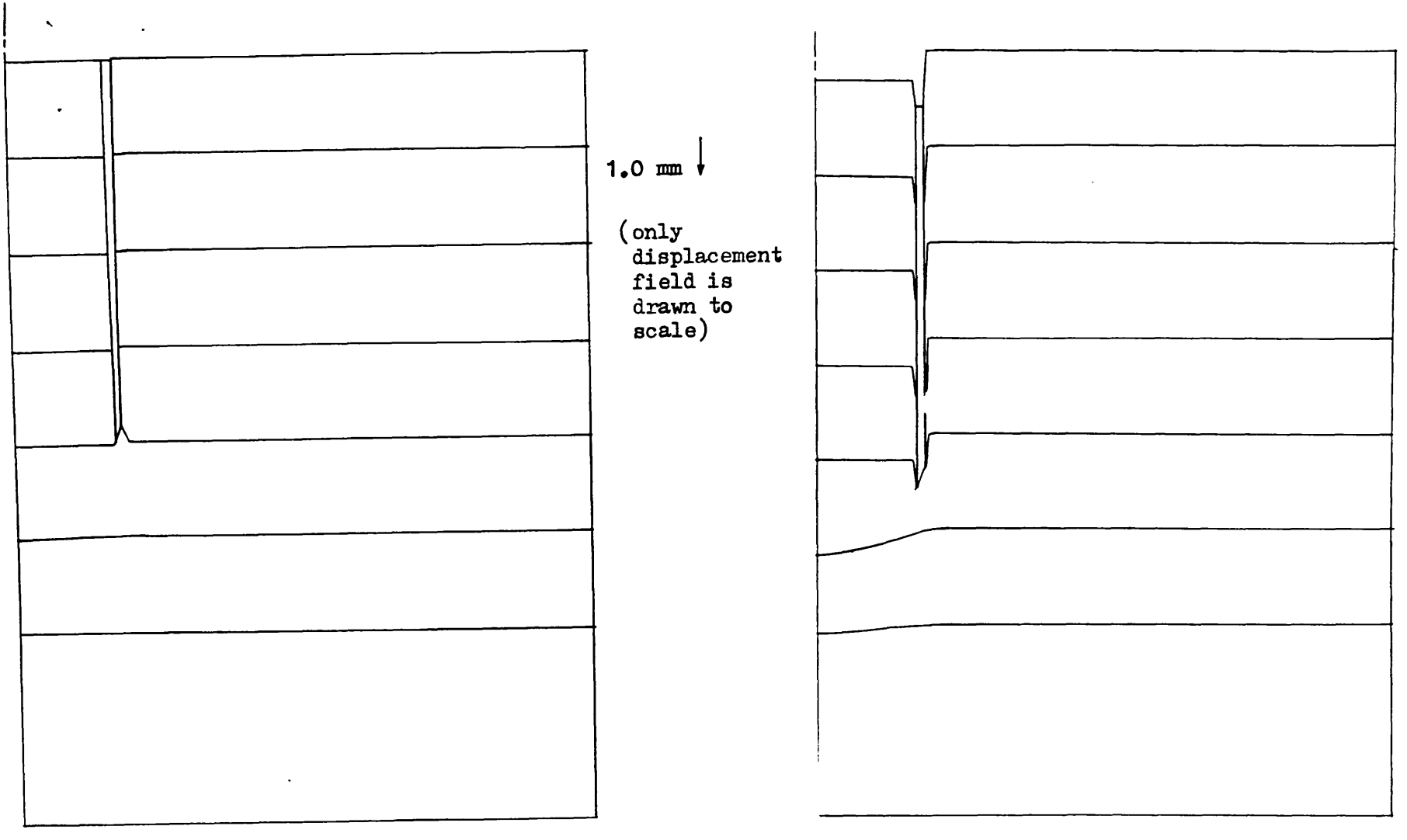

d = 0.1 mm Cuttig shoe angle = 20

d = 1.5 mm Cutting shoe angle = 20

Fig. 4.85 Displacement field in the vicinity of the sampling tube

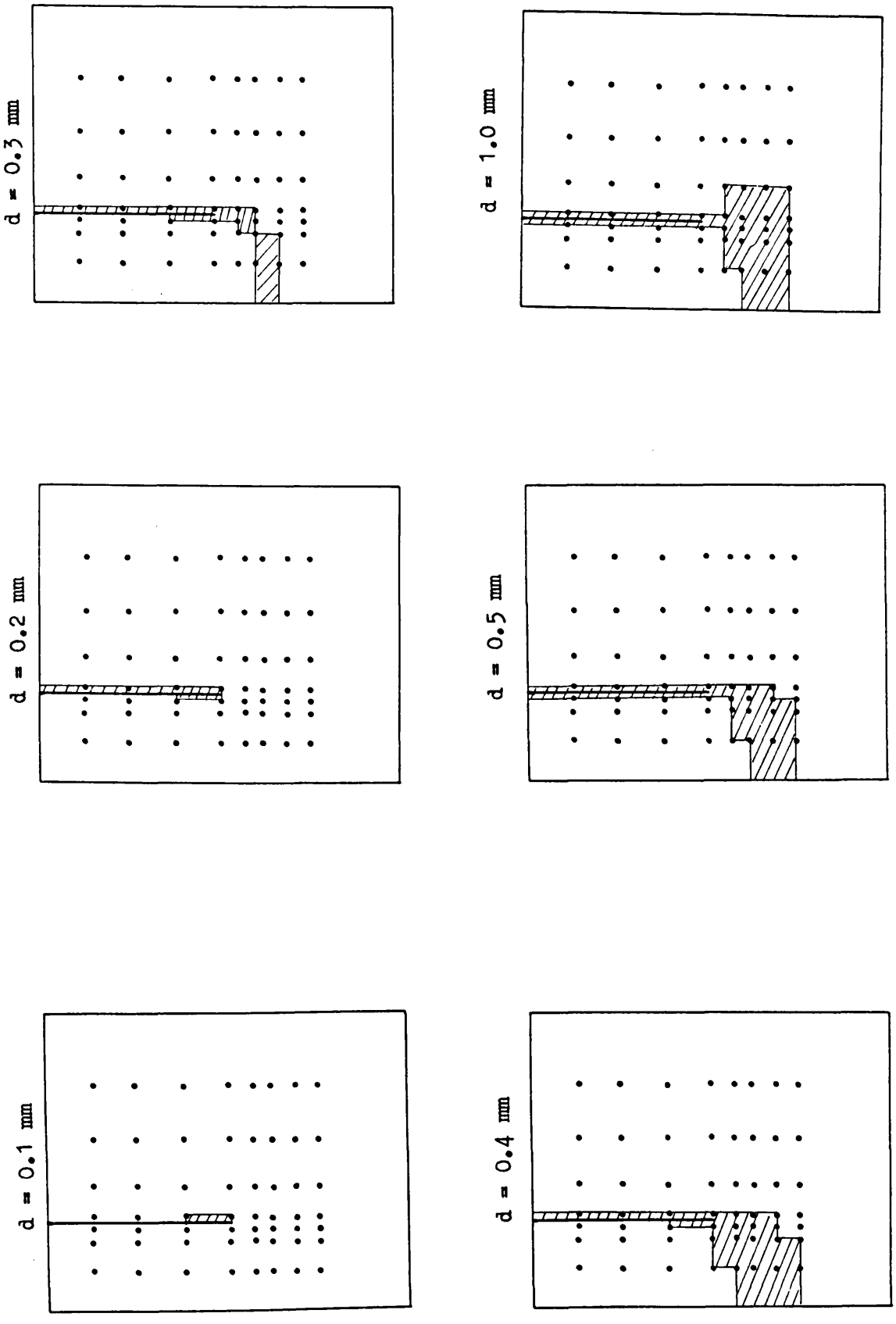

Fig. 4.86 Growth of failure zones at various stages of penetration , Cutting shoe angle = 20°

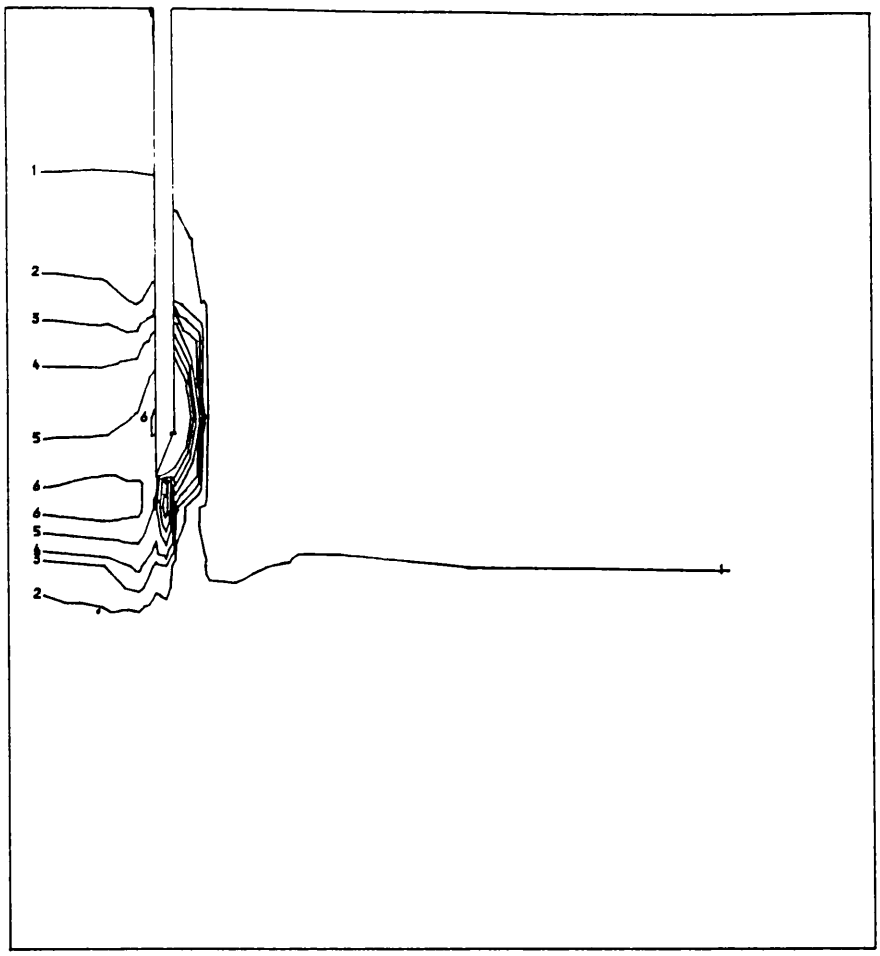

Fig. 4.87
Vertical stress contours in elastic state (d=0.1mm)
Cutting shoe angle= 20°

Key:		
1	0.02	N/mm2
2	0.04	
3	0.05	
4	0.06	
5	0.08	
6	0.1	
7	0.12	
8	0.14	

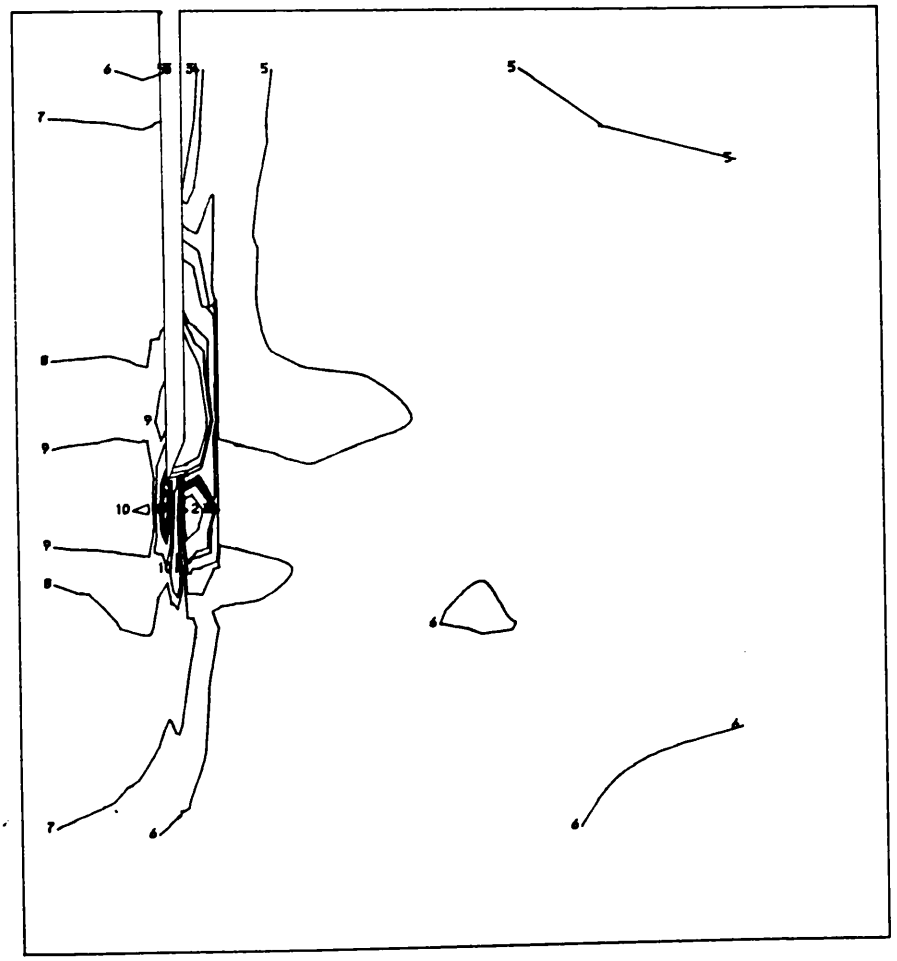

Fig. 4.88
Vertical stress contours at ultimate state (d=1.5mm)
Cutting shoe angle= 20°

Key:		
1	-0.6	N/mm2
2	-0.3	
3	-0.08	
4	-0.05	
5	0.01	
6	0.05	
7	0.1	
8	0.3	
9	0.4	
10	0.6	

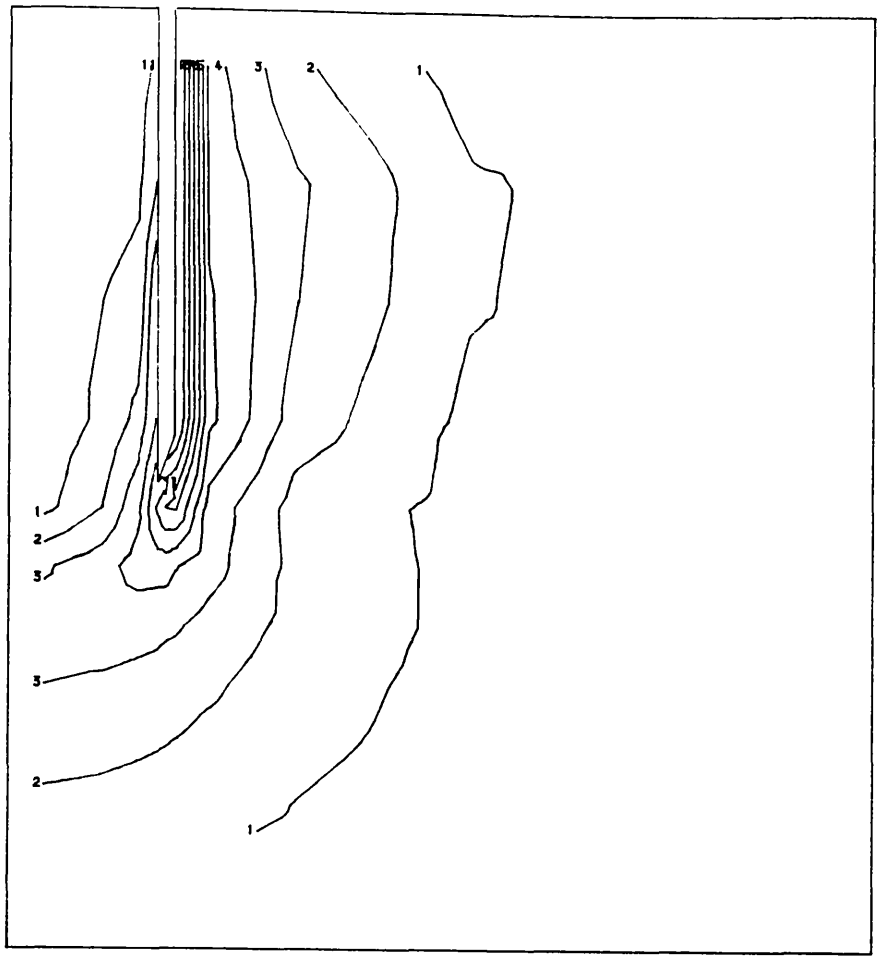

Fig. 4.89
$(\sigma 1-\sigma 3)/2Cu$ contours
in elastic state
(d=0.1mm)
Cutting shoe angle= 20°

Key:	
1	0.1
2	0.2
3	0.3
4	0.4
5	0.5
6	0.6
7	0.7
8	0.8
9	0.9
10	1.0

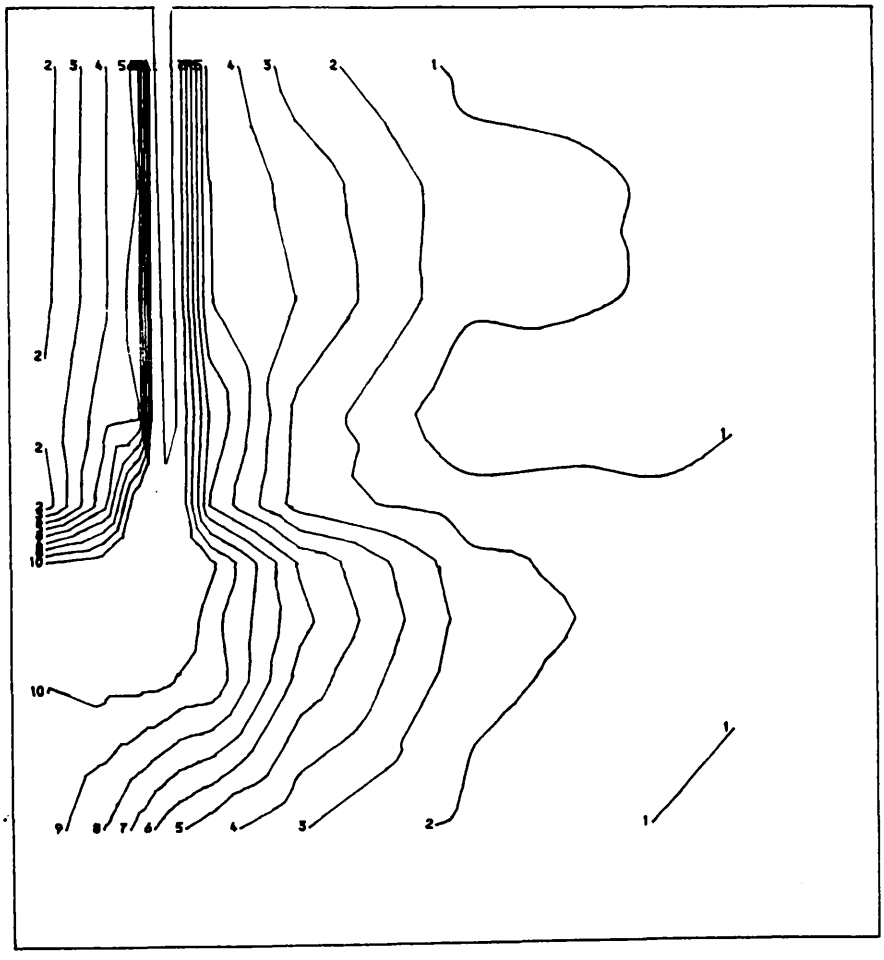

Fig. 4.90
$(\sigma 1-\sigma 3)/2Cu$ contours
at ultimate state
(d=1.5mm)
Cutting shoe angle= 20°

Key:	
1	0.1
2	0.2
3	0.3
4	0.4
5	0.5
6	0.6
7	0.7
8	0.8
9	0.9
10	1.0

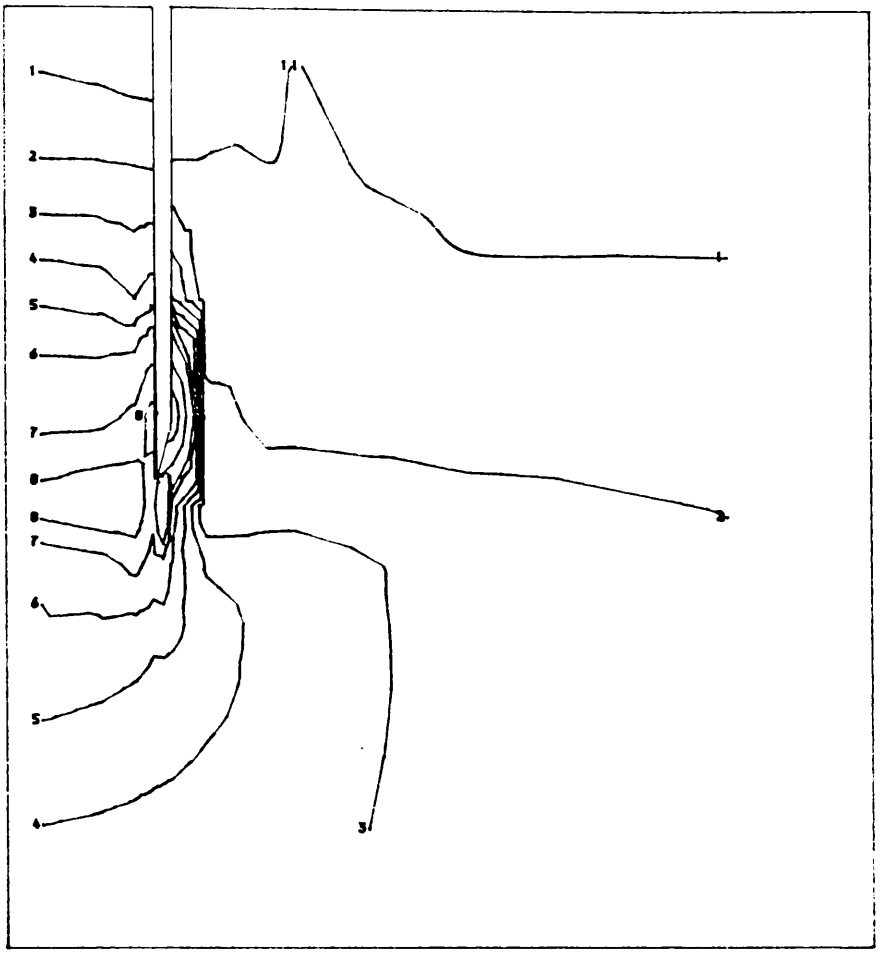

Fig. 4.91
Mean effective stress contours in elastic state (d=0.1mm)
Cutting shoe angle= 20°

Key:		
1	0.01	N/mm2
2	0.02	
3	0.03	
4	0.04	
5	0.05	
6	0.06	
7	0.08	
8	0.10	
9	0.15	
10	0.20	

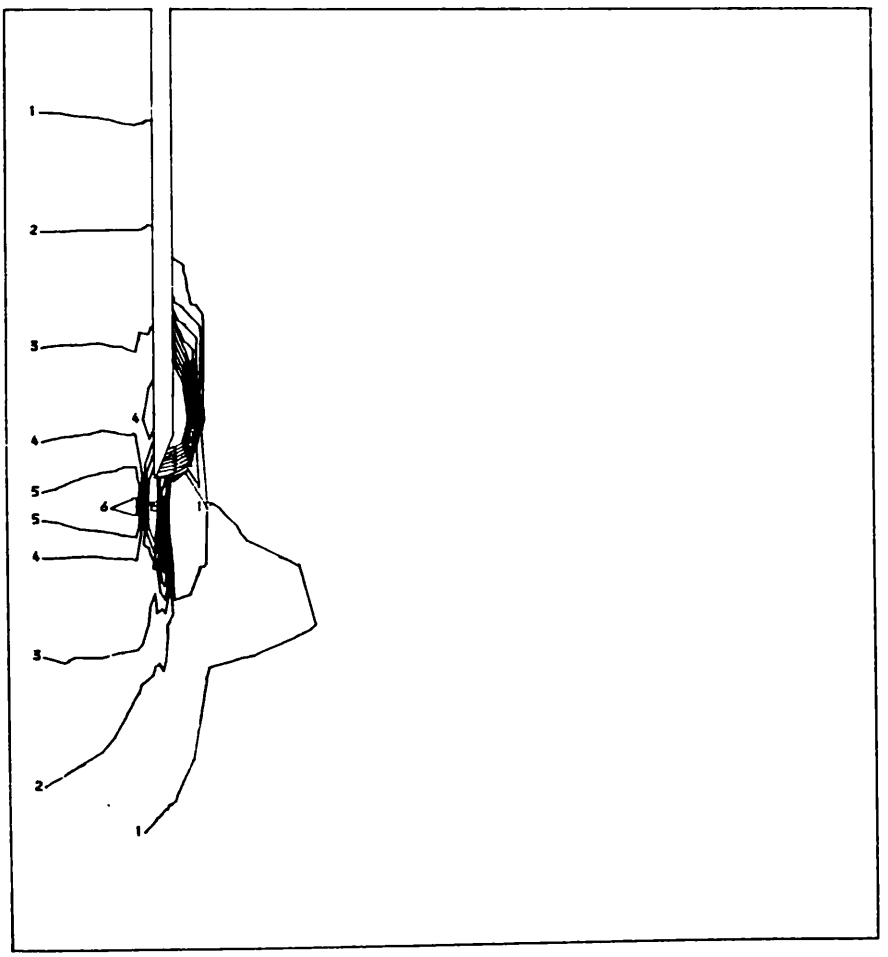

Fig. 4.92
Mean effective stress contours at ultimate state (d=1.5mm)
Cutting shoe angle= 20°

Key:		
1	0.1	N/mm2
2	0.2	
3	0.3	
4	0.4	
5	0.5	
6	0.6	
7	0.7	
8	0.8	
9	0.9	
10	1.0	

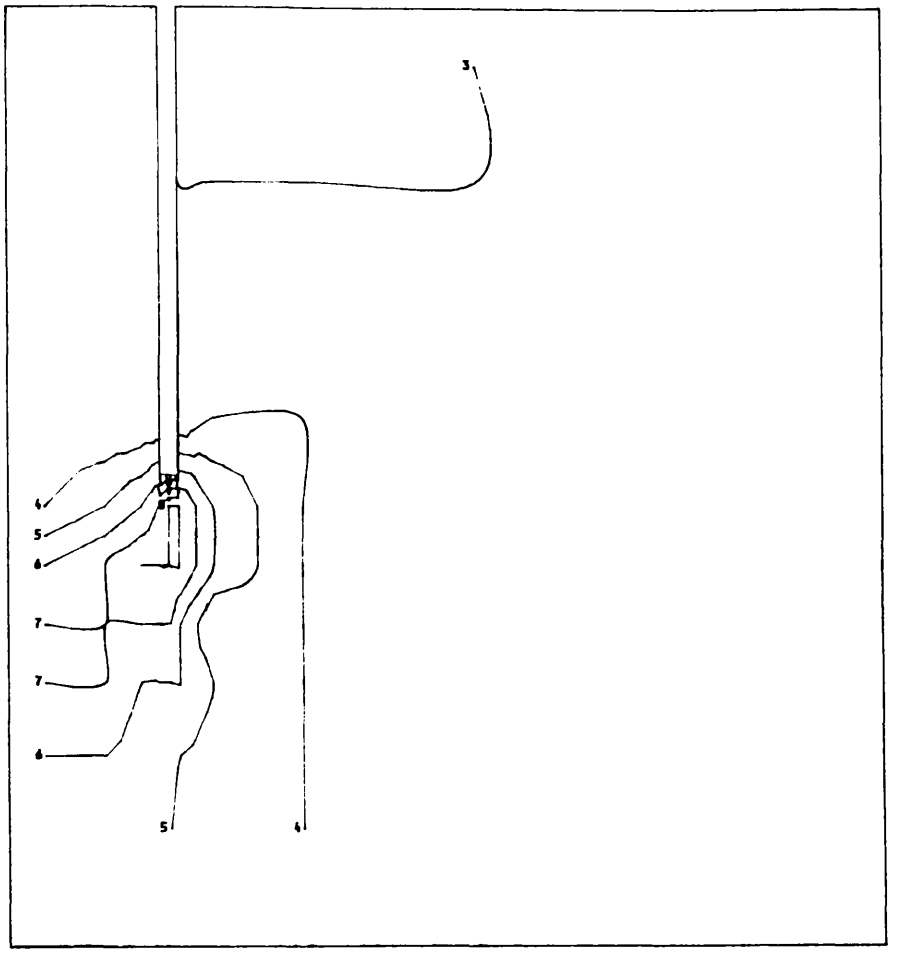

Fig. 4.93
Effective vertical stress contours
OCR = 10
Elastic state

Key:

1	0.08 N/mm2
2	0.09
3	0.1
4	0.11
5	0.12
6	0.13
7	0.14
8	0.15

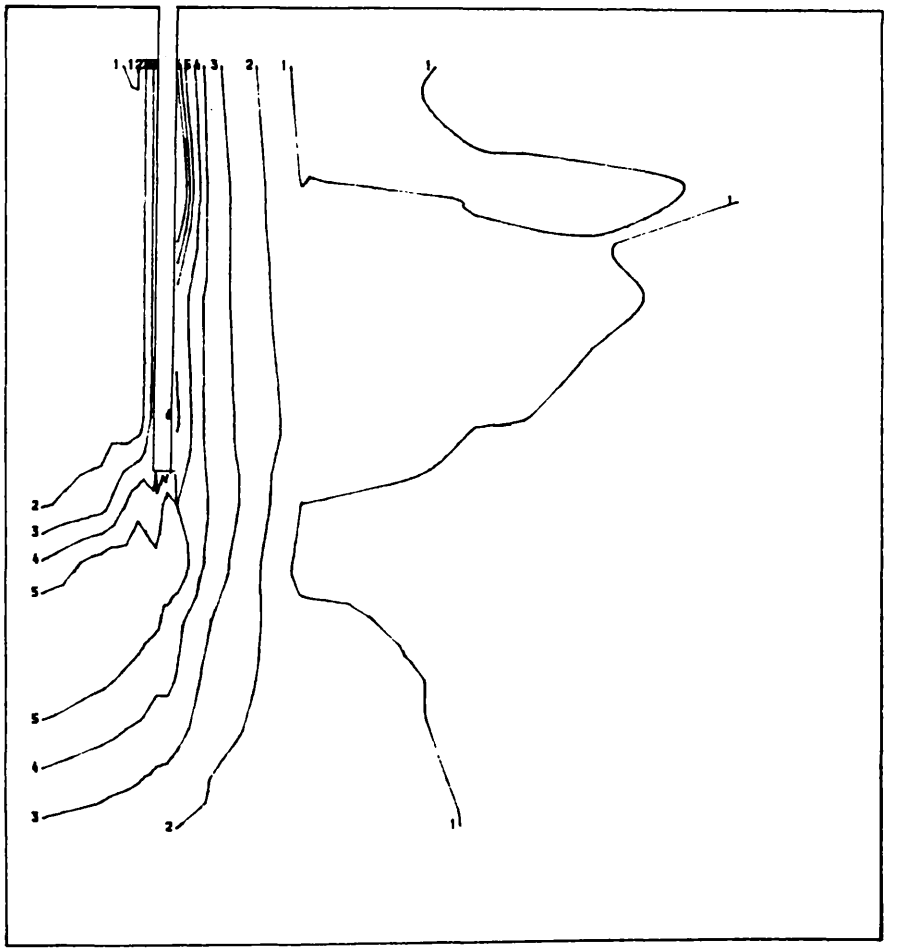

Fig. 4.94
Effective vertical stress contours
OCR = 10
Plastic state

Key:

1	0.1 N/mm2
2	0.2
3	0.3
4	0.4
5	0.5
6	0.6
7	0.65

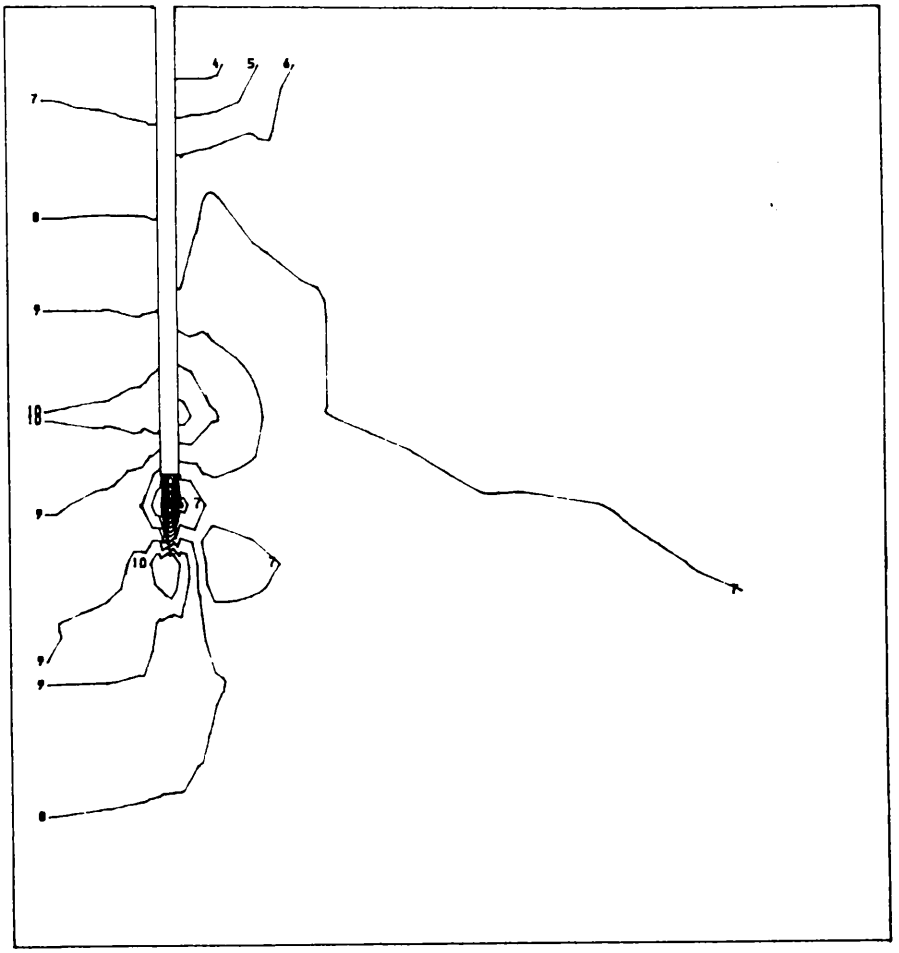

Fig. 4.95
Pore water pressure contours , OCR = 10
Elastic state

Key:	
1	-0.2 N/mm2
2	-0.18
3	-0.16
4	-0.14
5	-0.12
6	-0.10
7	-0.08
8	-0.06
9	-0.04
10	-0.02

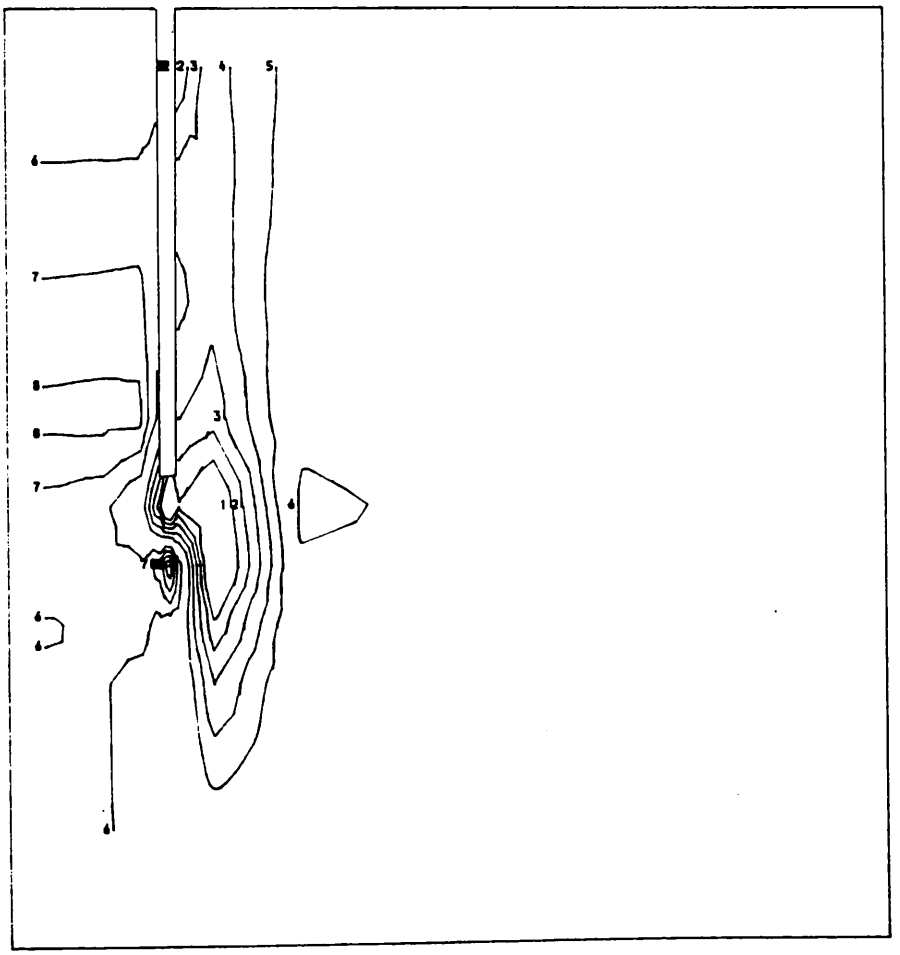

Fig. 4.96
Pore water pressure contours , OCR = 10
Plastic state

Key:	
1	-1.3 N/mm2
2	-1.0
3	-0.8
4	-0.6
5	-0.4
6	-0.2
7	0.2
8	0.4
9	0.6
10	0.7

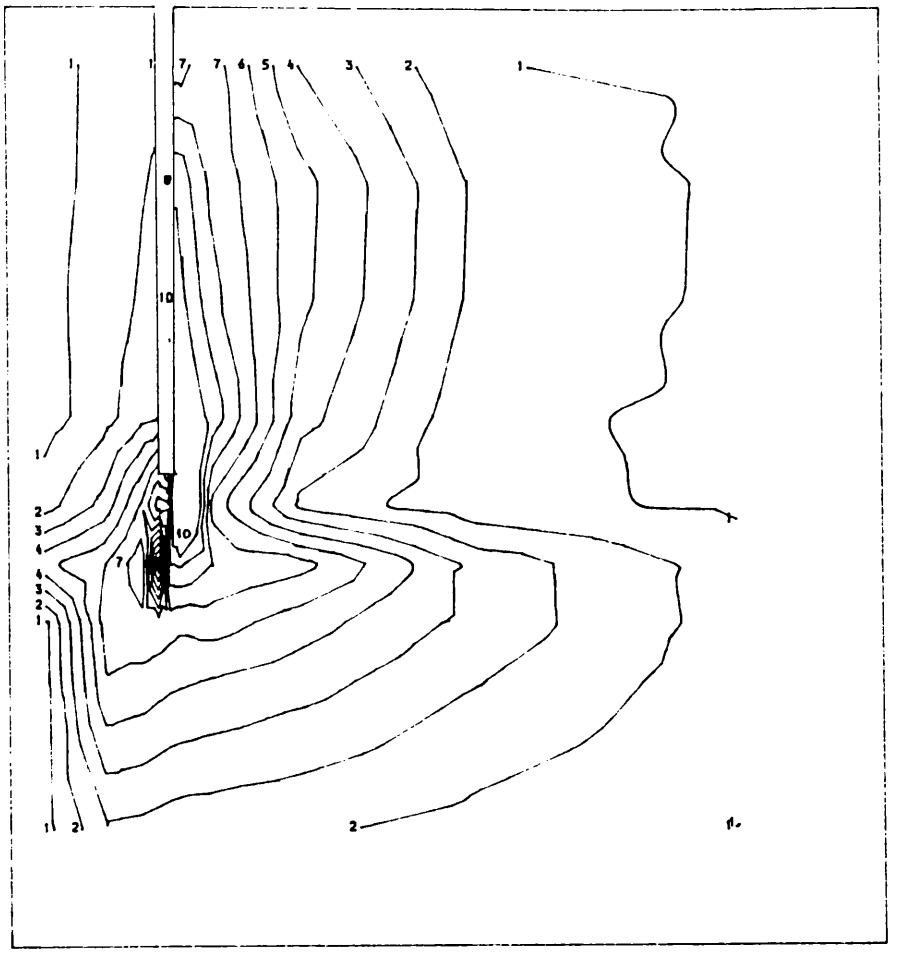

Fig. 4.97
Deviator stress contours , CCR = 10
Elastic state

Key:

1	0.01 N/mm2
2	0.02
3	0.03
4	0.04
5	0.05
6	0.06
7	0.07
8	0.08
9	0.09
10	0.1

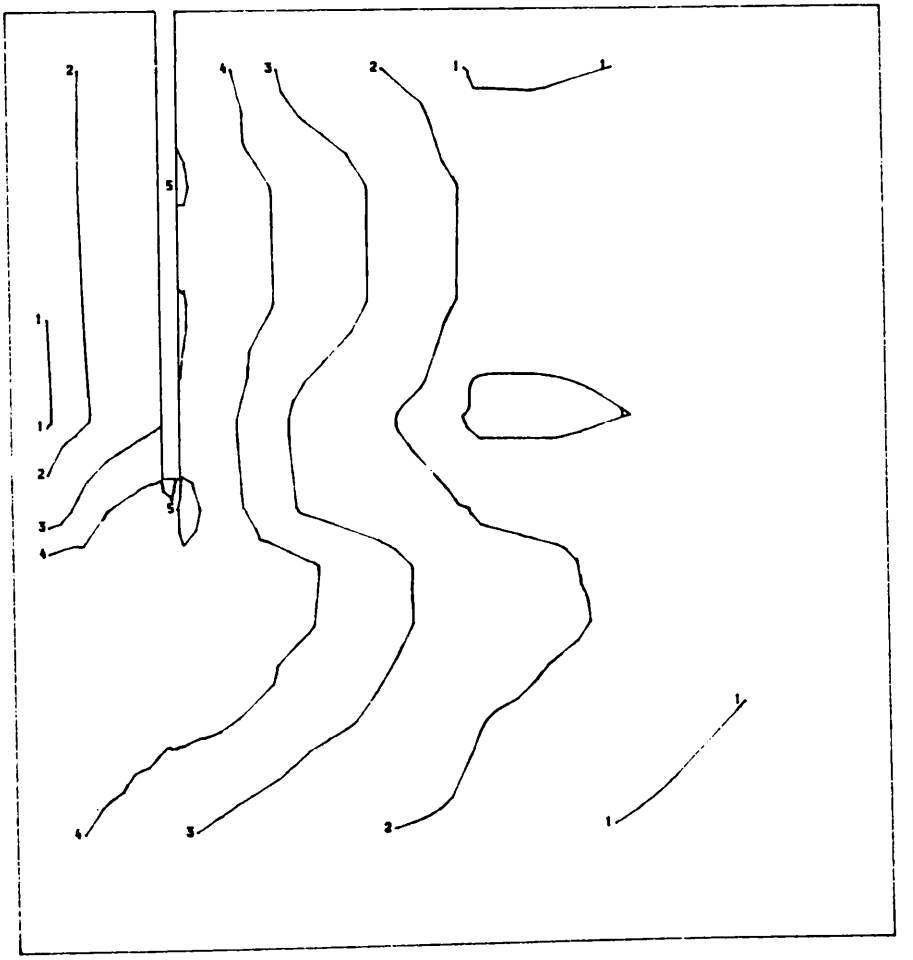

Fig. 4.98
Deviator stress contours , CCR = 10
Plastic state

Key:

1	0.05 N/mm2
2	0.1
3	0.2
4	0.3
5	0.4
6	0.45

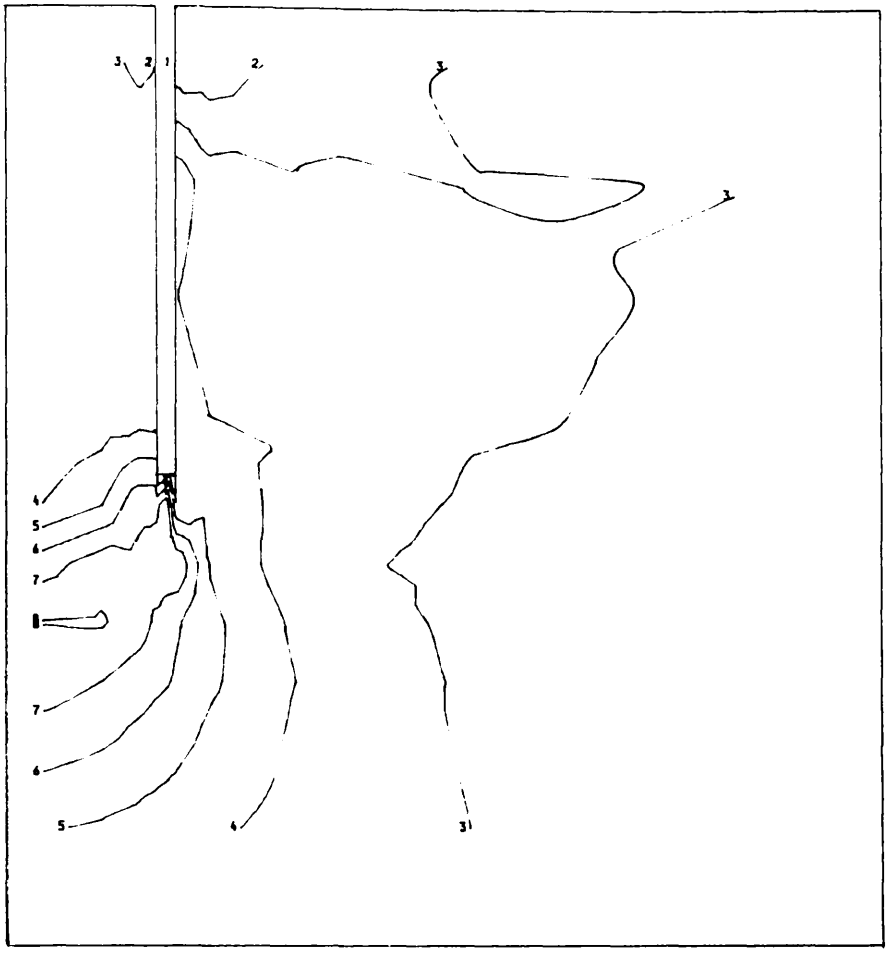

Fig. 4.99
Effective vertical stress contours
OCR = 1.5
Elastic state

Key:

1	0.08 N/mm2
2	0.09
3	0.1
4	0.11
5	0.12
6	0.13
7	0.14
8	0.15

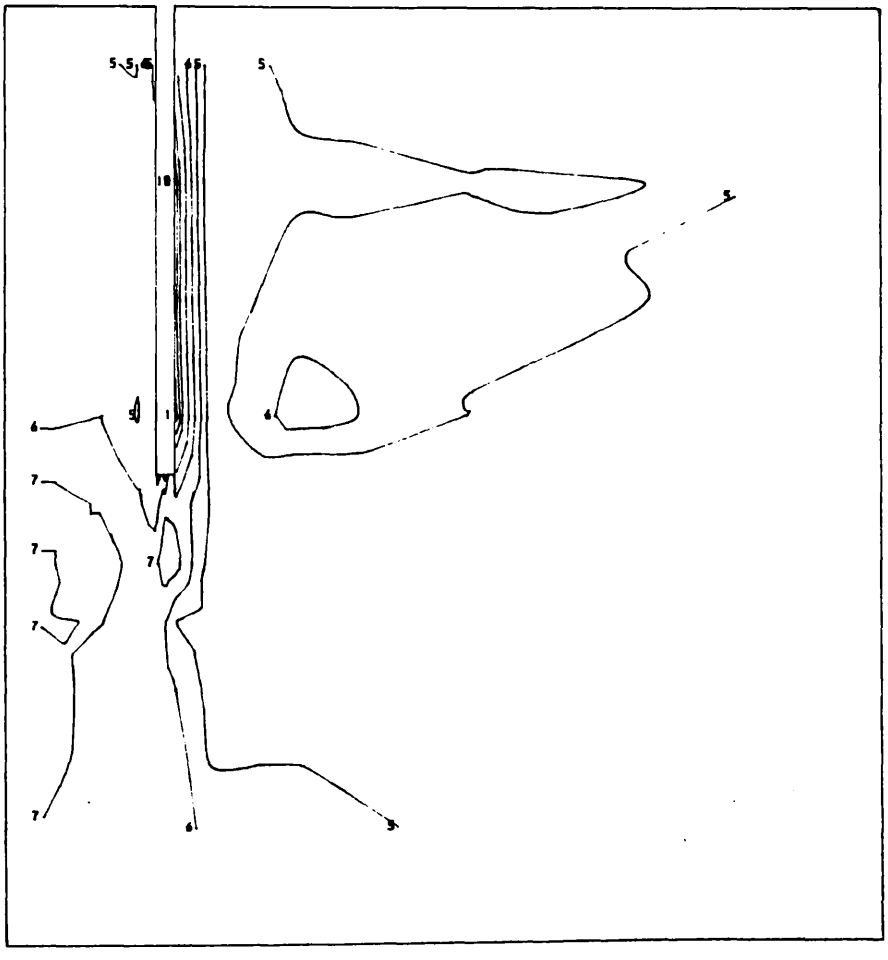

Fig. 4.100
Effective vertical stress contours
OCR = 1.5

Key:

1	0.02 N/mm2
2	0.04
3	0.06
4	0.08
5	0.1
6	0.12
7	0.14
8	0.16
9	0.18
10	0.19

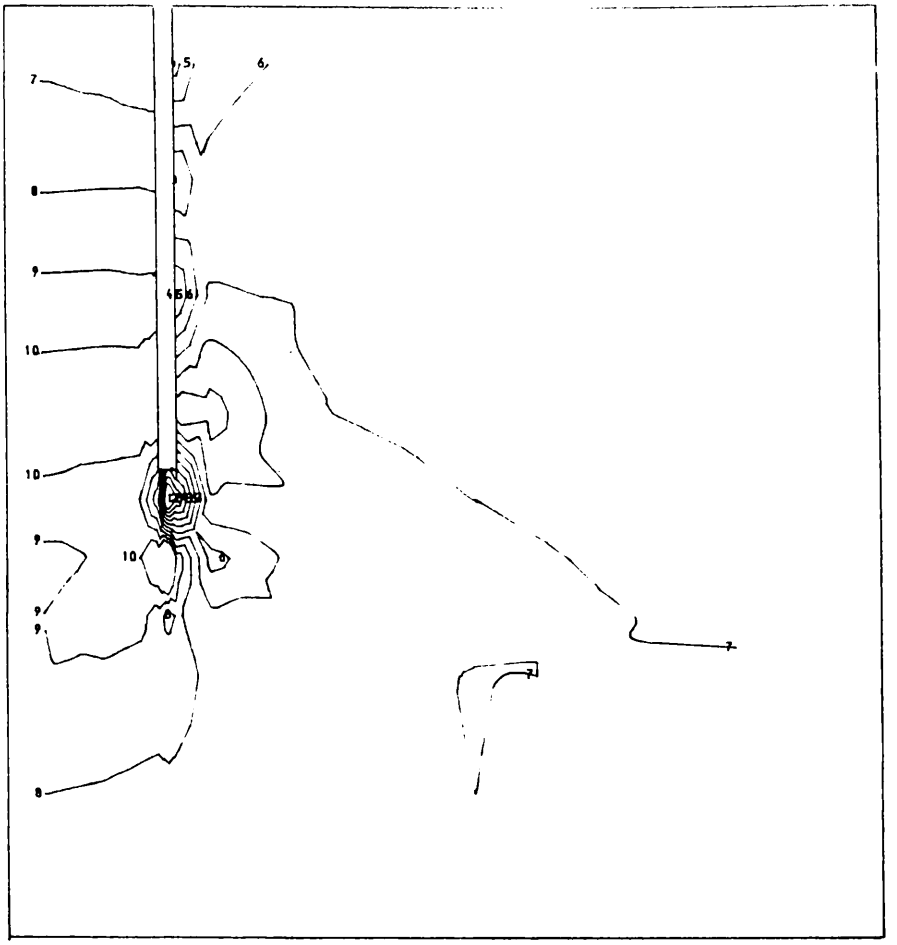

Fig. 4.101
Pore water pressure contours , OCR = 1.5
Elastic state

Key:	
1	-0.2 N/mm2
2	-0.18
3	-0.16
4	-0.14
5	-0.12
6	-0.10
7	-0.08
8	-0.06
9	-0.04
10	-0.02

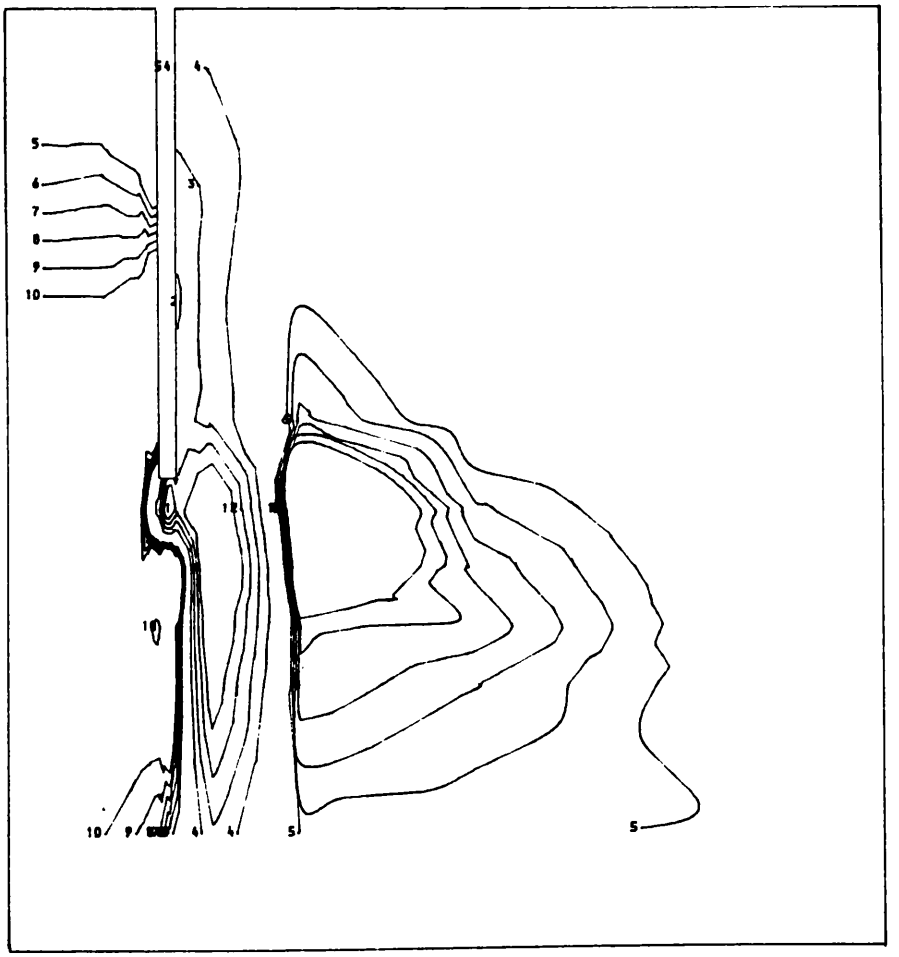

Fig. 4.102
Pore water pressure contours , OCR = 1.5
Plastic state

Key:	
1	-0.5 N/mm2
2	-0.4
3	-0.3
4	-0.2
5	0.0
6	0.02
7	0.04
8	0.06
9	0.08
10	0.1

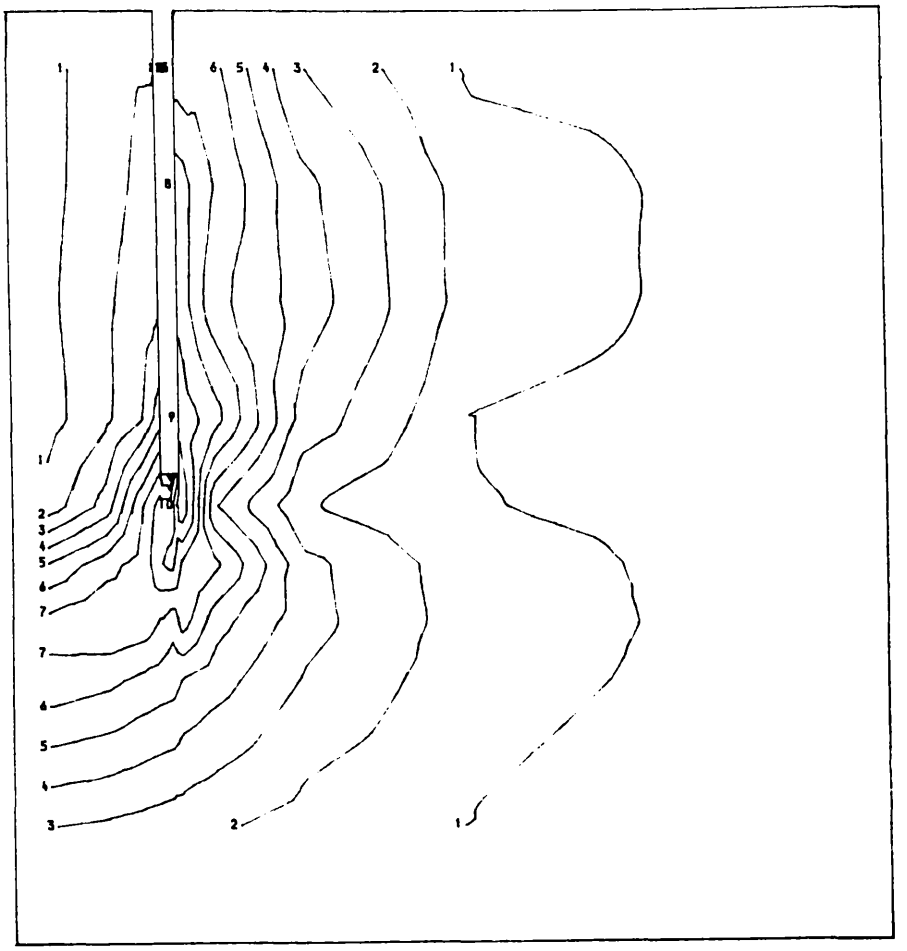

Fig. 4.103
Deviator stress
contours , OCR = 1.5
Elastic state

Key:		
1	0.01	N/mm2
2	0.02	
3	0.03	
4	0.04	
5	0.05	
6	0.06	
7	0.07	
8	0.08	
9	0.09	
10	0.1	

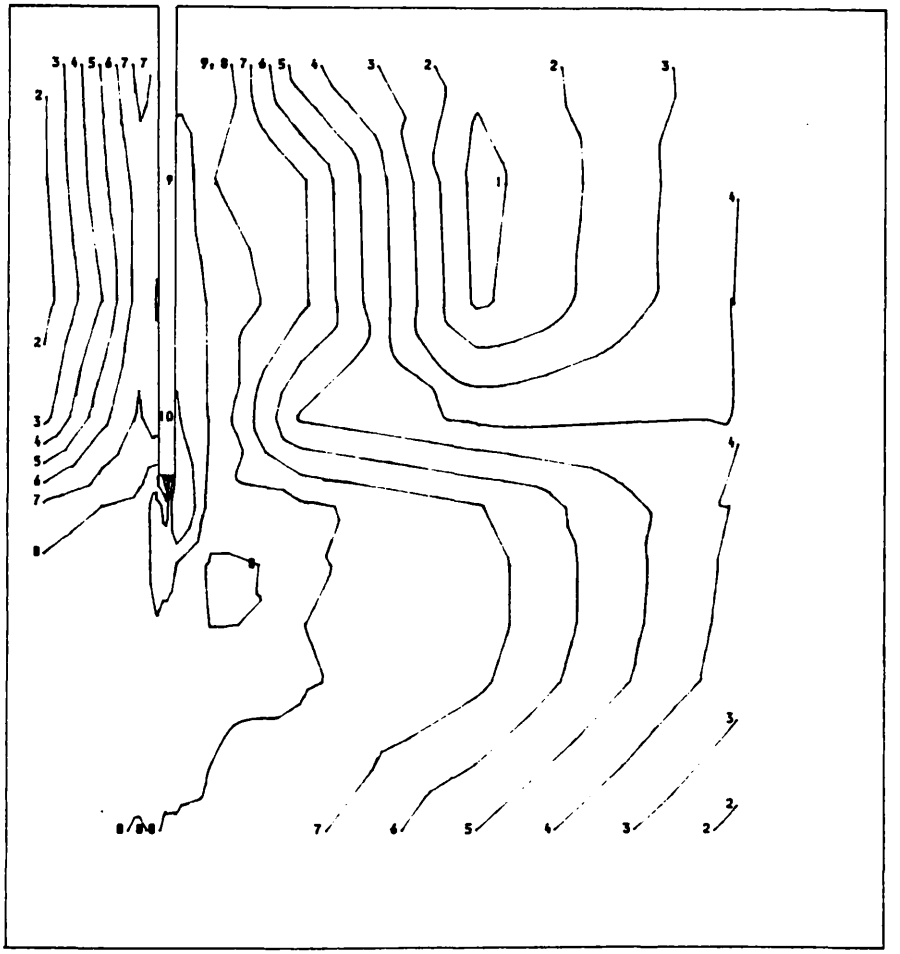

Fig. 4.104
Deviator stress
contours , OCR = 1.5

Key:		
1	0.01	N/mm2
2	0.02	
3	0.03	
4	0.04	
5	0.05	
6	0.06	
7	0.07	
8	0.08	
9	0.09	
10	0.1	

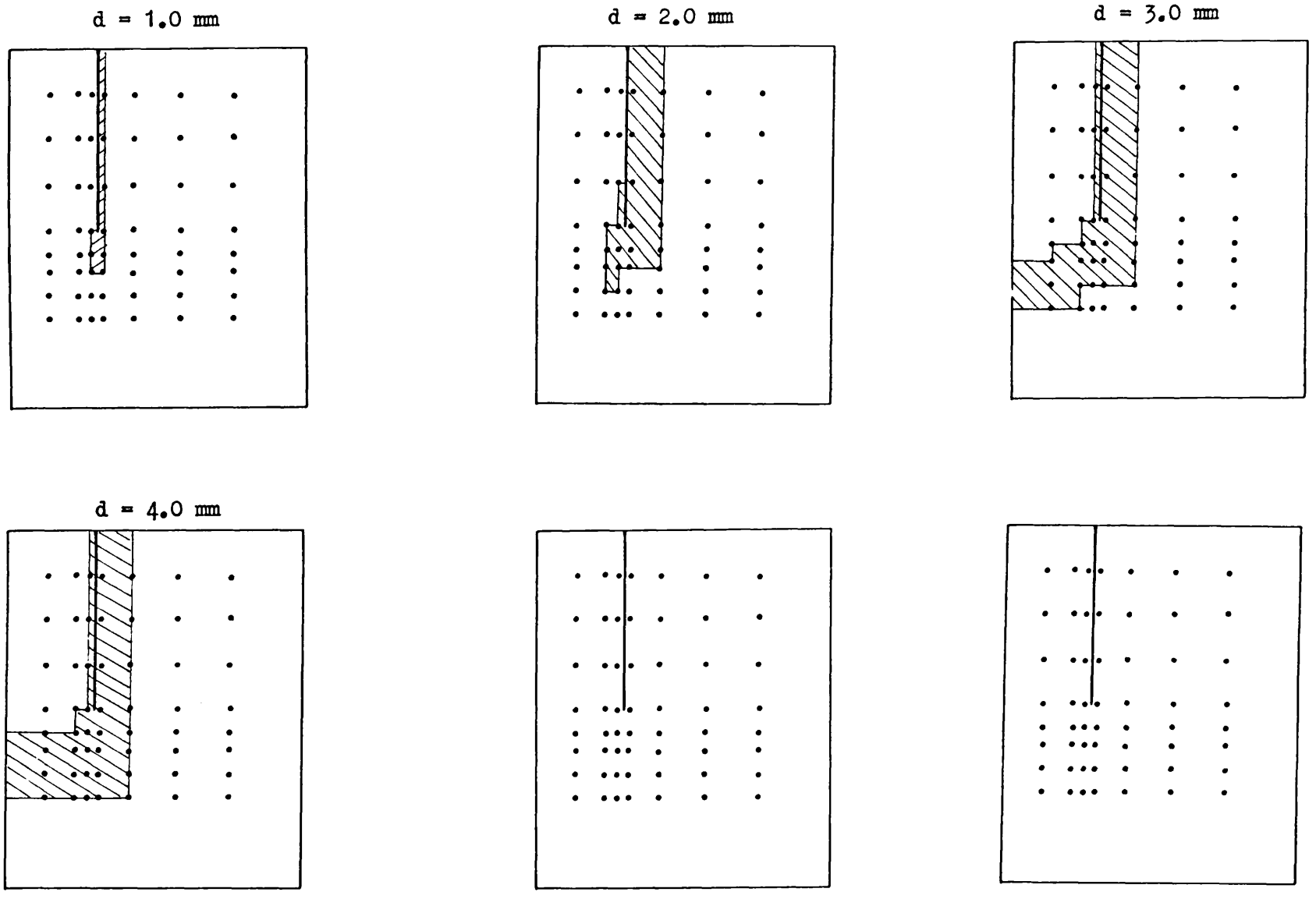

Fig. 4.105 Growth of failure zones at various stages of penetration , OCR = 1.5

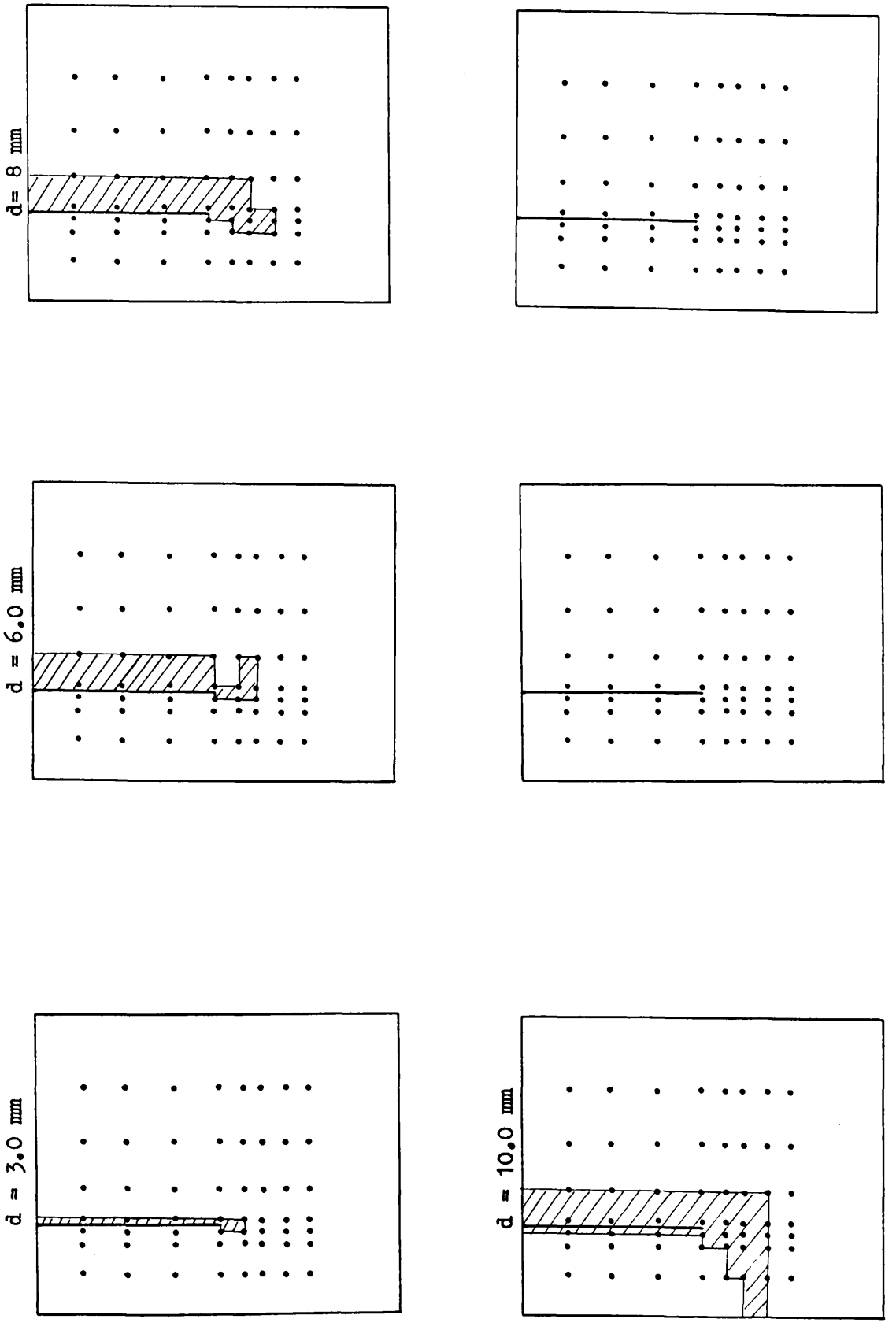

Fig. 4.106 Growth of failure zones at various stages of penetration , OCR = 10.0

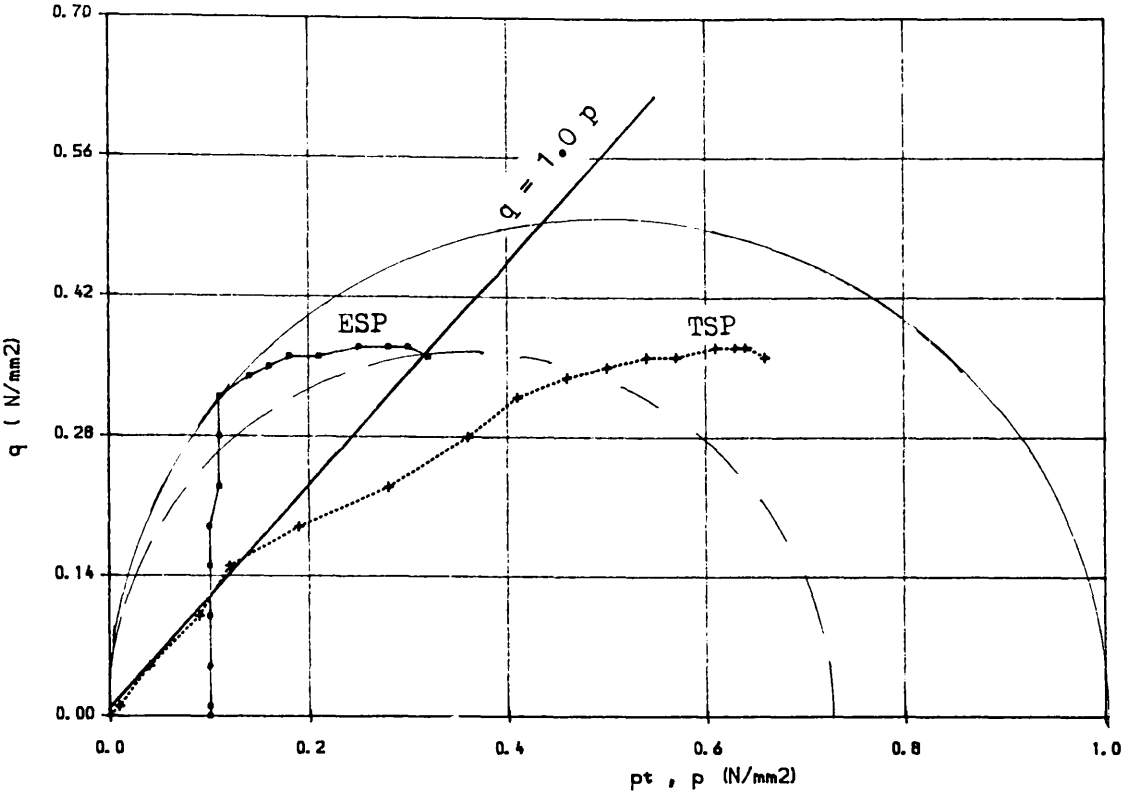

FIG. 4.107 STRESS PATHS FOR OC SOIL , ELEMENT 47
(Undrained conditions)

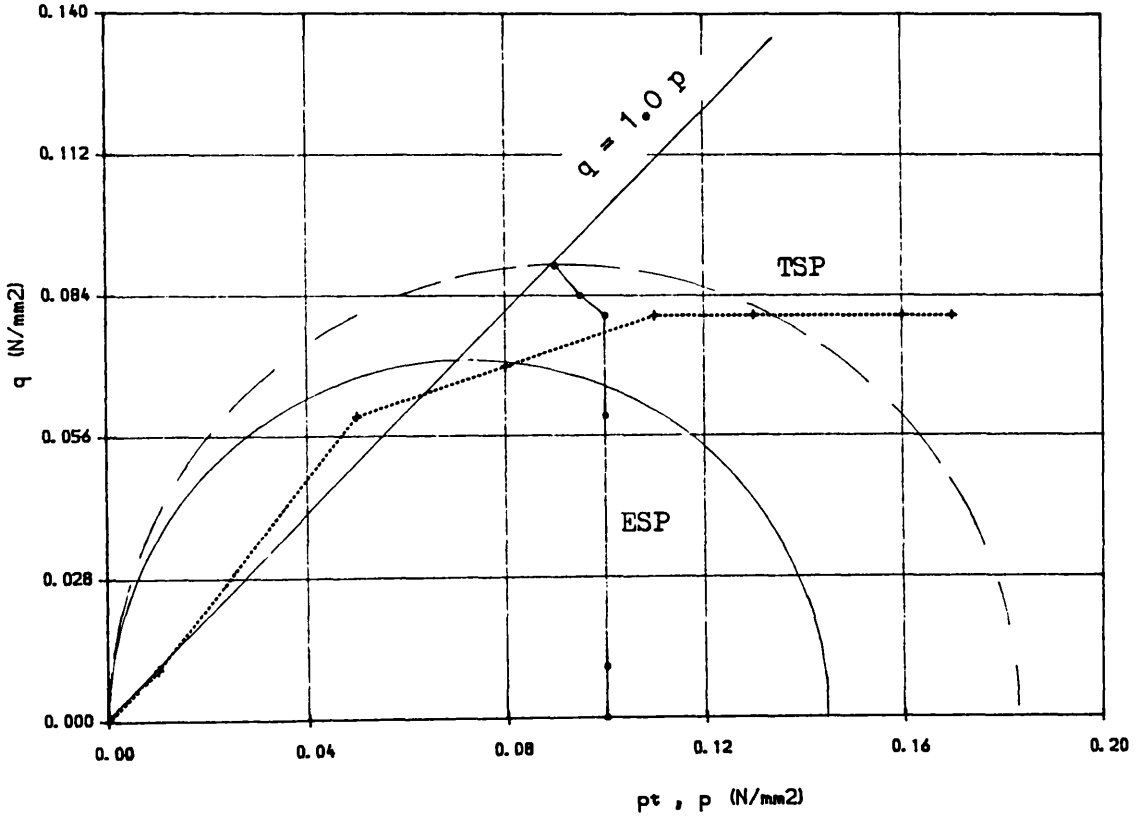

FIG. 4.108 STRESS PATHS FOR NC SOIL , ELEMENT 47
(Undrained conditions)

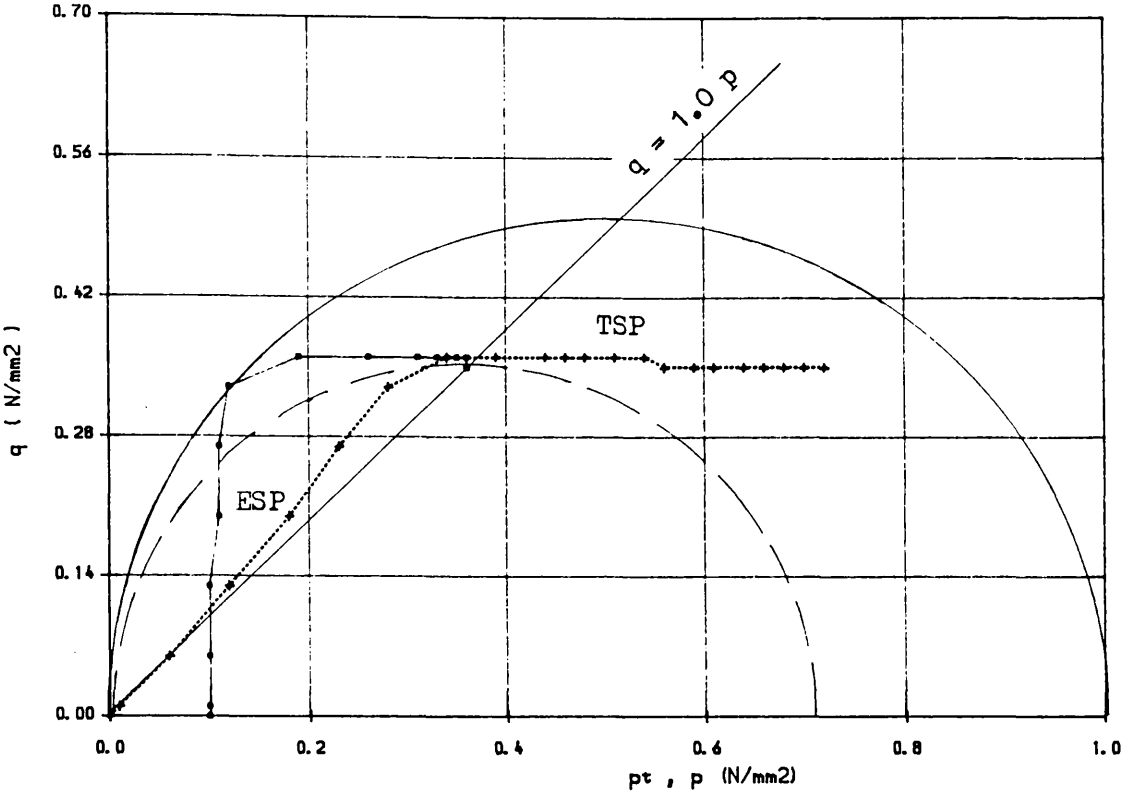

FIG. 4.109 STRESS PATHS FOR OC SOIL , ELEMENT 57
(Undrained conditions)

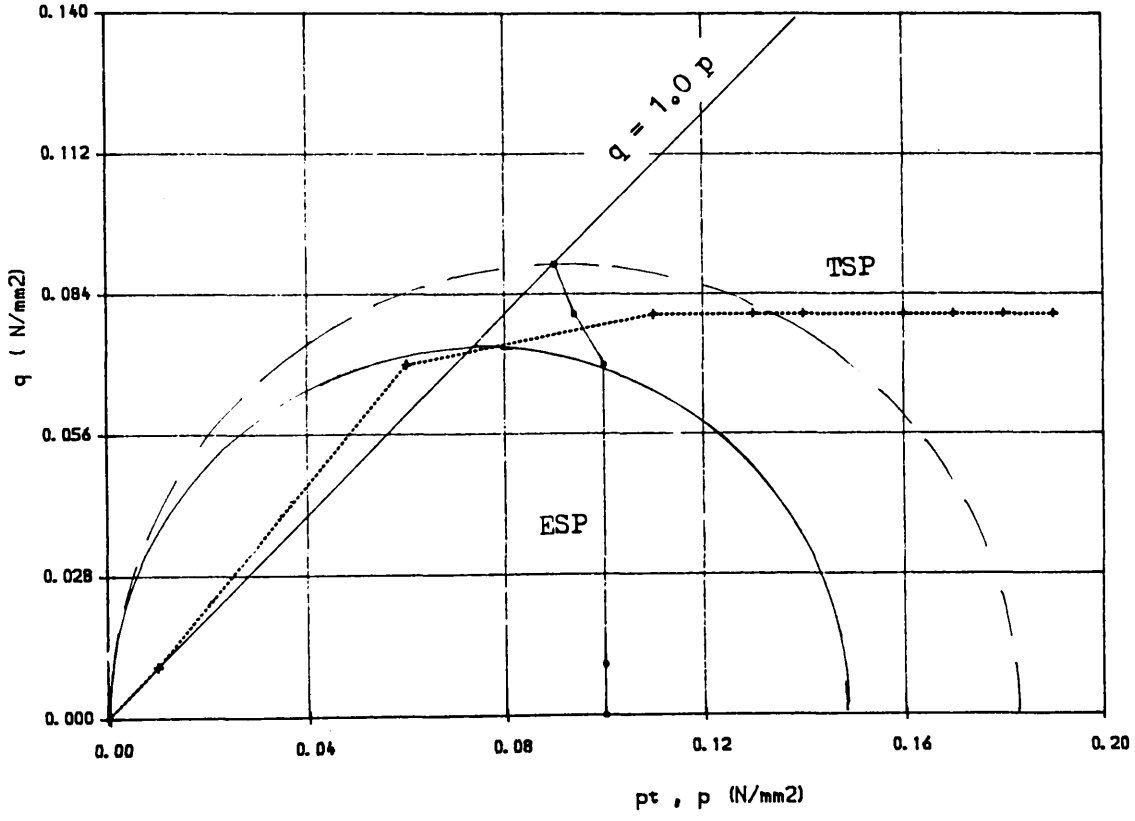

FIG. 4.110 STRESS PATHS FOR NC SOIL , ELEMENT 57
(Undrained conditions)

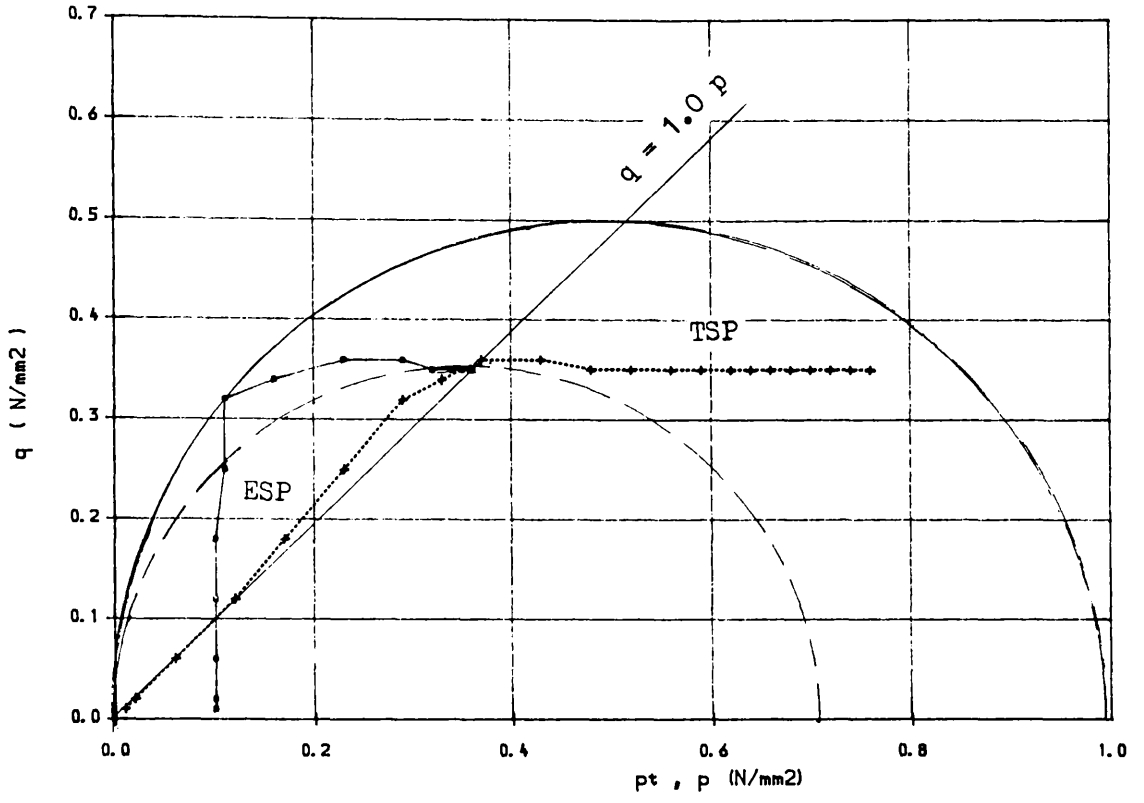

FIG. 4.111 STRESS PATHS FOR OC SOIL , ELEMENT 67
(Undrained conditions)

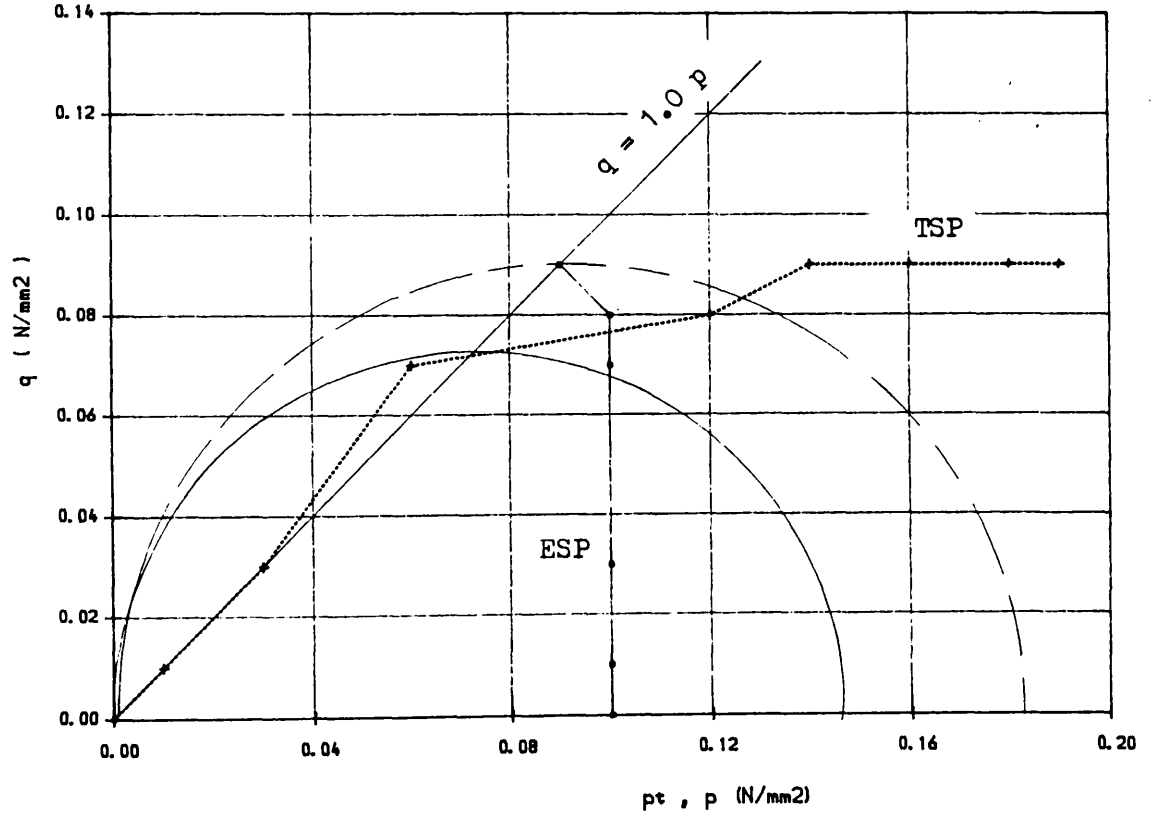

FIG. 4.112 STRESS PATHS FOR NC SOIL, ELEMENT 67
(Undrained conditions)

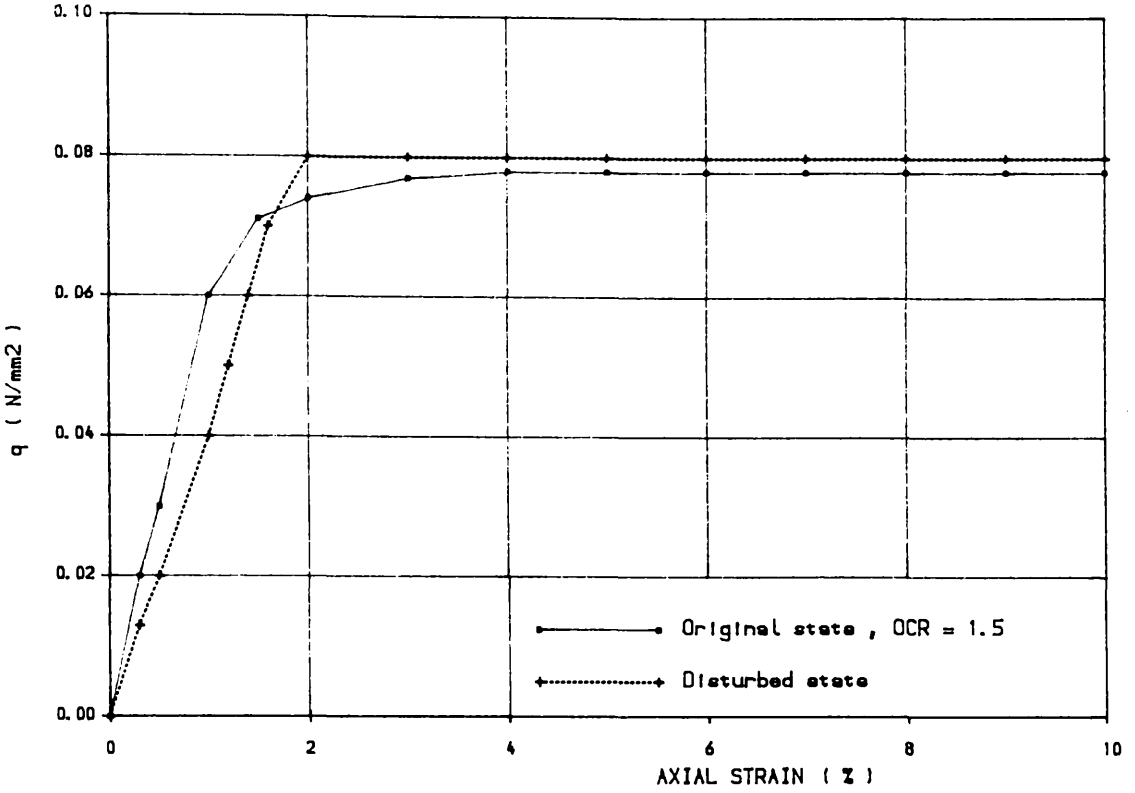

FIG. 4.113 STRESS-STRAIN BEHAVIOUR OF AMC CLAY
(Undrained test)

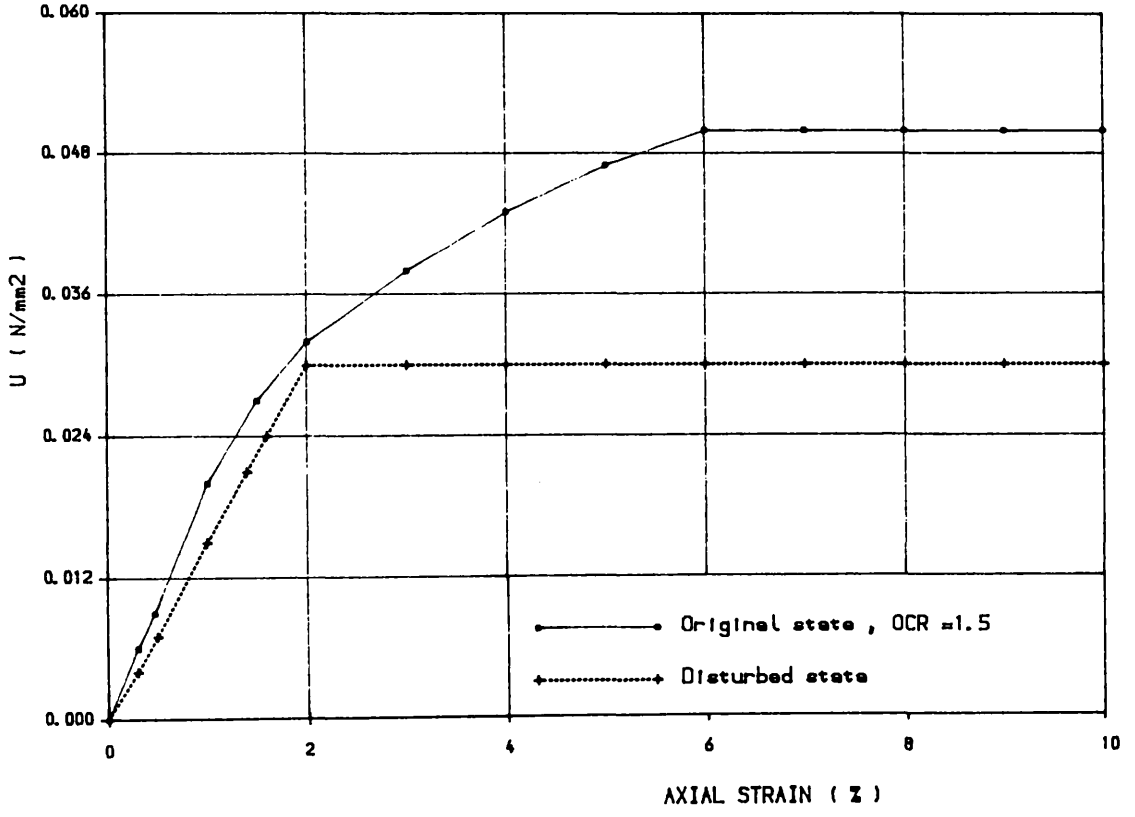

FIG. 4.114 PORE WATER PRESSURE RESPONSE OF AMC CLAY.
(Undrained test)

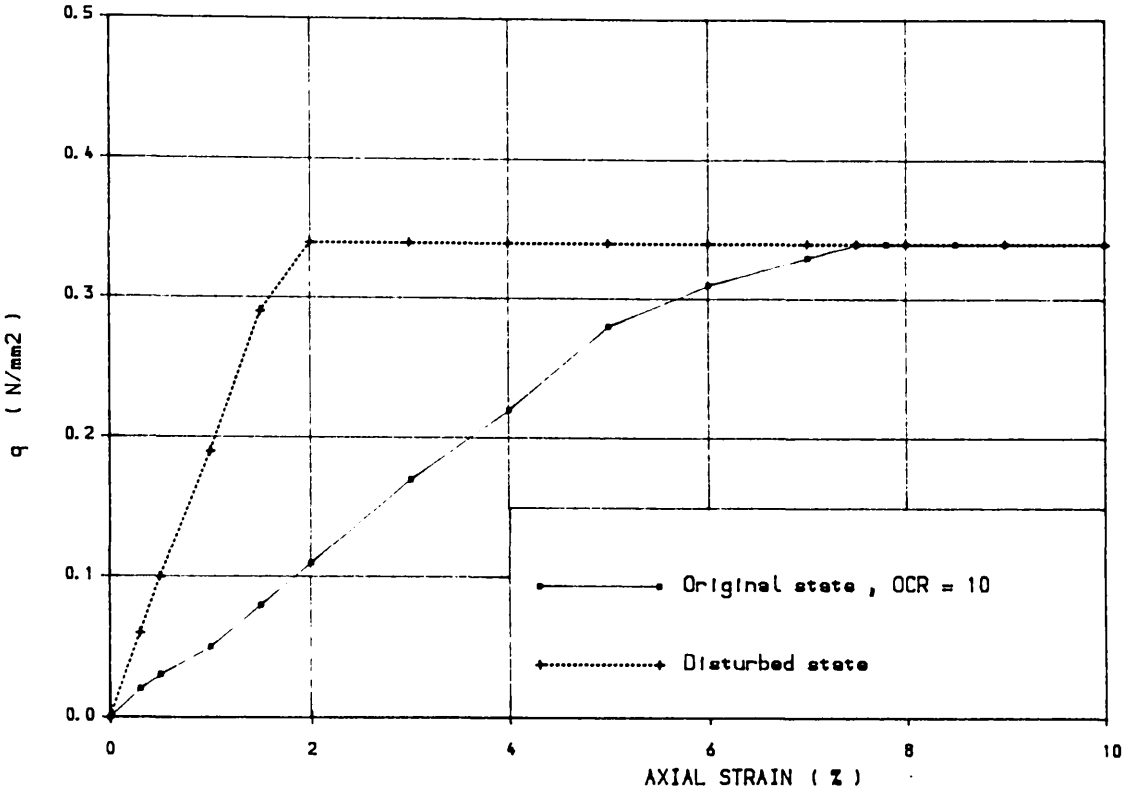

FIG. 4.115 STRESS-STRAIN BEHAVIOUR OF AMC CLAY
(Undrained test)

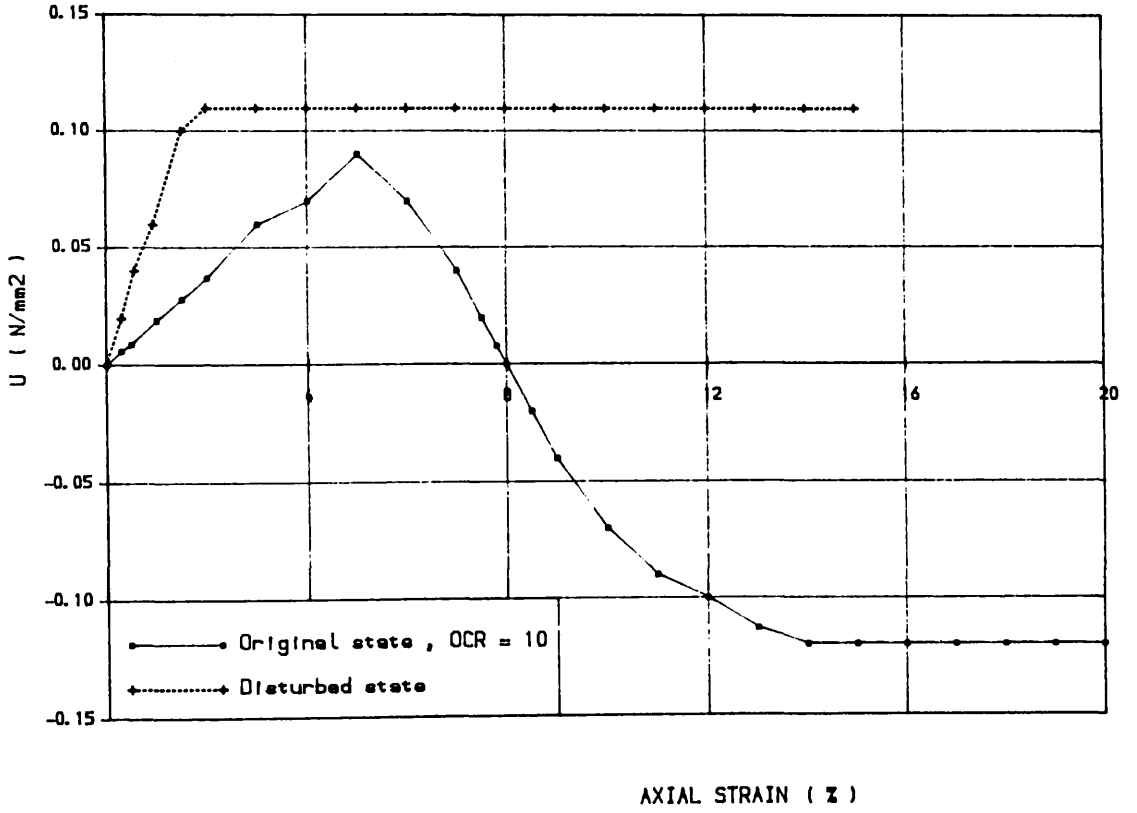

FIG. 4.116 PORE WATER PRESSURE RESPONSE OF AMC CLAY
(Undrained test)

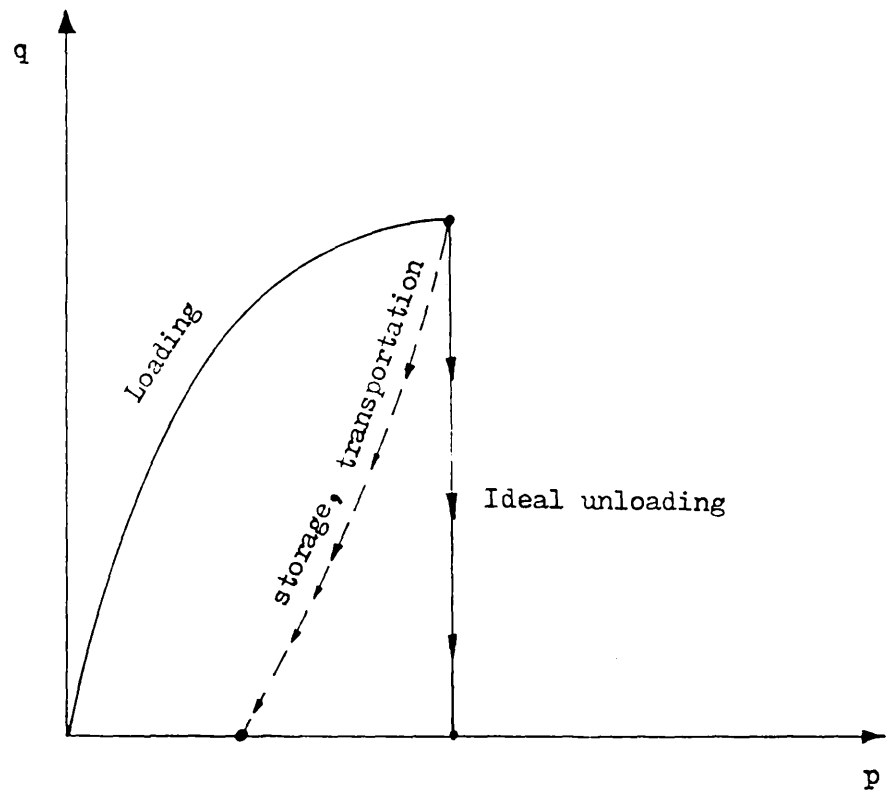

Fig. 4.117 Loading and unloading of a sample.

CHAPTER 5

GENERAL CONCLUSIONS AND RECOMMENDATIONS FOR FUTURE WORK

The work presented in this thesis describes a numerical (Finite Element Method) analysis of sampling disturbance in clay soils during the sampling operation. A review of previous theoretical and experimental studies illustrated the need for such an investigation since very few numerical studies have been reported in the literature. From the results obtained in this study it is shown that the factors having the greatest effects on sampling disturbance include sampler geometry (Diameter to thickness ratio (D/t), angle of cutting shoe, etc.), roughness of the sampling tube and soil history. Simulation of friction at the sampler/soil interface was made possible by the use of slip elements consisting of ordinary rectangular eight noded elements with aspect ratios (Length/thickness) of approximately 1/30 and specification of an adhesion factor α to model the reduced strength of the interface .

A total stress analysis under undrained conditions using the Von Mises criterion was carried out followed by an effective stress analysis using a critical state elastoplastic model. This chapter summarizes the most important conclusions which have been discussed in the two previous chapters and gives some suggestions for futur work.

5.1 Conclusions

a) Total stress analysis.

The results obtained in this section are most relevant to highly overconsolidated soils and the conclusions may be briefly summarized as follows:

1– Rough thick–walled tubes cause the greatest downdrag on samples during

penetration.

2– Significant shear develops between rough samplers and the surrounding soil resulting in greatly increased penetration resistance and considerable disturbance to the soil.

3– An increase in tube thickness results in increased disturbance to the soil, as defined by the area of yielded soil.

4– In general, yielding of the soil initiates close to the sampler tip and propagates along both sides of the sampling tube and into the soil below the sampler. Eventually, the yield zone reaches the central part of the sample ahead of the sampler tube.

5– The pore water pressure increases with depth along the centroidal axis of the sampler reaching a maximum value for rough thick tubes of 4 Cu. The maximum pore water pressures develop close to the tip and presumably water would migrate from the sides to the central portion of the sample. Negative pore water pressures may also develop locally as a result of severe shearing of the soil during the sampling operation.

b) Effective stress analysis.

This section was concerned with the effect of stress history of clay soils on sampling disturbance.

1– In the elastic state, the stress history has no effect on the soil response during the sampling operation.

2– In the plastic state, the effect of stress history on soil response is significant. For instance, the stress–strain behaviour and pore water pressure response are quite different for a highly overconsolidated clay in its original state and after sampling . Smaller differences in pore water pressure response and stress–strain behaviour were observed for a lightly overconsolidated clay.

5.2 Recommendations for future work.

Based on the findings of the present study, the following suggestions are made for further investigation.

1– To study further the problem of sampling disturbance using results obtained from instrumented tests on carefully controlled sampling operations.

2– To carry out further parametric studies for a wider range of soil properties and stress histories (perhaps using more sophisticated soil models).

3– To undetake a more rigorous treatment of the problem by means of a large deformation algorithm to trace the response throughout the sampling process.

4– To extend the scope of the study to incorporate the effects of subsequent extrusion and storage on soil properties.

REFERENCES

1- ALONSO,E., ONATE, E., and CARANOVAS, J.

An investigation into sampling disturbance.

Proceedings of the 10th international conference on soil mechanics and foundation engineering, 1981, Vol. 2, pp 419-423.

2- ARMAN, A., and McMANIS, K.L.

Effects of storage and extrusion on sample properties.

Soil specimen preparation for laboratory testing, ASTM, STP 599, American society for testing and materials, 1976, pp 56-87.

3- ATKINSON, J.H.

Foundations and slopes. An introduction to applications of critical state soil mechanics.

McGraw-Hill, 1981, London (U.K).

4- ATKINSON, J.H, and BRANSBY, P.L.

The Mechanics of Soils.

McGraw-Hill, 1978, London (U.K).

5- ATKINSON, J.H, and KUBBA, L.M.

Some effects on sample disturbance of soft clay.

Proceedings of the 10th international conference on soil mechanics and foundation engineering, Vol. 2, 1981, pp 423-426.

6- BALIGH, M.M.

The strain path method.

Journal of geotechnical engineering, ASCE, 1984, Vol 111, No 9, pp 1108-1136.

7– BALIGH, M.M, AZZOUZ, A.S and CHEN, C.T.

Disturbances due to "ideal" tube sampling.

Journal of geotechnical engineering, ASCE, 1987, Vol 113, No 7, pp 739–757.

8– BJERRUM, L.

Problems of soil mechanics and construction of soft clays.

State–of–the–art report to session 4, 8th international conference on soil mechanics and foundation engineering, 1973, Moscow, Vol 3, pp 111–153.

9– BISHOP, A.W., and HENKEL, D.J.

The measurement of soil properties in the triaxial test.

Edward Arnolds, 1962, 2nd. edition, London (U.K).

10– BRITTO, A.M., and GUNN, M.J.,

Critical state soil mechanics via finite elements.

Ellis Horwood Ltd, 1987, p 488.

11– BROMS, B

Soil sampling in Europe: State-of-the-art.

Journal of the geotechnical engineering division, 1980, ASCE, Vol. 106 SM1, pp 65–98.

12– CARTER, J.P., SMALL, J.C. and BOOKER, J.R.

A theory of finite elastic consolidation.

International journal of solids and structures, 1977, Vol 13, pp 467–478.

13– CHENG, Y.K., and YEO, M.F.

A practical introduction to finite element analysis.

Pitman publication Ltd, 1979.

14– DESAI, C.S.

Soil-structure interaction and simulation problems.

Chap. 7 in G. Gudehus (Ed.), Finite elements in geomechanics, Chichester, 1977.

15– DESAI, C.S.

Behaviour of interfaces between structural and geological media.

Proc. Int. Conf. on recent advances in geotech. earthquake eng. and soil dynamics, St Louis, Mo., 1981.

16– DESAI, C.S. and SIRIWARDANE, H.J.

Constitutive laws for engineering materials with emphasis on geological materials.

Prentice Hall, Inc., Englwood Cliffs, N.J., 1983.

17- DESAI, C.S., ZAMAN, M.M., LIGHTNER, J.G. and SIRAWARDANE, H.J.

Thin layer element for interfaces and joints.

Int. J. Anal. Methods Geom., 1984, Vol. 8, pp 19-43.

18– DAVIES, T.G. and BANERJEE, P.K.

Constitutive equations for ocean sediments subjected to stress and temperature gradients.

AERE–R–9775, HMSO, 1980, p 89.

19– EDEN, W.J.

Sampler trials in overconsolidated sensitive clays

Sampling of soil and rock, ASTM, STP 483, American society for testing and materials., 1971, pp 132–142.

20– GHABOUSSI, J., WILSON, E.L., ISENBERG, J.

Finite elements for rock joints and interfaces.

ASCE Soil mechanics, 1973, SM10, Vol. 99, pp 833–848.

21– GOODMAN, R.E., and TAYLOR, R.L.

A model for the mechanics of jointed rock.

ASCE Soil mechanics, 1968, SM3, Vol. 94, pp 637–659.

22– GRIFFITHS, D.V.

Numerical modeling of interfaces using conventional finite elements.

5th international conference on numerical methods in geomechanics, Vol. 9, pp 837–844. 1982

23– HERRMAN, L.R.

Finite element analysis of contact problems.

Journal of engineering division, 1978, ASCE, 104, EMS, pp 1043–1057.

24– HEUZE, F.E. and BARBOUR, T.G.

New models for rock joints and interfaces.

Journal of geotechnical division, ASCE, 1973, Vol. 99, pp 887–908.

25– HINTON, E. and OWEN, D.R

Finite element programming.

Academic press, 1977.

26– OWEN, D.R and HINTON, E.

Finite elements in plasticity.

Pineridge Press, 1980

27– HVORSLEV, M.J.

Subsurface exploration and sampling of soils for civil engineering purposes.

Report on a research project of ASCE, U.S.Army, 1949, Engineer experiment station, Vicksburg.

28– KALLSTENIUS, T.

Discussions, specialty session on techniques of field measurement and sampling.

Proceedings, 4th international conference on soil mechanics and foundation engineering, London, 1957.

29– *KALLSTENIUS, T.*

Mechanical disturbances in clay samples taken with piston sampler.

Proceedings of the Swedish geotechnical institute, 1958, No 16, Stockholm.

30– KALLSTENIUS, T.

Studies on clay samples taken with standard piston sampler.

Proceedings of the Swedish geotechnical institute, 1963, No. 21, p 207.

31– KALLSTENIUS, T.

Secondary mechanical disturbance effects in cohesive soil samples.

Proceedings on specialty session, quality of soil sampling, 4th Asian conference, international society for soil mechanics and foundation engineering, Bangkok, 1971.

32– KARIM, U.F.

Large deformation analysis of penetration problems involving piles and sampling tubes in soils.

Ph.D thesis, State university of New York at Buffalo, 1984, p159.

33– KATONA, M.G.

A simple contact-friction interface element with applications to buried culverts.

International journal for numerical and analytical methods in geomechanics, 1983, Vol. 7, pp 371–384.

34– KIMURA, T. and SAITOH, M.

The influence of disturbance due to sample preparation on the undrained strength of saturated cohesive soil.

Soils and foundations, Japan society of soil mechanics and foundation engineering, 1982, Vol. 22, No. 4, pp 109–120.

35– KIRKPATRICK, W.M. and RENNIE, I.A.

Stress relief effects in deep sampling operations.

Underwater construction conference , University College, Cardiff, 1975.

36– LADD, C.C. and LAMBE, T.W.

The strength of undisturbed clay determined from undrained tests.

Laboratory shear testing of soils, ASTM, STP 361, 1963, pp 342–371.

37– LADD, C.C and BAILEY, W.A.

Correspondence on the behaviour of saturated clays during sampling and testing.

Geotechnique, Vol. 4, No. 4, 1964, pp 353–358.

38– LAMBE, T.W.

Residual pore pressures in compacted clay.

Proceedings, 5th international conference on soil mechanics and foundation engineering,1961, Vol. 1, pp 207–211.

39– LAMBE, T.W. and WHITMAN, R.V.

Soil mechanics, SI version.

John Wiley and sons, 1979.

40– LANG, J.G.

Longitudinal variations of soil distribution within tube samplers.

Proceedings of the 5th Australian–New Zealand conference on soil mechanics and foundation, 1967, Vol. 1, pp 39–42.

41– LANG, J.G.

Forces on an open-drive sample in stiff clay.

Proceedings of the specialty session on quality in soil sampling, 4th Asian conference, international society of soil mechanics and foundation eng., Bangkok, 1971.

42– LA ROCHELLE, P. and LEFEVRE, G.

Sampling disturbance in Champlain clays.

A.S.T.M., 1971, pp 143–163.

43– LA ROCHELLE, P., SARRAILH, J., TAVENAS, F., ROY, M. and LEROUEIL,S.

Causes of sampling disturbance and design of a new sampler for sensitive soils.

Canadian geo. journal, Vol. 18, 1981, pp 52–66.

44– MEROUANI, Z.

A numerical study of plate anchors embedded in sand.

MSc thesis, Glasgow university (U.K.), 1988, p 212.

45– NAYLOR, D.J. and PANDE, G.N.

Finite elements in geotechnical engineering

Pineridge press, Swansea, U.K., 1981.

46– NOORANY, I., and SMITH, H.B.

In-situ strength characteristics of soft clays.
Journal of the soil mechanics and foundation division, ASCE, Vol. 91, SM2, Proceeding paper 4274, 1965, pp 49–50.

47– OKUMURA, T.
The variation of mechanical properties of clay sampling depending on its degree of disturbance.
Proceedings of the specialty session on quality in soil sampling, Bangkok, 1971, pp 73–81.

48– PANDE, G.N. and SHARMA, K.G.
On joint/interface elements and associated problems of numerical ill-conditioning .
Int. J. Num. Anal. Methods Geom., Vol. 3, 1979, pp 293–300.

49– ROSCOE, K.H., SCHOFIELD, A.N. and WROTH, C.P.
On yielding of soils.
Geotechnique, 1958, 8, No. 1, pp 22–53.

50– SCHJETNE, K.
The measuremant of pore pressure during sampling.
Proceedings on the specialty session on quality in soil sampling, 1971, pp 12–15.

51– SEED, H.B., NOORANY, I. and SMITH, I.M.
Effects of sampling and disturbance on the strength of soft clays.
Report No. TE–64–1, Institute of engineering research , university of California, Berkeley, 1964.

52– SKEMPTON, A.W. and SOWA, V.A.

The behaviour of saturated clays during sampling and testing.

Geotechnique, Vol. 13, No. 4, 1963, pp 269–290.

53– SLOAN, S.W. and RANDOLPH, M.F.

Numerical prediction of collapse loads using finite element methods.

Int. J. Num. Anal. Methods Geom., 1982, 6, pp 47–76.

54– SOAN, S., TSUCHIYA, H. and SAITO, Y.

The deformation of a soil sample during extrusion from a sample tube.

Proceedings of the specialty session on quality in soil sampling, Bangkok, 1971, pp 3–6.

55– TAYLOR, D.W.

Fundamentals of soil mechanics.

Wiley, New York, 1948.

56– TERZAGHI, K. and PECK, R.

Soil mechanics in engineering practice.

Wiley and Sons, 1967, Second edition.

57– TIMOSHENKO, S.P and GOODER, J.N.

Theory of elasticity.

Third edition, 1970, Mc Graw–Hill, New York.

58– WILSON, E.L.

Finite elements for foundations, joints and fluids.

Chapter 10 in G. Gudehus (Ed), Finite elements in geomechanics, Wiley, Chichester, 1977.

59– ZAMAN, M.M., DESAI, .C.S. and DRUMN, C.

Interface model for dynamic soil-structure interaction.

J. of Geo. Eng., ASCE, Vol. 110, No. 9, 1984, pp 1257–1273.

60– ZAMAN, M.M.

Thin layer element and modelling of interface behaviour in soil– structure interaction.

Fifth Int. Conf. on Num. Methods Geom., Nagoya, 1985, pp 1796–1803.

61– ZIENKIEWICZ, O.C.

The finite element method.

Third edition, 1977, Mc Graw–Hill, London.

62– ZIENKIEWICZ, O.C., JAIN, P. and ONATE, E.

Flow of solids during forming and extrusion: some aspects of numerical solutions.

International journal of solids and structures, Vol. 14, pp 15–38, 1978.

APPENDIX

```
      PROGRAM CLAYS
C*************************************************
C  *
C  *                    CLAYS
C  *     THIS PROGRAM SIMULATES SOIL BEHAVIOUR
C  *    UNDER DRAINED AND UNDRAINED CONDITIONS.
C  *     TEST CONDITIONS. IT GIVES THE EFFECTIVE
C  *     AND TOTAL STRESS VECTORS FOLLOWING
C  *      A STRAIN PATH.
C  *     MODEL: "ASSOCIATED MODIFIED CAM CLAY"
C  *     THE YIELD SURFACE IS ELLIPTIC AND
C  *     THE FLOW RULE IS ASSOCIATED.
C  *
C*************************************************************
    C
      COMMON/PA/AX(4),BX(4),DX(4,4),DPX(4,4),DA(4),BD(4),DABD(4,4)
      COMMON/PB/AMDA,CAPA,PS,E0,ES,PHI,DEVP,DEDP,EE
      COMMON/PC/ESTRS(4),STRES(4),STRAN(4),SS(4),SN(4)
      COMMON/PD/P0,EM,PP,QQ,IYILD,NLOAD,ILOAD
      COMMON/PE/IDRAN,NYILD(10),NLOOP,NPRINT
C
C*****      READ DATA****
C
      READ(5,*) IDRAN
      READ(5,*) NLOAD
      READ(5,*) (STRES(I),I=1,4)
      READ(5,*) (SN(I),I=1,4)
      WRITE(6,112) SN
 112  FORMAT(1P4E11.2)
      READ(5,*) AMDA,CAPA,PS,E0,PHI
      READ(5,*) P0
C
C***      INITIALIZATION OF VARIABLES ****
C
      DO 5 I=1,4
      STRAN(I)=0.0
      ESTRS(I)=STRES(I)
5          CONTINUE
      EPSIV=0.0
      EPSID=0.0
      DEVP=0.0
      DEDP=0.0
      QQ0=0.0
      PWP=0.0
      EE=E0
      PI23=2.0944
      EPSH=0.01
       TP=(STRES(1)+STRES(2)+STRES(3))/3.0

      P00=P0
      NLOOP=10
      NPRINT=NLOAD/NLOOP
      WRITE(6,820)
      WRITE(6,830)
      IF(IDRAN.EQ.0) THEN
      WRITE(6,840)
      ELSE
      WRITE(6,845)
      ENDIF
      WRITE(6,850) AMDA,CAPA,PS,E0,PHI
      WRITE(6,860) P0
      WRITE(6,870)
      PHI=0.01745*PHI
C
```

```
C***       LOOP OVER LOADS , COMPUTING DEVIATORIC
C    *    AND MEAN STRESSES.
C
      DO 810 IPRINT=1,NPRINT
      DO 800 ILOOP=1,NLOOP
      QA=(ESTRS(1)-ESTRS(2))**2
      QB=(ESTRS(2)-ESTRS(3))**2
      QC=(ESTRS(3)-ESTRS(1))**2
      QD=6.0*ESTRS(4)*ESTRS(4)
      QE=0.5*(QA+QB+QC+QD)
      QQ=SQRT(QE)
      PP=(ESTRS(1)+ESTRS(2)+ESTRS(3))/3.0
C
C***       PRINCIPAL STRESSES AND MOHR-COULOMB
C***     COEFFICIENT  (M)
C
      IF(SN(2).EQ.SN(3)) THETA=0.5236
      IF(SN(2).EQ.SN(1)) THETA=-0.5236
      SIGMA1=PP-2.0*QQ*SIN(THETA-PI23)/3.0
      SIGMA2=PP-2.0*QQ*SIN(THETA)/3.0
      SIGMA3=PP-2.0*QQ*SIN(THETA+PI23)/3.0
      RATIO=(SN(2)-SN(3))/(SN(1)-SN(3))
      EM0=6.0*SIN(PHI)/(3+SIN(PHI))
      EM1=6.0*SIN(PHI)/(3-SIN(PHI))
      EM=(1.0-RATIO)*EM1+RATIO*EM0
C          SLOPE=(1.0+RATIO)/3.0
      SLOPE=1.0/3.0
      ES=3.0*PP*(1.0+EE)*(1.0-2.0*PS)/CAPA
C
C***       ELASTIC CONSTITUTIVE MATRIX **
C
      DO 10 I=1,4
      DO 10 J=1,4
 10   DX(I,J)=0.0
      CA=ES/((1+PS)*(1.0-2.0*PS))
      CB=1.0-PS
      DX(1,1)=CB*CA
      DX(1,2)=PS*CA
      DX(1,3)=PS*CA
      DX(2,1)=PS*CA
      DX(2,2)=CB*CA
      DX(2,3)=PS*CA
      DX(3,1)=PS*CA
      DX(3,2)=PS*CA
      DX(3,3)=CB*CA
      DX(4,4)=0.5*ES/(1.0+PS)
C
C****       CHECK IF ELEMENT HAS YIELDED
C
      IYILD=1
      F=PP*PP-PP*P0+QQ*QQ/(EM*EM)
      P0C=PP+QQ*QQ/(PP*EM*EM)
      EPS=EPSH*P0*P0
      EPS=ABS(EPS)
      IF(F.GT.EPS.OR.F.LT.-EPS) THEN
      IYILD=0.0
      DO 300 I=1,4
      DO 300 J=1,4
 300  DPX(I,J)=DX(I,J)
      ELSE
      EPSI=ABS(P0-P0C)/P0
      IF(EPSI.GE.0.01) IYILD=2
      CALL DPMAT
      ENDIF
```

```
      NYILD(ILOOP)=IYILD
C
C***      COMPUTE NEW STRAINS AND STRESSES ***
C
      DO 210 I=1,4
 210  SS(I)=0.0
      DO 220 I=1,4
      DO 220 J=1,4
      SS(I)=SS(I)+DPX(I,J)*SN(J)
 220  CONTINUE
      DO 240 K=1,4
      STRAN(K)=STRAN(K)+SN(K)
      ESTRS(K)=ESTRS(K)+SS(K)
 240  CONTINUE
C
C      *** COMPUTE EFFECTIVE AND TOTAL STRESSES  ***
C      *** COMPUTE PORE WATER PRESSURE ***
C
      QAD=(SS(1)-SS(2))**2
      QBD=(SS(2)-SS(3))**2
      QCD=(SS(3)-SS(1))**2
      QDD=6.0*SS(4)*SS(4)
      QED=0.5*(QAD+QBD+QCD+QDD)
      QQDOT=SQRT(QED)
      EPDOT=(SS(1)+SS(2)+SS(3))/3.0
      IF(IDRAN.EQ.0) GOTO 760
      TPDOT=EPDOT
      DEVE=3.0*EPDOT*(1.0-2.0*PS)/ES
      DEVEP=DEVE+DEVP
      EPSIV=EPSIV+DEVEP
      DEDE=2.0*(1.0+PS)*QQDOT/(3.0*ES)
      DEDEP=DEDE+DEDP
      EPSID=EPSID+DEDEP
      EDOT=-(1.0+EE)*DEVEP
      EE=EE+EDOT
      IF(EE.LT.0.0) THEN
      WRITE(6,960)
      STOP
      ELSE
      CONTINUE
      ENDIF
      GO TO 780
 760  CONTINUE
      TPDOT=SLOPE*QQDOT
      IF(QQ0.GT.QQ) TPDOT=-TPDOT
      DEVP=-3.0*EPDOT*(1.0-2.0*PS)/ES
 780  CONTINUE
      UDOT=TPDOT-EPDOT
      PWP=PWP+UDOT
      DO 790 I=1,3
 790  STRES(I)=STRES(I)+SS(I)+UDOT
      STRES(4)=STRES(4)+SS(4)
      TP=TP+TPDOT
      UDP=PWP/P00
      QDP=QQ/P00
      QQ0=QQ
      P0=P0+(1.0+EE)*P0*DEVP/(AMDA-CAPA)
C
 800  CONTINUE
      WRITE(6,920) STRAN(1),STRES(1),ESTRS(1),EE,TP
     .      ,PP,QQ,PO,UDP,EPSIV,EPSID
      WRITE(6,930) STRAN(2),STRES(2),ESTRS(2)
      WRITE(6,930) STRAN(3),STRES(3),ESTRS(3)
      WRITE(6,940) STRAN(4),STRES(4),ESTRS(4),(NYILD(I),I=1,10),EM
```

```
 810  CONTINUE
 820  FORMAT(20X,36HELASTO-PLASTIC BEHAVIOUR OF CAM CLAY,///)
 830  FORMAT(10X,33HN.C. CLAY - Q=ELLIPSE   F=ELLIPSE,/)
 840  FORMAT(10X,19HUNDRAINED BEHAVIOUR,//)
 845  FORMAT(10X,17HDRAINED BEHAVIOUR,//)
 850  FORMAT(4X,7HLAMDA =,1PE10.2,5X,7HKAPPA =
     .          ,1P10.2,5X,9HPOISSON =,1PE10.2,
.    5X,6HVOID =, 1PE10.2,5X,5HPHI =,1PE10.2)
 860  FORMAT(4X,21HPAST MAXIMUM STRESS =,1PE10.2)
 870  FORMAT(//,1H0,'STRAIN   TOT.STRESS  EFF.STRESS
. VOID   TOT.P    EFF.P    Q      EFF.P0
. Q/P0  U/P0   V-STRAIN  D-STRAIN)
 920  FORMAT(/,1P12E11.2)
 930  FORMAT(1P3E11.2)
 940  FORMAT(1P3E11.2,4X,10I1,4X,3HM =,1PE9.2)
 950  FORMAT(7HSIGMA1=,1PE9.2,5X,7HSIGMA2=
     .  ,1PE9.2,FHSIGMA3=,1PE9.2)
 960  FORMAT(36H*** NEGATIVE VALUE OF VOID RATIO ***)
      STOP
      END
      SUBROUTINE DPMAT
C
C-       - - - - - - - - - - - - - - - - - - - - - - - - - - - - -
C          **   THIS SUBROUTINE COMPUTES THE ELASTO-PLASTIC
C                    CONSTITUTIVE MATRIX
C
C-       - - - - - - - - - - - - - -  - - - - - - - - - - - - - -
      COMMON/PA/AX(4),BX(4),DX(4,4),DPX(4,4),DA(4),BD(4),DABD(4,4)
      COMMON/PB/AMDA,CAPA,PS,E0,ES,PHI,DEVP,DEDP,EE
      COMMON/PC/ESTRS(4),STRES(4),STRAN(4),SS(4),SN(4)
      COMMON/PD/P0,EM,PP,QQ,IYILD,NLOAD,ILOAD
      COMMON/PE/IDRAN,NYILD(10),NLOOP,NPRINT
C
      EM2=EM*EM
C
C***              ..... DERIVATIVES .....
C
      DP=1.0/3.0
      IF(QQ.EQ.00) THEN
      DQA=1.5
      DQB=1.5


      DQC=1.5
      DQD=1.5
      ELSE
      DQA=1.5*(ESTRS(1)-PP)/QQ
      DQB=1.5*(ESTRS(2)-PP)/QQ
      DQC=1.5*(ESTRS(3)-PP)/QQ
      DQD=3.0*ESTRS(4)/QQ
      ENDIF
C
      DPE=P0*(1.0+EE)/(AMDA-CAPA)
      DQE=0.0
C
      DFP=2.0*PP-P0
      DFQ=2.0*QQ/EM2
      DQP=DFP
      DQQ=DFQ
      DFP0=-PP
      DFQ0=0.0
      DQQP=DQQ/DQP
      GAMA=DFP0*DPE*DQP+DFQ0*DQE*DQQ
C
```

```
      AX(1)=DP*DQP+DQA*DQQ
      AX(2)=DP*DQP+DQB*DQQ
      AX(3)=DP*DQP+DQC*DQQ
      AX(4)= DQD*DQQ
      BX(1)=AX(1)
      BX(2)=AX(2)
      BX(3)=AX(3)
      BX(4)=AX(4)
C
CC       ***  ELASTO-PLASTIC CONSTITUTIVE MATRIX ***
C
      DO 30 I=1,4
      DA(I)=0.0
      DO 20 K=1,4
      DA(I)=DA(I)+DX(I,K)*AX(K)
   20 CONTINUE
   30 CONTINUE
      DO 50 J=1,4
      BD(J)=0.0
      DO 40 K=1,4
      BD(J)=BD(J)+BX(K)*DX(K,J)
   40 CONTINUE
   50 CONTINUE
      DO 70 I=1,4
      DO 60 J=1,4
      DABD(I,J)=DA(I)*BD(J)
   60 CONTINUE
   70 CONTINUE
      BDA=0.0
      DO 80 I=1,4
      BDA=BDA+BD(I)*AX(I)
   80 CONTINUE
      CONST=1.0/(BDA-GAMA)
      DO 100 I=1,4
      DO  90 J=1,4
      DPX(I,J)=DX(I,J)-CONST*DABD(I,J)
   90 CONTINUE
  100 CONTINUE
      IF(IDRAN.EQ.0.0) RETURN
      BDSN=0.0
      DO 110 I=1,4
      BDSN=BDSN+BD(I)*SN(I)
  110 CONTINUE
      DAMDA=BDSN*CONST
      DEVP=DAMDA*DQP
      DEDP=DAMDA*DQQ
      RETURN
      END
```